UNIVERSIDADE DE LISBOA
FACULDADE DE CIÊNCIAS
DEPARTAMENTO DE ENGENHARIA GEOGRÁFICA, GEOFÍSICA E ENERGIA


# The land-atmosphere coupling and climate extremes in Africa

João António Martins Careto

**Mestrado em Ciências Geofísicas**
Especialização em Meteorologia

Dissertação orientada por:
Doutora Rita M. Cardoso
E
Professor Doutor Pedro M.M Soares

2017

# Dedicatory

To my advisors Professor Doctor Pedro Soares and Doctor Rita Cardoso for the introduction in this thematic, as well for the precious teachings and advices which contributed to the valorization of this work.

To *Climate Research Unit, Global Precipitation Climatology Centre, FLUXNET* global network and *Global Land Evaporation Amsterdam Model* for the available observationally based data.

To my colleagues from the Climate Modeling Laboratory, from the Instituto D. Luiz (Faculdade de Ciências da Universidade de Lisboa), for all the availability, help and precious advices given.

To my friends and colleagues from Faculdade de Ciências da Universidade de Lisboa, for all the support and help during this work.

To my family and friends, for all the support, help and understanding, making this work possible.

To all of you that somehow supported and helped me, facilitating the development of this work.

# Abstract

Soil moisture is one of the most important variables of the climate system as it constrains evapotranspiration, affecting the water and energy balances at the surface, mainly over transition areas between humid and dry climates. An analysis of the energy and moisture balance, heat waves and droughts for the Africa Coordinated Regional Downscaling Experiment (Africa-CORDEX) is performed in present climate and used to evaluate heat and moisture projections for the future. Two different RCM sets from Africa-CORDEX were exploited. One is driven by ERA-Interim reanalysis (1990-2008) and the other by Atmosphere-Ocean Global Circulation Models (AOGCMs) from the Coupled Model Intercomparison Project (CMIP5, 1960-2100), featuring the Intergovernmental Panel on Climate Change (IPCC) RCP4.5 and RCP8.5 scenarios, and focused in two periods (1971-2000 and 2071-2100). Multi-Model ensembles means were produced, for better assessing changes for the future, as well as the relationship between the fluxes partitioning and heat waves. Precipitation, Soil Moisture, Latent and Sensible Heat Fluxes, Mean, Maximum and Minimum Temperatures are also assessed and validated against observationally based databases (CRU, GPCC, FLUXNET and GLEAM) for seasonal and climatological time-scales. Overall, models display a good agreement with observations, except for some cases where strong biases are found over large areas of Africa. The multi-model ensemble is found to perform better than individual models. However, the few observations over Africa, limit the validation of individual variables and different metrics. The 10 days non-overlapping mean correlations between latent and sensible heat fluxes and, between latent and maximum temperatures are used to assess the seasonal coupling strength. Also, the Bowen ratio and the Evaporative Fraction are computed in order to evaluate the different climate evolutions and coupling for each model. Overall, all models can represent the strong soil moisture-temperature coupling regions, where those areas coincide with transition zones identified on both Bowen ratio and Evaporative Fraction. However, differences are found for individual RCMs meaning that each model represents its own reality. These strong coupling regions also correspond to regions of more heat wave events in present climate. Nonetheless, in present climate, soil moisture-temperature feedback not influence heat wave event duration, which seems to be controlled by the synoptic conditions. In future, more heat waves are expected in Africa due to an increase of mean surface temperature, but also due to changes in the spatial distribution of strong coupling regions. Drought is assessed for both Hindcast and CMIP5 simulations (Historic, RCP8.5 and RCP4.5) with the SPEI index. In the future, for both scenarios, all models agree with longer and more intense droughts over Africa. Additionally, a new coupling metric is introduced, for monthly time-scales, which considers the positive temperature extremes and the negative latent heat flux extremes. In areas where negative soil moisture anomalies influence the flux partitioning, leading to a surface increase of temperature, this metric correlate well with lower mean SPEI values for a determined period.

Keywords: CORDEX; Coupling; Heat Wave; SPEI; Magnitude.

# Resumo

A humidade do solo é uma das variáveis mais importantes no contexto do acoplamento terra-atmosfera. Em certas regiões, a humidade do solo é a principal variável que constringe a evapotranspiração, afetando o balanço energético à superfície, podendo assim afetar a temperatura na baixa troposfera. Em regiões onde anomalias negativas de humidade do solo influenciem a temperatura, eventos de seca podem levar a situações em que anomalias da temperatura sejam muito superiores áquilo que seriam em condições normais e a intensificação de eventos de onda de calor. Neste trabalho, efetua-se uma comparação entre as regiões de forte e fraco acoplamento com a distribuição espacial do número e duração média de eventos de ondas de calor, bem como uma caracterização presente e futura de secas sobre o continente africano, tendo como base modelos regionais retirados do portal do Coordinated Regional Downscaling Experiment (Africa-CORDEX) para a região de África. Duas simulações foram consideradas, uma onde os modelos regionais são forçados pela reanálise ERA-Interim (simulação *Hindcast*) de 1990 a 2008, e outra onde os modelos regionais são forçados por modelos de circulação global (Atmosphere Ocean Coupled Circulation Models, AOGCMs) de 1960 a 2100. O forçamento dos AOGCMs foi obtido a partir do portal do projeto de Intercompação de modelos fase 5 (Coupled Model Intercomparison Project Phase 5, CMIP5), considerando dois senários de forçamento radiativo no final do século XXI do IPCC: RCP 4.5 e RCP 8.5. Neste ultimo caso, a simulação é dividida em dois períodos: *Historic* (1971-2000) para caracterizar o clima presente, e *Future* (RCP4.5 e RCP8.5 ambos no período 2071-2100) para caracterizar o clima futuro. A análise para o clima presente é feita principalmente com *Historic*, onde a simulação *Hindcast* é usada para validar as diferentes métricas consideradas, e para o RCP8.5, onde neste caso, anomalias entre RCP8.5 e *Historic* são consideradas. Ambos os cenários apresentam resultados semelhantes, mas a amplitude das diferenças para o RCP8.5 é superior. Todas as variáveis consideradas neste trabalho (precipitação, humidade do solo, fluxos de calor latente e sensível e ainda temperaturas médias, máximas e mínimas) foram avaliadas e validadas, à escala sazonal e também à escala climatológica, em relação a bases de dados construídas baseadas em observações (CRU, GPCC, FLUXNET e GLEAM). A validação é feita tendo como base mapas sazonais e climatológicos de viés para a precipitação e temperaturas, e mapas sazonais de viés para as outras variáveis. Diagramas de Taylor foram também considerados. Estes diagramas são úteis, pois permitem avaliar um modelo, em relação a uma referência, em termos de desvio padrão, correlação e erro médio quadrático para médias sazonais e climatológicas. De um modo geral, com algumas exceções, todos os modelos conseguem caracterizar o clima médio e sazonal de África. No entanto alguns modelos, em certas regiões apresentam anomalias elevadas relativamente às observações. O acoplamento entre a humidade do solo e temperatura é avaliado sazonalmente para África, considerando as correlações entre calor latente e sensível e entre calor latente e temperatura máxima, calculadas a partir de médias de 10 dias não sobrepostas. De modo geral, todos os modelos são capazes de representar as principais zonas de forte acoplamento, apresentando diferenças nas distribuições espaciais destas regiões, e que comparando com a razão de Bowen e Fração Evaporativa, correspondem a zonas de transição entre climas húmidos e áridos (i.e., climas tipo mediterrâneo). Para as ondas de calor, foi calculado o número médio de eventos normalizado pelo número de anos de cada modelo, e ainda a duração média das ondas de calor. Ambas as métricas foram determinadas para todos os períodos. No clima presente, não existe qualquer relação entre a duração média de eventos com as zonas de forte e fraco acoplamento, onde a duração é controlada principalmente pelas condições sinóticas. No entanto, existe uma relação entre o número de ondas de calor com as zonas de forte acoplamento, onde mais eventos são espectáveis de ocorrer nestas zonas em relação à média. No futuro, num cenário de alterações climáticas e com o

incremento do balanço de radiação à superfície, tanto o calor latente como o calor sensível também aumentam, de modo a manter o balanço energético à superfície, o que consequentemente leva a um aumento da temperatura à superfície. No entanto, previsões de alterações nos padrões e frequência de precipitação a nível global e aumento da capacidade de retenção de água pela atmosfera, devido ao incremento da temperatura, podem levar a uma redução geral da humidade do solo, especialmente em zonas de forte acoplamento. Esta diminuição da água disponível provoca uma anomalia negativa permanente da evapotranspiração em relação às condições presentes, levando a um subsequente aumento do fluxo de calor sensível e consequente aumento da temperatura. Para além disso, no futuro, uma expansão das regiões de forte acoplamento é previsível, onde em algumas situações, zonas que no presente são consideradas de fraco acoplamento, periodicamente ou permanentemente poderão passar a ser consideradas de regiões de forte acoplamento. Nas áreas consideradas de forte acoplamento, no presente, onde a evapotranspiração não é muito elevada, no futuro transformar-se-ão em zonas áridas ocorrendo um desacoplamento da superfície. Para além disso, no futuro, um aumento significativo na frequência e duração de ondas de calor é esperado por toda a África, exceto nas zonas mais áridas. Este aumento deve-se essencialmente ao incremento da temperatura média, mas também devido ao aumento da média e variabilidade da temperatura, provocadas pelo diferente balanço entre os fluxos. A caracterização dos eventos de secas é feita para cada período usando o índice SPEI (Standardized Precipitation Evapotranspiration Index), de modo a determinar o número de meses, fração da área com diferentes intensidades (moderada, severa e extrema) e duração média de cada evento de seca. O índice SPEI para ambos os cenários RCP, é calibrado com os valores referentes ao período *Historic*. No futuro, apesar dos modelos exibirem diferentes resultados entre si, todos apontam no sentido de um aumento da duração e intensidade de eventos de seca. Para além da análise feita anteriormente, uma nova medida para o acoplamento entre a humidade do solo e temperatura é introduzida aqui. Esta nova métrica resulta da soma, num determinado número de meses, da multiplicação diária entre extremos positivos da temperatura máxima e extremos negativos do fluxo de calor latente, sendo comparável com os valores médios do SPEI para esses meses. Esta métrica é avaliada para períodos de ondas de calor no continente Africano, já estudadas anteriormente. Magnitudes elevadas desta métrica correspondem a situações em que anomalias negativas da humidade do solo, efetivamente influenciam a temperatura à superfície durante ondas de calor, para uma região específica. Nessa região, existe alguma correspondência com valores negativos médios do índice SPEI. No entanto em zonas de fraco acoplamento, eventos de seca muito intensos e duradouros podem provocar situações onde a evapotranspiração passe a ser restringida pela humidade do solo e não pela energia disponível.

Palavras-chaves: CORDEX; Acoplamento; Ondas de Calor; SPEI; Magnitude.

# Index

# List of Figures

# List of Tables

# List of abbreviations, acronyms and symbols

AOGCM - Atmosphere-Ocean Coupled Global Circulation Model;
CDF - Cumulative Distribution Function;
CORDEX - Coordinated Regional Downscaling Experiment;
CRU - Climate Research Unit;
ECMWF - European Centre for Medium-Range Weather Forecasts;
EVAPFR – Evaporative Fraction;
GLACE - Global Land-Atmosphere Coupling Experiment;
GLEAM - Global Land Evaporation Amsterdam Model;
GPCC - Global Precipitation Climatology Centre;
HFLS - Surface Upward Latent Heat Flux;
HFSS - Surface Upward Sensible Heat Flux;
IPCC - Intergovernmental Panel on Climate Change;
IQR – Inter-Quartile Range ;
ITCZ - Intertropical Convergence Zone ;
LETCM - Latent Heat Flux-Temperature Coupling Magnitude;
MH - Latent Heat Flux Magnitude;
MT - Temperature Magnitude;
MRSO – Total (i.e. vertically integrated) Soil Moisture Content;
PDF - Probability Density Function;
PDSI - Palmer Drought Severity Index;
PET - Potential Evapotranspiration;
PR - Precipitation;
RCM - Regional Climate Model;
RCP - Representative Concentration Pathways;
RMSE - Root Mean Square Error;
RSDS - Shortwave Downwelling Radiation;
SD - Standard Deviation;
SPEI - Standardized Precipitation Evapotranspiration Index;
TAS - Near-Surface Air Temperature;
TASMAX - Daily-Maximum Near-Surface Air Temperature;
TASMIN - Daily-Minimum Near-Surface Air Temperature;
DJF - December, January and February season;
MAM - March, April and May season;
JJA - June, July and August season;
SON - September, October and November season;

NA-SA - Northern Africa Semi-Arid region;
NA-SW - Northern Africa Semi-Humid region;
EA - East Africa region;
CNA – Central Northern Africa region;
CSA - Central Southern Africa region;
SA-W - South Africa-West region;

# 1. Introduction

Droughts and heat wave events are some of the most deadly and costly climate extremes (Easterling et al., 2000a and b; Robinson., 2001; Vicente-Serrano., 2006; Vicente-Serrano et al., 2010) and are projected to be more frequent and intense in the future (Schär et al., 2004; Seneviratne et al., 2006, 2010, Fontaine et al., 2013; Russo et al., 2014, 2016; Lorenz et al., 2015). In certain areas of the globe (e.g. Mediterranean and Sahel), drought and heat waves are tightly connected, as a dry spell might induce stronger heat waves through land-atmosphere coupling (Fischer et al., 2007a and b; Fischer and Schär., 2010; Seneviratne et al., 2010; Hirschi et al., 2011; Miralles et al., 2012). Conversely, heat waves might cause soil dissection leading to or intensifying a drought event.

Transition areas between wet and dry climates are considered regions of strong land-atmosphere coupling (Koster et al., 2006; Seneviratne et al., 2006, 2010, 2012; Fischer et al., 2007a and b; Miralles et al., 2012; Lorenz et al., 2015; Knist et al., 2017). The variability of these transition areas is higher, for variables such as the surface or root-zone soil moisture, latent heat flux (or evapotranspiration), sensible heat flux and surface temperature (e.g. Seneviratne et al., 2006; 2010; Lorenz et al., 2015). A large part of this variability is due to the soil moisture-temperature feedback (Seneviratne et al., 2006, 2010; Fischer et al., 2007a and b; Fischer and Schär., 2010). In the literature, the terms coupling and feedback are used indifferently. Seneviratne et al. (2010) defined coupling as the degree to which one variable controls another. A two-way coupling is called feedback, and represents the interactions between two or more variables. Coupling isn't limited to states or processes (e.g. soil moisture-temperature coupling), it could be related to interfaces, just as the interface between the soil and atmosphere (e.g. land-atmosphere coupling). In this case, it relates to the degree in which ground processes will affect the lower atmosphere. Koster et al. (2006) defined land-atmosphere coupling strength as the degree to which anomalies at the land surface will affect or interact with low tropospheric processes. Coupling cannot be determined a priori by looking at the code of a model, neither is explicitly parametrized. However, it results from complex interactions between numerous processes, which are frequently parametrized, e.g., evapotranspiration.

One of the most important variables in the context of land-atmosphere coupling is soil moisture. Generally, soil moisture is defined as the water present in unsaturated soil (Seneviratne et al., 2010). In the context of the current work only the land energy balance and the feedback between surface properties and temperature is relevant. The energy balance at the surface considers the radiative balance, storage, transport, sensible and latent heat fluxes. The radiative balance at the surface, during the day is positive, meaning an excess of energy. This excess of energy is mostly compensated by sensible and latent heat fluxes towards the atmosphere which are highly relevant to the soil moisture-temperature feedback. This feedback has three components: first, the relationship between soil moisture and latent heat flux; second, the balance between latent and sensible heat fluxes; third, the relationship between sensible heat flux and near surface temperature. If there is an increase of radiation at the surface, latent heat flux or evapotranspiration rises, through the evaporation of soil moisture. If there is no reestablishment over time, soil moisture decreases, leading to a possible drought event and to a decrease of the latent heat flux. To keep the surface energy balance, and considering that transport and storage of energy is negligible, a decrease of the latent heat flux will lead to an increase of the sensible heat flux, which in turn, will lead to an increase of surface temperature. This soil moisture-temperature feedback may progress until there is no more soil water to evaporate, reaching a maximum temperature or, more plausible, as long as synoptic conditions would allow it, and that may evolve to a heat wave event (Miralles et al., 2014).

One of the first metrics created to quantify the land-atmosphere coupling was developed by Koster et al. (2002, 2004, 2006), the Global Land-Atmosphere Coupling Experiment (GLACE). GLACE is a model inter-comparison study and consists of two idealized ensembles. The first is a 'write' ensemble, where soil moisture is computed and saved at each time-step. The second is a 'read' ensemble, where, at each time step, soil moisture is substituted by the climatological soil moisture of the first ensemble. The coupling metric is obtained by the difference between normalised variances of two ensembles under investigation (Lorenz et al., 2015). The objective of this study is the identification of "hot spots" or regions of strong coupling for numerous models, and is focused on impacts of soil moisture on sub-seasonal climate variability. While GLACE only considers an ensemble simulation for a single year or season, Seneviratne et al. (2006) proposed an alternative, to access the impact of soil moisture-temperature coupling on longer time scales, in which a multiyear simulation is considered. Seneviratne et al. (2006) also proposed a variance analysis, using a coupled and an uncoupled simulation, which describes the percentage of inter-annual variance of the mean seasonal temperatures that can be explained by land-atmosphere coupling. This is computed as the subtraction of the variances of the coupled and uncoupled simulations, divided by the variance of the coupled simulation. Both metrics are similar, as both explain the amount of variance due only to land-atmosphere coupling. GLACE-type experiments are complex and computationally demanding (Lorenz et al., 2015), therefore, over time, other coupling metrics were developed (e.g. Dirmeyer, 2011; Findell et al., 2011; Miralles et al., 2012 and Decker et al., 2015). Miralles et al., (2012) proposed two soil moisture-temperature coupling metrics, based on observations. The first is based in the difference between two long-term correlations: one between temperature and sensible heat flux, and the other between temperature and an energy term. This energy term is computed as the difference between radiative balance minus potential latent heat flux. The second is a daily coupling metric based in anomalies of the same three terms described, all normalized by the standard deviation of each term. The correlation between latent and sensible heat fluxes and the correlation between surface air temperature and latent heat flux are also considered a useful land-atmosphere coupling metrics, as both variables are components of the surface energy balance (Knist et al., 2017). These types of metrics could be depicted as a reverse measure of the soil moisture-temperature coupling and are only meaningful on regions where evapotranspiration is relatively large (Seneviratne et al., 2006; 2010). These two metrics (Miralles et al., 2012; Knist et al., 2017) have the advantage of being able to be computed on standard model outputs and do not require special experimental designs, such as GLACE, allowing an inter-comparison between different models. Each metric described, addresses individual processes in the land-atmosphere feedback system and they can show different results. Great care should be taken when comparing different metrics, since each have different units and ranges which can lead to inconsistent inferences. Also, the definition of "strong" and "weak" coupling may not be consistent for different studies (Knist et al., 2017).

Heat waves are phenomena that often lead to high mortality, particularly in risk groups such as the elderly, infants and persons with pre-existing cardiovascular and respiratory diseases (Fischer and Schär., 2010) Heat waves are sustained periods of time when temperature is higher than a defined threshold. It is accepted that heat waves in Europe or North America requires subsidence with clear skies and advection of warm air, characteristics of a stationary anticyclonic system (Xoplaki et al., 2003; Black et al., 2004; Meehl and Tebaldi., 2004). If a stationary anticyclonic system due to a blocking pattern is present, then under these conditions, a heat wave event has a high probability of occurrence. Additionally, anomalously strong coupling may be found in areas of negative soil moisture anomalies and high atmospheric demand of water. Or, in other words, the continuous depletion of soil moisture and subsequent reduction of evapotranspiration could amplify air temperatures through the soil moisture-temperature feedback (Teuling et al., 2010; Miralles et al., 2012). Nevertheless, soil dissection and rainfall deficits, before and during a heat wave do not play a major role in the event duration, since the latter is mainly influenced by the synoptic conditions (Miralles et al., 2014). Fischer et al. (2007a b)

and Fischer and Schär. (2010) computed the number of hot days for two simulations, one fully coupled and other uncoupled, for past and future climates. In these studies, the impact of different soil moisture amounts on temperature for the 2003 European heat wave is assessed, and it is shown that negative soil moisture anomalies, due to springtime precipitation deficits and high atmospheric demand of water, effectively affected surface temperatures, with stronger anomalies over regions of soil moisture deficits.

Drought is one of the main natural hazards that causes environmental, agricultural and economic damages (Vicente-Serrano et al., 2010). This phenomenon occurs when water availability is significantly below normal levels, which could be due to precipitation deficits over prolonged periods and/or high demand of water by the atmosphere (Vicente-Serrano, 2013). Drought are different from other natural disasters, since its effects accumulate slowly over time and its consequences may be present over extended periods after the event (Wilhite, 2000). Because of this, it is difficult to assess its start, duration and end, making it very problematic to quantify its intensity, magnitude and spatial extent. Drought also has a time multi-scalar characteristic (McKee et al, 1993). For example, for lower timescales in a certain period, wet and dry spells may occur intercalated, but, on longer timescales for that same period, it could be a single drought. Drought time-scales refer to the time lag that normally exists between the beginning of a drought event, and the identification of its consequences (Vicente-Serrano, 2013). Different ecosystems respond in diverse ways to drought. For example, vegetation in arid biomes react as soon as there is a water deficit. In humid biomes, plants also react to shorter time scales, but in this case, plants have poor adaptability to water shortage. On the other hand, the vegetation on transition zones respond to long time scales, since plants can withstand water deficits, but lack the fast response of arid biomes to drought (Vicente-Serrano, 2013). On long timescales, drought can not only contribute to an increase in aridity associated to the wilting of the vegetation or its replacement by sparser and more drought resistant species but also severely affect hydrological systems (Koster et al., 2004; Vautard et al., 2007; AghaKouchak et al., 2010; Dai, 2011; Dai, 1013; Vautard et al., 2007).

One of the first indices developed to objectively quantify drought was the Palmer Drought Severity Index (PDSI, Palmer., 1965). PDSI is a two-layer bucked type index that considers a simple water balance between precipitation and potential evapotranspiration for a single site (Alley, 1984). One of the main criticisms of PDSI over the years is that PDSI values are not comparable between two different locations (Alley, 1984; Karl, 1983; Soulé, 1992; Akinremi et al., 1996; Weber and Kkemdirim, 1998). Another problem with PDSI is that it does not consider the multi-scalar characteristic of drought. Subsequently, other indices appeared, such as the self-calibrated-PDSI (sc-PDSI, Wells et al., 2004) that solved most of the mentioned problems. Nevertheless, the main shortcoming of the PDSI was not solved and it relates to its fixed timescale (9 to 12 months).

The Standardized Precipitation Index (SPI, McKee et al., 1993; Vicente-Serrano., 2006) was developed and has a multi-scalar characteristic. This index can be computed for timescales higher than one month and since it is standardized it can be compared over time and space. Although the main variable that controls the beginning, duration, end and intensity of droughts is precipitation (Chang and Kleopa, 1991; Heim, 2002), the main criticism of SPI is that it does not consider other variables that can influence drought, such as evapotranspiration or wind speed. For this reason, a new index was developed, designated Standardized Precipitation Evapotranspiration Index (SPEI, Vicente-Serrano et al., 2010). SPEI combines the multi-temporal nature of SPI with the sensitivity of PDSI to changes in evapotranspiration demand, and similarly to SPI, SPEI values are comparable over time and space.

Over the last century, temperatures in Africa have risen by more than $0.5^{o}C$ (Jones and Moberg, 2003; Kruger and Shongwe, 2004; Schreck and Semazzi, 2004; Christy et al., 2009; Collins, 2011), increasing the probability of heat wave events in some regions (Fontain et al., 2013). In a climate change scenario, where mean temperature increases (Hulme et al., 2001; Serdeczny et al., 2017), the probability of temperatures extremes is enhanced, and as never seen before heat waves could become more frequent,

more intense and last longer (Min et al, 2011; Coumou and Rahmstorf, 2012; IPCC, 2012; Russo et al., 2014, 2016).

One of the most useful techniques to obtain regional climate projections is the dynamical downscaling approach in which a regional climate model at high resolution, takes initial and boundary conditions from an Atmosphere-Ocean coupled Global Circulation Models (AOGCMs) with lower resolution. In this approach, the input data for climatic projections should be carefully chosen (León et al., 2012). Recently a downscaling program named Coordinated Regional Downscaling Experiment, supported by the World Climate Research Program (WCRP, CORDEX) was implemented. The project aims to develop a coordinated ensemble of high-resolution Regional Climate projections in order to produce detailed climate data for all land regions of the world, at user-relevant scales and support climate change impact and adaptation research (Jones et al., 2012; 2013; Lennard and Kalognoumou, 2013). CORDEX involves 2 phases. In a first stage, Regional Climate Models (RCMs) are run for common continental regions for the recent past (1989-2008), forced by the European Centre for Medium-Range Weather Forecasts (ECMWF) Era-Interim reanalysis (Dee et al., 2011). In the second pahse regional climate simulations were performed, driven by many AOGCMs, participants of the Coupled Model Intercomparison Project, Phase 5 (CMIP5). The latter cover the period 1960-2100 providing projections for different greenhouse gas concentrations according to the Intergovernmental Panel on Climate Change Representative Concentration Pathways scenarios (IPCC RCP scenarios). The Representative Concentration Pathways are four greenhouse gas concentration scenarios (RCP2.6, RCP4.5, RCP6.0 and RCP8.5) adopted for the IPCC fifth assessment report (AR5) in 2014 (Moss et al., 2010). These scenarios describe four possible outcomes of how much will be the radiative forcing values in the year 2100, relative to pre-industrial values (Moss et al., 2010). Given that climate change in Africa has been overlooked, it was identified as the priority domain.

Model results from the Africa-CORDEX ensemble, forced by Era-Interim reanalysis, were assessed and validated in the recent past. For example, Nikulin et al. (2012) evaluates precipitation against CRU, GPCP and other observational based databases where all RCM analysed can reproduce the main details of precipitation over Africa. However, individual models display substantial biases depending on season and region. Overall, the multi-model mean ensemble outperforms individual models in most cases. Kim et al. (2014) validates precipitation, mean, maximum and minimum temperatures with a previous version of CRU database. All models analysed can simulate the precipitation climatology with mean biases inferior to 10%. Spatially, all models correlate well with CRU, but individual RCMs overestimates the spatial variability of precipitation. For temperatures, on general, models perform better for mean and maximum temperature than for minimum temperature. Buontempo et al., (2015) assess and validates ensembles from HadRM3P RCM over Africa for precipitation and temperature and advances that dynamical downscaling it is an asset for assessing recent past a future climate. Panitz et al. (2014) validates precipitation for COSMO-CLM model for 0.11º and 0.44 resolution, against numerous observationally based databases. Results shows the ability of CCLM to maintain the large-scale information from the driving model and results for mean annual and inter-annnual variability are better than the forcing simulation. However, results are not satisfactory enough to reproduce the complex African climate and further research is needed.

The African continent spans a myriad of climates, that range from very dry (e.g. Sahara or Kalahari deserts) to very wet climates such as the tropical rainforests of the Democratic Republic of Congo (Peel et al., 2007). It is one of the most vulnerable continent to climate extremes such as drought and heat waves, due to its exposure to high temperatures and low adaptive capacity (IPCC, 2014). Overall Africa despite having contributed little to climate change, it is likely to pay a heavy price in the future (IPCC, 2014; Russo et al., 2016). To improve the understanding of the climate change impact on the coupling between atmosphere-land, its link to heat waves and droughts, data from the Africa Coordinated Regional Downscaling Experiment (Africa-CORDEX, Giorgi et al., 2009) is used in the current thesis.

Firstly, all models used are assessed and validated against observationally based databases such as GPCC, CRU, GLEAM and FLUXNET. Secondly, coupling strength, heat waves and drought are evaluated for present climate and as anomalies between future (2071-2100) and present climate (1971-2000).

As mentioned, the main objective of this work is to assess the future changes in heat waves and droughts, and the relationship between soil moisture and temperatures anomalies in the context of Land-Atmosphere Coupling. Toward that end, two coupling metrics were considered, as well as the number and mean duration of heat wave events. To evaluate duration and intensity of drought events, SPEI index is computed for all periods. Additionally, to the state-of-the-art methods for coupling characterization, following the amplitude metric proposed by Russo et al. (2016), a new Latent Heat Flux-Temperature Coupling Magnitude is introduced and is applied to heat waves periods. This metric is based only on maximum temperature and upward latent heat flux to assess the relationship between these variables and is compared with the SPEI values. In the next chapter, an introduction to the data, methods and metrics is performed. In Chapter 3, all variables, for Hindcast and Historic simulation are evaluated and validated for the Africa-CORDEX domain. The analysis of land-atmosphere coupling, heat waves and droughts over Africa is done in Chapter 4 and for the future in Chapter 5. In Chapter 6 conclusions are drawn.

# 2. Data and Methods

## 2.1 Africa-CORDEX RCM Simulations

This study is based on data from Africa-CORDEX RCM simulations. The Africa-CORDEX focus domain is shown in Figure 2.1, covering an area comprised between $45.76ºS$ to $42.24ºN$ and between $24.64ºW$ to $60.28ºE$.

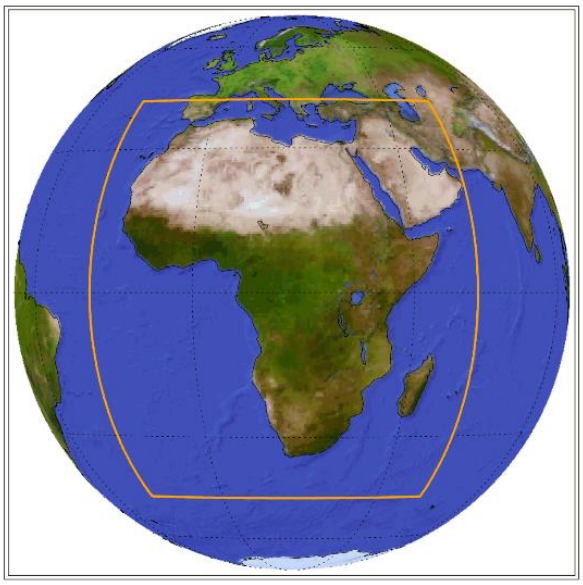

*Fig 2.1.* Africa-CORDEX domain[1].

Four different simulations/periods from CORDEX portal were used: 1) RCMs forced by the Era-Interim reanalysis simulation from 1989 to 2008 (from now on: Hindcast); 2) RCMs forced by CMIP5 AOGCMs simulation from 1971 to 2000 (from now on: Historic); 3) the same RCMs forced by the same CMIP5 AOGCMS forced by two IPCC RCP scenarios (RCP 8.5 and RCP 4.5, or Future when referring to both scenarios), both with a time span from 2071 to 2100. All RCMs have a 0.44º resolution. The variables considered are: Surface Upward Latent Heat Flux (or HFLS, $Wm^{-2}$); Surface Upward Sensible Heat Flux (or HFSS, $Wm^{-2}$); Total (i.e. vertically integrated) Soil Moisture Content, or total amount of soil water in solid and liquid state present in a soil column (or MRSO, $kgm^{-2}$); Precipitation, in both solid and liquid state (or PR), with units $kgm^{-2}s^{-1}$ or mm $day^{-1}$ by multiplying by 86400 sec; Daily-Mean Near-Surface Air Temperature, at 2m (or TAS, K); Daily-Maximum Near-Surface Air Temperature, (or TASMAX, K); Daily-Minimum Near-Surface Air Temperature (or TASMIN, K); and Downwelling Shortwave Radiation (RSDS, $Wm^{-2}$).

Since the Historic and Future simulations are forced by free-running GCMs, the climates of each individual RCM are not synchronized. Thus, for building the ensemble, each common day of the year, between all models for each variable was averaged, with the same weight, in order to build a mean day year.

[1] http://www.cordex.org/images/pdf/documentation/CORDEX_domain_description_230615.pdf , consulted in April/2017

## a. Hindcast Simulation

The output from 7 RCMs driven by Era-Interim reanalysis simulations are used as benchmark to the results obtained from the Historic. The models used are summarized in Table 2.1. Note that only data from 1990 onwards was used since it is the common time span to all models.

*Table 2.1.* Africa-CORDEX Hindcast RCMs.

| AOGCM MODEL ID | Institution | RCM MODEL ID | Institution | Calendar | Period | Acronyms |
|---|---|---|---|---|---|---|
| ECMWF-ERAINT | European Centre for Medium-Range Weather Forecasts | CLMcom-CCLM4-8-17 | Climate Limited-area Modelling Community | Proleptic Gregorian | 1989 2008 | CCLM4 ERAINT |
| ECMWF-ERAINT | European Centre for Medium-Range Weather Forecasts | DMI-HIRHAM5 | Danish Meteorological Institute | Proleptic Gregorian | 1989 2010 | HIRHAM5 ERAINT |
| ECMWF-ERAINT | European Centre for Medium-Range Weather Forecasts | KNMI-RACMO22T | Royal Netherlands Meteorological Institute, De Bilt, The Netherlands | Standard | 1979 2012 | RACMO22T ERAINT |
| ECMWF-ERAINT | European Centre for Medium-Range Weather Forecasts | MOHC-HadGEM3-RA | Met Office Hadley Centre | Proleptic Gregorian | 1990 2008 | HADGEM3-RA ERAINT |
| ECMWF-ERAINT | European Centre for Medium-Range Weather Forecasts | MOHC-HadRM3P | Met Office Hadley Centre | Proleptic Gregorian | 1990 2011 | HADRM3P ERAINT |
| ECMWF-ERAINT | European Centre for Medium-Range Weather Forecasts | SMHI-RCA4 | Swedish Meteorological and Hydrological Institute, Rossby Centre | Standard | 1980 2010 | RCA4 ERAINT |
| ECMWF-ERAINT | European Centre for Medium-Range Weather Forecasts | MPI-CSC-REMO2009 | Helmholtz-Zentrum Geesthacht, Climate Service Centre, Max Planck Institute for Meteorology | Proleptic Gregorian | 1989 2008 | REMOO2009 ERAINT |

## b. Historic and Future Simulations

The model characteristics for both the Historic and Future periods are summarized on Table 2.2. The output from 9 RCMs driven by CMIP5 ensemble models are analysed and validated. The Historic period is used to characterize the present climate over Africa while the RCP4.5 and RCP8.5 scenarios are used to evaluate the future changes.

*Table 2.2.* Africa-CORDEX Historic and Future RCMs.

| AOGCM MODEL ID | Institution | RCM MODEL ID | Institution | Calendar | Period | | Acronyms |
|---|---|---|---|---|---|---|---|
| | | | | | Historic | Future | |
| CNRM-CM5 | Centre National de Recherches Météorologiques/Centre Européen de Recherche et de Formation Avancées en Calcul Scientifique, France | CLMcom-CCLM4-8-17 | Climate Limited-area Modelling Community | Proleptic Gregorian | 1971 2000 | 2071 2100 | CCLM4 CM5 |
| CSIRO-Mk3-6-0 | Commonwealth Scientific and Industrial Research Organization in collaboration with the Queensland Climate Change Centre of Excellence, Australia | SMHI-RCA4 | Swedish Meteorological and Hydrological Institute, Rossby Centre | 365 days | 1971 2000 | 2071 2100 | RCA4 MK3-6-0 |
| ICHEC-EC-EARTH | EC-EARTH consortium | KNMI-RACMO22T | Royal Netherlands Meteorological Institute, De Bilt, The Netherlands | Standard | 1971 2000 | 2071 2100 | RACMO22T EC-EARTH |
| ICHEC-EC-EARTH | EC-EARTH consortium | DMI-HIRHAM5 | Danish Meteorological Institute | Proleptic Gregorian | 1971 2000 | 2071 2100 | HIRHAM5 EC-EARTH |
| ICHEC-EC-EARTH | EC-EARTH consortium | CLMcom-CCLM4-8-17 | Climate Limited-area Modelling Community | Proleptic Gregorian | 1971 2000 | 2071 2100 | CCLM4 EC-EARTH |
| MOHC-HadGEM2-ES | Met Office Hadley Centre | CLMcom-CCLM4-8-17 | Climate Limited-area Modelling Community | 360 day | 1971 2000 | 2071 2099 | CCLM4 HADGEM2 |
| MOHC-HadGEM2-ES | Met Office Hadley Centre | KNMI-RACMO22T | Royal Netherlands Meteorological Institute, De Bilt, The Netherlands | 360 day | 1971 2000 | 2071 2099 | RACMO22T HADGEM2 |
| MPI-ESM-LR | Helmholtz-Zentrum Geesthacht, Climate Service Centre, Max Planck Institute for Meteorology | CLMcom-CCLM4-8-17 | Climate Limited-area Modelling Community | Proleptic Gregorian | 1971 2000 | 2071 2100 | CCLM4 ESM-LR |
| NCC-NorESM1-M | Norwegian Climate Centre, Norway | DMI-HIRHAM5 | Danish Meteorological Institute | Proleptic Gregorian | 1971 2000 | 2071 2100 | HIRHAM5 NORESM1-M |

## 2.2 Observational Data Sets

To compare TAS, TASMAX, TASMIN and PR variables, from Historic and Hindcast simulations, with CRU and GPCC databases, the first step needed is to interpolate this data from the CORDEX resolution of 0.44º to 0.5º (resolution of both databases), to avoid the introduction of spurious values. For temperatures, the interpolation is done in the MATLAB® environment with the bilinear method. For precipitation, a mass conservative interpolation is required, to avoid changes in the amount of water in a grid cell. The first order conservative remapping command from the CDO software was selected[2] (CDO user's guide: Schulzweida et al., 2006). The root zone soil moisture from GLEAM (section c) was also interpolated from the original 0.25º grid to the Africa-CORDEX resolution (0.44º) with CDO conservative remapping.

### a. Climate Research Unit

The Climate Research Unit Time series version 4 (CRU TS v. 4.00; more information about this database in Jones and Harris., 2008; Harris et al., 2014 and Harris and Jones., 2017) is a global climate dataset that covers all land areas except Antarctica, at 0.5º resolution. This version was released in 13 March 2017 and covers the period 1901-2015. CRU database includes near surface air maximum, mean and minimum temperatures, precipitation, cloud cover, diurnal temperature range, ground frost frequency, potential evapotranspiration, vapour pressure and wet day frequency. This database is built based on the compilation of multiple variables from stations and numerous data sources into a consistent format and uses station data to compute variables such as potential evapotranspiration, diurnal temperature range, and number of wet days. One of the key limitations of this database is that most of the input data were homogenized, but the data itself is not strictly homogenous.

### b. Global Precipitation Climatology Centre

Global Precipitation Climatology Centre (GPCC[3]) is composed of multiple products, with resolutions between 0.25º to 2.5º, and covers different periods, available at the GPCC portal. The construction of this database is based on rain data from stations, satellites and sounding observations. GPCC uses more stations than CRU and data over ocean is also available providing global coverage, which is useful for model validation (GCMs or RCMs) and for climate variability studies. Yet, complex algorithms are required to process indirect and infrequent satellite measurements and the use of different satellites at different latitudes can lead to some spatial heterogeneity. Trenberth et al. (2014) emphasises that the use of more stations does not guarantee an improved coverage if the extra stations are all in the same area. Fewer and more evenly distributed records should provide more reliable time series, and this is the base behind the construction of the CRU database.

From all the products available, the GPCC Full Data Reanalysis Version 7.0 for the period 1971 to 2000 at 0.5º resolution was chosen. This product is based on quality-controlled data from all stations in GPCC's database and is optimized for best spatial coverage and use for hydrological studies.

[2] https://code.zmaw.de/projects/cdo , Consulted in July 2017.

[3] https://www.esrl.noaa.gov/psd/data/gridded/data.gpcc.html and references therein, Consulted in March 2017.

## c. FLUXNET

The construction of the FLUXNET[4] database (Baldocchi et al., 2001) is based on observations of eddy covariance flux and contains preprocessed, quality-checked and instrument error corrected data from observations. Although these measurements could be systematically lower than reality and the energy balance is often not closed (Knist et al., 2017). Only three stations for the entire domain were avaiable. The number of available stations on Africa is reduced and many of them have poor data quality. Stations main characteristics are summarized in Table 2.3. Only daily values were used, without any kind of restrictions, because the main objective was to check if Historic and Hindcast ensembles could reproduce the mean seasonal cycles.

*Table 2.3.* Africa FLUXNET stations characteristics.

| Country | Coordinates | | Period | Elevation (m) | IGBP | Mean Annual Temperature (ºC) | Mean Annual Precipitation (mm) |
|---|---|---|---|---|---|---|---|
| | Latitude | Longitude | | | | | |
| Senegal | 15.4028ºN | 15.4322ºW | 2010-2013 | 40 | SAV (Savannas) | 29 | 404 |
| Sudan | 13.2829ºN | 30.4783ºE | 2005-2009 | 500 | SAV (Savannas) | 26 | 320 |
| South Africa | 25.0197ºS | 31.4969ºE | 2000-2013 | 359 | SAV (Savannas) | 21,9 | 547 |

## d. GLEAM

The Global Land Evaporation Amsterdam Model (GLEAM) data set v3.1a (Miralles et al., 2011; Martens et al., 2017) is based in a set of algorithms based on satellite-observed soil moisture through data assimilation of the European space Agency Climate Change Initiative Soil Moisture (ESA CCI SM; Liu et al., 2011; Wagner et al., 2012), snow water equivalents (Armstrong et al., 2005), Era-Interim reanalysis (Dee et al., 2011) air temperature and radiation, vegetation optical depth (VOD, Liu et al., 2011), and the Multi-Source Weighted-Ensemble Precipitation (MSWEP) product (Beck et al., 2017). This version covers a 37-year period, from 1980 to 2016, of daily data at 0.25º resolution and is based on reanalysis of net radiation and air temperature, satellite and gauged-based precipitation, Vegetation Optical Depth (VOD), soil moisture and snow water equivalent. GLEAM separately estimates the different components of land evapotranspiration and provides surface and root-zone soil moisture, potential evapotranspiration, computed with the Priestley and Taylor (1972) method, and evaporative stress conditions (for more details see: Miralles et al., 2010, 2011a and b; Martens et al., 2016, 2017).

[4] http://fluxnet.fluxdata.org , Consulted in March 2017.

## 2.3 Land-Atmosphere Coupling Metrics

To quantify the soil moisture-temperature coupling, 10 days of non-overlapping means correlation between latent and sensible heat fluxes (HFLS-HFSS correlation) and the 10 days of non-overlapping means correlation between latent heat flux and maximum temperature (HFLS-TASMAX correlation) were computed for the four seasons, each with a duration of 3 months across the simulation period: March, April and May (MAM); June, July and August (JJA); September, October and November (SON); December, January and February (DJF). The use of 10 days of non-overlapping means acts as a filter strengthening the correlations. In climates where soil moisture is available in sufficient amounts (e.g. energy-limited or tropical climates) it is expected that when an increase of radiation at the surface exists, there is an increase of both latent and sensible heat fluxes, because enough water is available to evaporate, meaning a positive correlation between these two fluxes, corresponding to weak land-atmosphere coupling regions. However, long and severe dry spells could lead to situations where the soil moisture-temperature feedback could act. While for water limited regions, like transition zones between the tropics and arid areas, soil moisture limits evapotranspiration, the correlation between latent and sensible heat fluxes in this case may be negative. In other words, when there is an increase of surface radiation there is a decrease of latent heat flux, because over time, less water is available to evaporate due to a lack of replenishment. To maintain the radiative balance at the surface, if the latent heat flux decreases, then the sensible heat flux must increase leading to an increase of surface temperature. In this case, the land-atmosphere coupling is strong since slight changes in soil moisture can significantly affect the lower atmosphere. On deserts or very arid biomes, the lack of water to evaporate translates in a very poor correlation, meaning that these kinds of metrics are only meaningful in regions where evapotranspiration is relatively large (Seneviratne et al., 2006; 2010). To further access the land-atmosphere coupling, the 10 days of non-overlapping means correlation between latent heat flux and daily maximum temperature is also used. This type of correlations was first introduced by Seneviratne et al. (2006) as a correlation between evapotranspiration and temperature and then by Knist et al. (2017) as a correlation between latent heat flux and near surface air temperatures. The HFLS-TASMAX correlation metric represents a one step further relative to the latent heat flux-temperature correlation, as the relationship between sensible heat flux and near surface air temperature is also assessed indirectly, meaning weaker correlations, namely in regions of strong temperature advection. These minor differences in correlations highlights the reason for being careful when comparing different coupling metrics. Both coupling metrics used describe the soil moisture-temperature feedback, the focus of this study.

The correlation between latent and sensible heat fluxes indicates the energy balance at the surface while the latent heat flux and maximum temperature describes the relationship between temperature and latent heat flux (Knist et al., 2017). The 10 days of non-overlapping means correlation between total soil moisture and the Evaporative Fraction (MRSO-EVAPFR correlation) is also used to access the link between soil moisture and the flux balance (ratio between latent heat flux and the sum of sensible and latent heat fluxes)

$$Evaporative\ Fraction = \frac{HFLS}{HFLS + HFSS} \tag{2.1}$$

where HFLS represents the surface upward latent heat flux and HFSS the surface upward sensible heat flux.

To complement the land-atmosphere coupling analysis, the Bowen ratio (ratio between surface sensible heat flux and latent heat flux)

$$Bowen\ ratio = \frac{HFSS}{HFLS} \quad (2.2)$$

is used alongside with the Evaporative Fraction, to distinguish between dry, humid and transition regions for each model and simulation.

## 2.4 Extremes

### a. Heat Waves Indices

To characterize heat waves, two metrics are computed: the yearly average number of heat waves and mean heat wave duration, for all models and periods to assess the spatial distribution of the number of heat waves and the mean duration. Heat waves usually refers to a consecutive number of days in which temperature is excessively higher than normal (Perkins et al. 2012). However, several authors use different definitions, which have significant influence on the assessment of the impact of climate change on this phenomenon (Jacob et al. 2014). Here, heat waves are computed based on the definition from the World Meteorology Organisation (Frich et al. 2002). Accordingly, heat waves are defined as periods of more than 5 consecutive days with maximum temperature exceeding the Historic period 90th percentile. The use of percentile based indices, not only allows a spatial comparison as "normal" temperature values varies across different climates, but also minimises the impact of model biases on results as percentiles are computed for each grid point. This approach is common and has been frequently used before (e.g. Meehl and Tebaldi, 2004; Fischer and Schär, 2010; Russo et al., 2016). Two different 90$^{th}$ percentile sets were computed, based on the definition proposed by Russo et al. (2015), one for the Historic and other for the Hindcast simulations. The Future periods use the 90$^{th}$ percentile set from the Historic simulation as the reference period. Each set is composed of daily values of the 90$^{th}$ percentile for an entire year. The percentile for a given day d is computed with a window composed of 31 days (15 days before and 15 after) considering all years composing the simulation period:

$$A_d = \bigcup_{y=year\ 1}^{final\ year} \bigcup_{i=d-15}^{d+15} T_{y,i} \qquad 2.3$$

where $\cup$ denotes the union of sets and $T_{y,i}$ is the daily maximum temperature of the day i and year y. The mean heat wave duration is defined as the ratio between the total number of days under heat wave by the total number of heat waves. In this work, a normalized version of the yearly average number of heat waves, for each model, is produced by the ratio between the number of events, over the simulation period, by the number of years, so it can be compared across models and simulations. A yearly analysis is made, instead of a seasonal one, to avoid cutting a single heat wave event into two.

### b. Drought Index (SPEI)

Drought is assessed using the Standardized Precipitation Evapotranspiration Index (SPEI). SPEI is an index developed by Vicente-Serrano et al. (2010) that uses the monthly difference between precipitation and potential evapotranspiration, or reference evapotranspiration (PET or $ET_0$ henceforth) computed at different time scales (more details about this index in Vicente-Serrano et al., 2010 and Beguería et al., 2014) for each location. This algorithm standardizes a variable following a distribution function, or in other words, it transforms the data into a standard Gaussian variate with zero mean and standard deviation of one (Guttman, 1998), and therefore can be compared with other SPEI values over time and space. This index is computed for a time scale of 12 months with the 'SPEI' package for the R environment (Beguería et al., 2014).

Firstly, PET has to be computed. This step is difficult due to the several parameters involved like surface temperature, wind, air humidity, radiation, upward latent and sensible heat fluxes, and others. Different methods have been proposed to estimate PET from meteorological parameters. One of most widely used methods is the Penman-Monteith equation (Monteith, 1965). This method estimates evapotranspiration based on wind speed, net radiation, vapour pressure deficit and other variables. The Thornthwaite (1948) method is the simplest and only requires the knowledge of monthly surface air temperature and latitude. Mavromatis (2007) showed that the use of simple or complex methods to estimate PET has a minor impact on the calculation of a drought index like PDSI (Palmer Drought Severity Index, Palmer 1965). On the other hand, Lockwood (1999) cautions that the Thornthwaite (1948) algorithm in future climate scenarios, where temperature is predicted to increase, overestimates PET since it overestimates solar radiation. Based on these assumptions a third method is considered here, the modified Hargreaves equation (Droogers and Allen, 2002). This method requires the knowledge of maximum and minimum temperature, radiation and precipitation. The monthly PET ($\mathrm{mm\ month^{-1}}$) can be obtained b

$$PET = 0.0013 * 0.408RA * (T_{avg} + 17.0) * (TD - 0.0123PR)^{0.76} \quad 2.4$$

where RA is the extraterrestrial radiation (expressed in $\mathrm{MJ\ m^{-2}d^{-1}}$) but in this case, the shortwave downwelling radiation (RSDS) was considered. While the extraterrestrial radiation is usually the solar radiation at the top of the atmosphere, the downwelling shortwave radiation is the solar radiation that reaches the Earth surface, indirectly considering the effects of clouds. The late, is able to reproduce results closer to the reality. $T_{avg}$ is the average temperature ($^{o}$C), TD is the temperature range computed as the difference between maximum and minimum monthly mean temperatures and PR is the monthly mean precipitation. The constant 0.408 is used to convert the radiation to evaporation equivalents in mm. The other constants were obtained by Droogers and Allen (2002) after testing various combinations based on the original equation (Hargreaves et al., 1985). The amount of rain for each month is used to correct $ET_0$ or PET as a proxy for insolation. If data of the external radiation isn't provided it can be estimated from the extra-terrestrial incident radiation taking the latitude and month of the year into account (Vicente-Serrano et al., 2010).

Given PET, then it's possible to compute the climatic water balance at the surface (precipitation minus potential evapotranspiration) for each month i and year j

$$D_{i,j} = P_{i,j} - PET_{i,j} \quad 2.5$$

Prior to the computation of SPEI, a kernel function is applied to the data to compute the accumulated water balance. This balance depends on the selected time scale. The application of a kernel (weighting factor) acts as a filter by smoothing the temporal variability of the resulting SPEI, allowing major patterns to emerge from the noise. The most common kernel function is rectangular, meaning that all data in the previous n steps is given equal weight, and that is the way SPEI was defined (Beguería et al., 2014). However, it can be considered that data from the past will have a decreasing influence in the current state as the temporal lag increases. 'SPEI' package allows the user to choose a different type of kernel: triangular, circular or Gaussian. If this is the case, the highest weight will be given to the observation of the current month. Beguería et al., (2014) also states that the use of a triangular or circular kernels gives similar results regarding a rectangular kernel, but the use of the Gaussian kernel will result in greater temporal variability. The accumulation for a certain month and year is:

$$X_{i,j}^{12} = K \sum_{i-(12-1)}^{i} D_{i,j} \quad 2.6$$

where 12 represents the selected time scale, $D_{i,j}$ is the series of the climate water balance ordered by year and month, and $K = \frac{1}{12}$ is the weighting factor (or kernel), which depends on type (rectangular, triangular, circular or Gaussian) and time scale considered. Because of this feature, and due to the selected time scale, the first 11 months will not be defined.

To test the most suitable probability distribution to model the $X_{i,j}^{12}$ values at different time scales, Vicente-Serrano et al. (2010) first used the L-moment ratio diagrams to determine which probability density function (PDF) is best suited. This approach allows the comparison between empirical frequency distribution of D series, computed at different time scales, with several theoretical distributions. The three parameter Log-logistic PDF was then selected to standardize the $X_{j,i}^{12}$ series to obtain SPEI and can be expressed by:

$$f(x) = \frac{\beta}{\alpha}\left(\frac{x-\gamma}{\alpha}\right)^{\beta-1}\left[1+\left(\frac{x-\gamma}{\alpha}\right)^{\beta}\right]^{-2} \quad 2.7$$

where $\alpha$, $\beta$ and $\gamma$ are scale, shape and location parameters respectively. This PDF also has the convenience of accepting negative values. The L-moment procedure was chosen to compute the parameters of the log-logistic distribution as it is the most robust and easy approach (Ahmad et al., 1988). To do this, the unbiased probability weighted moments or 'ub-PWMs' (Greenwood et al., 1979; Hosking. 1990; Stedinger 1993; Asquith.2011) of order *s* was computed for each month i

$$w_{s,i} = \frac{1}{N}\binom{N-1}{s}^{-1}\sum_{j=1}^{N}\binom{j-1}{s}X_{i,j}^{12} = \frac{1}{N}\frac{s!\,(N-1-s)!}{(N-1)!}\sum_{j=1}^{N}\frac{(j-1)!}{s!\,(j-1-s)!}X_{i,j}^{12} \quad 2.8$$

where N is the number of years, and i is the corresponding month of the year. Following Beguería et al. (2014), the 'ub-PWMs' is better than the plotting position method to standardize SPEI at different time scales, as the first led to biased standard deviations. The parameters of the log-logistic distribution for each month of the year can then be obtained by using:

$$\beta_i = \frac{2w_{1,i} - w_{0,i}}{6w_{1,i} - w_{0,i} - 6w_{2,i}} \quad 2.9$$

$$\alpha_i = \frac{(w_{0,i} - 2w_{1,i})\beta_i}{\Gamma\left(1+\frac{1}{\beta_i}\right)\Gamma\left(1-\frac{1}{\beta_i}\right)} \quad 2.10$$

$$\gamma_i = w_{0,i} - \alpha_i\Gamma\left(\frac{1+1}{\beta_i}\right)\Gamma\left(\frac{1-1}{\beta_i}\right) \quad 2.11$$

where $\Gamma(\beta_i)$ is the gamma function of $\beta_i$.

According to the log-logistic distribution, the cumulative distribution function (CDF) of the $X_{i,j}^{12}$ series for each month of the year is represented by:

$$F_i\left(X_{i,j}^{12}\right) = \left[1+\left(\frac{\alpha_i}{X_{i,j}^{12}-\gamma_i}\right)^{\beta_i}\right]^{-1} \quad 2.12$$

12 sets of the log-logistic CDF were computed (one for each month i of the year) and each $F(X_{i,j}^{12})$ value represents the accumulated probability of a certain accumulated water balance value ($X_{i,j}^{12}$). Finally, with all $F_i(X_{i,j}^{12})$ values it is possible to compute SPEI with a zero mean and a standard deviation of one. This standardization process is done by reading the probability ($F_i(X_{i,j}^{12})$) into a standard normal CDF that was

expanded by integrating by parts (up until the second order), and SPEI will be the value corresponding to that probability:

$$SPEI_{i,j} = W_{i,j} - \frac{2.515517 + 0.802853W_{i,j} + 0.010328W_{i,j}^2}{1 + 1.432788W_{i,j} + 0.189269W_{i,j}^2 + 0.001308W_{i,j}^3} \quad 2.13$$

$$W_{i,j} = \sqrt{-2\ln(P_{i,j})} \text{ if } P_{i,j} \leq 0.5$$
$$W_{i,j} = \sqrt{-2\ln(1 - P_{i,j})} \text{ if } P_{i,j} > 0.5 \quad 2.14$$

where $P_{i,j}$ is the probability of exceeding a determined $X_{j,i}^{12}$ value:

$$P_{i,j} = 1 - F(X_{i,j}^{12}) \quad 2.15$$

Based on SPEI, a percentage of months in drought, fraction area in drought and mean drought event duration were computed for all cases. Depending on the SPEI value, a drought (humid period) event could be more intense or not with lower (higher) SPEI values. For both RCP4.5 and RCP8.5, SPEI was computed by considering the Historic as the reference period. On Table 2.4 is the drought category for each SPEI interval (adapted from McKee et al., 1993; Rhee and Cho, 2016).

*Table2.4.* Drought index classifications for SPEI.

| Classification | SPEI values |
|---|---|
| Extremely wet | $\geq 2.00$ |
| Very wet | $From\ 1.50\ to\ 1.99$ |
| Moderately wet | $From\ 1.00\ to\ 1.49$ |
| Near normal | $From\ 0.99\ to -0.99$ |
| Moderate drought | $From -1.00\ to -1.49$ |
| Severe drought | $From -1.50\ to -1.99$ |
| Extreme drought | $\leq -2.00$ |

## c. Latent Heat Flux-Temperature Coupling Magnitude

To assess the relationship between heat waves with soil moisture and droughts, a Latent Heat Flux-Temperature Coupling Magnitude (LETCM) based on Russo et al. (2015) and (2016), were also computed, by considering the multiplication between a maximum temperature magnitude and an upward latent heat flux magnitude. The daily maximum temperature magnitude, $MT(T_d)$, as defined by Russo et al. (2015) is computed by:

$$MT(T_d) = \begin{cases} \frac{T_d - P_{t25}}{P_{t75} - P_{t25}} & if\ T_d > P_{t25} \\ 0 & if\ T_d < P_{t25} \end{cases} \quad 2.16$$

where $T_d$ is the daily maximum temperatures and $P_{t25}$ and $P_{t75}$ are the 25$^{th}$ and 75$^{th}$ percentiles of a series composed by the annual maximum temperatures. This magnitude considers the positive maximum temperature extremes. To know if in a certain time and location, temperatures were higher than what should have been in normal conditions, then a latent heat flux magnitude should be considered. This magnitude is computed by considering the negative extremes:

$$MH(HFLS_d) = -\begin{cases} \frac{HFLS_d - PR_{h_{75}}}{PR_{h_{75}} - PR_{h25}} & if\ HFLS_d < PR75 \\ 0 & if\ HFLS_d > PR75 \end{cases} \quad 2.17$$

where $HFLS_d$ is the daily latent heat flux and $PR_{h25}$ and $PR_{h75}$ are the 25th and 75th percentiles of a series composed by the annual minimum latent heat flux values. The negative signal transforms these values into positive, so areas where latent heat flux were lower than the given threshold, will have positive values. While MH can distinguish between wet and dry areas, it cannot distinguish between areas of strong and weak coupling. In strong coupling regions, when temperature rises, the latent heat flux descends, while for weak coupling regions, when the temperature descends, the latent heat flux also decreases.

The annual coupling magnitude is given by:

$$LETCM = \sum_{March,1}^{February,28} M_t(T_d) * M_t(HFLS_d) \quad 2.18$$

This annual coupling magnitude is computed from the beginning of March until the end of February of next year to consider both boreal and austral summers. However, the accumulation period is arbitrary and, for example, could match the SPEI time-scale. If high values are found on a certain region, then temperatures were higher than normal because of low evapotranspiration rates, or in other words, strong coupling. Nevertheless, in transition climates, higher values of LETCM, which indicates a strong influence of latent heat flux in temperature (strong coupling), should correspond to negative soil moisture anomalies and consequently to lower SPEI values.

This coupling magnitude is assessed as the probability of exceedance, for each land point of the Africa-CORDEX domain. Following Figure 2.2, the most suited distribution for all periods is the Generalized Pareto distribution. Great care should be taken as not always the first result is best suited to the data. The sorting is done by the 'allfitdist' toolbox for the MATLAB® environment and is based on Bayesian information criterion.

LETCM values lower than 2 were dismissed, since the number of point below a magnitude of 2, for the Historic and Hindcast, vastly outnumbers the number of points with higher magnitude. Values higher than the 99th percentile were also screened out, because both RCP4.5 and RCP8.5 have isolated points with magnitudes much higher than 500 and 1500, respectively. The generalized Pareto distribution with shape parameter $k \neq 0$, scale parameter $\sigma \geq 0$, and threshold parameter $\theta$ is:

$$f(MC|k,\sigma,\theta) = \left(\frac{1}{\sigma}\right)\left(1 + k\frac{(MC-\theta)}{\sigma}\right)^{-1-\frac{1}{k}} \quad 2.19$$

where MC is the coupling magnitude. The corresponding cumulative distribution function is represented:

$$F(MC) = \left(1 + k\frac{(MC-\theta)}{\sigma}\right)^{-\frac{1}{k}} \quad 2.20$$

With the CDF, the probability of exceedance is then given by:

$$P = 1 - F(MC) \quad 2.21$$

LETCM is also assessed for specific examples, only for the Hindcast ensemble, following documented heat waves periods over Africa, from Russo et al. (2016).

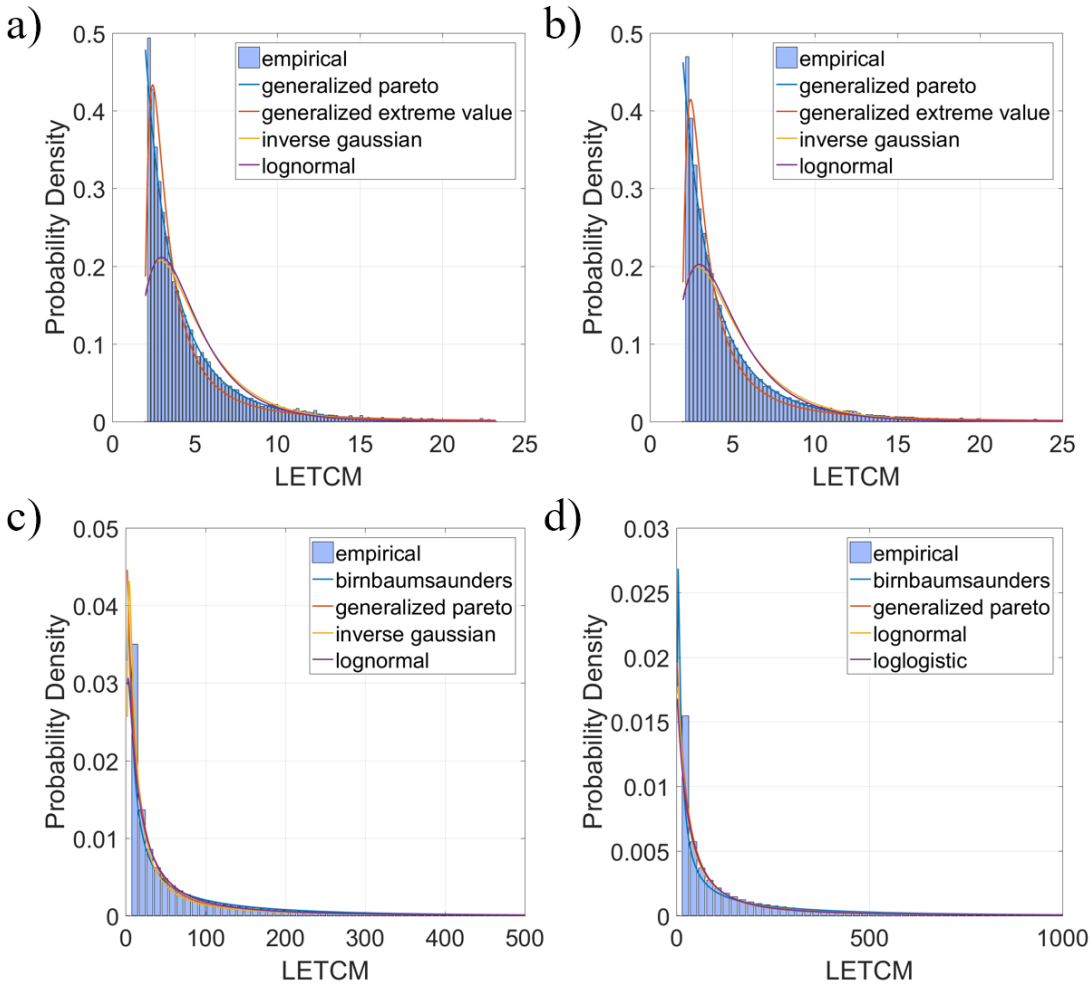


*Fig 2.2.* PDF test, from 'allfitdist' toolbox for MATLAB® environment for (a) Hindcast, (b) Historic, (c) RCP4.5 and (d) RCP8.5 based on Bayesian information criterion.

# 3. Model and ensemble validation

The models from Table 2.1, forced by Era-Interim reanalysis have been assessed and validated for the period 1990-2005 and similarly the results for the Historic period (1971-2000) were also assessed against the observational datasets. For brevity, the analysis presented in this section will be focused on the Historic results and when appropriate the results for the Hindcast ensemble will be shown.

## 3.1 Climatological Precipitation, Maximum, Mean and Minimum Temperatures against CRU database

The climatological mean Precipitation (PR), mean temperature (TAS), maximum temperature (TASMAX) and minimum temperature (TASMIN) are evaluated and validated here against CRU database (see section 3.2a) by using Taylor diagrams (Taylor., 2001) and bias maps. First, the CORDEX variables must be interpolated to the same grid used by the CRU databased (see chapter 2.2).

The climatological precipitation as described by CRU has a strong meridional gradient, with higher mean values over central Africa, and lower values over Northern and Southern Africa, particularly in the desert areas (Figure 3.1.a for Historic and Figure A.1.a for Hindcast). There is also a zonal gradient with wet western and dry eastern regions in the northern hemisphere. In the southern hemisphere, this gradient is reversed with high values over Madagascar. In the case of TAS (Figures 3.1b and A.1b), TASMAX (Figures 3.1c and A.1c) and TASMIN (Figures 3.1d and A.1d) there also exists a meridional gradient with higher values for all temperatures centred in the Sahel region. For both Historic and Hindcast simulations (Figures 3.1 and A.1), values and patterns are similar.

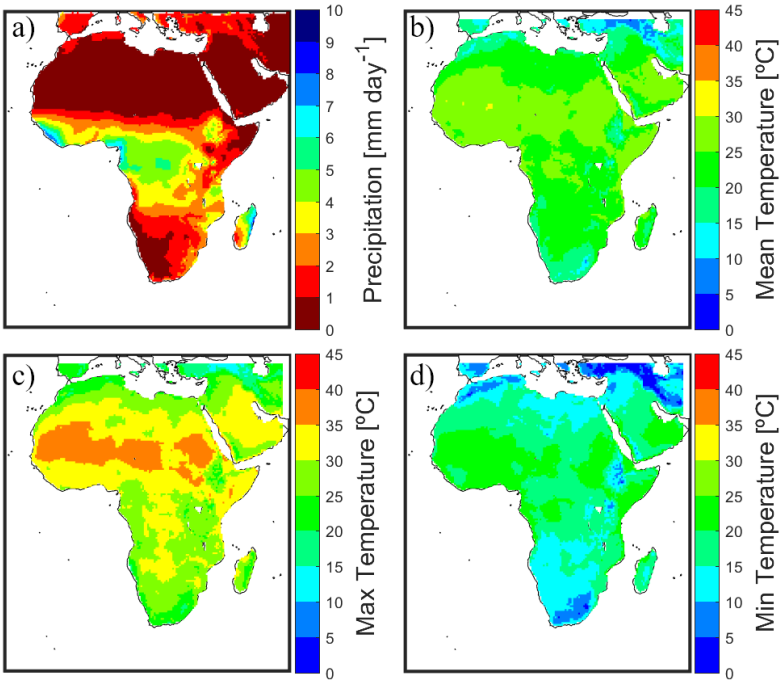


*Fig 3.1.* Climatological mean (a) Precipitation in $mm\ day^{-1}$, (b) Mean Daily temperature in $^{o}C$, (c) Maximum Daily Temperature in $^{o}C$ and (d) Minimum Daily Temperature in $^{o}C$, derived from the Climate Research Unit (CRU) gridded monthly data for the Historic period (1971 to 2000).

The model bias for the Historic simulation (i.e. the difference between model and observations) are shown on Figures 3.2 to 3.5 for the same variables (in order: PR, TAS, TASMAX, TASMIN), and in Figures A.2 to A.5 for the Hindcast simulation. Overall all ensembles for both simulations display a good agreement with CRU for the respective periods.

In the Historic simulations (Figure 3.2), there is a dry bias over Guinea, Sierra Leone, Liberia and Republic of Côte d'Ivoire and a wet bias over the western side of central Africa. There is also a dry bias over central Africa for all RCMs except in HIRHAM5 NORESM1-M. This RCM displays a dry bias over the eastern side of Africa and Madagascar. For the Hindcast simulation (Figure A.2), the pattern is similar with dry bias over countries of west Africa and on central Africa for CCLM4 ERAINT and RCA4 ERAINT, and a positive bias over the Sahel region for RACMO22T ERAINT. The ensemble of both simulations is similar, with a small positive bias over the most part of the continent (between -2 and 2 $mmday^{-1}$). For TAS (Figures 3.3) all Historic RCM models show a slight negative bias over Africa, except the HIRHAM5 NORESM1-M with strong positive bias over large areas of southern and eastern Africa and over the Sahel region. A stronger negative bias is found over the Sahel region for CCLM4 CM5, CCLM4 EC-EARTH, RACMO22T EC-EARTH and RACMO22T HADGEM2. Over the west coast of Angola and Namibia the RCM models shown higher temperatures. Benguela, on Angola, is an upwelling region characterized by lower surface air temperatures. RCMs resolution is not fine enough and, therefore, models are not able to reproduce the lower temperatures observed. Overall, for the Hindcast simulation (Figure A.3) the climatological TAS for models is higher than CRU, particularly in the west coast of Angola for all cases. In general, the Historic ensemble shows a small negative bias over Africa, while the Hindcast ensemble display a slightly positive bias over large areas of the continent.

The performance of Historic models for TASMAX is poorer than for TAS for large areas, with a negative bias over Sahel, central Africa, and in some cases for South Africa for CCLM4 CM5, CCLM4 EC-EARTH and RACMO22T EC-EARTH (Figure 3.4). Again, for all RCM including the ensemble, there is a strong positive bias over the west coast of Angola and Namibia and, in some cases. HIRHAM5 NORESM1-M model shows again higher temperature values than CRU for some parts of the southern Africa. This strong positive bias over the west coast of Angola and Namibia and in the southernmost part of the Arabian Peninsula, is also present in the Hindcast RCM models and ensemble (Figure A.4). In general, the Historic and Hindcast ensembles show a slight negative bias.

Overall, for TASMIN, the Historic RCM models (Figure 3.5) displays a positive bias over large areas except RACMO22T EC-EARTH, CCLM4 CM5 and CCLM4 EC-EARTH which show a negative bias over Sahel. HIRHAM5 NORESM1-M displays a very evident and strong bias, over $10^{o}C$ in southern Africa and in large areas of the Sahel region, having this variable and model the worst performance so far. The Hindcast simulation displays similar results (Figure A.5) with HIRHAM5 ERAINT exhibiting the worst performance. The other RCMs also display a positive bias, particularly over central Africa, and, in some cases, a negative bias over the Arabian Peninsula. For this variable, both ensembles render higher values than CRU for the respective periods, having the Hindcast ensemble a worse performance than Historic one.

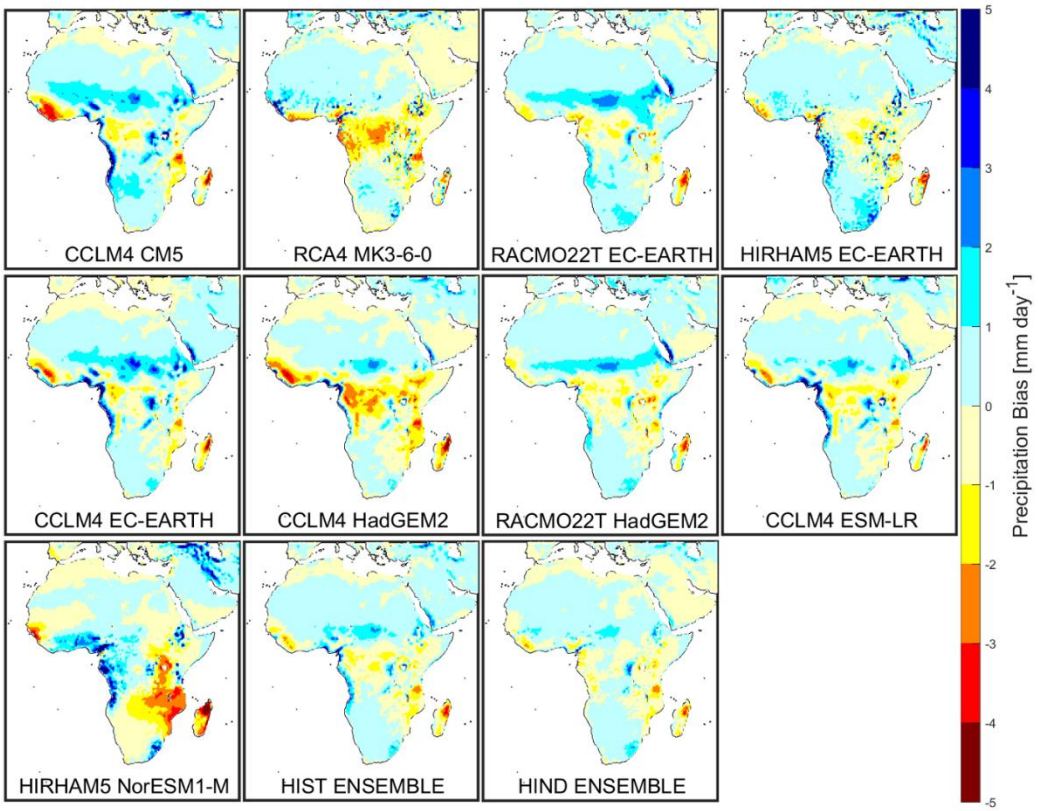


*Fig 3.2.* Precipitation (PR) bias in $mm\ day^{-1}$ relative to CRU database (Figure 3.1a) for the climatological mean for Historic (1971-2000) models and ensemble and for the Hindcast ensemble (1990-2000).

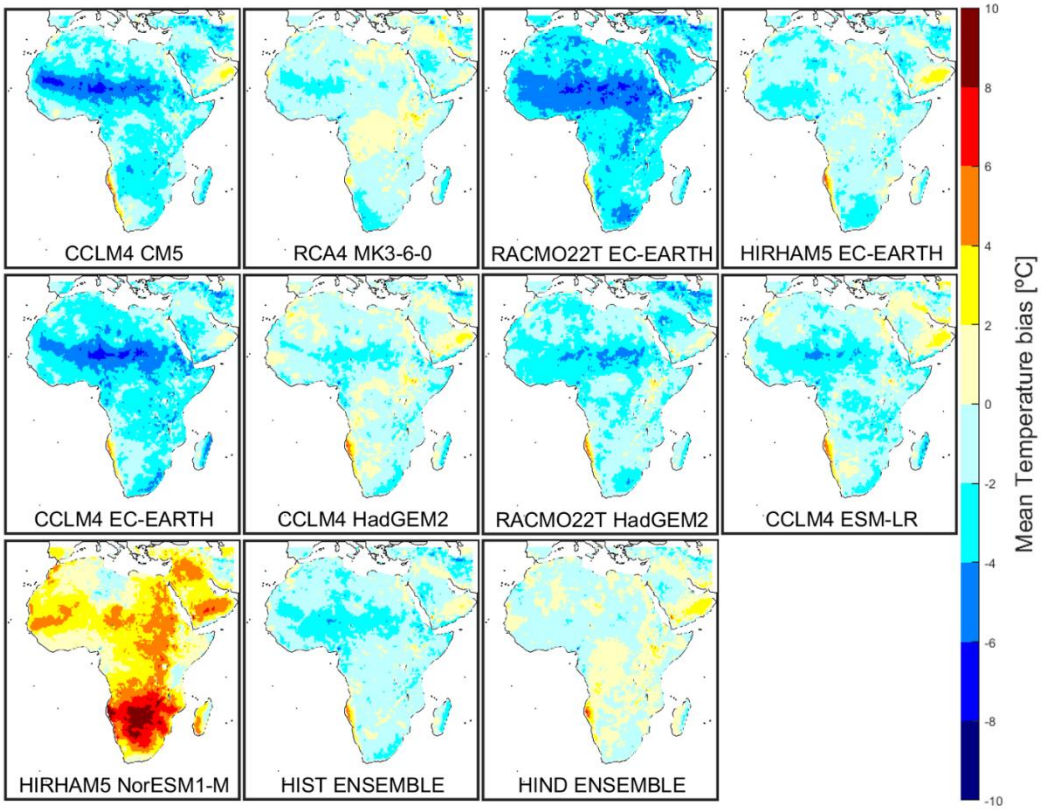


*Fig 3.3.* Mean temperature bias in $ºC$ relative to CRU database (Figure 3.1b) for the climatological mean for Historic (1971-2000) models. Hindcast (1990-2008) ensemble is also shown.

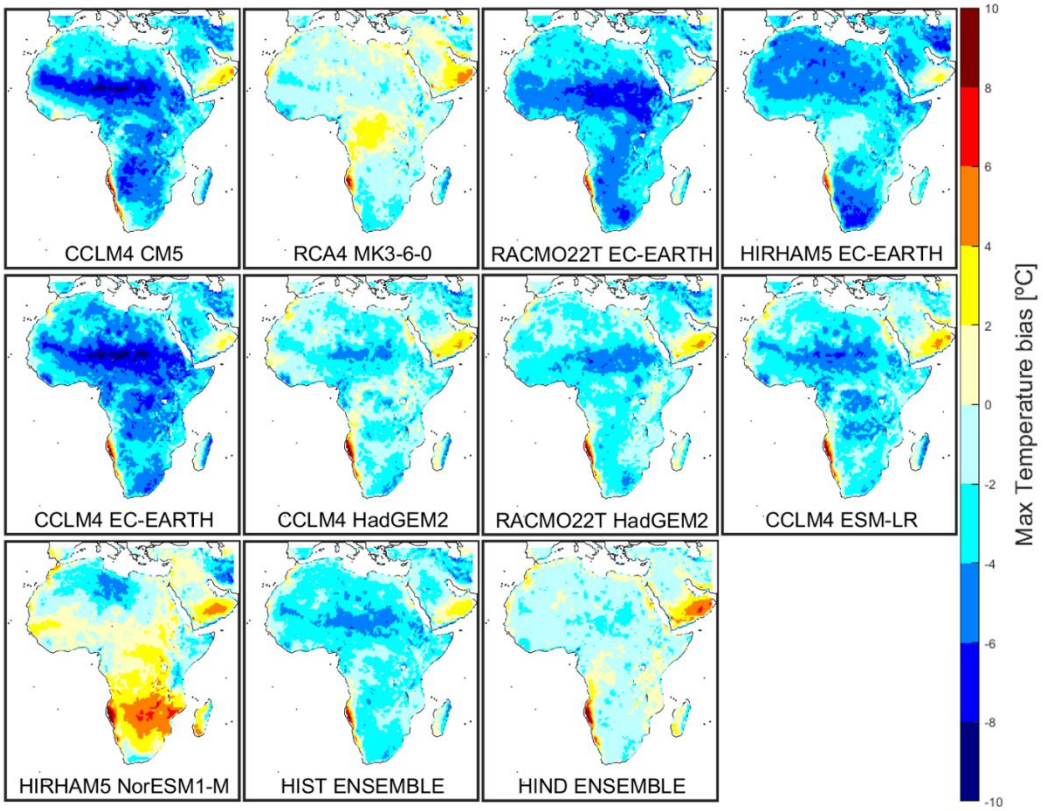


*Fig 3.4.* Maximum temperature (TASMAX) bias in $^{o}C$ relative to CRU database (Figure 3.1c) for the climatological mean for Historic (1971-2000) models and ensemble. Hindcast (1990-2008) ensemble is also shown.

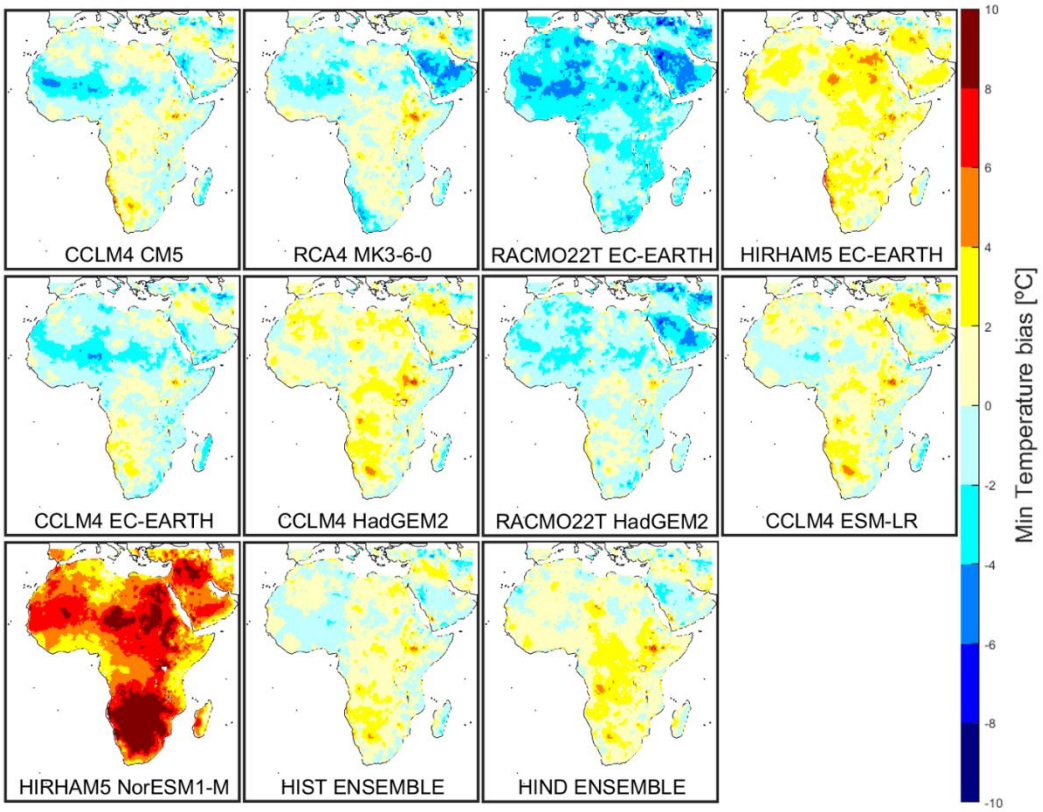


*Fig 3.5.* Minimum temperature (TASMIN) bias in $^{o}C$ relative to CRU database (Figure 3.1d) for the climatological mean for Historic (1971-2000) models and ensemble. Hindcast (1990-2008) ensemble is also shown.

The model performance can be further assessed with the use of Taylor diagrams (Taylor, 2001). These diagrams evaluate a model against a reference through three parameters: standard deviation (SD), correlation and root mean square error (RMSE). Normalized SD values by the reference (CRU dataset) were used in all cases. All models for almost all variables, for both simulations, display higher spatial variability than CRU, i.e., normalized standard deviations greater than one (Figure 3.6). The exception is the precipitation for CCLM4 ERAINT (A), RCA4 ERAINT (F), RACMO22T ERAINT (C) for Hindcast and RACMO22T EC-EARTH (C), CCLM4 HADGEM2 (F) and RACMO22T HADGEM2 (G) with better results. Overall, the ensemble (in red) for each variable and simulation displays the best performance, with the highest correlation and minimal RMSE. As expected, HIRHAM5 NORESM1-M (I) for the Historic simulation is the model that represents the worst score, with the lowest correlation, and highest RMSE value.

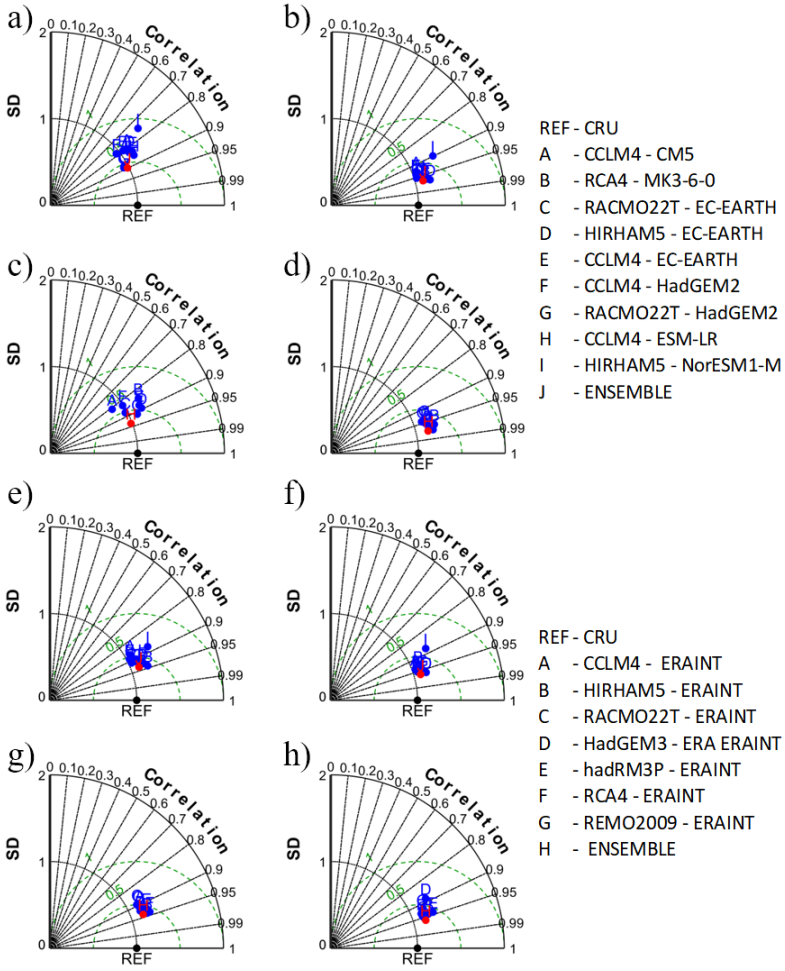


*Fig 3.6.* Taylor diagram of Historic, a) Precipitation, b) Daily Mean Temperature, c) Daily Maximum Temperature, d) Daily Minimum Temperature and for Hindcast, e) Precipitation, f) Daily Mean Temperature, g) Daily Maximum Temperature, h) Daily Minimum Temperature relative to CRU database. On each diagram, the red dot denotes the ensemble mean.

The seasonal TAS, TASMAX and TASMIN variables from the Historic simulation are also assessed and validated here relative to the CRU database (Figure 3.7). In some cases (e.g. Figure 3.7 h), the RCMs display higher inter-model dispersion and almost all models have the same variability, with higher values regarding the reference and correlations between 0.8 to 0.95 (similar to the correlations observed in Figure 3.6 b-d). In some seasons, a single model can display a better seasonal score than the ensemble

(e.g. HIRHAM5 EC-EARTH for Figure 3.10 e, h and i). Between variables, the TASMAX RCM cluster display the worst score with the highest RMSE values for all seasons.

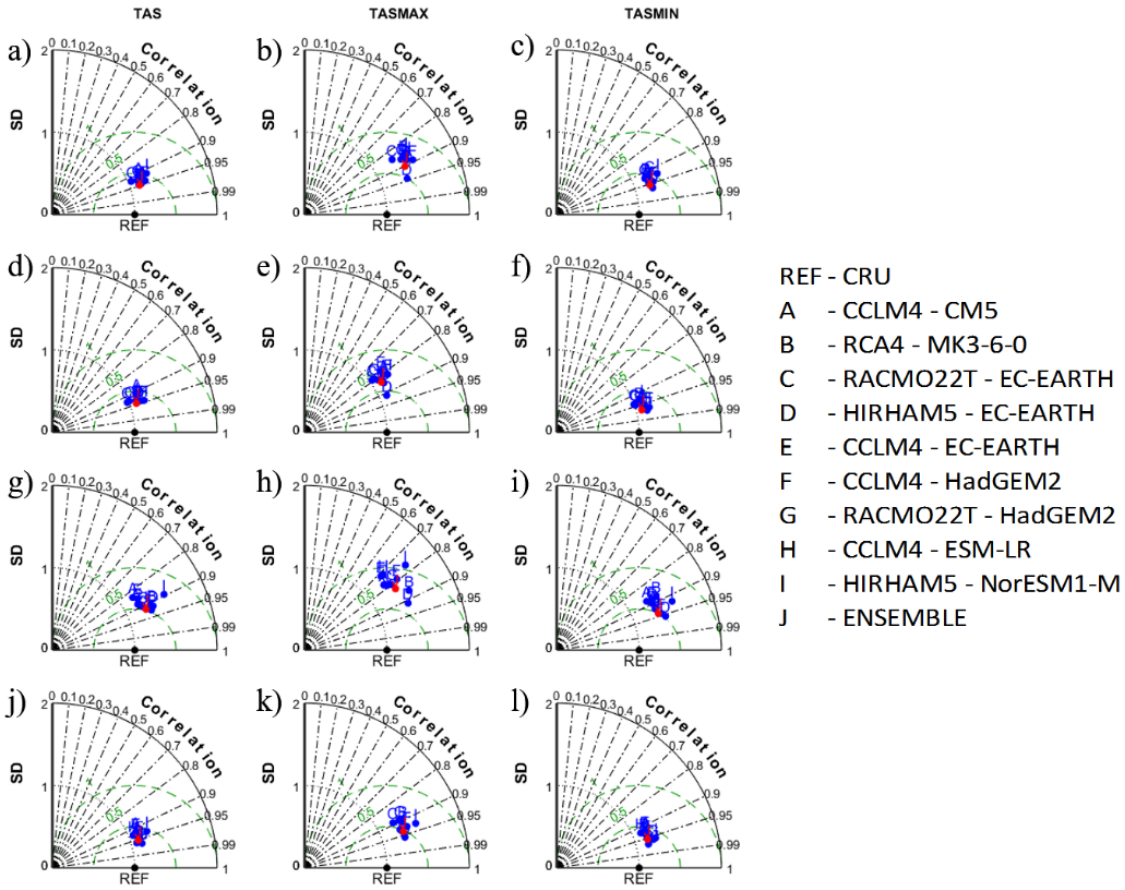


*Fig 3.7.* Seasonal Taylor diagrams for the Historic (1971-2000) for (columns) TAS, TASMAX and TASMIN. The seasons are (rows) MAM, JJA, SON and DJF. On each diagram, the red dot denotes the ensemble mean.

## 3.2 Precipitation against GPCC database

Seasonal and climatological precipitation for the Historic is also validated against the GPCC database. Similar to the analysis in the previous section, all data from the Historic (climatological and seasonal) must be interpolated before. There are some differences between the CRU and GPCC databases (see section 2.2b). Figure 3.8 displays the seasonal and climatological precipitation of the GPCC database for the Historic period. Comparing with Figure 3.1, the GPCC database is less homogeneous, but nevertheless the same precipitation regimes are visible with a drier northern and southern Africa, with almost no precipitation, and a wetter centre, being the west side more humid than the east side in the northern hemisphere, and the opposite in the southern hemisphere. This disparity in the climatological precipitation is due to differences in the Intertropical Convergence Zone (ITCZ) position.

The ITCZ or doldrums[5] (Figure 3 from Burrough and Thomas, 2013), is an area encircling Earth near the Equator, where the northeast and southeast trade winds converge. The ITCZ can be observed from space as a band of clouds, usually thunderstorms. The location of the ITCZ gradually varies with seasons (Nikulin et al., 2012) and over land it moves back and forth following the position of the Sun at noon. In the oceans, ITCZ is better defined and this seasonal cycle is more attenuated, as convection is constrained by the temperature distributions of the oceans. In Africa, the position of ITCZ, or African Monsoon, strongly affects precipitation across seasons. During MAM (Figure 3.7 a) ITCZ is located on the northern hemisphere, around 10º North and curves toward southeast in Sudan. During this season, precipitation concentrates more over western Africa (countries located north of the Guinea basin) and the western side of central Africa. During JJA (Figure 3.7 b), the ITCZ reaches its northernmost position, around 15º North on Africa mainland, bringing rain to the Sahel region. In SON (Figure 3.7 c) the ITCZ shifts southward, keeping its zonal configuration. Throughout this season the asymmetries west-east in central Africa are evident, with more precipitation on the western side. In western Africa this seasonal precipitation cycle is known as the west Africa Monsoon. During DJF (Figure 3.7 d) ITCZ is located near the coast of western Africa, curving southeast over central Africa. During this season, and for the south hemisphere, there is more precipitation over the eastern side, including Madagascar, than on the western side. This curvature of the ITCZ is due to the smaller variations of its position over the oceans. Also, the ITCZ moves further from the Equator during the boreal summer than on austral summer due to the heavier arrangements of the continents.

Overall, the precipitation bias of the Historic simulation (Figure 3.9), pattern and values relative to GPCC database is similar to the one relative to CRU. In all models and ensemble there is a pronounced wet bias over the Sahel region and a small positive bias over desert areas, except for HIRHAM5 NORESM1-M model. In central Africa, all models and ensembles have a dry bias, namely RCA4 MK3-6-0 and CCLM4 HADGEM2. In general, the Historic simulation models cannot reproduce the high precipitation values in west Africa and models give less precipitation over east Africa. Except for HIRHAM5 NORESM1-M, in central Africa there is a very strong wet bias over the west side, and a very strong dry bias over the eastern side, meaning that this model will give much more precipitation than observed in the west side, and less precipitation in the east side. The ensemble climatological precipitation values are close to GPCC, having Africa mainland small biases over large areas, except for the west coast of central Africa with a wet bias, and some isolated points south of Sahel region, north of Madagascar island and some isolated points in east Africa with dry biases.

[5] Designation given by sailors to the ITCZ area where the prevailing winds are calm

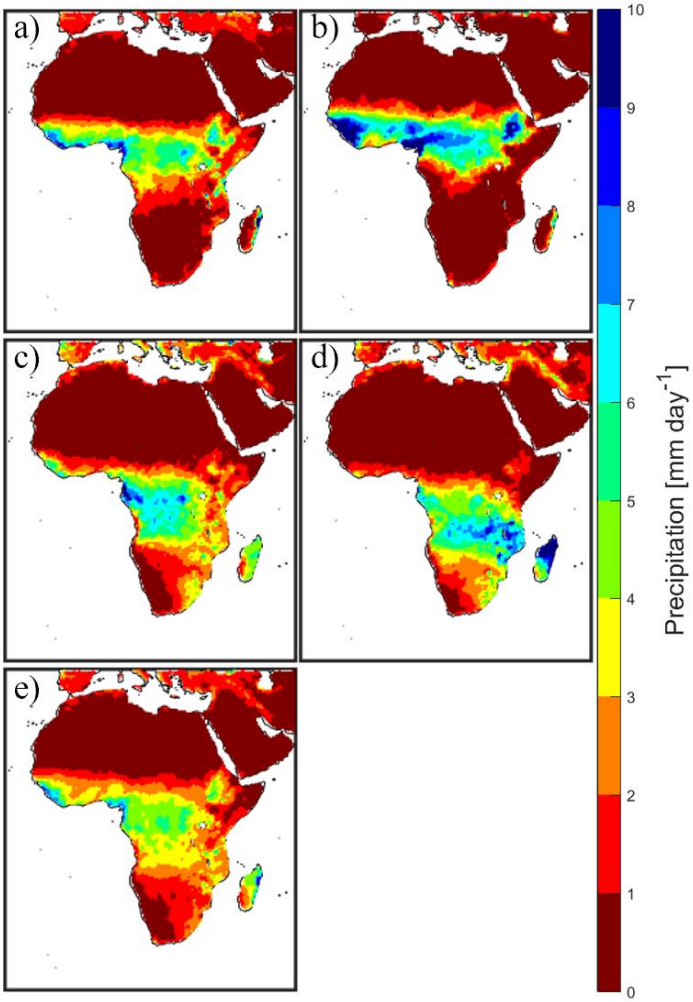


*Fig 3.8.* Seasonal and climatological precipitation derived from the Global Precipitation Climatology Centre (GPCC) for the Historic period (1971-2000) for (a) March-April-May (MAM), (b) June-July-August (JJA), (c) September-October-November (SON), (d) December-January-February (DJF) and (e) climatological.

Figure 3.10 shows the Taylor diagrams for precipitation for all models of the Historic simulation at the seasonal (Figure 3.10 a, b, d and e) and climatological scales (Figure 3.10 c). Since the climatological values of the GPCC database are less homogeneous relative to CRU (Figure 3.8 relative to Figure 3.1), overall, the spatial correlation is lower (Figure 3.10 e). Once more, the HIRHAM5 NORESM1-M (I) model has the worst performance with lowest correlation and highest variability (higher RMSE) regarding other RCMs. RACMO22T EC-EARTH (C), CCLM4 HADGEM2 (F) and RACMO22T HADGEM2 (G) models display lower spatial variability, while the other RCMs show higher variability. RCA4 MK3-6-0 (B) is however an exception with values closer to those observed. In this case, the Historic simulation ensemble (in red) represents better the reality with the lowest RMSE value relative to each single RCM.

The seasonal Taylor diagrams (Figure 3.10 a, b, d and e) for the RCM display similar correlation values regarding the climatological diagram with an increase in the inter-model variability relative to the reference. The worst performance with the highest RMSE is the HIRHAM5 NORESM1-M (I) model for SON and DJF seasons and sometimes a single model has better results than ensemble (both RACMO22T for MAM, RACMO22T EC-EARTH and RACMO22T HADGEM2 for SON and, RACMO22T HADGEM2 for DJF).

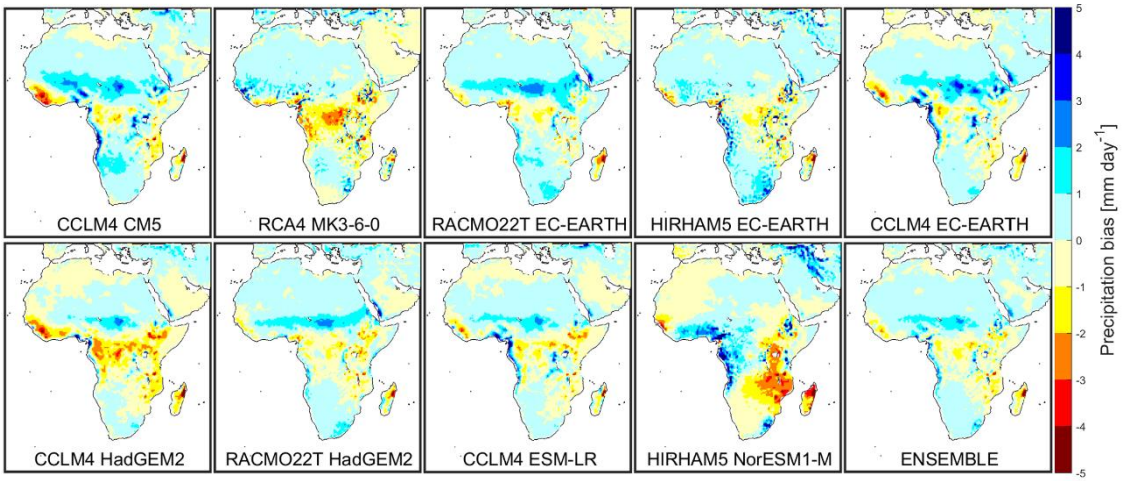


*Fig 3.9.* Historic model and ensemble precipitation biases relative to the GPCC database (Figure 3.7) for the period 1971 to 2000.

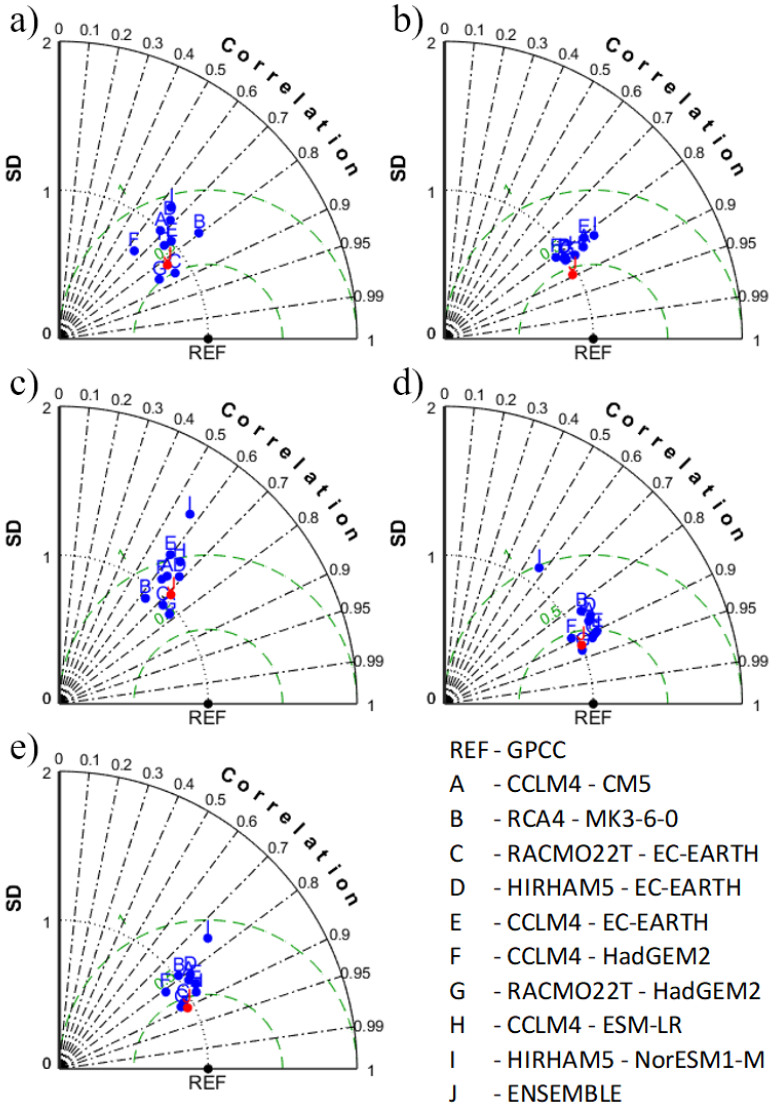


*Fig 3.10.* Taylor diagrams for precipitation of all models and ensemble from the Historic (1971-2000) relative to GPCC database for a) MAM, b) JJA, c) SON, d) DJF and e) climatological. On each diagram, the red dot denotes the ensemble mean.

## 3.3 Seasonal Upward Surface Fluxes and Soil Moisture

HFLS, HFSS and MRSO must be evaluated against the Hindcast simulation (Figure 3.11). For both fluxes, the lack of observations in Africa prevents model validation against observations as only three FLUXNET stations were considered. MRSO is also compared against the GLEAM database in the form of regional and total spatial correlations (Table 3.1 for Historic simulation and Table A.1 for Hindcast simulation). The GLEAM database provides only the root zone soil moisture, while all data used here considers the vertically integrated total amount of water in a soil column, thus we consider solely correlations. For this reason, it is not possible to compute a Taylor diagram for MRSO due to different orders of magnitude which would influence the standard deviation.

For all four seasons, HFLS (Figure 3.11 a, d, g and j), from all Historical RCM agree well with the Hindcast ensemble, with low RMSE values. There is a larger spread of the RCM scores for DJF relative to other seasons. The Historic ensemble, in this case, improves the single RCM performance, with correlations values higher than 0.95 and standard deviations close to the Hindcast ensemble. In the case of HFSS, (Figure 3.11 b, e, h and k), there is a larger spread comparatively to HFLS diagrams. Again, the ensemble improves significantly the single model performance, for all seasons, with correlations values higher than 0.95 and variability close to the reference. While for HFLS and HFSS variables, individual RCMs have standard deviations values close to the Hindcast ensemble, this is not the case for MRSO (Figure 3.11 c, f, i, and l). Excluding HIRHAM5 EC-EARTH and HIRHAM5 NORESM1-M, all models shows a lower variability than Hindcast ensemble. The former has standard deviation values more than 2.5 times higher than the latter. Despite this, and similar to previous cases, the ensemble shows better results with higher spatial correlation values, but unlike HFLS and HFSS, this ensemble displays lower variability, consequence of the lower RCM standard deviation values.

To better assess MRSO, the Africa-CORDEX domain is divided into regions (Table 3.1 for the borders coordinates and Figure A.6 for the regions geographical locations). The choice of these regions is based on results about land-atmosphere coupling strength from Koster et al. (2006); Miralles et al. (2012) and from the regions used by Hernández-Díaz et al. (2013). NA-SA region includes the Sahel, a transition zone with 1000 km wide and 5400 km long on north Africa between the Sudan savannah in the south and the Sahara Desert in the north. From this point onward, each time Sahel region is specified, it is referred to NA-SA region. NA-SW is a region south of the previous one, over western Africa. EA is located on the eastern side of Africa, and goes from NA-SW to CSA regions encompasses countries such as Kenia, Tanzania and Mozambique. CAN is located on the western side of central Africa (Cameroon, Equatorial Guinea, Congo, Republic Democratic of Congo, Gabon and northern Angola). CSA region is located essentially on southern Angola and Zambia. SAW region is situated on the western side of south Africa.

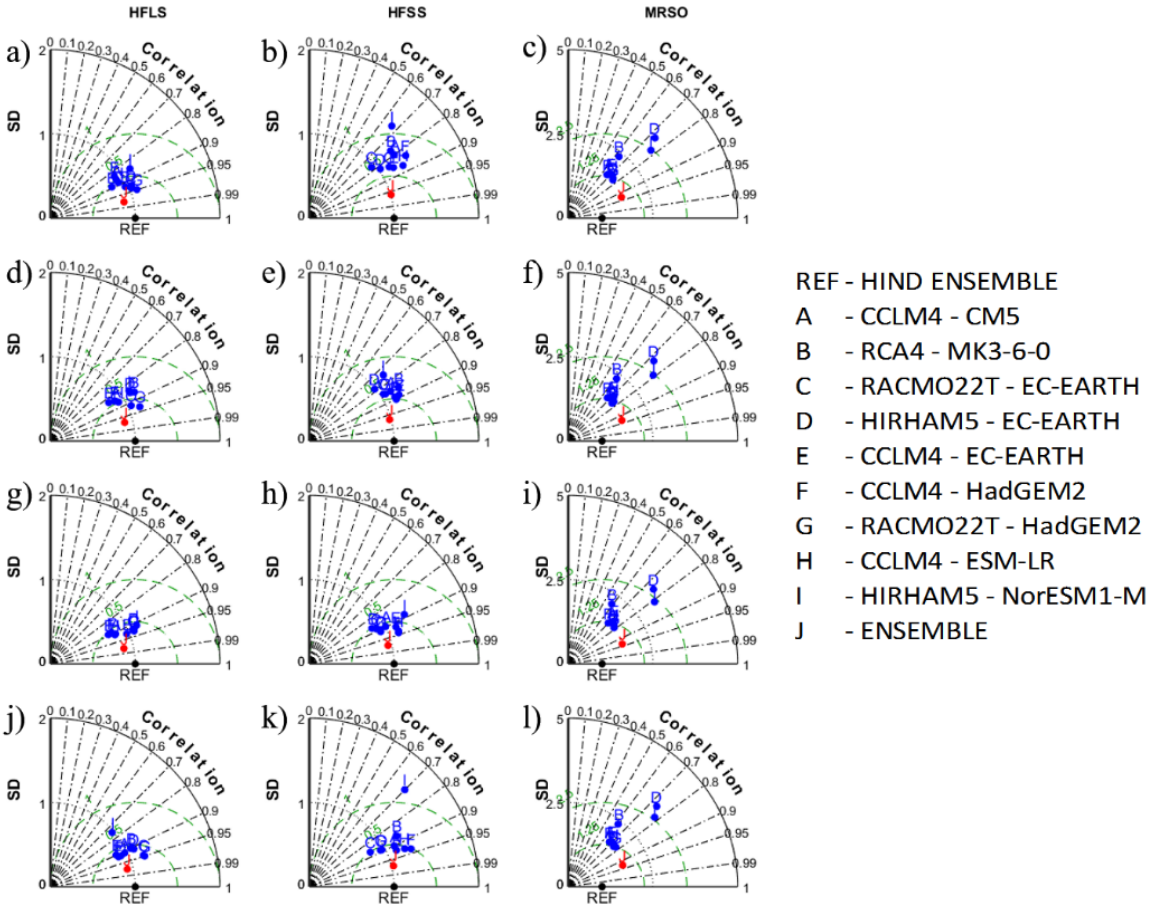


*Fig 3.11.* Seasonal Taylor diagrams for the Historic (1971-2000) for (columns) HFLS, HFSS and MRSO. The seasons (rows) are MAM, JJA, SON and DJF. On each diagram, the red dot denotes the ensemble mean.

*Table 3.1.* Regional boxes (vertices).

| Domain | Region | Northern Border | Southern Border | Western Border | Eastern Border |
|---|---|---|---|---|---|
| NA-SA | Northern Africa Semi-Arid | 20ºN | 10ºN | 20ºW | 40ºW |
| NA-SW | Northern Africa Semi-Humid | 10ºN | 05ºN | 10ºW | 40ºE |
| EA | East Africa | 5ºN | 20ºS | 30ºE | 40ºE |
| CNA | Central Northern Africa | 5ºN | 10ºS | 10ºE | 30ºE |
| CSA | Central Southern Africa | 10ºS | 20ºS | 10ºE | 30ºE |
| SA-W | South Africa-West | 22ºS | 35ºS | 13ºE | 20ºE |

Table 3.2 shows the correlation values for the African domain and regions for the Historic simulation models and ensemble and additionally the Hindcast ensemble. Hindcast simulation results are shown in Table A.2. Overall, all RCMs show a good agreement against GLEAM, with correlations over 0.5, having the RCA4 MK3-6-0 the highest score for Historic and HADRM3P ERAINT the highest score for Hindcast. In both simulations, the ensemble displays the best results with correlations of 0.813 for

Historic and 0.889 for Hindcast. HIRHAM5 group (HIRHAM5 EC-EARTH and HIRHAM5 NORESM1-M from Historic and HIRHAM5 ERAINT from Hindcast) is the model with the poorest performance, with near zero correlation values over NA-SA, NA-SW, EA and CAN regions.

The daily annual cycle for the nearest neighbour grid point of upward latent (HFLS) and sensible heat (HFSS) fluxes for Historic and Hindcast ensembles, are compared against three FLUXNET stations (Figure 3.12 for latent heat flux and Figure 3.13 for sensible heat flux). All three stations are classified as savannah (Table 2.4). Due to the lack of observations in Africa, no restrictions were made to the data, and extended periods of low data quality are likely. Overall, for all cases, the ensembles are able to capture the annual cycle of both variables. In the case of HFLS, and for SD-DEM and SN-DHR (Figure 3.12 a and b), both ensembles underestimate the observed values, while for ZA-KRU station (figure 3.12 c), both ensembles follow the observations, with slightly higher daily values. For HFSS (Figure 3.13), the seasonal cycle is well captured on both ensembles, with a good agreement for ZA-KRU station. In the other two cases, the ensembles overestimate HFSS throughout the year.

*Table 3.2.* Pearson correlations between Historic (1980-2000) total soil moisture and root-zone soil moisture taken from GLEAM database for the Africa-CORDEX focus domain and regions defined on Table 3.1. The correlation for the Hindcast ensemble (1990-2008) is also shown.

| RCM | AFRICA | NA-SA | NA-SW | EA | CNA | CSA | SA-W |
|---|---|---|---|---|---|---|---|
| CCLM4 CM5 | 0.5370 | 0.6135 | 0.1356 | 0.3393 | 0.5612 | 0.3316 | 0.1991 |
| RCA4 MK3-6-0 | 0.6961 | 0.8777 | 0.5932 | 0.6086 | 0.6946 | 0.7743 | 0.7234 |
| RACMO22T EC-EARTH | 0.6635 | 0.6361 | 0.3761 | 0.5329 | 0.3618 | 0.4801 | 0.1677 |
| HIRHAM5 EC-EARTH | 0.6164 | 0.7650 | -0.0644 | 0.3369 | -0.2982 | 0.0681 | 0.5190 |
| CCLM4 EC-EARTH | 0.5594 | 0.6042 | 0.2118 | 0.3369 | 0.6020 | 0.4857 | 0.3350 |
| CCLM4 HadGEM2 | 0.5235 | 0.6500 | 0.2685 | 0.4161 | 0.5020 | 0.5167 | 0.4044 |
| RACMO22T HadGEM2 | 0.6841 | 0.6193 | 0.3631 | 0.5047 | 0.4405 | 0.5430 | 0.0864 |
| CCLM4 ESM-LR | 0.6082 | 0.6835 | 0.2117 | 0.3933 | 0.6090 | 0.4828 | 0.4177 |
| HIRHAM5 NorESM1-M | 0.6850 | 0.7732 | -0.0303 | -0.0025 | -0.1572 | 0.1540 | 0.6238 |
| ENSEMBLE HISTORIC | 0.8136 | 0.8370 | 0.3172 | 0.5786 | 0.6017 | 0.5815 | 0.5495 |
| ENSEMBLE HINDCAST | 0.8897 | 0.9117 | 0.5066 | 0.6981 | 0.8608 | 0.7652 | 0.7003 |

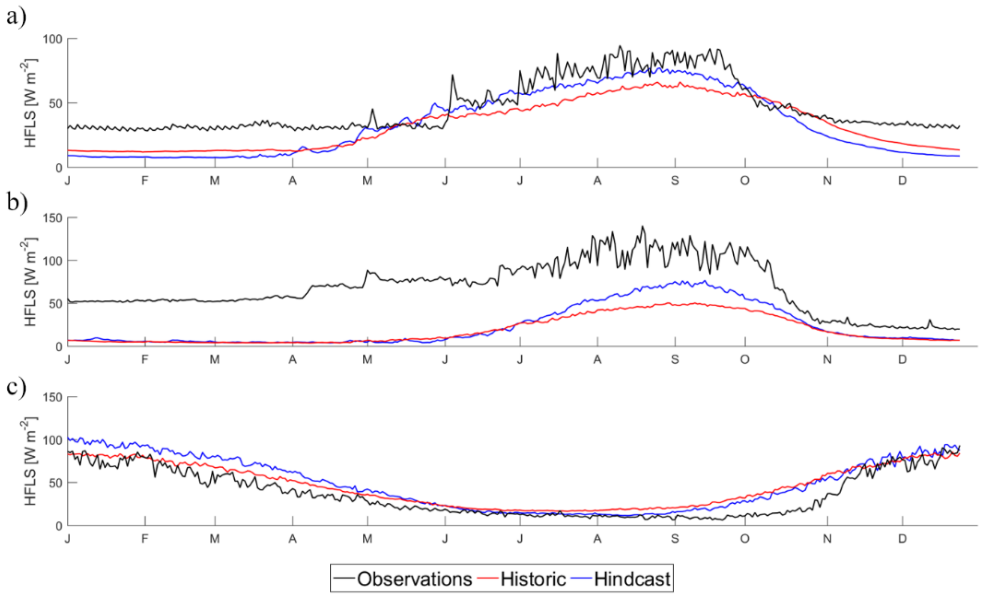


*Fig 3.12.* Mean daily cycles of the nearest grid point from the Historic and Hindcast ensemble for the HFLS against three FLUXNET stations: a) SD-DEM, b) SN-DHR and c) ZA-KRU.

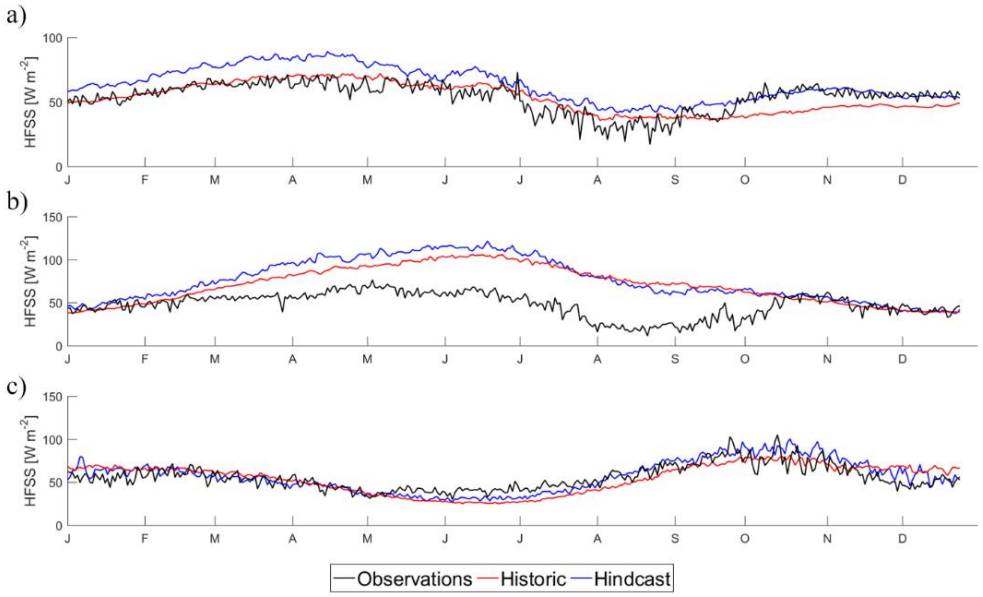


*Fig 3.13.* Mean daily cycles of the nearest grid point from the Historic and Hindcast ensemble for the HFSS against three FLUXNET stations: a) SD-DEM, b) SN-DHR and c) ZA-KRU.

# 4. Land-Atmosphere Coupling and Extremes in Present Climate

In the present chapter, a characterisation for the present climate of the land-atmosphere coupling in Africa is done using Bowen ratio and Evaporative Fraction. In this way, the models ability to portray the present climate's moisture and energy fluxes can be evaluated. Correlation between soil moisture and Evaporative Fraction is used to assess the relationship between soil moisture and the flux partitioning, while the correlation between latent and sensible heat flux is used to evaluate the long-term balance between both fluxes for different climates. Also, the correlation between latent heat flux and maximum temperature is considered here to assess how the latent heat flux could affect surface temperature in certain climates. Annual mean number of heat waves and mean heat wave duration is used to evaluate where temperature extremes are more frequent, and SPEI characterises dry spells over Africa, in the present. Finally, a Latent Heat Flux-Temperature Coupling Magnitude (LETCM) for known heat waves periods is computed, only for the Hindcast ensemble, to evaluate if during certain periods temperatures were higher due to soil moisture-temperature coupling.

## 4.1 Surface Fluxes

The following section investigates the RCMs representation of latent and sensible heat fluxes and how well this balance is represented for different climates at the seasonal scale.

The Bowen ratio (eq. 2.2) is the fraction between sensible and latent heat fluxes and varies across different climates, from daily to seasonal scales, depending on the balance between both fluxes (Figures 4.1a, 4.2a, 4.3a, 4.4a, for Historic and Figures A.7a, A.8a, A.9a, A.10a, for Hindcast). This ratio is small over humid climates where most of the energy goes into evapotranspiration and larger over dry surfaces where most of the energy goes into sensible heating (Stull, 1998). Typical values range from more than 5 over dry regions, 5 over semi-arid regions, 0.5 over grasslands and forests, 0.1 over oceans and possible negative values over oases. Another useful way to assess the flux partitioning across different climates is through the Evaporative Fraction (Figures 4.1b, 4.2b, 4.3b, 4.4b and Figures A.7b, A.8b, A.9b, A10b). Unlike Bowen's ratio, where values don't fall into a fixed interval, the Evaporative Fraction or the ratio between latent heat flux and the sum of latent with sensible heat fluxes, varies between 0 to 1. The typical values over desert areas are close to 0, where evapotranspiration is small and sensible heat flux dominates, and over humid areas, where there is always water to evaporate, values are close to 1, since the energy needed for evaporating water surpasses the sensible heating. Transition zones are easily identified, as values for these regions lie between 0.2 to 0.7. Both metrics are useful on land, but not over oceans, as there is always water to evaporate, yielding low Bowen ratio values or high Evaporative Fraction values. Depending on the season, lower (higher) Bowen ratio (Evaporative Fraction) values on regions of high rainfall rates is expected.

During MAM, there is more precipitation over the western side of Africa in the northern hemisphere (Figure 3.7 a). The pattern between the Bowen ratio and Evaporative Fraction is similar with both Sahara and Namib deserts visible (depicted as red in Figure 4.1 for Historic and Figure A.7 for Hindcast) and a more humid central Africa (shown in blue). All models can reproduce a more humid region over western Africa, except for CCLM4 CM5 (relative to Figure A.6). HIRHAM5 NORESM1-M also displays

anomalous high (low) Bowen ratio (Evaporative Fraction) values over Botswana, Zimbabwe and Mozambique, regions where all the other models classify as transition areas.

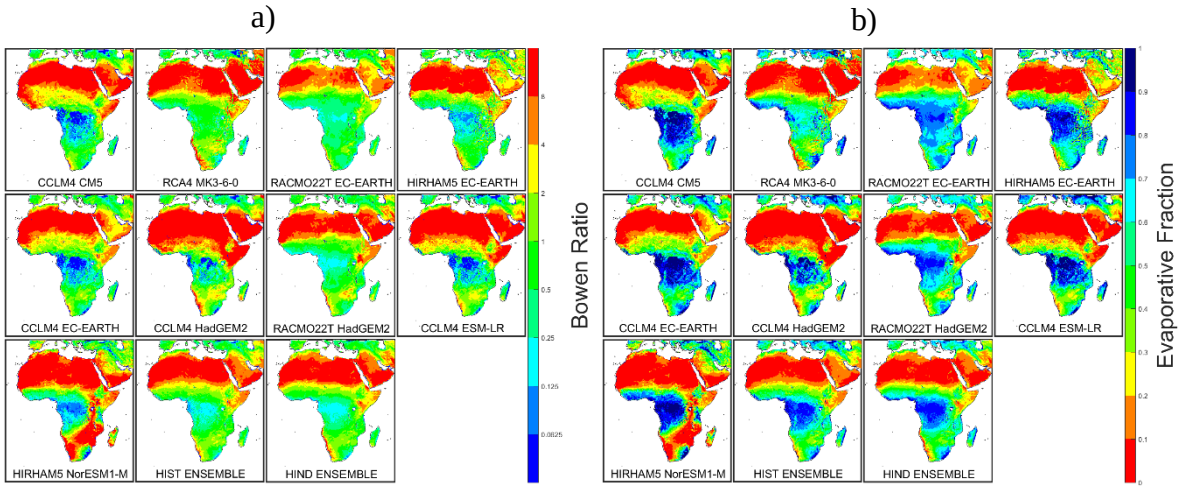


*Fig 4.1.* MAM (a) Bowen ratio and (b) Evaporative Fraction for Historic (1971-2000). The Hindcast (1990-2008) ensemble is also shown.

During summer in the northern hemisphere (JJA), the ITCZ is at its northernmost position, with precipitation in the Sahel region and rainfall on western Africa at its maximum. This displacement and a more humid western Africa is well captured by almost all models and ensembles with a shift towards north of higher (lower) Bowen ratio (Evaporative Fraction) values (depicted as red in Figures 4.2 for Historic and A.8 for Hindcast). The position of this border for HIRHAM5 NORESM1-M model is further south comparing with other models and, together with RCA4 MK3-6-0 and CCLM4 HADGEM2, all these three RCMs displays higher values over southern Africa. In this area, there is a clear difference in both ensembles, with Namib Desert still visible on Hindcast ensemble. Also, some noise is visible for models in the CCLM4 group (all versions of this model on Historic and Hindcast) over southern Africa.

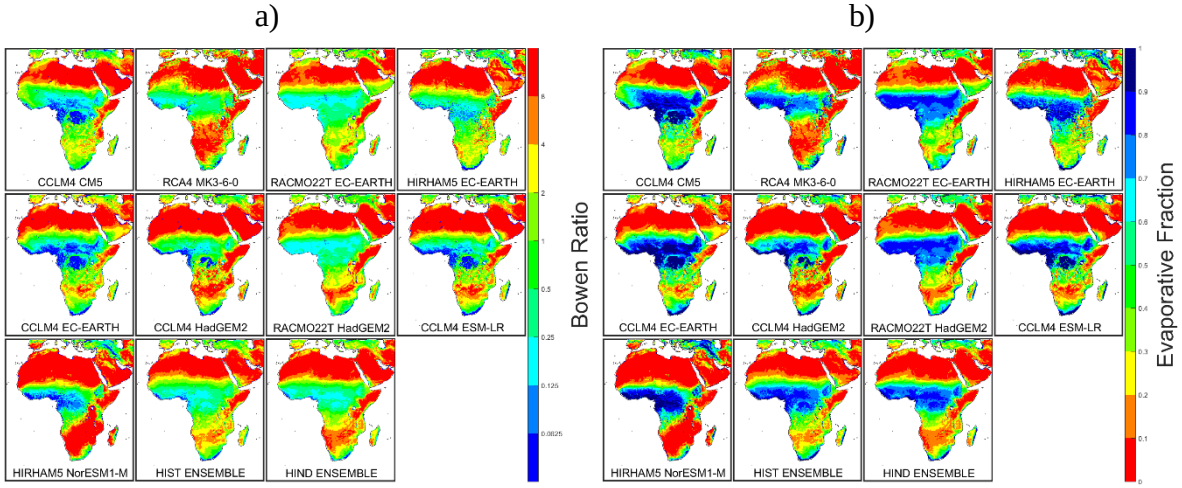


*Fig 4.2.* JJA (a) Bowen ratio and (b) Evaporative Fraction for Historic (1971-2000). The Hindcast (1990-2008) ensemble is also shown.

For SON (Figures 4.3 for Historic and A.9 for Hindcast), the ITCZ moves towards the Equator. In this season, there is much more precipitation in the western side of central Africa than on the eastern side, for the north hemisphere. Only the CLM and HIRHAM5 group, from Historic and Hindcast, and

REMOO2009 ERAINT RCMs can portray a more humid central Africa (low Bowen ratio values or higher Evaporative Fraction values). However, for this season, HIRHAM5 NORESM1-M shows a very dry northern and southern Africa. While both ensembles cannot depict a more humid central Africa, they are coherent between themselves. Also, the CCLM4 group displays a more humid western Sahara. Overall, both Namib and Sahara deserts are visible.

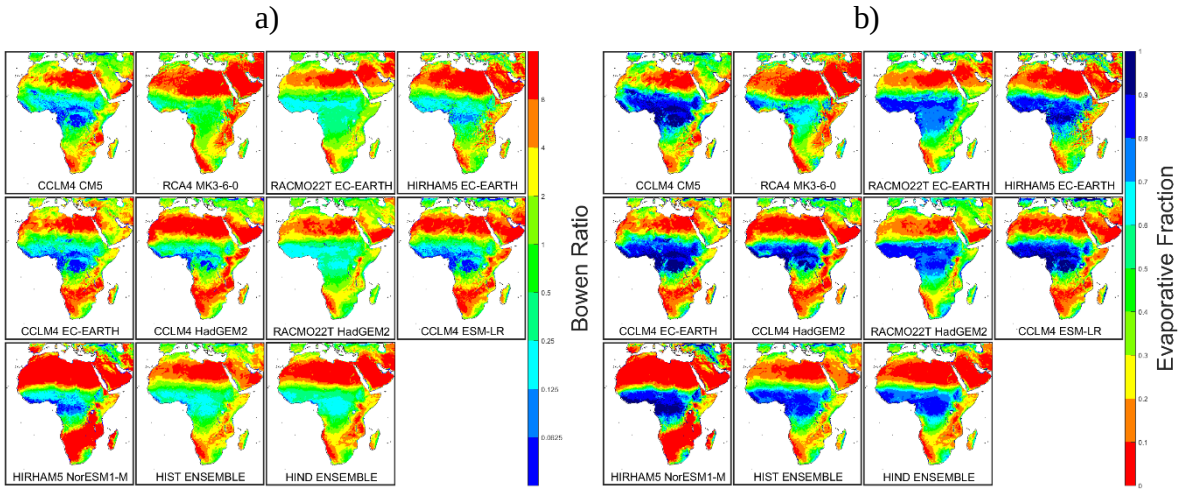


*Fig 4.3.* SON (a) Bowen ratio and (b) Evaporative Fraction for Historic (1971-2000). The Hindcast (1990-2008) ensemble is also shown.

The CLM RCM group for DJF on both Bowen ratio and Evaporative Fraction (Figure 4.4 for Historic and Figure A.10 for Hindcast), displays a noisy pattern with very low values over north Africa. This noisy pattern is due to low mean values of both fluxes over the Sahara Desert, mainly on the western side. In this season, ITCZ curves to south of Equator bringing more rain into the southeastern side of central Africa. Except for HIRHAM5 NORESM1-M, all models and ensembles display a more humid eastern Africa. The ITCZ during this season is at its southernmost position bringing precipitation mainly to the eastern side of central Africa in the southouthern hemisphere and to Madagascar Island. The ensembles of Historic and Hindcast agree showing three dryer areas (Sahara, Somalia Deserts and to a lesser extent the Namib) and a more humid central and eastern Africa. HIRHAM5 NORESM1-M models also displays extensive dryer areas (Mozambique, Zambia Tanzania), on both metrics, due to high sensible heat values in this season.

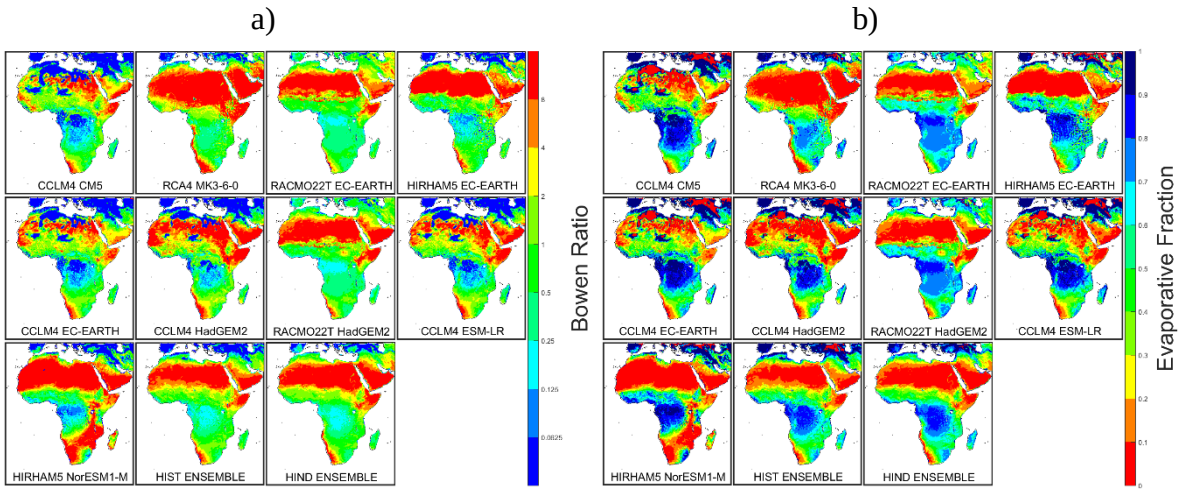


*Fig 4.4.* DJF (a) Bowen ratio and (b) Evaporative Fraction for Historic (1971-2000). The Hindcast (1990-2008) ensemble is also shown.

From all Historic RCMs, the HIRHAM5 NORESM1-M displays higher (lower) Bowen ratio (Evaporative Fraction) values, over larger areas that are not classified as deserts on other models. This RCM also had the highest seasonal and climatological RMSE (Chapter 3) for almost all variables, with possible unrealistic results for some areas, if not in the entire domain. For both metrics, almost all models are coherent with a seasonal variation (between wet and dry seasons) that depends on the position of the ITCZ and are also coherent with the Köppen-Geiger climate classification (Figure A.6). With some exceptions, all models show 3 dryer areas on Africa mainland (corresponding to the red areas on Figure A.6: Sahara, Namib and Somalia deserts) visible for all seasons; and a permanent very humid region (dark blue on Figure A.6) over the central Democratic Republic of Congo. The transition areas between these two types of climates is also visible in all cases, with a seasonal variation and with some inter-model variance (all values higher than 0.5 and lower than 4 for Bowen ration and all values higher than 0.2 and lower than 0.7 for the Evaporative Fraction), this corresponds to Mediterranean type climates (depicted as orange, yellow and green on Figure A.6). These are the regions where the interaction between soil moisture and temperature is more relevant in the context of land-atmosphere coupling. The regions are: NA-SA (Sahel), NA-SW, EA and CSA (Figure A.6).

## 4.2 Pearson Correlations

### a. Evaporative Fraction and Soil Moisture

The first step in the soil moisture-temperature feedback is the connection between soil moisture and the flux partitioning. This connection is indicated here by the 10 days of nonoverlapping means seasonal correlation between Evaporative Fraction (ratio between latent heat flux with the sum of latent and sensible heat fluxes) and total (i.e. vertically integrated) soil moisture (Figures 4.5 to 4.8 for Historic and Figures A.11 to A.14 for Hindcast). Positive correlations are expected as an increasing (decreasing) in soil moisture leads to an increasing (decreasing) of the Evaporative Fraction. Overall, strong correlations are expected in humid and transition climates, since both soil moisture and Evaporative Fraction are relatively high in these regions, and lower correlations are expected on desert areas where Evaporative Fraction is lower, but MRSO can, however, display high values, indicating the presence of ground water.

For MAM (Figure 4.5 for Historic and Figure A.11 for Hindcast), both ensembles display a similar pattern with high correlations on southern and central Africa, notably in Angola, Zambia and Democratic Republic of Congo, and lower correlation values over northern Africa. These lower correlations are due to the dry conditions observed in this area. The individual models display very different results, namely the RCA4 MK3-6-0 and RCA4 ERAINT with very high correlations over Africa mainland and Madagascar island. These higher correlations could be due to wrong values of MRSO over the domain, as high soil water content is found over central Africa and low water content in the surroundings, while the other models indicate high MRSO throughout the domain.

During JJA the ensembles (Figure 4.6 for Historic and Figure A.12 for Hindcast) exhibit different correlation values, namely on the eastern side of central Africa with lower correlations on Hindcast ensemble and, also on the Namib Desert with correlations below 0. In this season, precipitation concentrates more on northern Africa, reaching Sahel (Figure 3.7 b), and very drier conditions are observed on southern Africa. The individual models show a large correlation spread within the RACMO22T group of simulations, HadGEM3-RA ERAINT and HadRM3P ERAINT models, all displaying lower correlations over the domain, with some negative values over western Africa. Also, some noise is visible for HadGEM3-RA ERAINT model, over northern Africa, with alternating values of high and low correlations. These anomalously high correlations are due to a total (i.e. vertically integrated) very low soil water content over these areas.

Analogous to the other seasons, in SON (Figure 4.7 for Historic and Figure A.13 for Hindcast) both Historic and Hindcast ensembles reveal similar correlation patterns, except in some areas of southern Africa with higher values in the Historic ensemble and over Central African Republic with some negative values. There is a clear difference between individual models over the Sahara Desert, with models from the CCLM4 group and almost all models from Hindcast, except RCA4 ERAINT and REMOO2009 ERAINT, showing a noisy pattern with areas of low correlation. Identically to MAM, RCA4 MK3-6-0 for both Historic an Hindcast displays very high correlations values over the entire domain. Finally, models from the RACMO22T and HIRHAM5 group also display a noisy pattern over west and central Africa with low and sometimes negative correlation values.

During DJF season (Figure 4.8 for Historic and Figure A.14 for Hindcast), precipitation is more concentrated in central southern Africa. High correlation values are found in these areas and a lower noisy correlation pattern over the Sahara Desert can be identified. Similarly, to the previous cases, RCA4 MK3-6-0 group displays high correlations over Africa. Both ensembles are in agreement, except near the Mediterranean coast which have higher correlations on Hindcast. On all cases, central Africa on the

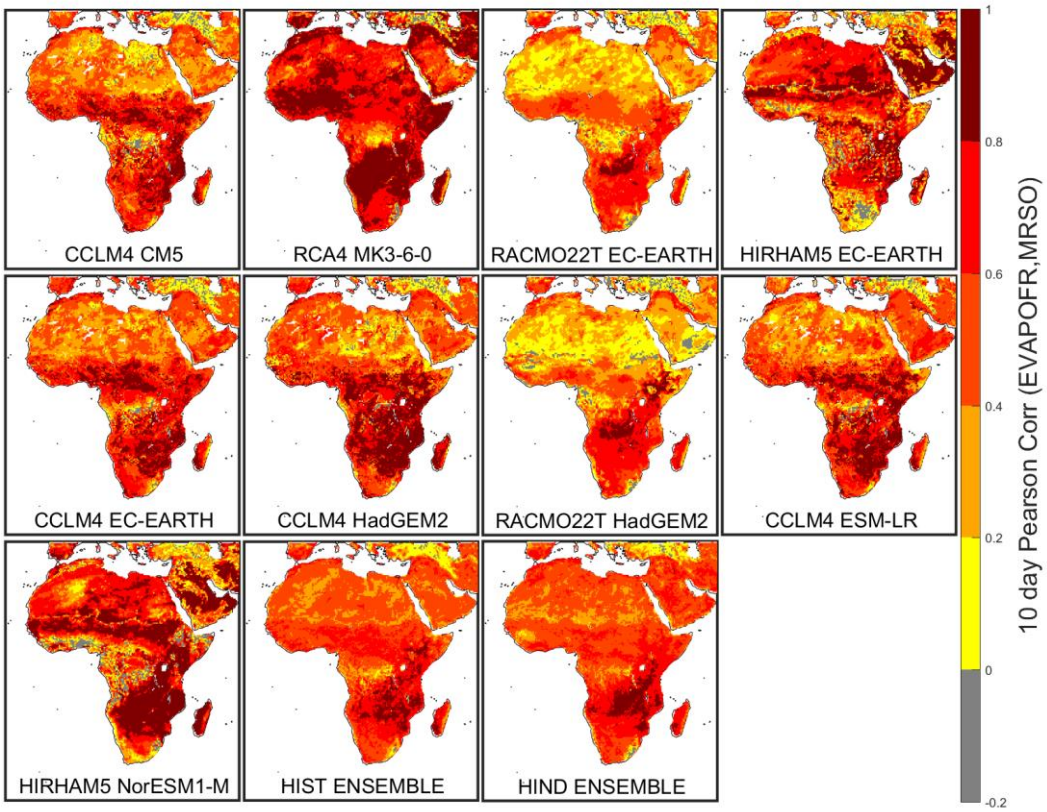


*Fig 4.5.* MAM 10 days of nonoverlapping means correlation between MRSO and Evaporative Fraction (EVAPFR) for Historic (1971-2000). The Hindcast (1990-2008) ensemble is also shown. Values lower than 0 are depicted as gray.

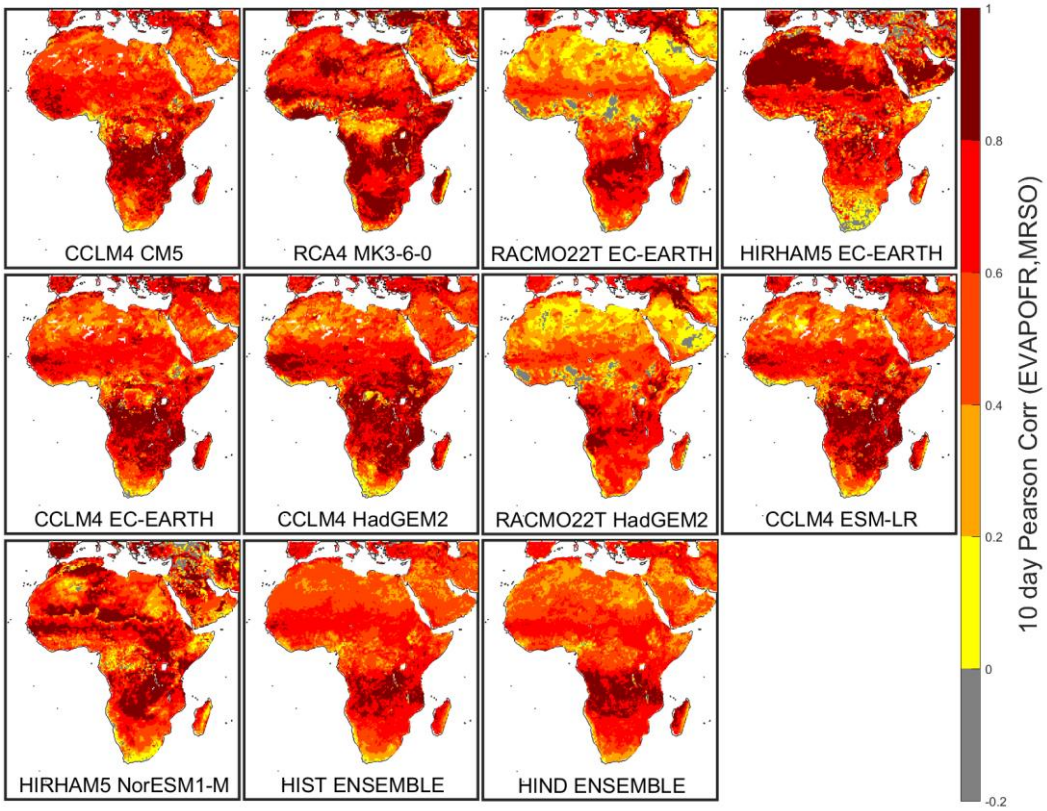


*Fig 4.6.* JJA 10 days of nonoverlapping means correlation between MRSO and Evaporative Fraction (EVAPFR) for Historic (1971-2000). The Hindcast (1990-2008) ensemble is also shown. Values lower than 0 are depicted as gray.

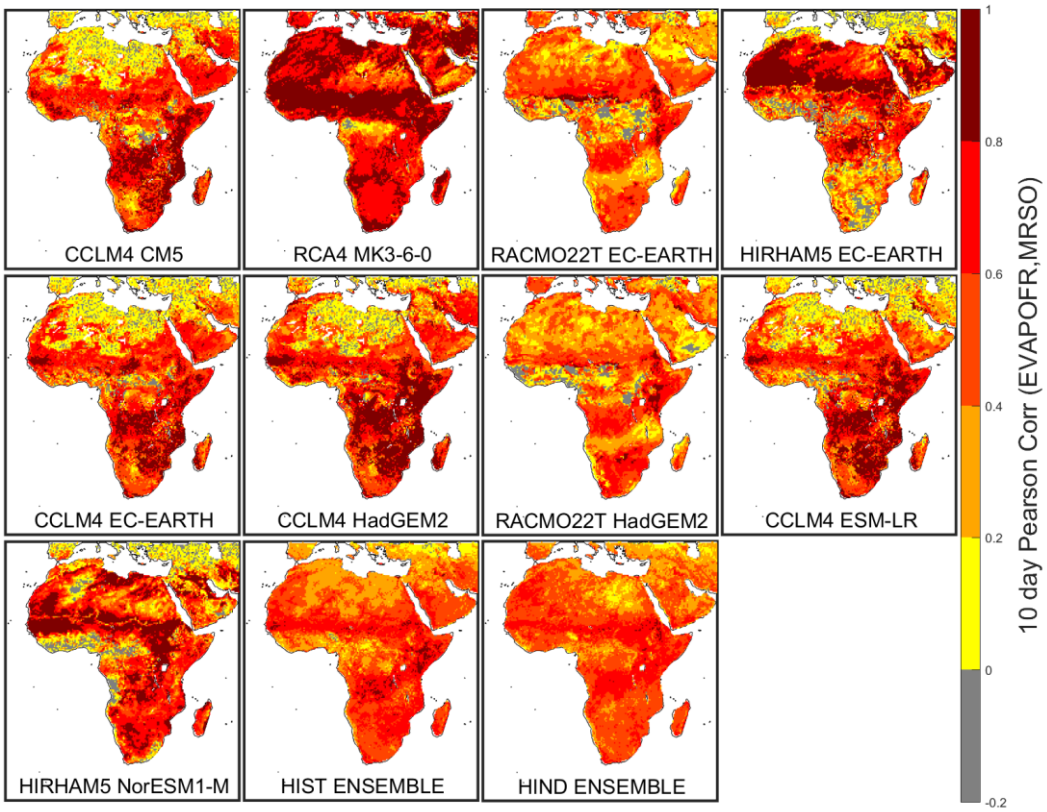


*Fig 4.7.* SON 10 days of nonoverlapping means correlation between MRSO and Evaporative Fraction (EVAPFR) for Historic (1971-2000). The Hindcast (1990-2008) ensemble is also shown. Values lower than 0 are depicted as gray.

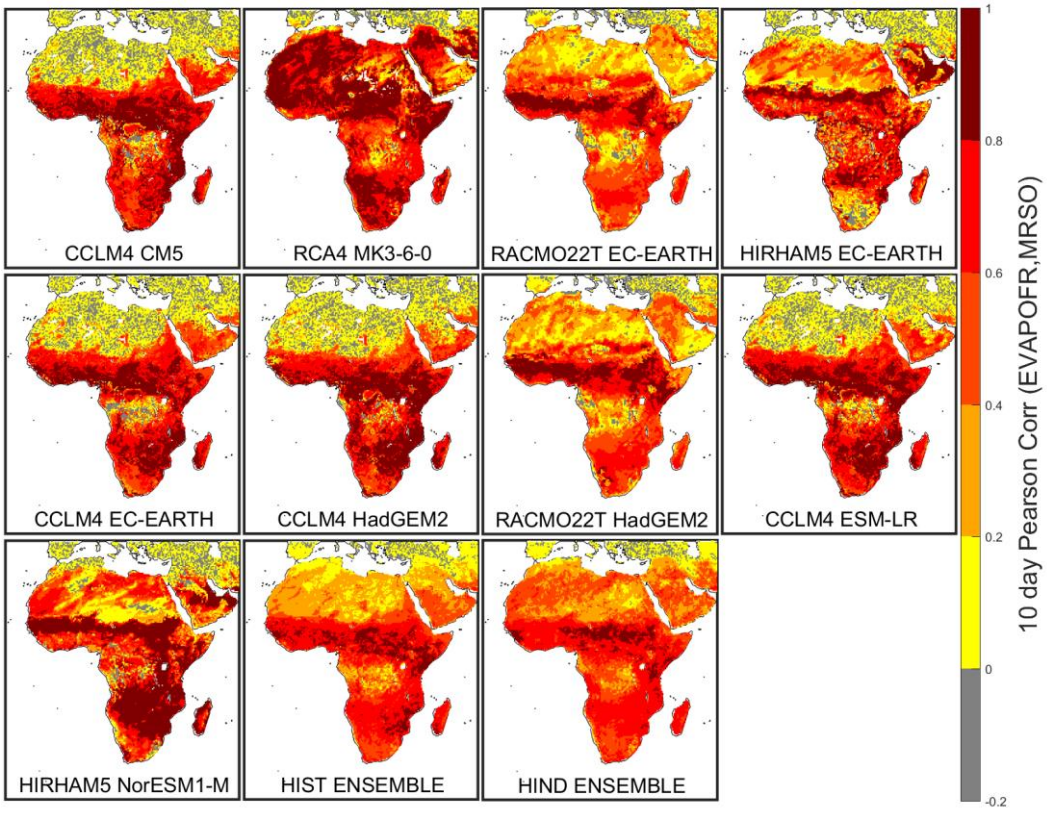


*Fig 4.8.* DJF 10 days of nonoverlapping means correlation between MRSO and Evaporative Fraction (EVAPFR) for Historic (1971-2000). The Hindcast (1990-2008) ensemble is also shown. Values lower than 0 are depicted as gray.

southern hemisphere shows lower correlations which could be due to the rainy season where more precipitation and lower Evaporative Fraction values prevail.

Overall, for all seasons and models there is a positive relationship between MRSO and Evaporative Fraction. The seasonal transition zones are identifiable as regions of very high correlations values. As expected, lower correlation values are found over deserts, where Evaporative Fraction is low and the connection with MRSO is weak. Lower correlations are sometimes found on humid regions, where there is always water available to evaporate and the Evaporative Fraction depends more on the surface radiative balance instead of the water availability.

### b. Latent and Sensible Heat Fluxes

The balance between Latent Heat (HFLS) and Sensible Heat (HFSS) fluxes is the most important, in the context of the soil moisture-temperature coupling in transition regions (Figures 4.9 to 4.12 for the 10 days of nonoverlapping means seasonal correlations for Historic and Figures A.15 to A.18 for the 10 days of nonoverlapping means seasonal correlation for the Hindcast (HFLS-HFSS correlation). This type of metric is only meaningful on regions with high evapotranspiration rates (Bowen ratio bellow 4 or Evaporative Fraction higher than 0.2), and therefore areas of low evapotranspiration must be excluded. Strong coupling is found in areas of negative correlations (depicted as red and yellow), weak coupling regions are found over areas of positive correlations (in blue and cyan) and regions of very limited coupling are found in areas of lower correlations and/or lower Evaporative Fraction values (represented in gray).

During MAM (Figure 4.9 for Historic and Figure A.15 for Hindcast), strong coupling regions are located south of Sahel, around the weak coupling region on the western side of central Africa. This weak coupling region overlaps well with the high rainfall rates observed during this season in this area (Figure 3.7 a). RCA4 MK3-6-0, CCLM4 HADGEM2 and RCA4 ERAINT are not able to represent this weak coupled region since all central and western Africa is depicted as a strong coupled region. Conversely, all models from the HIRHAM5 group and REMOO2009 ERAINT display a weaker than average strong coupling regions. Both ensembles show the same strong coupling regions, but differ for the weak coupling regions (e.g. southern Africa).

In JJA (Figure 4.10 for Historic and Figure A.16 for Hindcast), weak coupling regions are mainly located over western Africa, in areas of strong precipitation due to the western Africa Monsoon. Strong coupling regions, in this season, are located mainly in Sahel and central Africa. There are significant differences between models, with RACMO22T EC-EARTH and RACMO22T HADGEM2 displaying stronger than average coupling regions and strong negative correlations over the Sahara Desert, while, on the other hand, HIRHAM5 NORESM1-M shows a reduced strong coupling region and a better defined weak coupling region. The large areas of no coupling on HIRHAM5 NORESM1-M, mainly on southern Africa, are due to the very low Evaporative Fraction values. CLM RCM group alongside with RACMO22T group, present a weak coupling region from through western to eastern Africa. Overall, all models and ensembles are able to reproduce the two main strong coupling regions of this season: Sahel and central Africa. Both ensembles are similar, but Historic ensemble displays lower correlations over the weak coupling region in western Africa.

In the course of boreal autumn (SON) (Figure 4.11 for Historic and A.17 for Hindcast), the weak and strong coupling regions migrate south along with the southern ITCZ. The strong coupled regions are now mainly located in central and southern Africa. All models can reproduce these regions, with some exceptions. HIRHAM5 EC-EARTH model displays a very noisy correlation pattern, with positive correlation over South Africa while HIRHAM5 NORESM1-M has limited coupling, again due to low

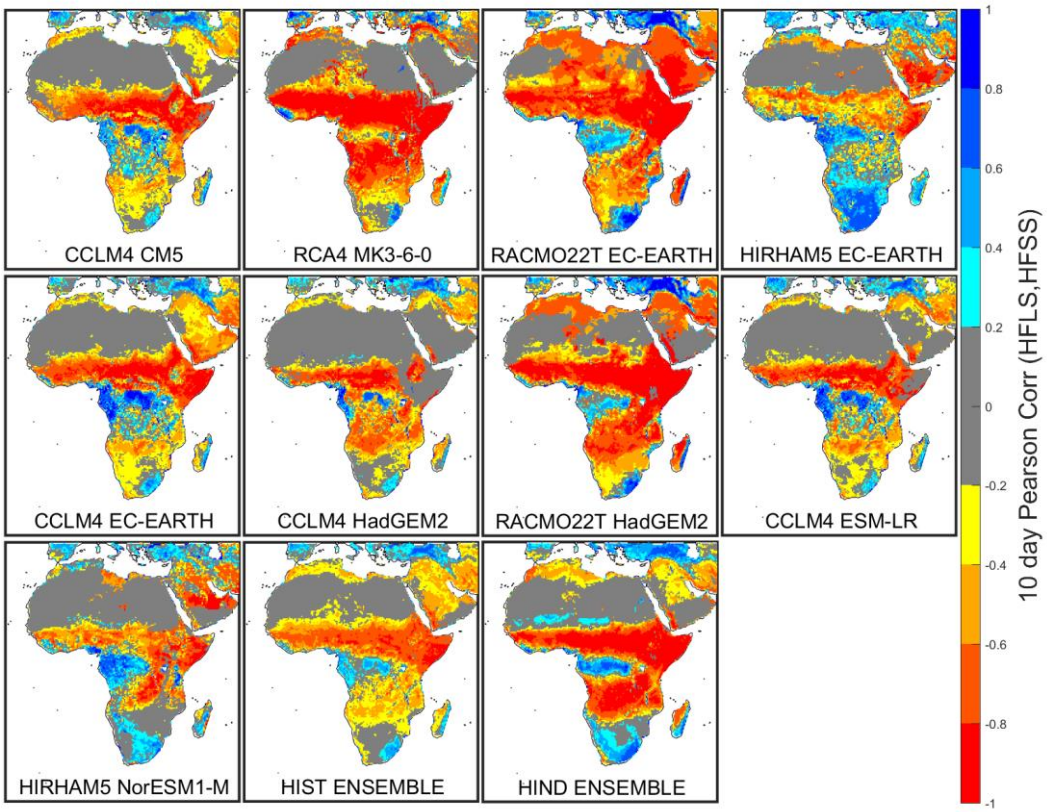


*Fig 4.9.* MAM 10 days of nonoverlapping means correlation between HFLS and HFSS for Historic (1971-2000). The Hindcast (1990-2008) ensemble is also shown. Correlations below the 20% significance level and areas of low Evaporative Fraction (less than 0.1) are depicted as gray.

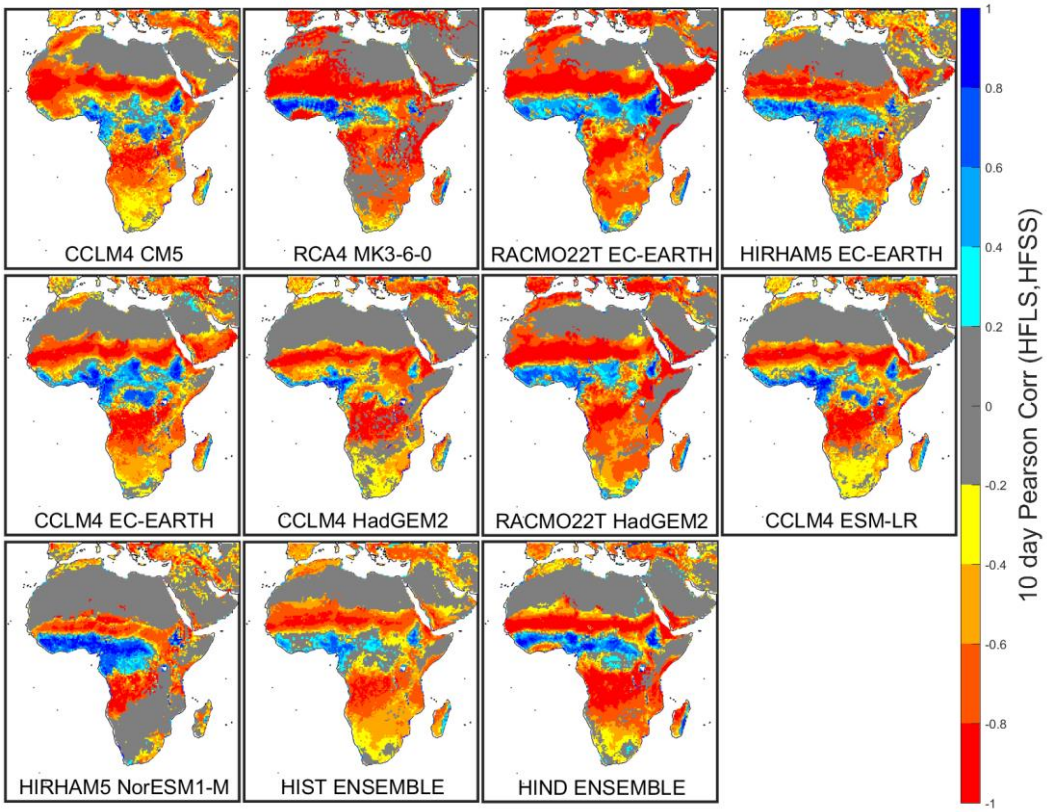


*Fig 4.10.* JJA 10 days of nonoverlapping means correlation between HFLS and HFSS for Historic (1971-2000). The Hindcast (1990-2008) ensemble is also shown. Correlations below the 20% significance level and areas of low Evaporative Fraction (less than 0.1) are depicted as gray.

Evaporative Fractions values and also to low correlation values. RCA4 has however very strong negative correlations over almost all Africa. In the Hindcast, a noisy correlation pattern is visible in HIRHAM5 ERAINT and HADRM3P ERAINT, nevertheless all models and ensemble can reproduce the strong coupling areas, except HIRHAM5 ERAINT and REMOO2009 ERAINT. There are some differences between Historic and Hindcast ensembles, with the latter displaying stronger correlations over western and central Africa and a weak positive correlation in the southwestern side of Africa.

In DJF (Figure 4.12 for Historic and A.18 for Hindcast), strong coupling regions envelop a weak coupling region located on the western side of central Africa. In this season, precipitation is mainly concentrated over the eastern side of central Africa in the southern hemisphere, but nevertheless, RCMs consider this area as a strong coupling region. All models can reproduce these results, with some differences, mainly HIRHAM5 NORESM1-M with a restricted coupling region and RCA4 MK3-6-0 with a smaller weak coupling region over central Africa. Similar to SON, a noisy pattern is visible in HIRHAM5 EC-EARTH, HIRHAM5 ERAINT and HADRM3P ERAINT models. Also, the ensembles display a very similar pattern, but the Historic ensemble displays weaker positive correlation over central Africa than the Hindcast ensemble.

These differences between each individual RCM are due to different Planetary Boundary Layer (PBL) schemes and different forcing climate models; namely precipitation and net radiation. Also, Land Surface Models (LSM) characteristics and land surface parametrizations (e.g. soil type, vegetation type, etc.) affect the coupling strength of different RCMs (Knist et al., 2017). Whenever a certain RCM fails to represent coupling strength, then it is quite probable that same model will underestimate (overestimate) heat waves (Vautard et al., 2013) contingent on the stronger (weaker) than average coupling strengths.

The 10 days of nonoverlapping means correlation (HFLS-TASMAX correlation) between Latent Heat Flux (HFLS) and Maximum Near Surface Air Temperature (TASMAX) represents, relatively to the correlation between latent and sensible heat fluxes, one step further in the relationship between soil moisture and surface air temperature (Figures A.19 to A.22 for Hindcast and Figures A.23 to A.26 for Historic), as anomalies in soil moisture lead to changes in the balance between latent and sensible heat fluxes, which in turn, lead to changes in near surface air temperature. However, temperature is also largely affected by advection and therefore, the HFLS-TASMAX correlation is slightly weaker, but displays nearly the same correlations patterns observed in the HFLS-HFSS correlation. The correlation between soil moisture and temperature is another viable way to assess the soil moisture-temperature coupling, which would result in lower correlation values, since the connection between soil moisture and latent heat flux isn't perfect (see Figures 4.9 to 412 for the 10 days of nonoverlapping means correlation between latent and sensible heat fluxes).

The variability of coupling strength, on a regional scale and throughout the seasons, is related with orography and, in this case, with the African Monsoon, which has impact on precipitation, temperatures and cloud cover. Overall, for both coupling metrics, weak coupled regions (denoted as positive correlations) follow the precipitation patterns (see Figure 3.7) of the African Monsoon, while very dry areas, such as Sahara or Kalahari deserts, which are considered regions of no soil moisture-temperature interaction throughout the year, have little to no seasonal variability, appearing to be static throughout the year. However, there are robust seasonal variations of strong coupled regions with relatively high soil moisture linked to the surface radiative balance (associated also to the Sun's zenith angle throughout the year), which connect well with the transition zones observed in the Bowen ratio and Evaporative Fraction. An exception is the austral summer (DFJ), on the eastern side of central Africa in the southern hemisphere (e.g. Mozambique, Zambia, Zimbabwe) which is portrayed as a region of strong soil moisture-temperature coupling (visible in both metrics), despite the high precipitation rates, characteristic of this season. This may be due to lower rainfall rates in other seasons, unlike other regions, such as western Africa, where it rains in three of the four seasons. Negative correlations of both

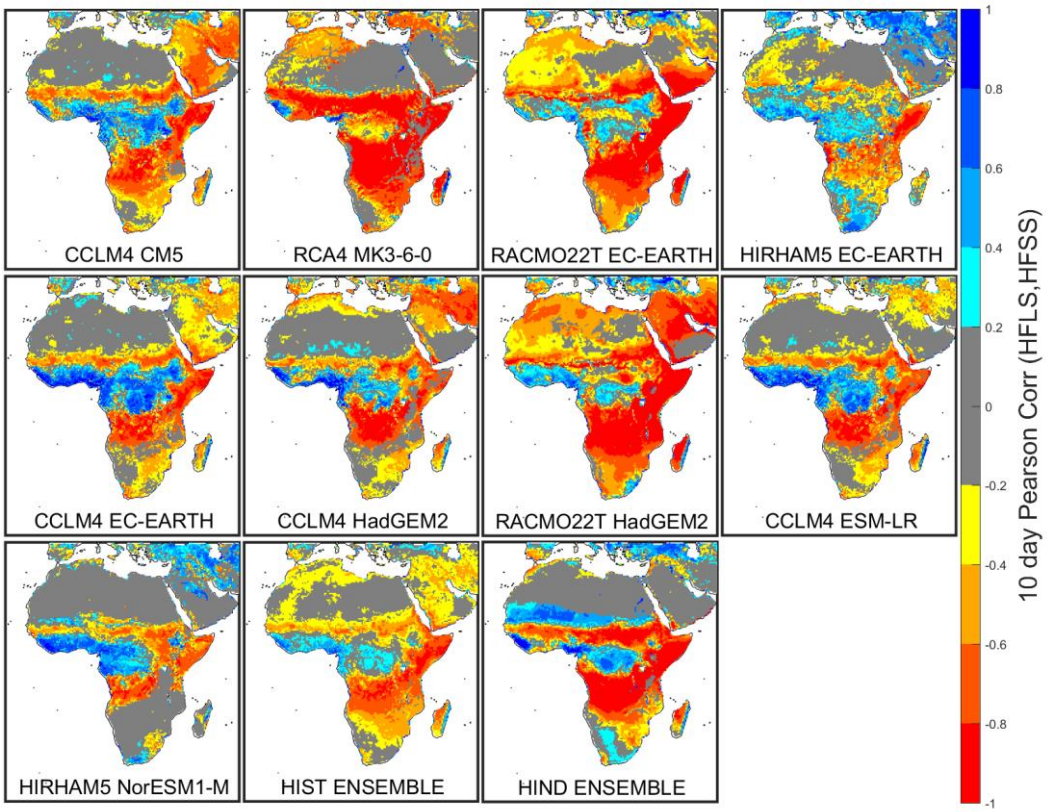


*Fig 4.11.* SON 10 days of nonoverlapping means correlation between HFLS and HFSS for Historic (1971-2000). The Hindcast (1990-2008) ensemble is also shown. Correlations below the 20% significance level and areas of low Evaporative Fraction (less than 0.1) are depicted as gray.

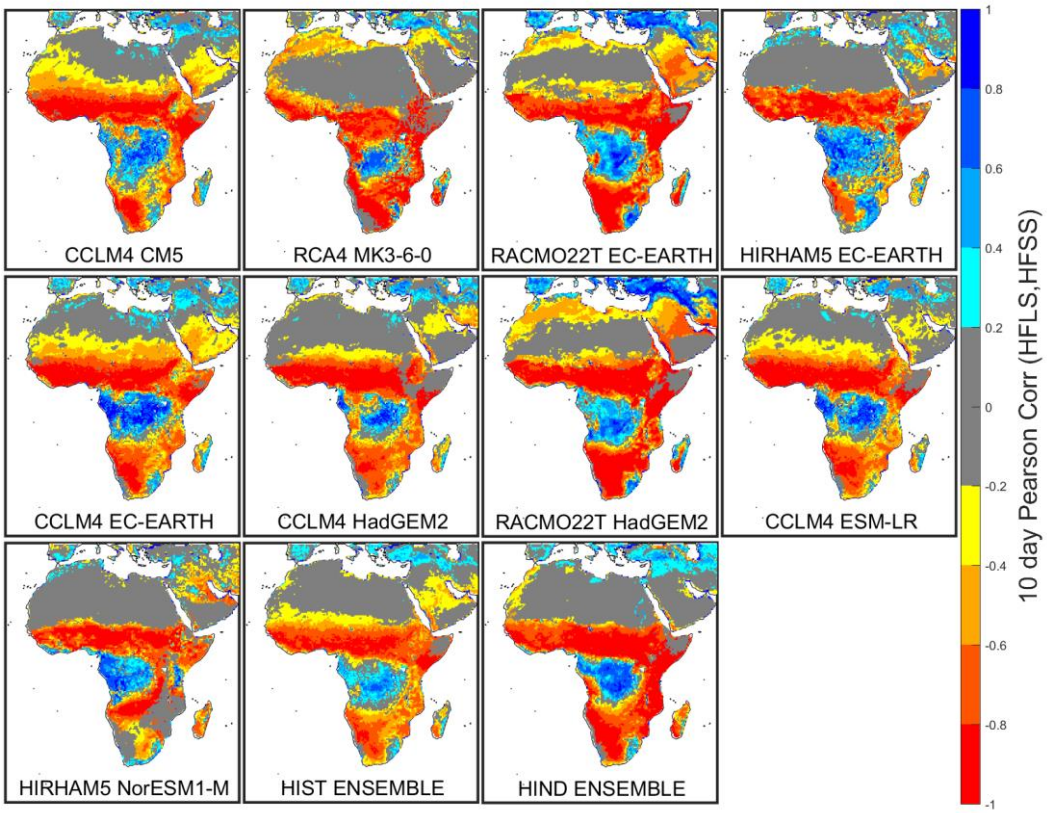


*Fig 4.12.* DJF 10 days of nonoverlapping means correlation between HFLS and HFSS for Historic (1971-2000). The Hindcast (1990-2008) ensemble is also shown. Correlations below the 20% significance level and areas of low Evaporative Fraction (less than 0.1) are depicted as gray

coupling metrics agree well with results from previous works that display or assess the coupling strength over the African continent (e.g. Koster et al., 2006; Seneviratne et al., 2006; 2010; Miralles et al., 2012; Lorenz et al., 2015).

The relationship between the three different types of coupling regions can further be assessed by comparing the mean values for the regions chosen on Table 3.1, against Africa-CORDEX focus domain (Table 4.1). Overall, the mean values for the HFLS-HFSS correlation, in JJA for NA-SA, and in DJF for NA-SW, EA and CSA are negative, indicating that these are strong coupling regions. The exception is CSA with a very low correlation mean due to the presence of positive correlations (weak coupling regions) over the northern border of this region. It is on these regions where the correlation between Evaporative Fraction and MRSO should be stronger. However, this is not the case, but the region sizes must be considered and contamination from other coupling types is likely. The negative correlation values over strong coupling regions correspond well with transition values on Bowen ratio (between 0.5 and 5) and with Evaporative Fraction (between 0.2 and 0.7).

*Table 4.1.* Seasonal Historic ensemble (1971-2000) Bowen ratio, Evaporative Fraction, 10 days of nonoverlapping means correlations between MRSO and HFLS, between HFLS and HFSS and between HFLS and TASMAX for all regions and Africa-CORDEX domain. Red values denote the JJA and DJF main strong coupling regions. Also, values for the domain mean for the same seasons are highlighted.

| Metric | Seasons | NA-SA | NA-SW | EA | CNA | CSA | SA-W | Africa |
|---|---|---|---|---|---|---|---|---|
| Bowen ratio | MAM | 5.08 | 1.03 | 1.26 | 0.29 | 0.64 | 1.44 | 2.47 |
| | JJA | 1.72 | 0.34 | 3.36 | 0.74 | 2.84 | 1.70 | 3.24 |
| | SON | 1.39 | 0.31 | 3.14 | 0.47 | 2.73 | 5.32 | 1.91 |
| | DJF | 4.84 | 1.14 | 1.18 | 0.33 | 0.53 | 3.36 | 2.11 |
| Evaporative Fraction | MAM | 0.29 | 0.54 | 0.53 | 0.79 | 0.65 | 0.60 | 0.67 |
| | JJA | 0.51 | 0.79 | 0.36 | 0.66 | 0.36 | 0.58 | 0.66 |
| | SON | 0.55 | 0.79 | 0.36 | 0.72 | 0.37 | 0.50 | 0.66 |
| | DJF | 0.30 | 0.52 | 0.56 | 0.77 | 0.69 | 0.56 | 0.27 |
| Correlation (MRSO, HFLS) | MAM | 0.50 | 0.61 | 0.73 | 0.52 | 0.73 | 0.54 | 0.57 |
| | JJA | 0.64 | 0.52 | 0.72 | 0.64 | 0.77 | 0.33 | 0.58 |
| | SON | 0.59 | 0.43 | 0.61 | 0.53 | 0.60 | 0.53 | 0.52 |
| | DJF | 0.58 | 0.77 | 0.70 | 0.48 | 0.65 | 0.53 | 0.50 |
| Correlation (HFLS, HFSS) | MAM | -0.37 | -0.55 | -0.33 | -0.01 | -0.21 | 0.29 | 0.26 |
| | JJA | -0.46 | 0.17 | -0.41 | -0.31 | -0.47 | 0.25 | 0.19 |
| | SON | -0.22 | 0.10 | -0.49 | -0.12 | -0.43 | 0.24 | 0.27 |
| | DJF | -0.40 | -0.72 | -0.35 | 0.11 | -0.06 | 0.04 | 0.26 |
| Correlation (HFLS, TASMAX) | MAM | -0.30 | -0.46 | -0.05 | 0.14 | 0.00 | -0.03 | -0.16 |
| | JJA | -0.37 | 0.30 | -0.22 | -0.09 | -0.21 | -0.19 | -0.11 |
| | SON | 0.01 | 0.33 | -0.23 | 0.01 | -0.43 | -0.09 | -0.20 |
| | DJF | -0.11 | -0.47 | -0.18 | 0.24 | 0.01 | -0.26 | -0.06 |

## 4.3 Heat Waves

In this section, the spatial distribution of the climatological number of heat waves (Figure 4.13 for Historic and A.27 for Hindcast) and the spatial distribution of mean heat wave duration (Figure 4.14 for Historic and A.28 for Hindcast) is evaluated and compared against the coupling results from the previous section. Since a direct comparison between the annual mean number of heat waves plus the mean heat wave duration, with the seasonal coupling is difficult, the results are compared mainly with the austral and boreal summers (DJF and JJA season respectively) coupling results (Table 4.2). Nevertheless, transition climates are considered strong coupling regions, where soil moisture anomalies could affect surface air temperature and therefore more heat waves are expected.

The pattern between different RCMs differs, but overall there are less heat waves over the western side of central Africa and over eastern Africa, indicating, more heat waves in transition and dry climates (Figure 4.13 for Historic and Figure A.27 for Hindcast). HIRHAM5 NORESM1-M and RCA4 ERAINT display more heat waves over eastern Sahara, while others over southern Africa (e.g. RACMO22T group). Comparing the ensemble with the Köppen-Geiger climate classification, it is over the transition climates where more heat wave events occur. This reinforces the importance of soil moisture-temperature feedback in areas where soil moisture limits evapotranspiration. Also, the annual mean number of heat waves for the Historic ensemble is higher, relative to Hindcast ensemble, which could be attributed to the different periods.

The duration of heat waves is essentially determined by the synoptic conditions, but in situations of strong soil moisture-temperature coupling, heat waves could last longer due to the balance between fluxes. Figure 4.14 for Historic and Figure A.28 for Hindcast display the mean heat wave duration and no clear connection is found with strong coupling areas or transition climates (Figure A.6). Overall, the Historic ensemble shows a higher heat wave duration relative to Hindcast ensemble. HIRHAM5 EC-EARTH and all models from Hindcast display a lower duration over South Africa, while the opposite is observable over northern Africa. Analogous to the annual mean number of heat waves, HIRHAM5 NORESM1-M RCM displays higher mean heat wave duration, over large areas of Sahara Desert and part of DJF strong coupling region, but no conclusions can be retrieved. In general, except for RCA4 MK3-6-0, RACMO22T EC-EARTH and RACMO22T HADGEM2, lower heat wave duration is observable on the western side of central Africa over the boreal summer (JJA) weak coupling region.

Table 4.2 displays the mean results for the annual mean number of heat waves, mean heat wave duration and the seasonal HFLS-HFSS correlation for all regions and Africa-CORDEX domain for Historic ensemble. The annual mean number of heat waves, for NA-SA, NA-SW, EA and CSA displays a much higher than mean values, meaning a higher number of heat waves on these regions. These are the same areas identified by the coupling metrics as strong coupling regions for boreal and austral summer (red values on Table 4.2). CNA also shows a higher than mean number of heat waves, inferior to the previous regions, but on this case, contamination on the borders is likely due to the region area.

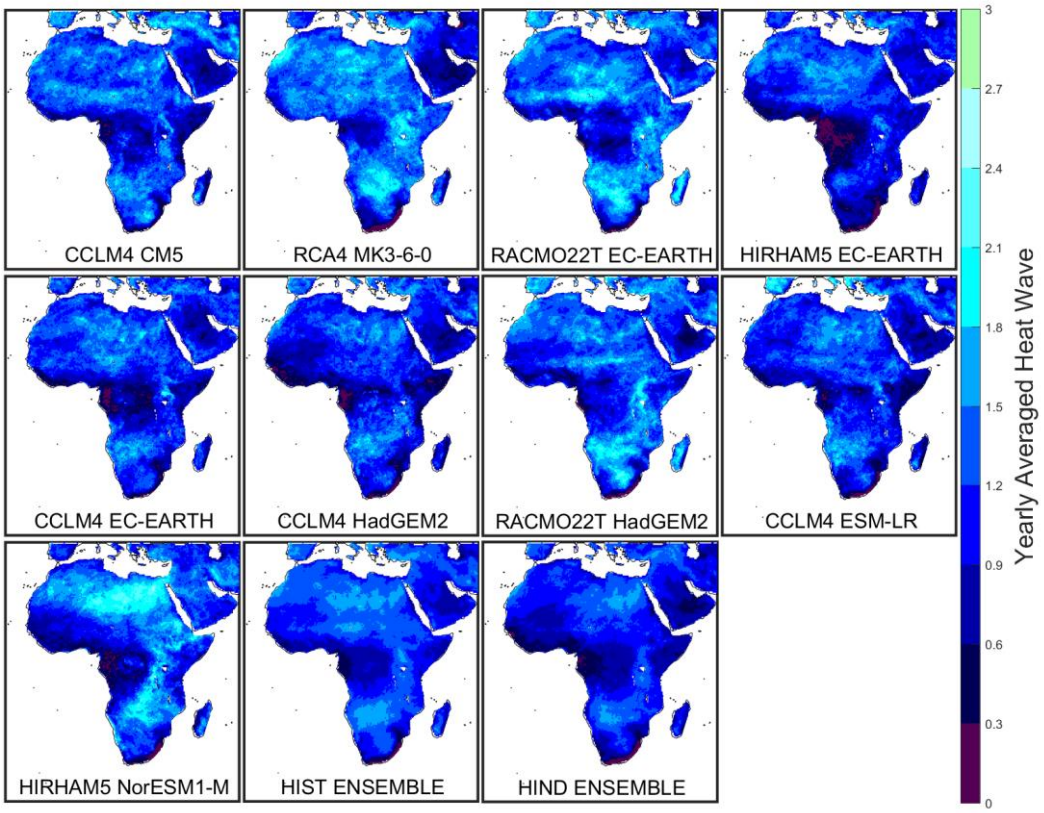


*Fig 4.13.* Yearly average number of heat waves for the Historic (1971-2000). Hindcast (1990-2008) ensemble is also shown.

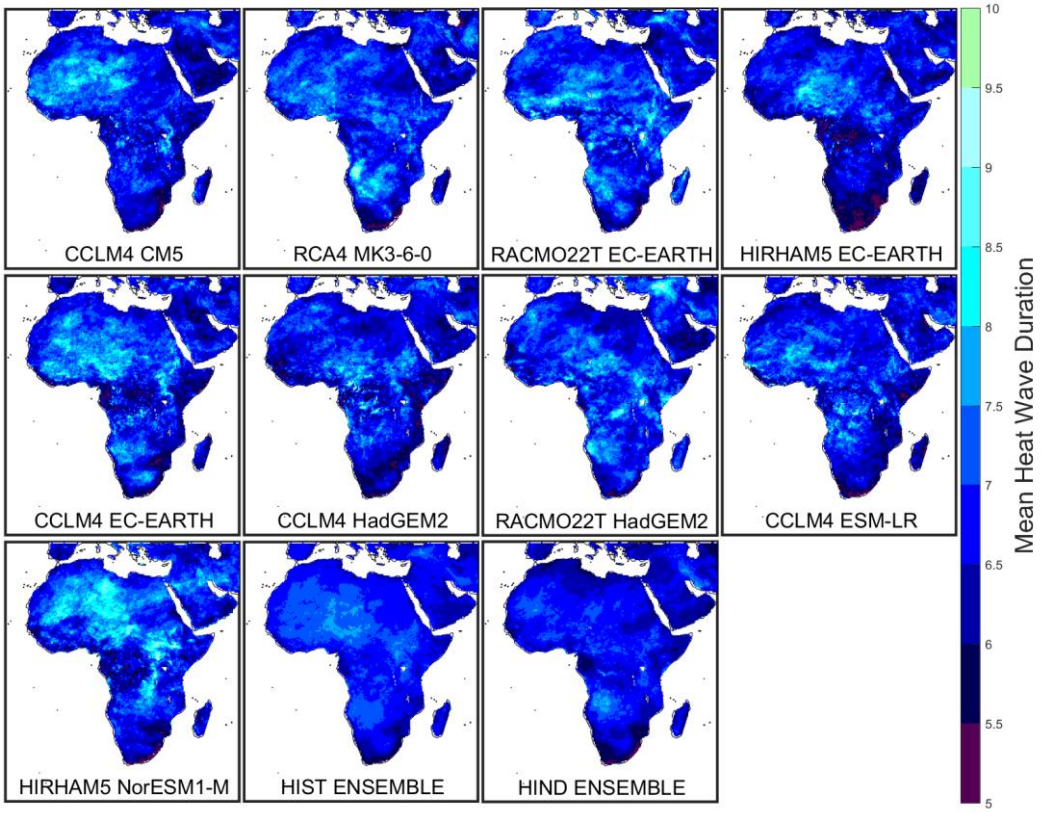


*Fig 4.14.* Mean heat wave duration for Historic (1971-2000). Hindcast (1990-2008) ensemble is also shown.

*Table 4.2.* Annual mean number of heat waves, mean heat wave duration and 10 days of nonoverlapping means correlation between HFLS and HFSS for the Historic ensemble (1971-2000). Values depicted as red represents the mean over the main strong coupling regions and Africa-CORDEX domain for JJA and DJF.

| Metric | Season | NA-SA | NA-SW | EA | CNA | CSA | SA-W | Africa |
|---|---|---|---|---|---|---|---|---|
| Heat Waves Number | - | 1.15 | 0.95 | 1.13 | 0.80 | 1.23 | 0.53 | 0.50 |
| Heat Waves Duration | - | 7.13 | 7.01 | 6.71 | 6.79 | 7.02 | 6.24 | 6.73 |
| Correlation (HFLS, HFSS) | MAM | -0.37 | -0.55 | -0.33 | -0.01 | -0.21 | 0.29 | -0.37 |
| | JJA | -0.46 | 0.17 | -0.41 | -0.31 | -0.47 | 0.25 | -0.46 |
| | SON | -0.22 | 0.10 | -0.49 | -0.12 | -0.43 | 0.24 | -0.22 |
| | DJF | -0.40 | -0.72 | -0.35 | 0.11 | -0.06 | 0.04 | -0.40 |

## 4.4 Drought, SPEI 12-months timescale

Droughts are assessed here as the percentage of the number of months in drought (Figure 4.15 for Historic and Figure A.34 for Hindcast), fraction area in drought (Figure 4.16 for Historic and figure A.36 for Hindcast) and mean drought duration (Figure 4.17 for Historic and Figure A.37 for Hindcast) computed based on the SPEI index. To assess these results, box and whiskers plot are used. The vertical lines represent the first, second and third quartiles (or the $25^{th}$ $50^{th}$ and $75^{th}$ percentiles, respectively). The whiskers, or lines that extend horizontally from the boxes (W1 and W2) are computed as:

$$W1 = Q1 - w(Q3 - Q1) \quad 2.14$$

$$W2 = Q3 + w(Q3 - Q1 \quad 2.15$$

where Q1 and Q3 are the first and third quartiles, $w = 1.5$. $Q3 - Q1$ represents the inter-quartile range (IQR) and can be seen as a measure of the spatial variability. Here, the ensemble is built by considering all data from models.

To assess and validate SPEI values across the Africa-CORDEX domain, the ensemble of Historic and Hindcast are compared against a SPEI computed with the CRU database for the period of each simulation respectively (Figures A.29 to A.33). A direct comparison is hampered because the modelled SPEI is computed by using the models solar radiation, while CRU database lacks this variable and therefore must be computed by using an empirical solar radiation and also uses the climatological monthly mean wind from 1961-1990. Nevertheless, the results are similar. Figure A.29 displays the modelled (blue boxplots) and CRU database (red boxplots) number of months in drought for Hindcast and Historic ensembles. In both cases, the median and IQR are similar. Figure A.30 shows the plotted fraction area in drought (moderate, severe and extreme) for all land points of the domain, only for the Hindcast ensemble, against the fraction area computed from CRU database (black lines). In this case, there are some differences, with the modelled data overestimating the fraction area in all types of drought defined. Figures A.31 and A.32 display, respectively, the Hindcast and Historic ensembles boxplots (blue) of the fraction area in different drought severities against the CRU database (red). The higher the drought magnitude, the greater the similarity with observations. The higher difference on moderate drought for the ensembles relative to CRU could be attributed to the way SPEI index was computed. Finally, Figure A.33 displays the annual drought duration for Historic and Hindcast ensembles against CRU database and results are close on both cases.

SPEI is a standardized index with zero mean and a standard deviation of one, which means the number of months with SPEI values bellow -1, or number of months in drought (Figure 4.15 for Historic and Figure A.34 for Hindcast) will, in theory, be equivalent to 15,87% of all simulation months. The Hindcast ensemble median (15.8590%, Table 4.3) falls approximately over this value. Historic ensemble exhibits a slightly higher median value (16.3889%, Table 5.2), which implies that more land points displays more months in drought. Historic ensemble also displays a lower IQR, which implies a slightly lower inter-model variability. But nevertheless, in both cases, the median and IQR range between models is very similar.

With this metric, the severity of drought events cannot be assessed. Figure A.35 displays the fraction area in drought (orange for moderate with SPEI between -1 and -1.5, red for severe with SPEI between -1.5 and -2, dark red for extreme drought with SPEI under -2), over time for Hindcast models and ensemble. Overall, there is a strong relationship between the different intensities in which, when more land points are classified as moderate drought, more points are also classified as severe or extreme drought, especially visible on the ensemble mean. Since the Historic models are not synchronized, the time factor must be eliminated in order to compare different RCMs. Figure 4.16 shows the boxplots of

the fraction area in drought, for all land points of Historic models and ensemble, plus Hindcast ensemble and Figure A.36 displays the results for Hindcast (same results of Figure A.35, but on boxplot form and with the same colour code). Again, the median and IQR is equivalent across different RCMs on both simulations. The Historic ensemble median (0.1049 for Moderate, 0.0438 for Severe and 0.0065 for Extreme drought, Table 4.3) and IQR for Moderate and Severe drought is close relatively to Hindcast ensemble, being overestimated for Extreme drought.

Figure 4.17 for Historic and Figure A.37 for Hindcast displays the drought duration (ratio between total number of months in drought by the total number of events). All models agree with similar median and IQR, with Historic ensemble overestimating the mean drought duration relative to Hindcast ensemble.

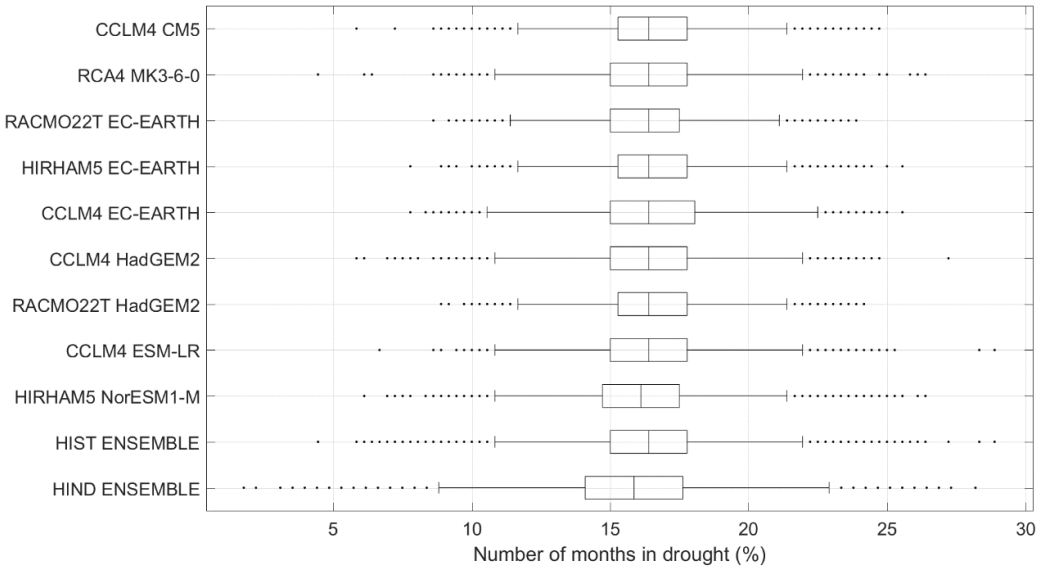


*Fig 4.15.* Boxplot of number of months in drought (percentage of months with SPEI below -1), for all land points of the Historic (1971-2000). The ensemble is the data of all models. Hindcast (1990-2008) ensemble is also shown.

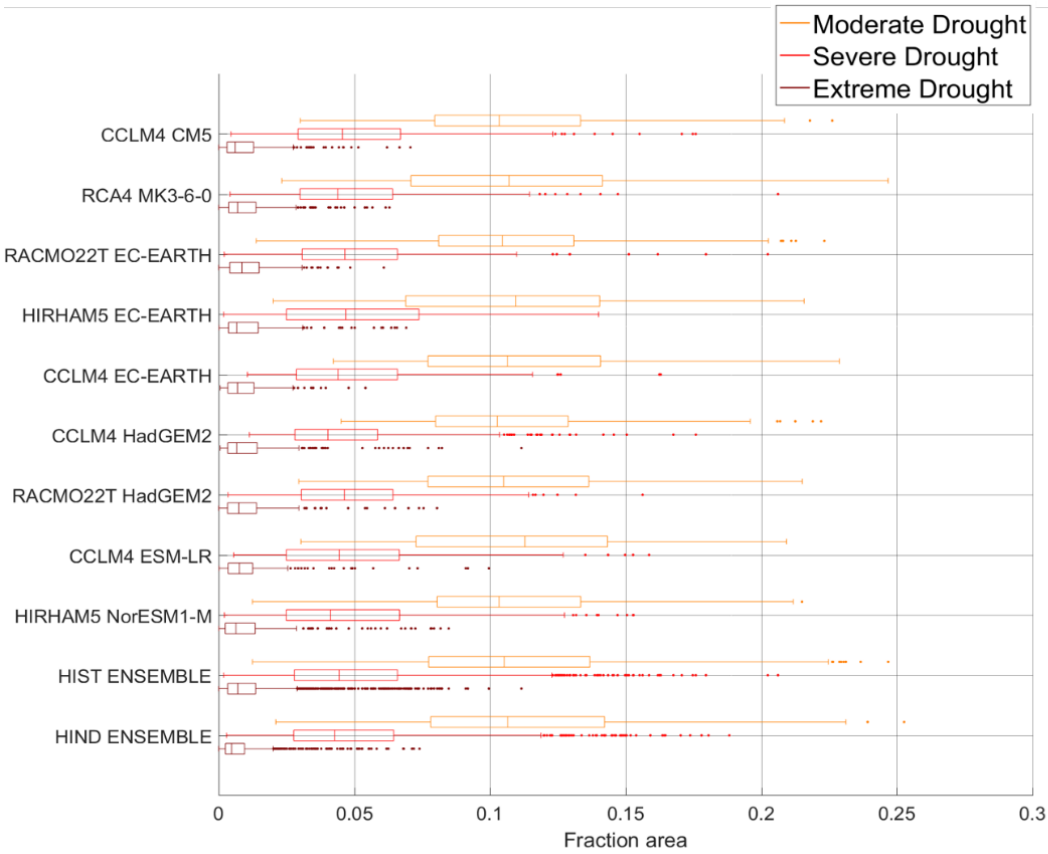


*Fig 4.16.* Boxplots of the fraction area in drought with different drought intensities (orange: fraction area in moderate drought; red: fraction area in severe drought; dark red: fraction area in extreme drought), over time for all land points for the Historic (1971-2000). The ensemble is the data of all models. Hindcast (1990-2008) ensemble is also shown.

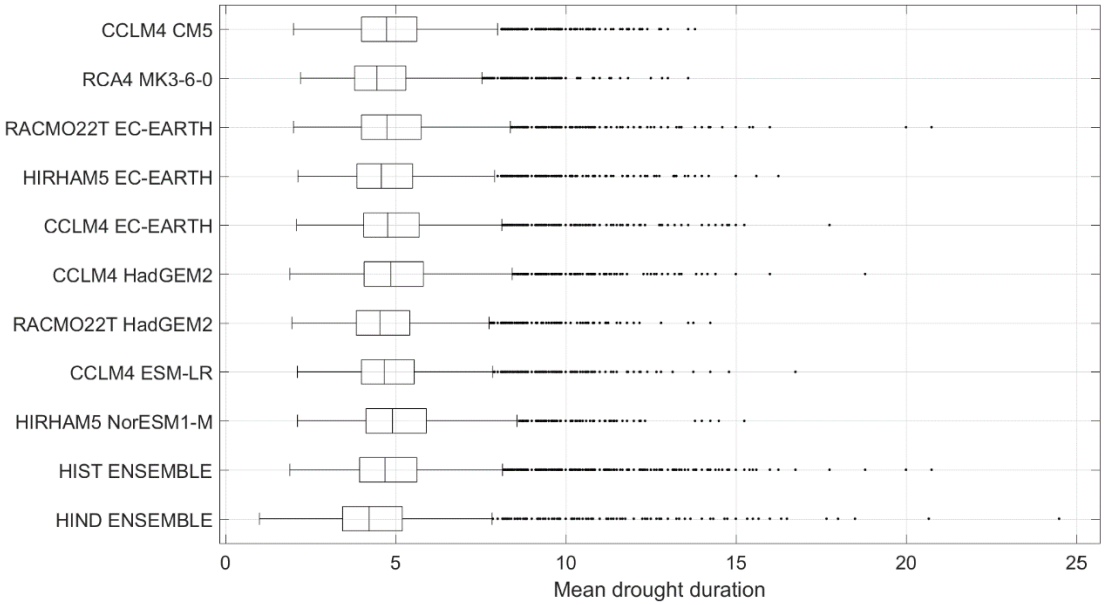


*Fig 4.17.* Boxplot of mean drought duration for all land points of Historic (1971-2000) normalized by the number of years of each model. The ensemble is the data of all models. Hindcast (1990-2008) ensemble is also shown.

Table 4.3. Median of the number of months in drought, fraction area in drought (moderate, severe and extreme) and number of droughts for the ensemble of Hindcast and Historic. Between parenthesis is the difference between Historic and Hindcast.

| | Number of months in drought (%) | Fraction area in: | | | Mean drought duration (months) |
|---|---|---|---|---|---|
| | | Moderate drought | Severe drought | Extreme drought | |
| Hindcast | 15.86 | 0.1065 | 0.0428 | 0.0047 | 4.22 |
| Historic | 16.39 (x1.033) | 0.1049 (x0.9849) | 0.0438 (x1.2336) | 0.0065 (x1.3630) | 4.69 (x1.111) |

## 4.5 Latent Heat Flux-Temperature Coupling Magnitude

Not all heat wave events on transition climates are affected by the soil moisture-temperature feedback. Sometimes, during a drought event, soil moisture is available in sufficient amounts and doesn't influence near surface air temperatures. For this feedback to act, evapotranspiration must be constrained by the available water and not by the available energy, or in other words by a strong enough drought event. Nevertheless, a drought event, which holds information of the water balance from the recent past, is not a necessary requirement. During a sufficiently longer and/or intense heat wave event, even if initially evapotranspiration rates were constrained by radiation and not by soil moisture amounts, anomalously high land-atmosphere coupling is possible due to the progressive soil dissection and increased water demand by the atmosphere. Figure 4.18 displays the Temperature Magnitude (MT), Latent Heat Flux Magnitude (MH), Latent Heat Flux-Temperature Coupling Magnitude (LETCM) and mean SPEI values for known heat wave periods (DJF 1997-1998; MAM 1998; DJF 2004-2005; SON 2008). These magnitudes and SPEI are computed only for the ensemble of the Hindcast, since it is the only simulation that is synchronized between the different RCMs and with observations.

Temperature Magnitude metric (MT, first row from top on Figure 4.18) doesn't distinguish a heat wave intensity, or temperature anomaly from an event duration. Nonetheless, MT is a good measure of strength and spatial extent of heat waves for a determined period. Russo et al. (2016) analysed ERA-Interim for the aforementioned periods and defined MT as the maximum magnitude, for each grid point, of a running three-month block. Russo et al. (2016) also interpolated the ERA-Interim grid to the Africa-CORDEX Domain. Here MT is defined as the sum of the daily magnitude over a three-month period and, therefore, differences are expected. For 1997-1998 (DJF) similar patterns are distinguishable with however higher magnitudes values are more to the south. In MAM 1998, high magnitude values go from west to east Africa through the Sahel and with a maximum just above it whilst in Russo et al. (2016) a single event with lower magnitude, overlapping the former area, is visible just above the Sahel. For DJF in 2004-2005 the spatial extent is slightly reduced but overlaps Russo's. Finally, for SON 2008 high magnitude values are only found over southern Africa in a slightly larger area.

Latent Heat Flux Magnitude (MH, second row from top on Figure 4.18) is computed for the negative extreme anomalies. This metric alone doesn't explain coupling, since in weak coupling situations, when temperature decreases (increases), latent heat flux also subsides (rises), while in strong coupling regions when temperature declines (intensifies), latent heat flux amplifies (wanes) as it is constrained by available water to evaporate. Nevertheless, and since MH considers extreme values, this metric can distinguish dry from transition and humid climates. The sum for a determined period of the product of daily MT by MH (LETCM, third row from top on Figure 4.18) returns the regions where temperatures were influenced by the flux partitioning. Black boxes denote regions where, approximately, temperatures were higher due to soil moisture deficits for MAM 1998 and DJF 2004-2005. In the other two events, temperatures weren't affected by soil moisture-temperature coupling. The last row (from top) of Figure 4.18 displays the mean SPEI index for the periods considered. Regions of strong coupling correspond to areas in drought, which means that a drought event is a period of soil moisture anomaly and, consequently as a period of reduced latent heat flux. For DJF 1997-1998, despite the lower SPEI values over Liberia and République de Côte d'Ivoire, and since this is a weak coupling region on almost all seasons, this drought event wasn't strong enough for the latent heat flux being constrained by the available water. In the other hand, on SON 2008, high MH values are found over the eastern side of central Africa, corresponding to a drought event identified in the area. However, in this case, high MT values are located on the western side, where temperatures are nor influenced by the flux partitioning.

Wang et al. (2015) found a relationship between soil moisture and numerous drought indexes, including SPEI, but some care must be taken when relating both variables as weak correlations were found.

Figure 4.19 displays the probability of exceedance of a certain LETCM value for all land points of each simulation. In this case, LETCM is computed from March to February for all years, to avoid cutting austral summer in half. For the future scenarios, Historic percentiles sets were considered as exceedance thresholds. Hindcast and Historic ensembles (bold lines) display very close results. Two very different realities between Future and Historic are observed. For example, the magnitude corresponding to a probability of 0.1 for Hindcast is 8.6487and 8.9609 for Historic, however for RCP4.5 this increases to 188.4486, and in RCP8.5 is 447.0603. These differences highlight how extreme future climate conditions could be relative to the recent past. These results also emphasise how extreme and drier the future climate will be over large areas, with permanent temperature and latent heat flux anomalies in some regions.

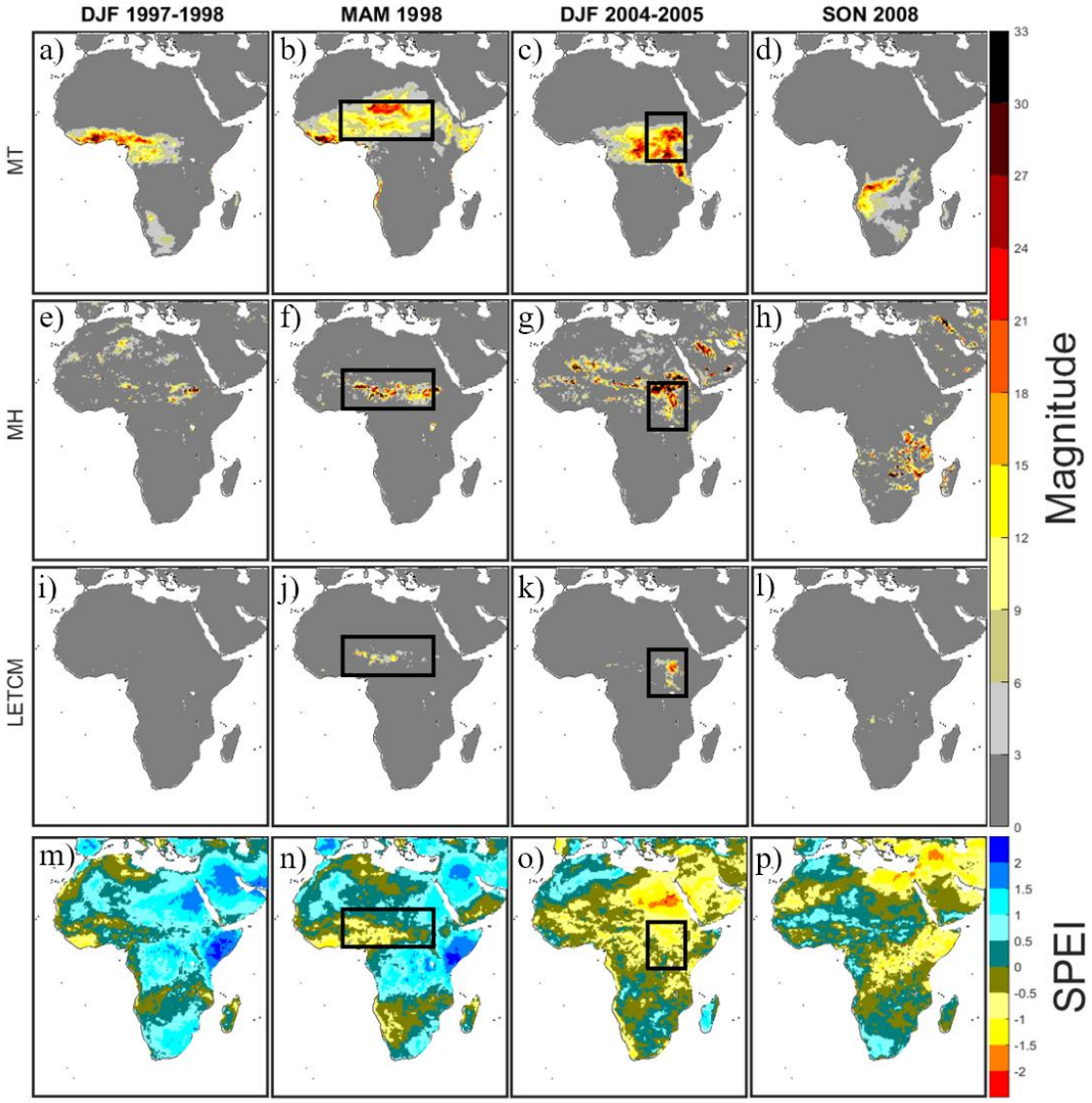


Fig 4.18. Magnitudes and SPEI index for known heat waves periods, based on Russo et al. (2016). Temperature Magnitude (MT) for (a) DJF of 1997-1998, (b) MAM of 1998, (c) DJF of 2004-2005 and (d) SON of 2008. Latent Heat Flux Magnitude (MH) (e) DJF of 1997-1998, (f) MAM of 1998, (g) DJF of 2004-2005 and (h) SON of 2008. Latent Heat Flux-Temperature Coupling Magnitude (LETCM) (i) DJF of 1997-1998, (j) MAM of 1998, (k) DJF of 2004-2005 and (l) SON of 2008. Mean values of SPEI index (m) DJF of 1997-1998, (n) MAM of 1998, (o) DJF of 2004-2005 and (p) SON of 2008. Black boxes denote areas of strong soil moisture-temperature coupling.

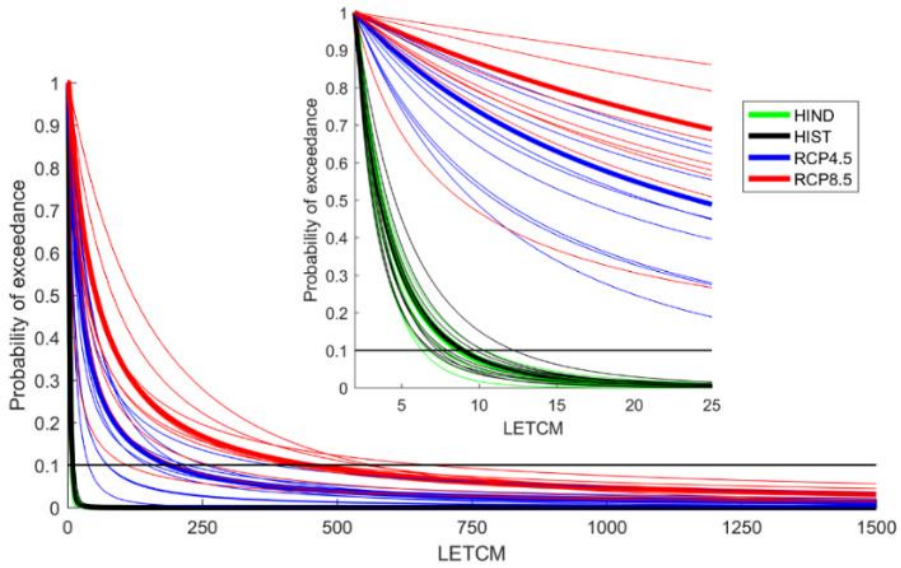


*Fig 4.19.* Probability of exceeding a certain Latent Heat Flux-Temperature Coupling Magnitude (LETCM) for Hindcast (green), Historic (black), RCP4.5 (blue) and RCP8.5 (red) for all land points of the Africa-CORDEX domain. These magnitudes are computed as the sum of a daily magnitude that results from the multiplication between the Temperature Magnitude (MT) and Latent Heat Flux Magnitude (MH) from March to February for all years of each. Bolt lines denotes the multi-model ensemble.

# 5. Land Atmosphere Coupling and Extremes in Future Climate

In this chapter, future changes in the surface fluxes, the correlations between latent and sensible heat fluxes and between latent heat flux and maximum temperature, the annual mean number of heat waves, heat wave mean duration and drought events is assessed. Two different RCP scenarios were considered (RCP 4.5 and RCP 8.5). The individual model results for RCP8.5 are depicted, and the ensemble results for both scenarios are also described. Moreover, in order to improve the understanding on the surface fluxes and coupling measure changes the anomalies (future – present) of precipitation and mean temperatures are also depicted.

With the predicted increase of surface income radiation (RCP scenarios), both latent and sensible heat fluxes may increase to maintain the surface energy balance (Figure 5.1). If sensible heat flux rises, then surface temperatures will consequently intensify. But, since the available water to evaporate (i.e. soil moisture) remains or is reduced over large areas (Figure 5.2), influenced by changes in precipitation patterns and frequency (De Wit and Stankiewicz., 2006; Shongwe et al., 2009; 2011; Sanderson et al., 2011), then, evapotranspiration, might be permanently constrained by water availability. This, in turn, may lead to a permanent surge of sensible heat flux and consequently to an escalation of surface temperature, relative to present climate conditions.

Figure 5.1 displays the seasonal anomaly between RCP8.5 scenario and Historic, for latent and sensible heat fluxes. In general, an increase of sensible heat flux is visible in all seasons, namely over Sahel and central Africa, during JJA and SON and over southern Africa for MAM, SON and DJF. In regions with more water availability, i.e. regions with a positive precipitation anomaly (e.g. western Africa, Figure 5.2) an increase of the latent heat flux can be observed, whereas sensible heat flux doesn't change. In the opposite case, in Sahel for JJA and in central/south eastern Africa for SON, less rainfall is projected, meaning less water available to evaporate. This water shortage translates into lower latent heat fluxes, which consequently, and to keep the surface energy balance, further increases in the sensible heat flux over these areas (Figure 5.1). Figure 5.2 also display the maximum and minimum temperature anomalies between RCP8.5 and Historic. Overall, both temperatures increase, mainly over dry and transition regions over Africa mainland. However, over western Africa, with higher mean projected precipitation, this temperature increase is lower.

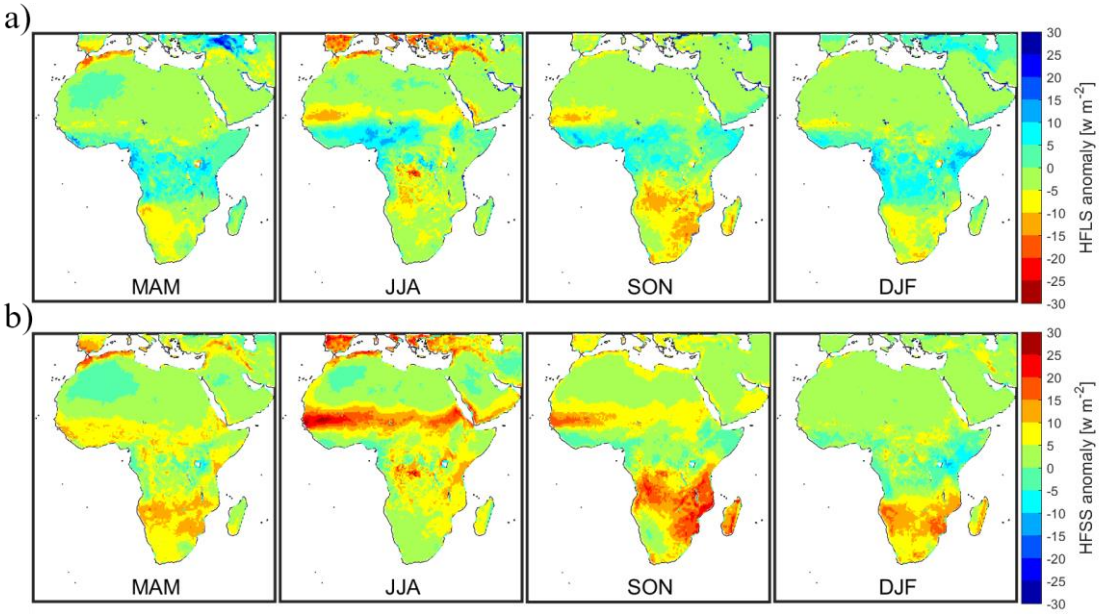


*Fig 5.1.* (a) HFLS and (b) HFSS anomalies between RCP8.5 (2071-2100) and Historic (1971-2000) ensembles.

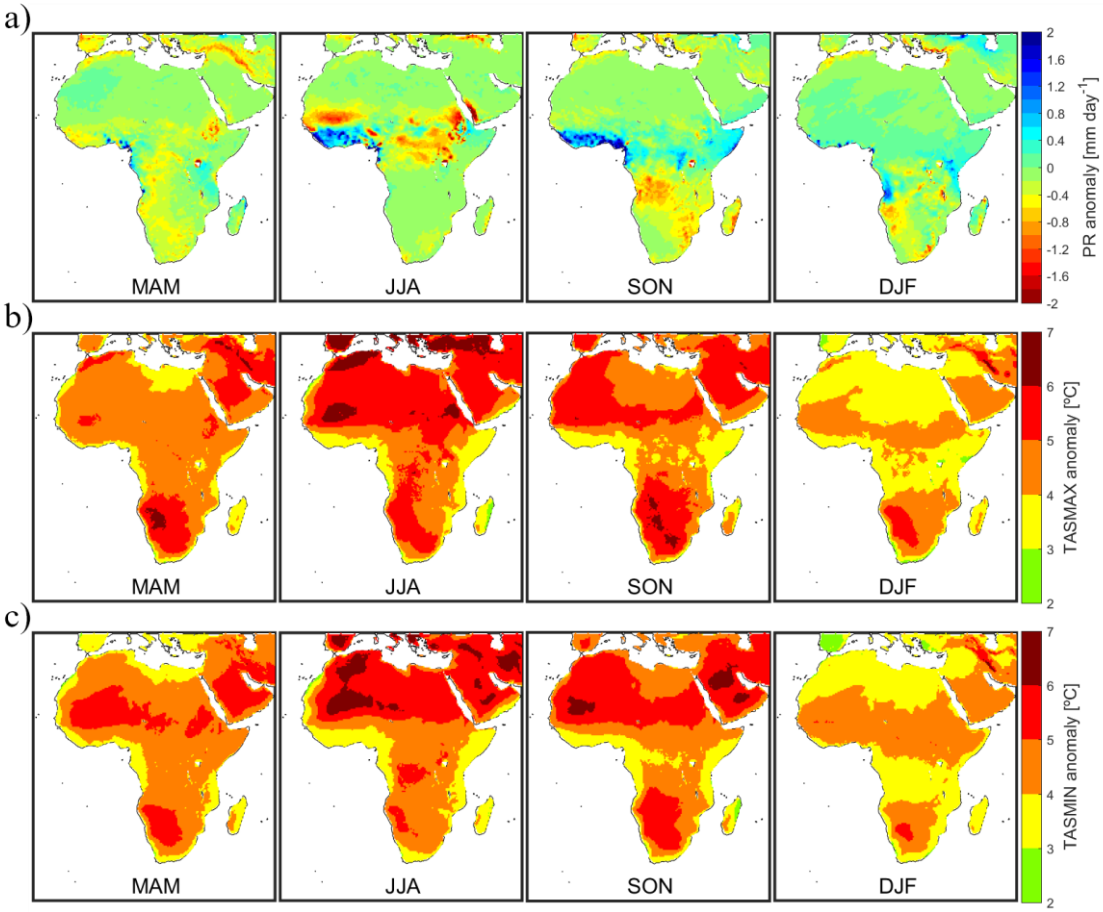


*Fig 5.2.* (a) PR, (b) TASMAX and (c) TASMIN anomalies between RCP8.5 (2071-2100) and Historic (1971-2000) ensembles.

## 5.1 Surface Fluxes

These future changes in precipitation, temperature and surface fluxes will lead towards a different future climate. Both Bowen ratio and Evaporative Fractions are a good estimative of different environments. Bowen ratio anomalies, between RCPs against Historic are shown in Figures A.38 to A.41 for RCP8.5 and figure A.42a, A.43a, A.44a and A.45a for RCP4.5. Note that scale ranges from -1 to 1 to better assess changes in humid and transition climates, although it saturates over large areas of Africa. In some regions lower anomalies are found, due to unusual high Bowen ratio values in the Historic results. Since Bowen ratio values are not limited into a fixed interval, this analysis will be mainly performed for the Evaporative Fraction.

For MAM (Figure 5.3 for RCP8.5 and Figure A.42b for RCP4.5) the RCP8.5 ensemble displays in general a small decrease of Evaporative Fraction throughout northern and central Africa. Nevertheless, some areas, such as Somalia Desert and over the west coast of central Africa, display a slight increase, while in Morocco and over southern Africa, there is a pronounced decline with anomalies higher than -0.1. Relative to the mean, the CLM RCM group displays strong negative anomalies over large areas of southern, central and western Africa. On the other hand, the RACMO22T group displays a general evapotranspiration increase, especially over central Africa. RCA4 MK3-6-0 also shows a strong upsurge over the Somalia Desert, indicating that area will be more humid on the future. HIRHAM5 and CCLM4 groups displays a general strong decrease over Sahel region and in some areas of southern Africa, which translates into less water available and some desertification is possible. HIRHAM5 NORESM1-M shows a slight anomaly decrease over central Africa and the opposite can be seem for HIRHAM5 EC-EARTH.

During the boreal summer, JJA, (Figure 5.3 for RCP8.5 and Figure A.43 b for RCP4.5) a general decrease of Evaporative Fraction values can be observed, namely over the Sahel and southern Africa. RCMs display very different reality, with CLM RCM group showing a large decrease of evapotranspiration over Africa, except over the Sahara Desert. RCA4 MK3-6-0 shows a slight increase in northern Africa and a strong negative anomaly over South Africa. RACMO22T group displays negative anomalies over Sahel and southern Africa, and positive anomalies over central Africa, especially over the west coast of central Africa.

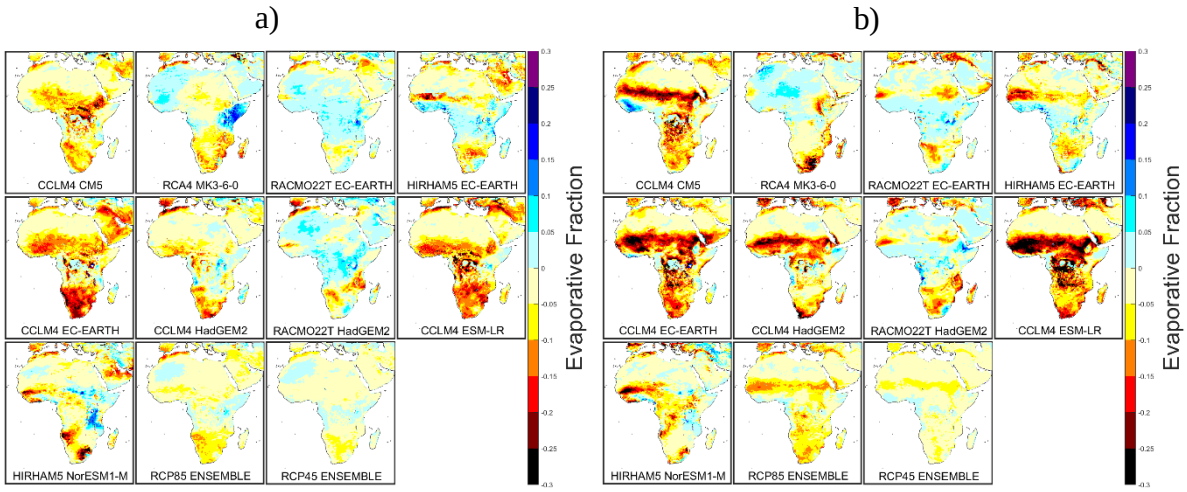


*Fig 5.3.* (a) MAM and (b) JJA Evaporative Fraction anomalies between RCP8.5 (2071-2100) and Historic (1971-2000). The RCP4.5 (2071-2100) ensemble is also shown.

Very similar patterns are observed for SON (Figure 5.4 for RCP8.5 and Figure A.44b for RCP4.5) with a general decrease of Evaporative Fraction values over Sahel, southern and central Africa and over northern Angola. Again, CLM RCP group displays higher than average changes with similar pattern between themselves. Overall, all models display a positive anomaly over western Africa, indicating a weaker Monsoon regime on this season.

In DFJ (Figure 5.4 for RCP8.5 and Figure A.45b for RCP4.5) the same noisy pattern as the one observed in Historic (Figures 4.1 to 4.4), around the Mediterranean and over Sahara Desert is visible for models from CLM and HIRHAM5 group. Excluding these areas, these models displays strong negative anomalies over southern Africa and near Sahel, while positive anomalies can be seen over the Somalia Desert, eastern Africa, and over the west coast of central Africa (CCLM4 group and HIRHAM5 EC-EARTH). Very strong positive anomalies are observed for RCA4 MK3-6-0 over the western and eastern coast of central Africa. A general Evaporative Fraction can be seen for the RACMO22T group over large areas. Overall, the RCP8.5 ensemble shows a drier Sahel and southern Africa and, a more humid western and eastern Africa.

This general decrease of Evaporation Fraction values indicates a lower latent heat flux, and/or higher sensible heat fluxes. Lower latent heat fluxes, or lower evapotranspiration rates indicates a drier climate throughout the African continent. During boreal (JJA) and austral (DJF) summer an overall decrease of Evaporative Fraction over the strong coupling regions are observed, mainly due to negative precipitation anomalies (Figure 5.2). Whereas, on weak coupled regions, essentially on central Africa Evaporative Fraction is lower largely due to a sensible heat flux increase. Overall, in southern Africa, for all seasons there is a decrease of Evaporative Fraction values due to the same reason.

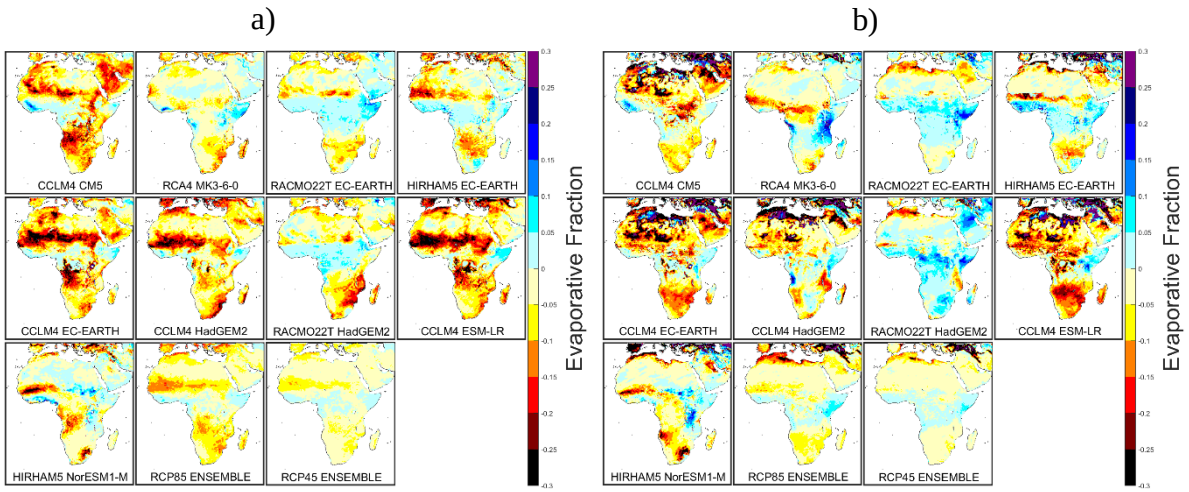


*Fig 5.4.* (a) SON and (b) DJF Evaporative Fraction anomalies between RCP8.5 (2071-2100) and Historic (1971-2000). The RCP4.5 (2071-2100) ensemble is also shown.

## 5.2 Pearson Correlations:

### a. Evaporative Fraction and Soil Moisture

The connection between soil moisture and the surface flux balance is one of the most important in the context of soil moisture-temperature coupling. In future, with an increment of surface income radiation relative to present conditions, and predicted temperature gain, latent heat flux should also rise due to an increase of the atmospheric water demand. However, areas that once always had enough water available, can now be considered strong coupling regions, where evapotranspiration is restricted by soil moisture availability and not by the radiative balance, this translates into an increase of the relationship between these two variables. On the other hand, over strong coupled regions where evapotranspiration is low enough, in the future due to climate change, these areas can be classified as non-coupling regions due to desertification.

In MAM (Figure 5.5 for RCP8.5 and Figure A.46 for RCP4.5) an increase of the correlation between MRSO and Evaporative Fraction is observed over central Africa for CCLM4 CM5, CCLM4 EC-EARTH, CCLM4 ESM-LR and HIRHAM5 NORESM1-M and over southern Africa for HIRHAM5 EC-EARTH. Over large areas of northern Africa, namely in HIRHAM5 NORESM1-M RCM a correlation decrease is displayed. In the ensemble mean, a small correlation increase is observed over central Africa.

For JJA (Figure 5.6 for RCP8.5 and Figure A.47 for RCP4.5) similar patterns are found, but reduced correlations can be seen over Sahel region for CML3 and CCLM4 ESM-LR and, over southern Africa for RCA4 MK3-6-0 model.

For SON (Figure 5.7 for RCP8.5 and Figure A.48 for RCP4.5), there is a small correlation increase over central Africa for the ensemble mean. HIRHAM5 NORESM1-M shows, over western Africa, a significant correlation increase, while over large areas of the Sahara Desert, it displays a negative anomaly. A positive correlation is also found for all models, except RCA4 MK3-6-0, over central Africa and over southern Africa for HIRHAM5 EC-EARTH.

In DJF (Figure 5.8 for RCP8.5 and Figure A.49 for RCP4.5) there is an increase of correlation over central Africa for CLM and HIRHAM5 group and, over southern Africa for HIRHAM5 EC-EARTH. CLM and HIRHAM5 group also display a noisy pattern over northern Africa. The CCLM4 group, over Sahel, also displays a negative anomaly. For RCA4 MK3-6-0, strong negative anomalies can be seen over western Sahel, and strong positive anomalies over eastern Sahel. Overall, this RCM displays large areas with a slight negative anomaly. The ensemble means, in general, displays large areas with a slight correlation increase, namely over central Africa.

In general, on areas where evapotranspiration is relatively large in the future, there is an increase correlation between soil moisture and latent heat flux. Over the present strong coupling areas, the drier future conditions observed (Figure 5.1 and 5.2) implies a higher control of the available water over evapotranspiration, which in turn would translate into a higher soil moisture control over temperature.

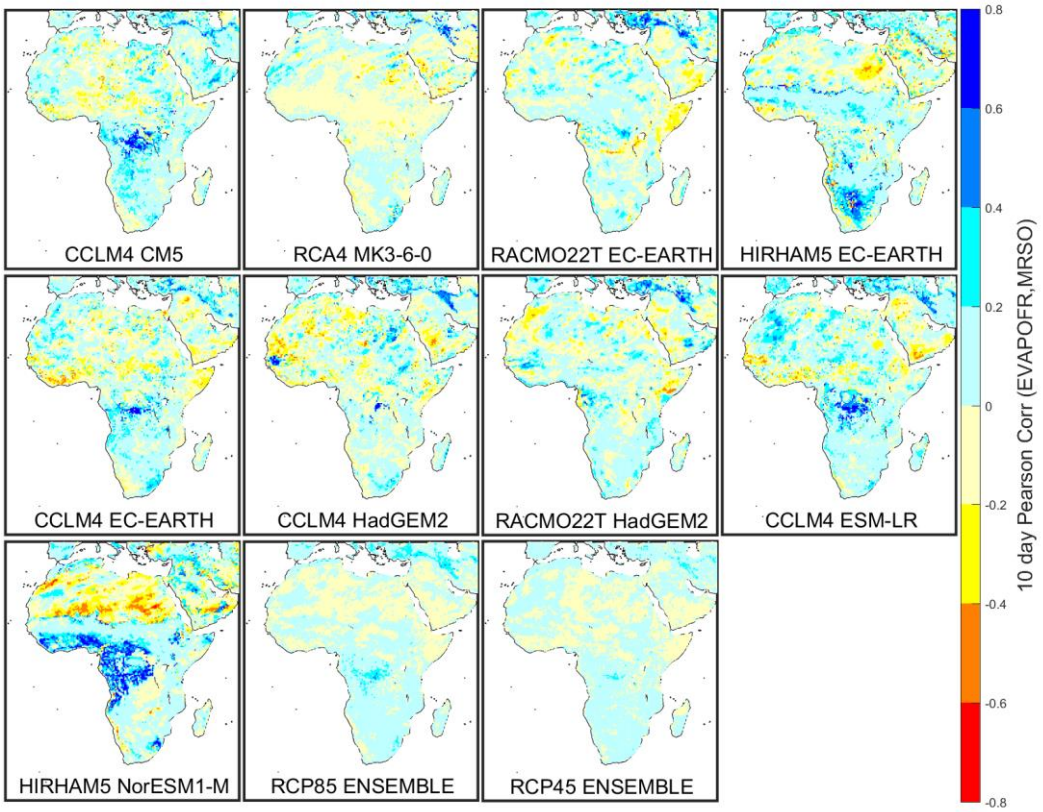


*Fig 5.5.* MAM 10 days of nonoverlapping means correlation between MRSO and Evaporative Fraction (EVAPOFR) anomalies between RCP8.5 (2071-2100) and Historic (1971-2000). The RCP4.5 (2071-2100) ensemble anomaly is also shown.

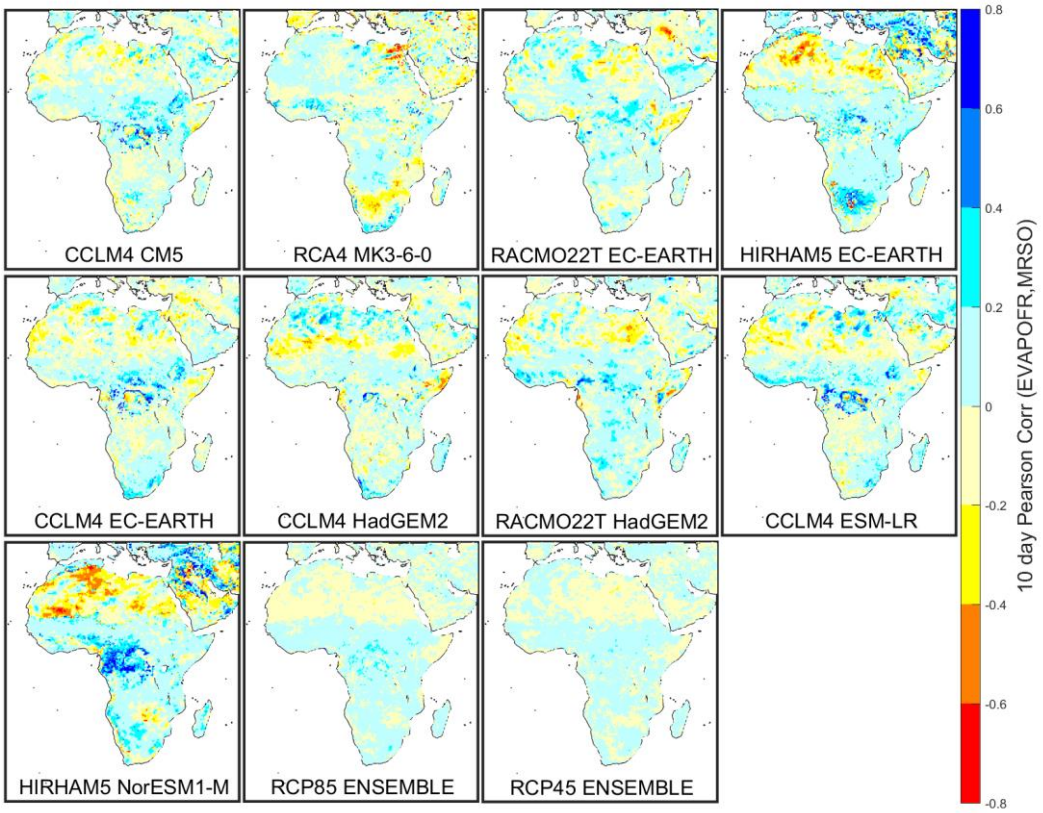


*Fig 5.6.* JJA 10 days of nonoverlapping means correlation between MRSO and Evaporative Fraction (EVAPOFR) anomalies between RCP8.5 (2071-2100) and Historic (1971-2000). The RCP4.5 (2071-2100) ensemble anomaly is also shown.

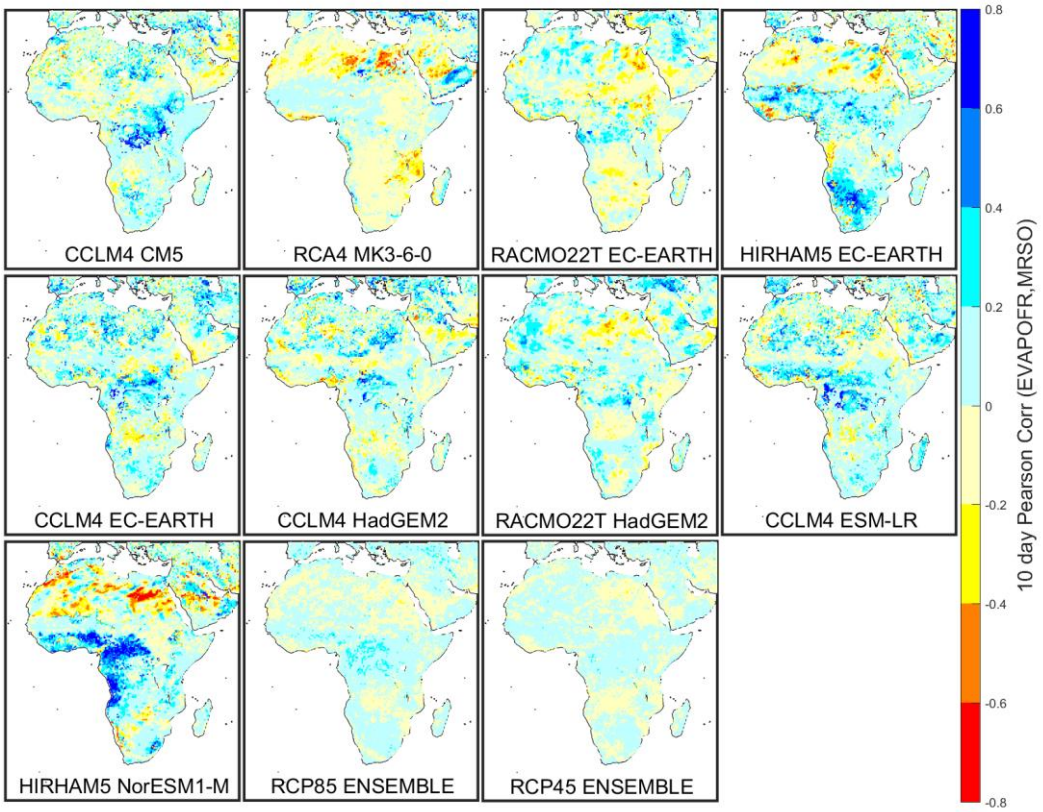


*Fig 5.7.* SON 10 days of nonoverlapping means correlation between MRSO and Evaporative Fraction (EVAPOFR) anomalies between RCP8.5 (2071-2100) and Historic (1971-2000). The RCP4.5 (2071-2100) ensemble anomaly is also shown.

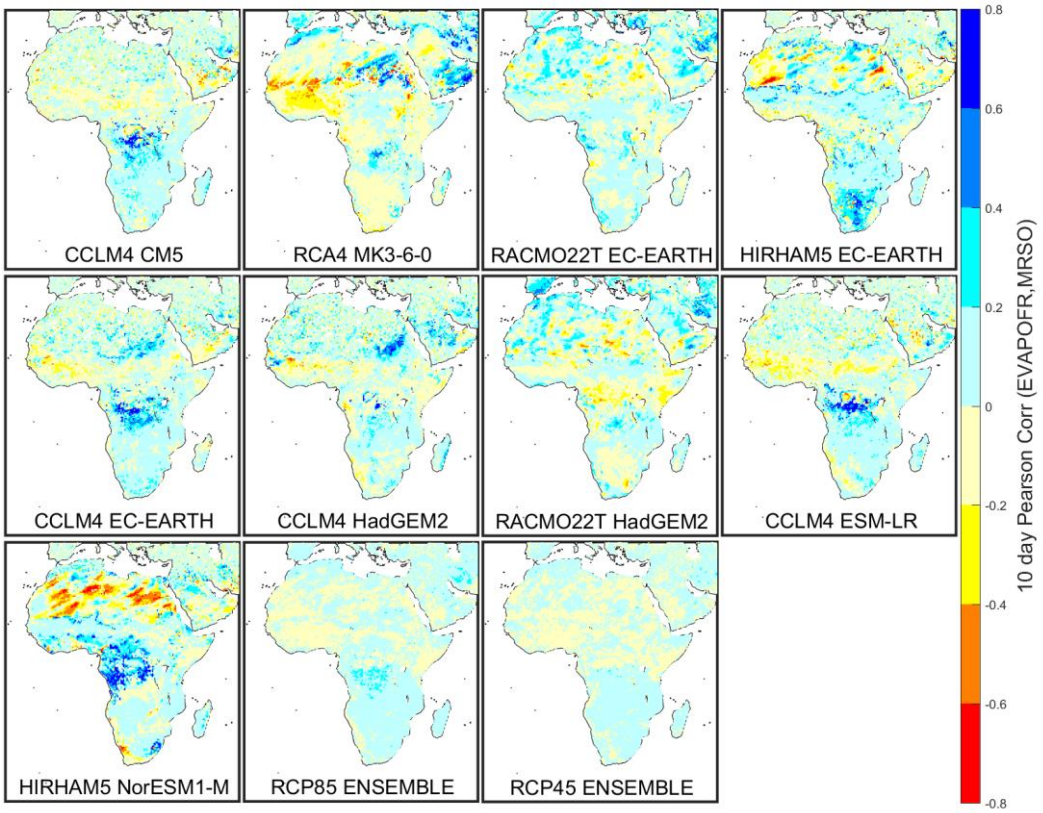


*Fig 5.8.* DJF 10 days of nonoverlapping means correlation between MRSO and Evaporative Fraction (EVAPOFR) anomalies between RCP8.5 (2071-2100) and Historic (1971-2000). The RCP4.5 (2071-2100) ensemble anomaly is also shown.

### b. Latent and Sensible Heat Fluxes correlations

Here, the results for the 10 days of non-overlapping mean correlations anomalies between latent and sensible heat fluxes are assessed (Figures 5.9 to 5.12 for RCP8.5 and Figures A.50 to A.53 for RCP4.5). The 10 days of non-overlapping mean correlation between latent heat flux and maximum temperature (Figures A.54 to A.57 for RCP4.5 and A.58 to A.61 for RCP8.5) display similar correlations anomalies relative to the HFLS-HFSS correlation and therefore are not analyzed.

During MAM (Figure 5.9 for RCP8.5 and Figure A.50 for RCP4.5) strong negative anomalies are observed over the western side of central Africa and slight negative anomalies can be observed over South Africa. CCLM4 CM5, CCLM4 EC-EARTH and CCLM4 ESM-LR display a negative anomaly over large areas of central Africa, but slight positive anomalies are found over the Sahel region. Overall, all models display a slight localized change over central and southern Africa, except HIRHAM5 NORESM1-M with a very strong negative correlation over the western side of central Africa.

In JJA (Figure 5.10 for RCP8.5 and Figure A.51 for RCP4.5) all models and ensemble display a strong negative anomaly over western Africa and south of Sahel. Negative values may also be found over some areas in southern Africa (e.g. RCA4 MK3-6-0, CCLM4 EC-EARTH, HIRHAM5 NORESM1-M).

A similar pattern is observable during SON (Figure 5.11 for RCP8.5 and Figure A.52 for RCP4.5). All models, except RCA4 MK3-6-0 group and RACMO22T EC-EARTH, display a negative anomaly over western and central Africa.

For DJF (Figure 5.11 for RCP8.5 and Figure A.52 for RCP4.5), all models, except the RACMO22T group, displays a negative correlation anomaly over the western side of central Africa and a slight negative anomaly over southern Africa.

With increasing temperatures and soil drying, areas that once were considered strong coupling regions could become no coupling regions (positive correlation anomalies over areas that are strong coupling in present climate) and areas that were considered weak coupling regions could become strong coupling regions (high negative anomalies over the present weak coupling zones). Overall, the largest changes are located in the present weak coupling regions, over central and western Africa, with a very strong negative correlation anomaly in both metrics and on all seasons.

In the future, with climate change, the climatic balance between fluxes over different regions will, change (Figure 5.1), changing the correlations values (Table 5.1). Table 5.1 displays the Bowen ratio, Evaporative Fraction, MRSO-EVAPFR correlation, HFLS-HFSS correlation and HFLS-TASMAX correlation for RCP8.5 for all regions defined in Table 3.1 and for the entire Africa-CORDEX domain. Overall, for all seasons and comparing with Historic, both Bowen ratio and Evaporative Fraction indicate a milder humid environment in the future, which could be attributed to the higher evapotranspiration rates over the weak coupling regions. The exception is for SON and DJF seasons which display higher Bowen ratio meaning a drier climate. This could be due to the Bowen ratio scale not being bounded to a fixed interval like Evaporative Fraction. For this reason, very high values over dry areas could bias the mean result. In the case of MRSO-EVAPFR correlation, the regional and domain mean results indicates a higher control of soil moisture over the evapotranspiration. Also, there is a strengthening of the mean correlations over the strong coupling regions in both coupling metrics, meaning a more intense and/or spatially distributed negative relationship between the surface heat fluxes. Overall, the same strong coupling regions observed in the present, most likely still exists on the future. However, on weak coupling regions, increasing radiation and precipitation pattern changes will, most likely transform these areas into strong coupling regions, where evapotranspiration is now constrained by the available water. One example of this behavior is CNA region for the DJF where, in the future, the correlation between fluxes is negative, MRSO-EVAFRC correlation is stronger and

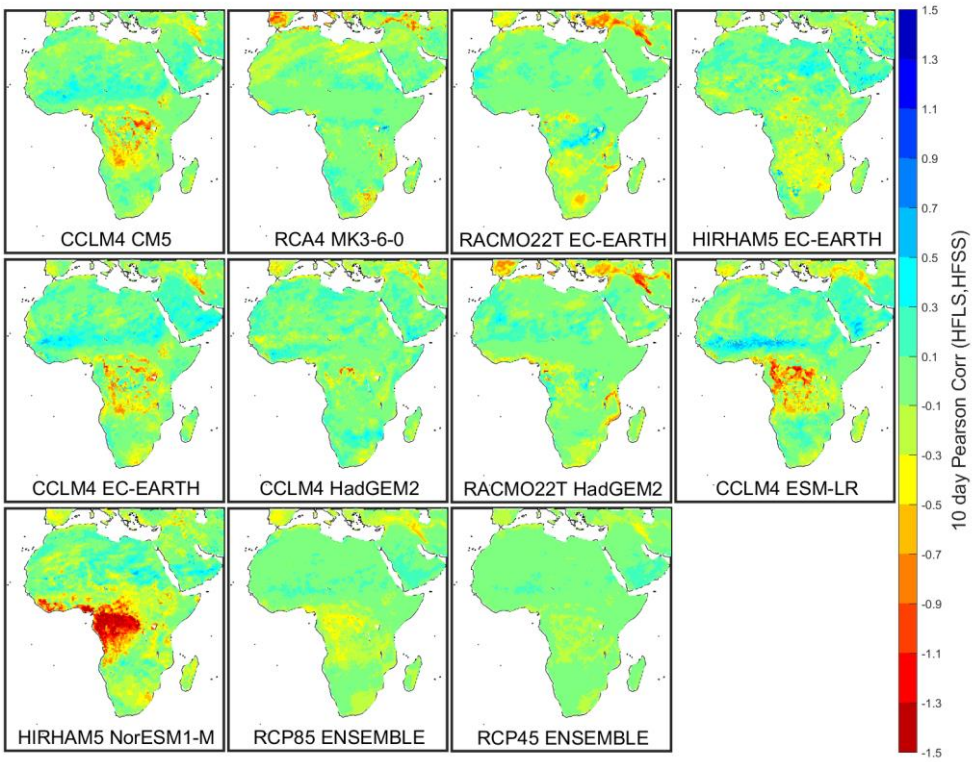


*Fig 5.9.* MAM 10 days of nonoverlapping means correlation between latent heat flux (HFLS) and sensible heat flux (HFSS) anomalies between RCP8.5 (2071-2100) and Historic (1971-2000). The RCP4.5 (2071-2100) ensemble is also shown.

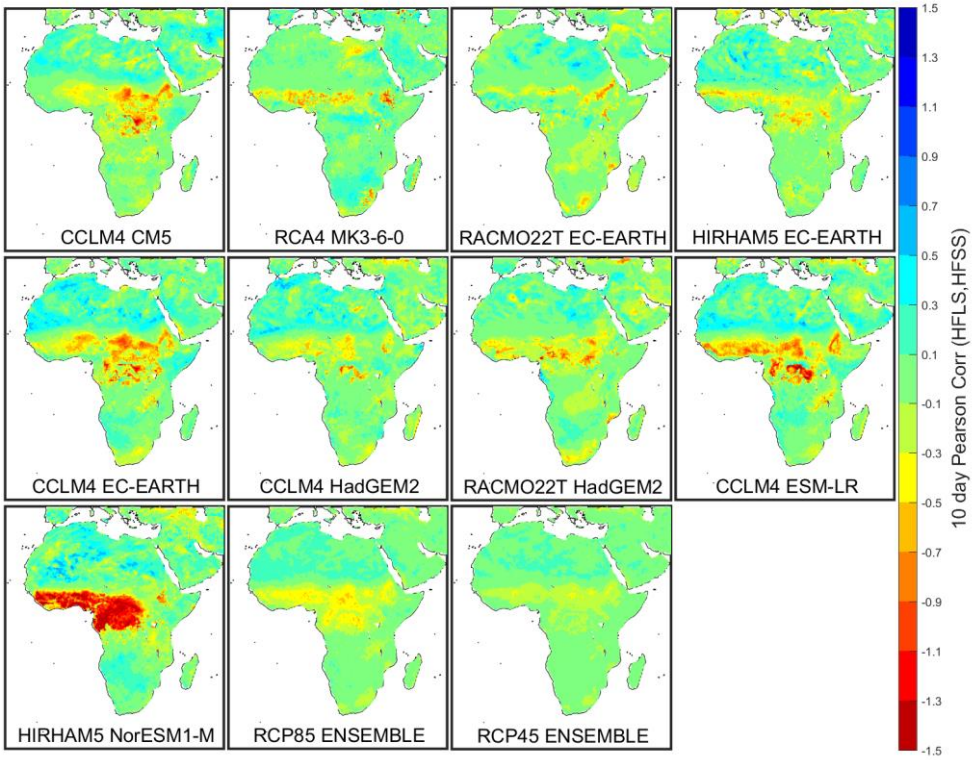


*Fig 5.10.* JJA 10 days of nonoverlapping means correlation between latent heat flux (HFLS) and sensible heat flux (HFSS) anomalies between RCP8.5 (2071-2100) and Historic (1971-2000). The RCP4.5 (2071-2100) ensemble is also shown.

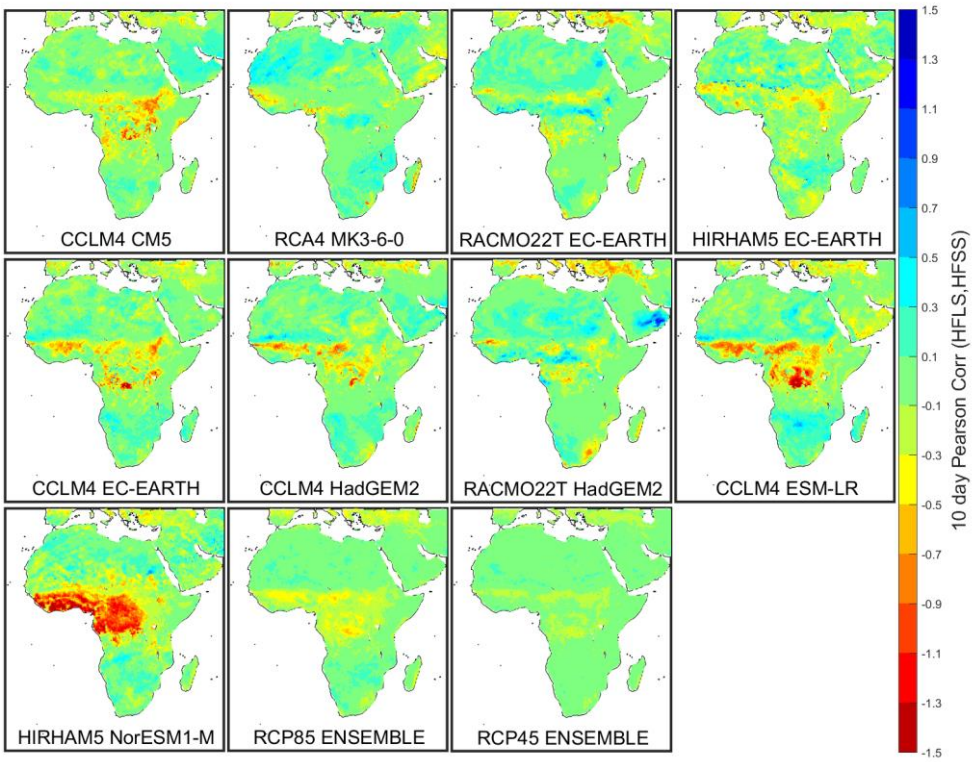


*Fig 5.11.* SON 10 days of nonoverlapping means correlation between latent heat flux (HFLS) and sensible heat flux (HFSS) anomalies between RCP8.5 (2071-2100) and Historic (1971-2000). The RCP4.5 (2071-2100) ensemble is also shown.

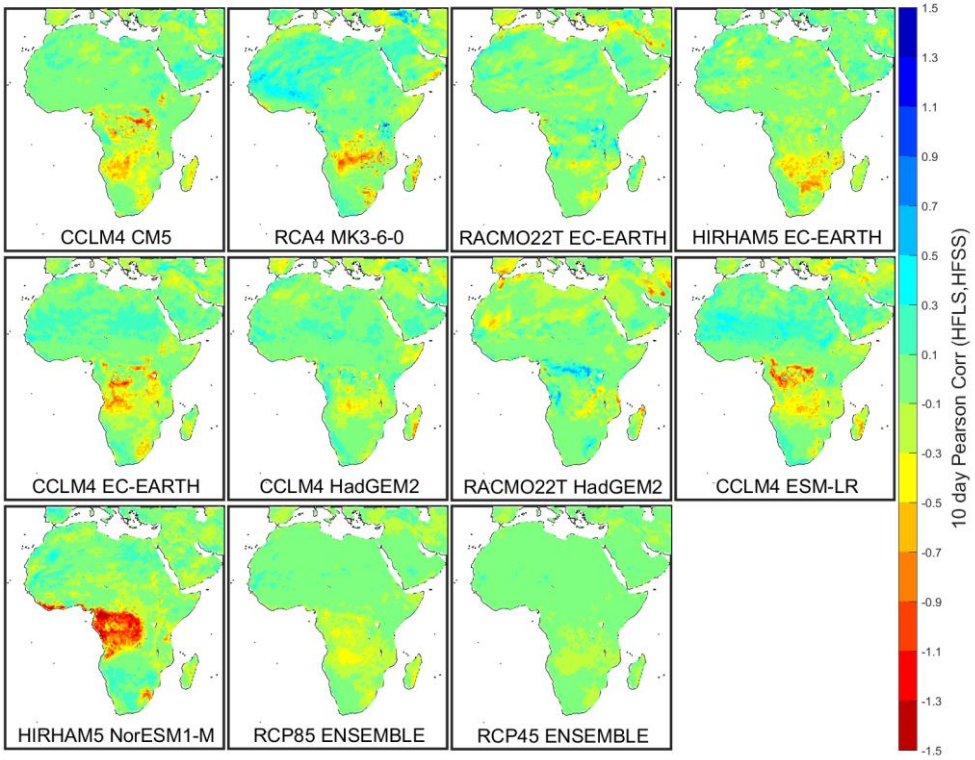


*Fig 5.12.* DJF 10 days of nonoverlapping means correlation between latent heat flux (HFLS) and sensible heat flux (HFSS) anomalies between RCP8.5 (2071-2100) and Historic (1971-2000). The RCP4.5 (2071-2100) ensemble is also shown.

Evaporative Fraction (Bowen ratio) indicates lower (higher) values, suggesting this conversion from weak to strong coupling region.

Table 5.1 Seasonal RCP8.5 ensemble (2071-2100) Bowen ratio, Evaporative Fraction, 10 days of nonoverlapping means correlations between MRSO and HFLS, between HFLS and HFSS and between HFLS and TASMAX for all regions and Africa-CORDEX domain. Red values denote the JJA and DJF main strong coupling regions. Also, values for the domain mean for the same seasons are highlighted. Blue values indicate the new strong coupling region for the JJA.

| Metric | Seasons | NA-SA | NA-SW | EA | CNA | CSA | SA-W | Africa |
|---|---|---|---|---|---|---|---|---|
| Bowen ratio | MAM | 6.42 | 1.17 | 1.29 | 0.32 | 0.83 | 2.15 | 2.94 |
| | JJA | 2.75 | 0.40 | 4.35 | 0.93 | 4.48 | 2.75 | 4.12 |
| | SON | 2.27 | 0.32 | 4.73 | 0.58 | 4.38 | 8.40 | 2.86 |
| | DJF | 6.99 | 1.18 | 1.09 | 0.33 | 0.64 | 4.54 | 2.81 |
| Evaporative Fraction | MAM | 0.26 | 0.51 | 0.53 | 0.77 | 0.61 | 0.57 | 0.67 |
| | JJA | 0.44 | 0.76 | 0.32 | 0.62 | 0.30 | 0.56 | 0.65 |
| | SON | 0.48 | 0.79 | 0.32 | 0.69 | 0.31 | 0.49 | 0.66 |
| | DJF | 0.27 | 0.52 | 0.57 | 0.77 | 0.66 | 0.55 | 0.70 |
| Correlation (MRSO, EVAPFR) | MAM | 0.51 | 0.64 | 0.76 | 0.61 | 0.79 | 0.55 | 0.57 |
| | JJA | 0.65 | 0.60 | 0.75 | 0.70 | 0.79 | 0.38 | 0.58 |
| | SON | 0.61 | 0.50 | 0.64 | 0.62 | 0.60 | 0.55 | 0.52 |
| | DJF | 0.57 | 0.77 | 0.73 | 0.57 | 0.70 | 0.53 | 0.50 |
| Correlation (HFLS, HFSS) | MAM | -0.33 | -0.63 | -0.43 | -0.22 | -0.32 | 0.28 | 0.26 |
| | JJA | -0.52 | -0.12 | -0.47 | -0.50 | -0.47 | 0.24 | 0.19 |
| | SON | -0.28 | -0.11 | -0.52 | -0.33 | -0.41 | 0.26 | 0.27 |
| | DJF | -0.38 | -0.75 | -0.46 | -0.07 | -0.26 | 0.05 | 0.26 |
| Correlation (HFLS, TASMAX) | MAM | -0.30 | -0.51 | -0.13 | -0.03 | -0.17 | -0.07 | -0.16 |
| | JJA | -0.46 | 0.08 | -0.25 | -0.23 | -0.24 | -0.19 | -0.11 |
| | SON | -0.13 | 0.16 | -0.28 | -0.16 | -0.43 | -0.08 | -0.20 |
| | DJF | -0.13 | -0.52 | -0.27 | 0.12 | -0.20 | -0.28 | -0.06 |

## 5.3 Heat Waves

In the future, with the increasing temperatures and changes in the flux partitioning, heat waves will be more frequent and lasting longer. Figure 5.13 for RCP8.5 and A.53 for RCP4.5 display the annual mean number of heat waves computed based in the Historic period 90$^{th}$ percentile. Since temperatures in the future will increase, the number of consecutive days with maximum temperature above the Historic 90$^{th}$ percentile will be much higher. There is an overall increase of the number of heat waves throughout the African continent relative to Historic. The maximum heat wave number in the Historic period was bellow three heat waves annually, while in RCP8.5 period, for some land points, almost all days have temperatures exceeding the Historic 90$^{th}$ percentile. For the CLM RCM group, a large number of heat waves are found over Africa, except over central and northern Africa. In the present, it is precisely over the western side of central Africa that less heat wave events occur. For the future this pattern is reversed in RCA4 MK3-6-0, HIRHAM5 EC-EARTH and RACMO22T group. In some areas, for the RCP8.5 ensemble against Historic ensemble, heat wave frequency will increase 10 fold or more.

The mean heat wave duration display an opposite pattern, with longer (shorter) heat waves in regions of less (more) events in CCLM4 group (Figure 5.14 for RCP8.5 and Figure A.54 for RCP4.5). RCA4 MK3-6-0 displays a high mean heat wave duration over almost all Africa, except near the Mediterranean, central and southernmost Africa. For HIRHAM5 group, the location of the longer events is over the Somalia desert, having the rest of the continent approximately the same duration of events. In the RACMO22T group, CCLM4 HADGEM2 and CCLM4 ESM-LR the largest duration is especially over western Africa. The ensemble mean displays events with more duration over central and western Africa, namely over the weak coupling regions. This increment is related to the increase of surface temperature (Figure 5.2) and not to strong coupling conditions. The present temperature variability over these areas is small throughout the year, meaning 90$^{th}$ percentiles closer to mean values. If mean temperature increases, then more days exceeds this threshold, relatively to stronger coupling areas, where temperature variability is higher and less sensitive to mean changes. Overall more and longer lasting heat waves are predicted throughout Africa continent.

Table 5.2 displays the annual mean number and duration of heat waves and the 10 days of non-overlapping means correlation between latent and sensible heat flux for the RCP8.5 regions defined on Table 3.1 and Figure A.6. Relatively to present conditions, over the strong coupling regions and CNA the yearly average number of heat waves is projected to increase more than 10 fold. On the other hand, the mean duration heat waves events doubles for strong and weak coupling regions, whereas over the Namib Desert (SA-W) heat waves will be shorter.

There is a clear difference between regions and the domain mean for the annual mean heat wave number, with higher than mean events over the selected regions. The SA-W region is however an exception, since it has values similar to the continent's mean. With the different climate conditions projected for the future, strong coupling periods are most likely to happen, even over weak coupling regions. This amounts to more frequent events over regions where evapotranspiration is relatively high. Over deserts, an increase of the yearly heat wave number is also visible, but in this case its values are closer to the domain mean. HFLS-HFSS correlation, displays for all regions, except in SA-W, mean negative correlations (stronger than in the historical period), indicating that this increase in the number of heat waves is most likely due to the negative relationship between fluxes over these areas. In the present, heat wave duration is found to have no connection with the soil moisture-temperature coupling. In future this isn't necessarily true, as all regions, except SA-W, displays longer events relative to the domain mean. Even if synoptic conditions stop being favorable to heat wave events, severe negative soil moisture anomalies imply strong temperature anomalies.

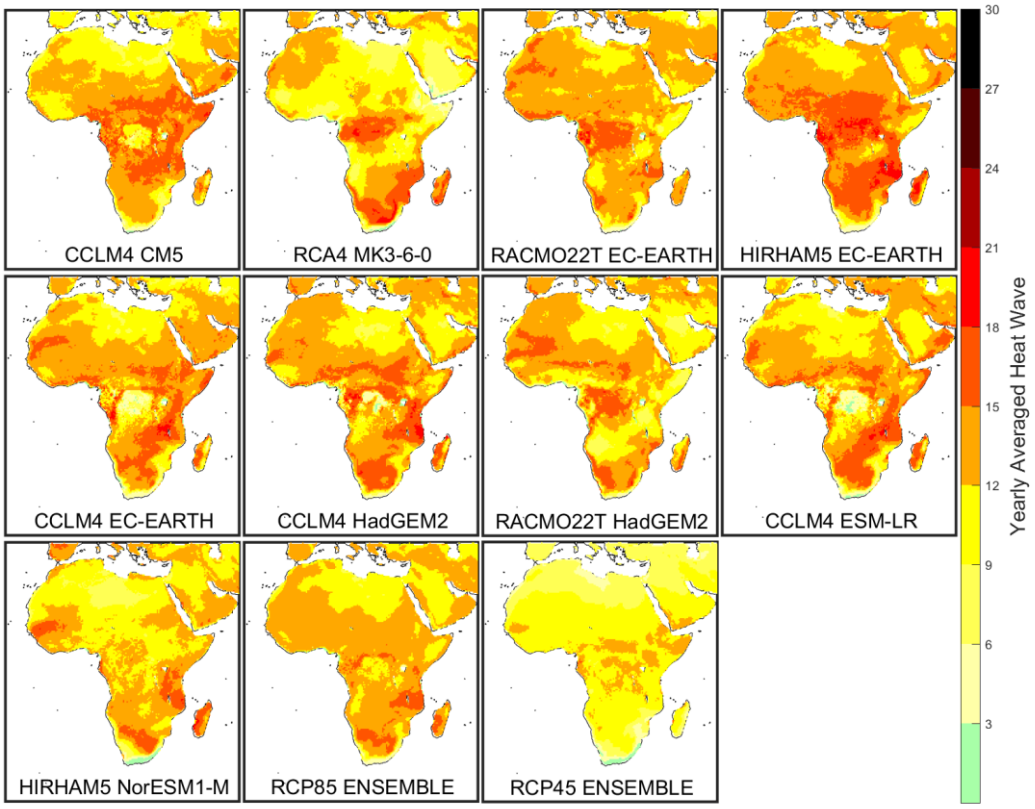


*Fig 5.13.* Yearly average number of heat waves for the RCP8.5 (2071-2100). RCP4.5 (2070-2100) ensemble is also shown. For the RCP8.5 and RCP4.5, the Historic 90$^{th}$ percentile was used.

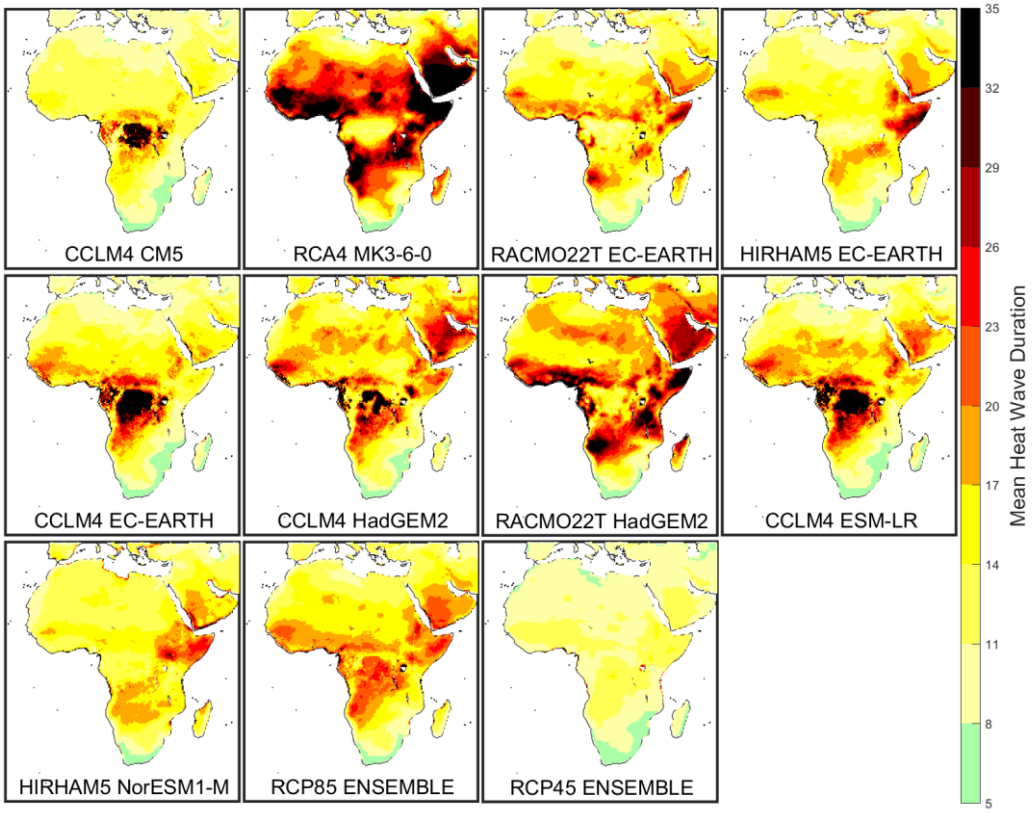


*Fig 5.14.* Mean heat wave duration for RCP8.5 (2071-2100). RCP4.5 (2071-2100) ensemble is also shown

Table 5.2. Annual mean number of heat waves, mean heat wave duration and 10 days of nonoverlapping means correlation between HFLS and HFSS for the RCP8.5 ensemble (1971-2000). Values depicted as red represents the mean over the main strong coupling regions and Africa-CORDEX domain for JJA and DJF.

| Metric | Seasons | NA-SA | NA-SW | EA | CNA | CSA | SA-W | Africa |
|---|---|---|---|---|---|---|---|---|
| Heat Waves Number | - | 12.00 | 12.66 | 12.67 | 12.18 | 11.40 | 6.27 | 5.38 |
| Heat Waves Duration | - | 15.56 | 20.59 | 15.93 | 18.89 | 15.78 | 5.44 | 7.03 |
| Correlation (HFLS, HFSS) | MAM | -0.33 | -0.63 | -0.43 | -0.22 | -0.32 | 0.28 | 0.26 |
| | JJA | -0.52 | -0.12 | -0.47 | -0.50 | -0.47 | 0.24 | 0.19 |
| | SON | -0.28 | -0.11 | -0.52 | -0.33 | -0.41 | 0.26 | 0.27 |
| | DJF | -0.38 | -0.75 | -0.46 | -0.07 | -0.26 | 0.05 | 0.26 |

## 5.4 Drought, SPEI 12-months timescale

In the future, the overall drier condition observed (mean temperature increase on Figure 5.2), translates into a decrease of evapotranspiration, which in turn is connected to soil moisture deficits, or drought. Therefore, and relative to present conditions, extended and intense drought events are expected. Figure 5.15 for RCP8.5 and Figure A.64 for RCP4.5 display the percentage of months in drought (SPEI bellow -1) for all land points of Africa-CORDEX domain. Overall, the intra-model variability (estimated with IQR) and median increase substantially, particularly some points might possibly be in a permanent drought condition. The fraction area with different drought intensities (Figure 5.16 for RCP8.5 and Figure A.65 for RCP4.5) displays, for both scenarios, a considerable increase in the number of points in Extreme drought (SPEI bellow -2) over the period. The moderate and severe drought events have, nonetheless, approximately the same probability. The strong increase of fraction area in extreme drought also limits the increase of the other two fraction areas. Finally, the mean drought duration (Figure 5.17 for RCP8.5 and Figure A.66 for RCP4.5) also increases substantially, with some points being in a permanent drought relative to present conditions. Overall, it is predicted that drought events will be much stronger (extreme events characterized by SPEI values bellow -2) and longer lasting.

Table 5.3 shows the median results for the ensemble for the Hindcast, Historic, RCP4.5 and RCP8.5 periods, of the percentage of months in drought, fraction area in different drought severities and mean event duration. The median is a good measure of the general changes and is less sensitive to extremes. Relative to Historic ensemble, the RCP4.5 ensemble increases by approximately 2.8 fold and RCP8.5 by 3.3 fold in the percentage of months in drought. For the fraction area in moderate, severe and extreme drought, the most considerable change goes for extreme drought with an increment of 44 fold for RCP8.5 and 23 for RCP4.5. The increase of extreme drought (SPEI bellow -2) indicates that extremes which rarely happened in present conditions will be much more frequent in the future. Finally, the mean event duration also increases, particularly for the RCP8.5 ensemble with a mean event duration superior to 12 months.

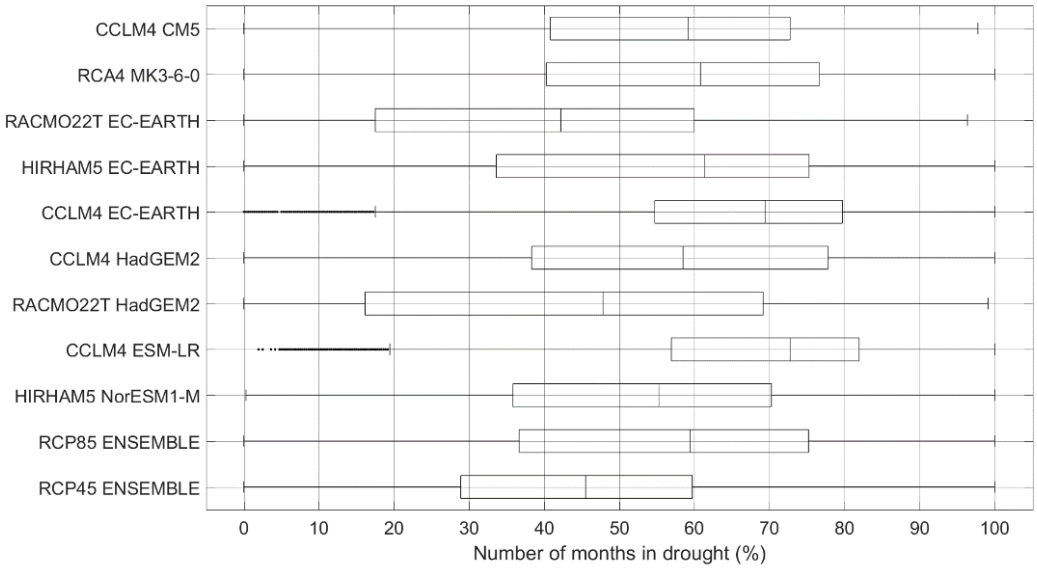


*Fig 5.15.* Boxplots of number of months in drought (percentage of months with SPEI below -1), for all land points of the RCP8.5 (2071-2100) models. The ensemble is the data of all models. RCP4.5 (2071-2100) ensemble is also shown. SPEI index for RCP8.5 and RCP4.5 are computed based on Historic as reference period.

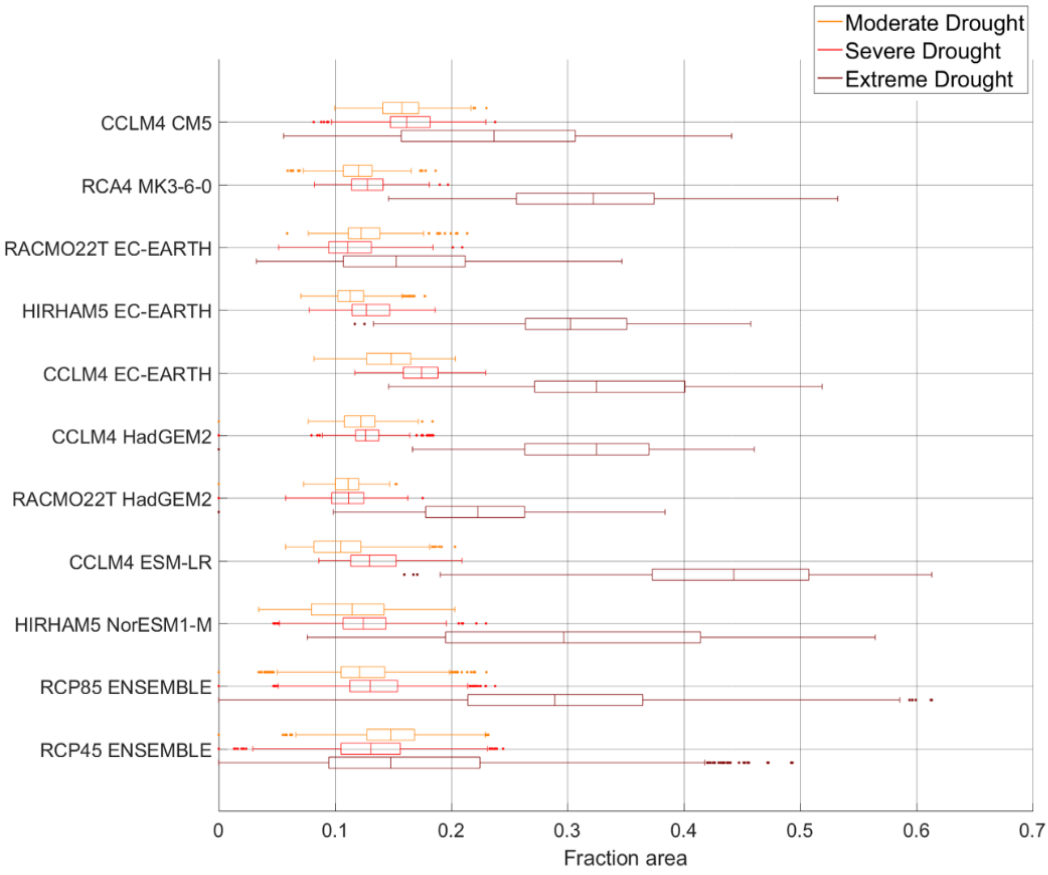


*Fig 5.16.* Fraction area in drought, with different intensities (orange: fraction area in moderate drought; red: fraction area in severe drought; dark red: fraction area in extreme drought), over time for all land points for the RCP8.5 (2071-2100) models. The ensemble is the data of all models. RCP4.5 (2071-2100) ensemble is also shown. SPEI index for RCP8.5 and RCP4.5 are computed based on Historic as reference period.

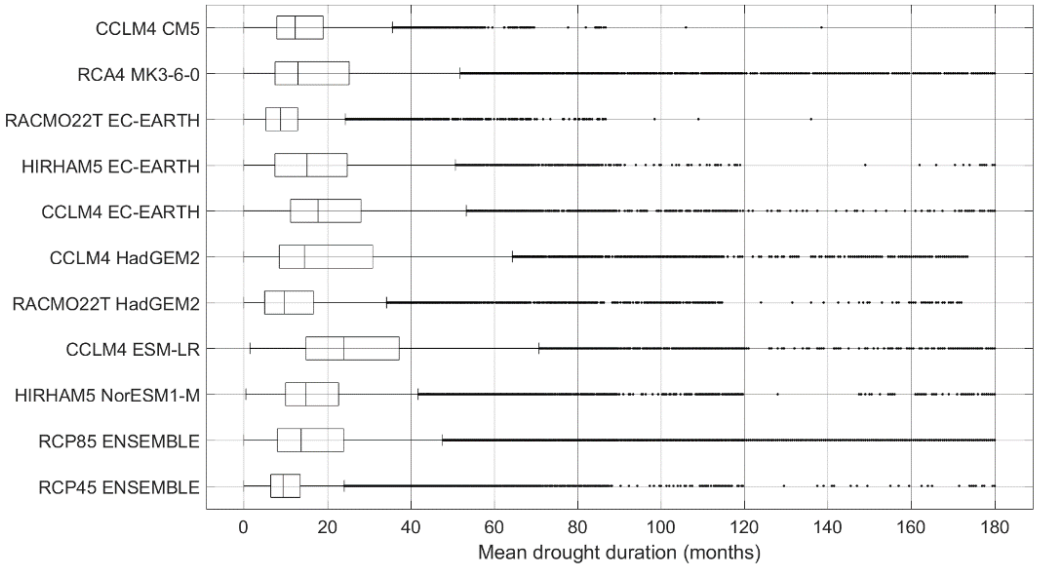


*Fig 5.17.* Boxplot of mean drought duration for all land points of RCP8.5 (2071-2100) normalized by the number of years of each model. The ensemble the data of all models. RCP4.5 (2071-2100) ensemble is also shown. SPEI index for RCP8.5 and RCP4.5 are computed based on Historic as reference period.

Table 5.3. Median of the number of months in drought, fraction area in drought (moderate, severe and extreme) and number of droughts for the ensemble of Historic, RCP4.5 and RCP8.5. Between parenthesis is the difference between RCP4.5 and Historic, RCP8.5 and Historic.

| | Number of months in drought (%) | Fraction area in: | | | Mean drought duration (months) |
|---|---|---|---|---|---|
| | | Moderate drought | Severe drought | Extreme drought | |
| Historic | 16.39 | 0.1 | 0.04 | 0.01 | 4.69 |
| RCP4.5 | 45.53 (x2.78) | 0.15 (x1.4) | 0.13 (x2.98) | 0.15 (x22.77) | 9.42 (x2.01) |
| RCP8.5 | 53.61 (x3.27) | 0.12 (x1.15) | 0.13 (x2.97) | 0.29 (x44.46) | 13.75 (x2.77) |

# 6. Conclusions

In this work, the soil moisture-temperature coupling, frequency and duration of heat wave events are characterized and compared amongst themselves for the Africa-CORDEX RCM simulations and ensemble for the present period. Individual variables (Precipitation, Soil Moisture, Latent and Sensible Heat Fluxes, Mean, Maximum and Minimum Temperatures) for Hindcast and Historic were assessed and validated against observationally based databases (CRU, GPCC, FLUXNET and GLEAM). Overall, all models can represent the seasonal and climatological climate over Africa. However strong biases are found for some regions in some models. An ensemble is built for each variable as it represents the best estimative of the reality. This multi-model mean ensemble is also evaluated and globally, it performs better than the individual RCMs. Future changes in coupling, heat waves and drought are evaluated with two IPCC RCP scenarios (RCP4.5 and RCP8.5). For all periods, intensity and mean drought duration is also assessed based in the SPEI index

The 10 days of non-overlapping mean correlation between latent and sensible heat flux and the 10 days of non-overlapping mean correlation between latent heat and maximum temperature are used to evaluate the seasonal coupling strength for the regional climate models. The former, evaluates the balance between the surface fluxes, while the latter also includes the relationship between sensible heat flux and temperature and so, weaker correlations are expected. In both coupling metrics, the seasonal transition climates (i.e. Mediterranean type climates) identified by the Bowen ratio and Evaporative Fraction are classified as strong coupling, where evapotranspiration is constrained by the soil moisture availability, whereas humid climates, following the seasonal African Monsoon and ITCZ position, are classified as weak coupling regions, where evapotranspiration is limited by the available energy and not by the available water. Dry climates (e.g. Sahara and Namib deserts) are classified as non-coupling regions since no water is available to evaporate. The correlation between total (i.e. vertically integrated) soil moisture and Evaporative Fraction is also assessed. In this case, lower correlations are found over deserts, where evapotranspiration is low throughout the seasons. However, the spatial extent of strong coupling regions fluctuates for different RCMs reinforcing the idea that each model has its own reality. In the future, with increase of incoming radiation and a generalized soil desiccation due mainly to precipitation pattern and frequency changes (De Wit and Stankiewicz, 2006; Shongwe et al., 2009; 2011; Sanderson et al., 2011) changes in the flux partitioning is expected. Higher correlations were found over the present strong coupling regions, whereas areas with low evapotranspiration rates could convert from transition to dry areas. Also, the present weak coupling regions, where evapotranspiration is constrained by the available energy, in the future, situations may arise where evapotranspiration becomes constrained by the water availability. The correlation between total (i.e. vertically integrated) soil moisture and Evaporative Fraction is a good measured to estimate the relationship between soil moisture and the flux partitioning. Higher correlations are found over strong coupling regions, whereas weaker correlations are found over weak coupling regions where evapotranspiration is not mainly controlled by the available water. Over dry areas, where evapotranspiration is small, low correlation values appear. For the end of the century, with less soil moisture available throughout the domain, higher correlations values are observed, due to an increase of soil moisture control over evapotranspiration.

In present climate conditions, in areas of strong soil moisture-temperature coupling, more intense and frequent heat waves events are expected to occur. To examine this behaviour the annual mean number of heat waves were computed for all periods. In fact, in the historical period, more heat waves are found over strong coupling regions relatively to the domain mean number of heat waves within the Africa-CORDEX. The higher number of heat waves in these transition climates (Figure A.6) occur mainly in austral summer (December-January-February, DJF) and to less extent, in boreal summer

(June-July-August, JJA). Mean heat wave duration is also assessed, but no relationship is found with coupling results, which implies that the event duration is controlled mainly by the synoptic conditions and not by the soil moisture-temperature feedback. In future, more heat waves, as well as a larger mean heat wave duration is projected over Africa, namely over central Africa. These changes over central Africa indicate that weak coupling regions could periodically or permanently become strong coupling regions as pointed out by the strong negative anomalies in the 10 days of nonoverlapping means correlation between latent and sensible heat fluxes.

The drought in Africa, for present and future climate was also studied in the current thesis, using the SPEI index and thus computing the percentage of months in drought, the fraction area under drought and the mean drought duration. Since SPEI is a normalized index, the total number of months in drought (SPEI bellow -1) should correspond to 15.73% of all months. The ensemble spatial median for present climate overestimates this value. Overall the Historic ensemble median percentage of months in drought, fraction area in moderate, severe and extreme drought, and the mean drought duration values are close to those observed over Hindcast simulation. SPEI index for RCP8.5 and RCP4.5 were computed having the Historic period as reference. Due to the projected drier environment in the future, more frequent, intense and longer lasting drought events are expected. The spatial median of total number of months in drought for RCP8.5 increases more than 3 fold while the spatial median for mean drought duration exceeds 12 months, while in present conditions is lower than 5 months. The biggest change is linked to the fraction area in extreme drought (SPEI bellow -2) which increases 44 times relatively to present conditions (from 0.6% to 29%). This implies that extreme events will be more likely over time and space, while moderate to severe events will occur approximately with the same frequency as in the present climate.

To better asses the link between temperature and soil moisture or evapotranspiration, a new coupling metric for shorter time scales is proposed; the Latent Heat Flux-Temperature Coupling Magnitude (LETCM) and is computed from the Maximum Temperature and a Latent Heat Flux Magnitude. Areas with positive magnitude values imply higher temperature anomaly, due to a negative latent heat flux anomaly. This metric is implemented here for known heat wave periods, already assessed in Russo et al. (2016). Strong coupling regions observed in LETCM correspond well to areas of negative mean SPEI values, namely over regions where evapotranspiration is constrained by the available water. In some regions, a drought event might not be strong enough for evapotranspiration be restrained by soil moisture deficits, whereas in other regions, negative soil moisture anomalies don't necessarily imply a drought event. This influence of drought on temperatures over transition climates has been assessed in the past for Europe for the 2003 and 2010 heat wave events. (Fischer et al., 2007a; 2007b; Fischer and Schär. 2010; Miralles et al., 2012; 2014; Hauser et al., 2016). While this metric can distinguish between periods of strong and weak coupling, it doesn't provide information if a specific heat wave period could be caused or intensified by a drought event, even if analysed at the daily scale. If surface or root-zone soil moisture is available, LETCM could be computed with one of these variables instead of the latent heat flux. In this form, anomalies in soil moisture can be directly compared against temperature anomalies.

From the research path and the results obtained in this thesis many issues and questions emerged. An important step for the evaluation of the models coupling strength is its confrontation against observations. However, the available ground-based observations over Africa is very limited, moreover the ones related to soil properties. For example, regarding surface fluxes only three FLUXNET stations for the entire African mainland are available. Only recently satellite based observations are becoming a solid option for validating models. In what regards to other coupling metrics, the soil moisture-temperature coupling metric, at the seasonal and daily scales, proposed by Miralles et al. (2012) was attempted. For some reason this metric failed, as high coupling values were found over desert areas, which probably could be due to the potential evapotranspiration computation. As an alternative, the magnitudes (MT, MH and LETCM) were computed to assess known heat wave periods. Also, for better

results, SPEI index can be computed with the use of an empirical cumulative distribution function (ECDF) instead of a Log-Logistic CDF. Another problem is the validation of SPEI results due to the different way it was computed for modelled data and for CRU database.

For future works, HIRHAM5 NORESM1-M RCM model is not recommend due to large biases and poor performance relatively to other models. RCA4 MK3-6-0, with wrong soil moisture values should also be excluded from a future analysis. Finally, the Latent Heat Flux Temperature Coupling Magnitude (LETCM) can be expanded to all models and periods, to assess changes in the future strongest heat wave events compared to the strongest event of the recent past.

# References


AghaKouchak, A., L. Cheng, O.Mazdiyasni, and A. Farahmand (2014), Global warming and changes in risk of concurrent climate extremes: Insights from the 2014 California drought, Geophys. Res. Lett., 41, 8847–8852, doi:10.1002/2014GL062308.

Ahmad, M. I., Sinclair, C. D., & Werritty, A. (1988). Log-logistic flood frequency analysis. Journal of Hydrology, 98(3-4), 205-224.

Akinremi, O. O., McGinn, S. M., & Barr, A. G. (1996). Evaluation of the Palmer drought index on the Canadian prairies. Journal of Climate, 9(5), 897-905.

Alley, W. M. (1984). The Palmer drought severity index: limitations and assumptions. Journal of climate and applied meteorology, 23(7), 1100-1109.

Armstrong, R. L., Brodzik, M. J., Knowles, K., & Savoie, M. (2005). Global monthly EASE-Grid snow water equivalent climatology. Boulder, CO: National Snow and Ice Data Center, Digital media.

Asquith, W. H. (2011). Distributional analysis with L-moment statistics using the R environment for statistical computing (2nd printing). Lubbock, Texas: Create Space Independent Publishing Platform.

Baldocchi, D., Falge, E., Gu, L., Olson, R., Hollinger, D., Running, S., ... & Fuentes, J. (2001). FLUXNET: A new tool to study the temporal and spatial variability of ecosystem–scale carbon dioxide, water vapor, and energy flux densities. Bulletin of the American Meteorological Society, 82, 2415-2434.

Beck, H. E., van Dijk, A. I., Levizzani, V., Schellekens, J., Miralles, D. G., Martens, B., & de Roo, A. (2017). MSWEP: 3-hourly 0.25 global gridded precipitation (1979-2015) by merging gauge, satellite, and reanalysis data. Hydrology and Earth System Sciences, 21(1), 589-615.

Beguería, S., Vicente-Serrano, S. M., Reig, F., & Latorre, B. (2014). Standardized precipitation evapotranspiration index (SPEI) revisited: parameter fitting, evapotranspiration models, tools, datasets and drought monitoring. International Journal of Climatology, 34(10), 3001-3023.

Black, E., Blackburn, M., Harrison, G., Hoskins, B., & Methven, J. (2004). Factors contributing to the summer 2003 European heatwave. Weather, 59(8), 217-223.

Buontempo, C., Mathison, C., Jones, R., Williams, K., Wang, C., & McSweeney, C. (2015). An ensemble climate projection for Africa. Climate dynamics, 44(7-8), 2097-2118.

Burrough, S. L., & Thomas, D. S. G. (2013). Central southern Africa at the time of the African Humid Period: a new analysis of Holocene palaeoenvironmental and palaeoclimate data. Quaternary Science Reviews, 80, 29-46.

Chang, T. J., & Kleopa, X. A. (1991). A proposed method for drought monitoring. Journal of the American Water Resources Association, 27(2), 275-281.

Christy, J. R., Norris, W. B., & McNider, R. T. (2009). Surface temperature variations in East Africa and possible causes. Journal of Climate, 22(12), 3342-3356.

Collins, J. M. (2011). Temperature variability over Africa. Journal of Climate, 24(14), 3649-3666.

Coumou, D., & Rahmstorf, S. (2012). A decade of weather extremes. Nature Climate Change, 2(7), 491-496.

Dai A. Drought under global warming: A review. WIREs Clim Change, 2011, 2: 45–65

Dai A. Increasing drought under global warming in observations and models. Nat Clim Change, 2013, 3: 52–58

De Wit, M., & Stankiewicz, J. (2006). Changes in surface water supply across Africa with predicted climate change. Science, 311(5769), 1917-1921.

Decker, M., Pitman, A., & Evans, J. (2015). Diagnosing the seasonal land–atmosphere correspondence over northern Australia: dependence on soil moisture state and correspondence strength definition. Hydrology and Earth System Sciences, 19(8), 3433-3447.

Dee DP, Uppala SM, Simmons AJ, Berrisford P, Poli P, Kobayashi S, Andrae U, Balmaseda MA, Balsamo G, Bauer P, Bechtold P, Beljaars ACM, van de Berg L, Bidlot J, Bormann N, Delsol C, Dragani R, Fuentes M, Geer AJ, Haimberger L, Healy SB, Hersbach H, Hólm EV, Isaksen L, Kållberg P, Köhler M, Matricardi M, McNally AP, Monge-Sanz BM, Morcrette JJ, Park BK, Peubey C, de Rosnay P, Tavolato C, Thépaut JN, Vitart F. 2011. The ERA-Interim reanalysis: configuration and performance of the data assimilation system. Q J Roy Meteorol Soc 137:553–597. doi:10.1002/qj.828

Dirmeyer, P. A. (2011). The terrestrial segment of soil moisture–climate coupling. Geophysical Research Letters, 38(16), L16702.

Droogers, P., & Allen, R. G. (2002). Estimating reference evapotranspiration under inaccurate data conditions. Journal of Irrigation and Drainage Systems, 16(1), 33-45.

Easterling, D. R., Evans, J. L., Groisman, P. Y., Karl, T. R., Kunkel, K. E., & Ambenje, P. (2000). Observed variability and trends in extreme climate events: a brief review. Bulletin of the American Meteorological Society, 81(3), 417-425.

Easterling, D. R., Meehl, G. A., Parmesan, C., Changnon, S. A., Karl, T. R., & Mearns, L. O. (2000). Climate extremes: observations, modeling, and impacts. science, 289(5487), 2068-2074.

Findell, K. L., Gentine, P., Lintner, B. R., & Kerr, C. (2011). Probability of afternoon precipitation in eastern United States and Mexico enhanced by high evaporation. Nature Geoscience, 4(7), 434-439.

Fischer, E. M., & Schär, C. (2010). Consistent geographical patterns of changes in high-impact European heatwaves. Nature Geoscience, 3(6), 398-403.

Fischer, E. M., Seneviratne, S. I., Vidale, P. L., Lüthi, D., & Schär, C. (2007a). Soil moisture–atmosphere interactions during the 2003 European summer heat wave. Journal of Climate, 20(20), 5081-5099.

Fischer, E. M., Seneviratne, S. I., Lüthi, D., & Schär, C. (2007b). Contribution of land-atmosphere coupling to recent European summer heat waves. Geophysical Research Letters, 34(6),L06107.

Fontaine, B., Janicot, S., & Monerie, P. A. (2013). Recent changes in air temperature, heat waves occurrences, and atmospheric circulation in Northern Africa. Journal of Geophysical Research: Atmospheres, 118(15), 8536-8552.
Frich P, Alexander LV, Della-Marta P, Gleason B, Haylock M, Klein Tank AMG, Peterson T (2002) Observed coherent changes in climatic extremes during the second half of the twentieth century. Clim Res 19:193–212. doi:10.3354/cr019193
Giorgi, F., Jones, C., & Asrar, G. R. (2009). Addressing climate information needs at the regional level: the CORDEX framework. World Meteorological Organization (WMO) Bulletin, 58(3), 175-183.
Greenwood, J. A., Landwehr, J. M., Matalas, N. C., & Wallis, J. R. (1979). Probability weighted moments: definition and relation to parameters of several distributions expressable in inverse form. Water Resources Research, 15(5), 1049-1054.
Guttman, N. B. (1998). Comparing the Palmer drought index and the standardized precipitation index. Journal of the American Water Resources Association, 34(1), 113-121.
Hargreaves, G. L., Hargreaves, G. H., & Riley, J. P. (1985). Agricultural benefits for Senegal River basin. Journal of Irrigation and Drainage Engineering, 111(2), 113-124.
Harris, I., Jones, P. D., Osborn, T. J., & Lister, D. H. (2014). Updated high-resolution grids of monthly climatic observations–the CRU TS3. 10 Dataset. International Journal of Climatology, 34(3), 623-642.
Harris, I. C., & Jones, P. D. (2017). CRU TS4.00: Climatic Research Unit (CRU) Time-Series (TS) version 4.00 of high resolution gridded data of month-by-month variation in climate (Jan. 1901-Dec. 2015). University of East Anglia Climatic Research Unit (CRU), Centre for Environmental Data Analysis.Heim Jr, R. R. (2002). A review of twentieth-century drought indices used in the United States. Bulletin of the American Meteorological Society, 83(8), 1149-1165.
Heim Jr, R. R. (2002). A review of twentieth-century drought indices used in the United States. Bulletin of the American Meteorological Society, 83(8), 1149-1165.
Hernández-Díaz, L., Laprise, R., Sushama, L., Martynov, A., Winger, K., & Dugas, B. (2013). Climate simulation over CORDEX Africa domain using the fifth-generation Canadian Regional Climate Model (CRCM5). Climate Dynamics, 40(5/6), 1415-1433.
Hirschi, M., Seneviratne, S. I., Alexandrov, V., Boberg, F., Boroneant, C., Christensen, O. B., ... & Stepanek, P. (2011). Observational evidence for soil-moisture impact on hot extremes in southeastern Europe. Nature Geoscience, 4(1), 17.
Hosking, J. R. (1990). L-moments: analysis and estimation of distributions using linear combinations of order statistics. Journal of the Royal Statistical Society. Series B (Methodological), 52(1), 105-124.
Hulme, M., Doherty, R., Ngara, T., New, M., & Lister, D. (2001). African climate change: 1900–2100. Climate Research, 17(2), 145-168.
IPCC (2012). Managing the Risks of Extreme Events and Disasters to Advance Climate Change Adaptation. A Special Report of Working Groups I and II of the Intergovernmental Panel on Climate Change. C. B. Field et al. (Ed.) Cambridge University Press, Cambridge, UK, and New York, NY, USA, 582 pp.
IPCC (2014). Climate Change 2014: Impacts, Adaptation, and Vulnerability: B. Regional Aspects. Contribution of Working Group II to the Fifth Assessment Report of the Intergovernmental Panel on Climate Change. C. B. Field et al. (Ed.) Cambridge University Press, Cambridge, United Kingdom and New York, NY, USA, 1132 pp.
Jones, P., & Harris, I. (2008). CRU Time Series (TS) high resolution gridded datasets. University of East Anglia Climatic Research Unit (CRU). Available at https://iridl.ldeo.columbia.edu/SOURCES/.UEA/.CRU/
Jones, P. D., & Moberg, A. (2003). Hemispheric and large-scale surface air temperature variations: An extensive revision and an update to 2001. Journal of Climate, 16(2), 206-223.
Jones, C., Nikulin, G., & Kjellström, E. (2012, April). Dynamical downscaling of CMIP5 GCM simulations over the Africa-CORDEX domain: Evaluating climate variability for the recent past. In EGU General Assembly Geophysical Research Abstracts (Vol. 14, p. 10251).
Jones, C., Nikulin, G., Gbobaniyi, E., & Kjellström, E. (2013, April). Precipitation variability in a suite of Africa-CORDEX simulations: The roles of model resolution, domain size and spectral nudging. In EGU General Assembly Geophysical Research Abstracts (Vol. 15, p. 7112-1).
Karl, T. R. (1983). Some spatial characteristics of drought duration in the United States. Journal of Climate and Applied Meteorology, 22(8), 1356-1366.
Kim, J., Waliser, D. E., Mattmann, C. A., Goodale, C. E., Hart, A. F., Zimdars, P. A., ... & Jack, C. (2014). Evaluation of the CORDEX-Africa multi-RCM hindcast: systematic model errors. Climate Dynamics, 42(5-6), 1189-1202.
Knist, S., Goergen, K., Buonomo, E., Christensen, O. B., Colette, A., Cardoso, R. M., ... & Kartsios, S. (2017). Land-atmosphere coupling in EURO-CORDEX evaluation experiments. Journal of Geophysical Research: Atmospheres, 122(1), 79-103.
Koster, R. D., Dirmeyer, P. A., Hahmann, A. N., Ijpelaar, R., Tyahla, L., Cox, P., & Suarez, M. J. (2002). Comparing the degree of land–atmosphere interaction in four atmospheric general circulation models. Journal of Hydrometeorology, 3(3), 363-375.
Koster, R. D., Dirmeyer, P. A., Guo, Z., Bonan, G., Chan, E., Cox, P., ... & Liu, P. (2004). Regions of strong coupling between soil moisture and precipitation. Science, 305(5687), 1138-1140.
Koster, R. D., Sud, Y. C., Guo, Z., Dirmeyer, P. A., Bonan, G., Oleson, K. W., ... & Kowalczyk, E. (2006). GLACE: the global land–atmosphere coupling experiment. Part I: overview. Journal of Hydrometeorology, 7(4), 590-610.
Kruger, A. C., & Shongwe, S. (2004). Temperature trends in South Africa: 1960–2003. International journal of Climatology, 24(15), 1929-1945.
Lennard, C., & Kalognoumou, L. (2013, April). Analysis of the Cordex evaluation runs (ERA_Interim) over Southern Africa. In EGU General Assembly Geophysical Research Abstracts (Vol. 15, p. 200-1).
León, M., González, Y., Díaz, J. P., Expósito, F. J., Pérez, J. C., & González, A. (2012, April). Intercomparison of IPCC AR4 models with ERA-40 and NCEP/NCAR reanalysis within the AFRICA-CORDEX domain. In EGU General Assembly Geophysical Research Abstracts (Vol. 14, p. 8662).

Liu, Y. Y., de Jeu, R. A., McCabe, M. F., Evans, J. P., & van Dijk, A. I. (2011). Global long-term passive microwave satellite-based retrievals of vegetation optical depth. Geophysical Research Letters, 38(18). L18402

Lockwood, J. G. (1999). Is potential evapotranspiration and its relationship with actual evapotranspiration sensitive to elevated atmospheric CO2 levels?. Climatic Change, 41(2), 193-212.

Lorenz, R., Pitman, A. J., Hirsch, A. L., & Srbinovsky, J. (2015). Intraseasonal versus interannual measures of land–atmosphere coupling strength in a global climate model: GLACE-1 versus GLACE-CMIP5 experiments in ACCESS1. 3b. Journal of Hydrometeorology, 16(5), 2276-2295.

Martens, B., Miralles, D., Lievens, H., Fernández-Prieto, D., & Verhoest, N. E. (2016). Improving terrestrial evaporation estimates over continental Australia through assimilation of SMOS soil moisture. International Journal of Applied Earth Observation and Geoinformation, 48, 146-162.

Martens, B., Gonzalez Miralles, D., Lievens, H., van der Schalie, R., de Jeu, R. A., Fernández-Prieto, D., ... & Verhoest, N. (2017). GLEAM v3: Satellite-based land evaporation and root-zone soil moisture. Geoscientific Model Development, 10(5), 1903-1925.

Mavromatis, T. (2007). Drought index evaluation for assessing future wheat production in Greece. International Journal of Climatology, 27(7), 911-924.

McKee, T. B., Doesken, N. J., & Kleist, J. (1993, January). The relationship of drought frequency and duration to time scales. In Proceedings of the 8th Conference on Applied Climatology (Vol. 17, No. 22, pp. 179-183). Boston, MA: American Meteorological Society.

Meehl, G. A., & Tebaldi, C. (2004). More intense, more frequent, and longer lasting heat waves in the 21st century. Science, 305(5686), 994-997.

Min, S. K., Zhang, X., Zwiers, F. W., & Hegerl, G. C. (2011). Human contribution to more-intense precipitation extremes. Nature, 470(7334), 378-381.

Miralles, D. G., van den Berg, M. V., Teuling, A. J., & Jeu, R. D. (2012). Soil moisture-temperature coupling: A multiscale observational analysis. Geophysical Research Letters, 39(21).

Miralles, D. G., Gash, J. H., Holmes, T. R., de Jeu, R. A., & Dolman, A. J. (2010). Global canopy interception from satellite observations. Journal of Geophysical Research: Atmospheres, 115. D16122.

Miralles, D. G., Holmes, T. R. H., de Jeu, R. A. M., Gash, J. H., Meesters, A. G. C. A., & Dolman, A. J. (2011a). Global land-surface evaporation estimated from satellite-based observations. Hydrology and Earth System Sciences, 15, 967-981.

Miralles, D. G., de Jeu, R. A. M., Gash, J. H., Holmes, T. R. H., & Dolman, A. J. (2011b). Magnitude and variability of land evaporation and its components at the global scale. Hydrology and Earth Systems Sciences, 15, 967-981

Miralles, D. G., Teuling, A. J., van Heerwaarden, C. C., & de Arellano, J.V.G. (2014). Mega-heatwave temperatures due to combined soil desiccation and atmospheric heat accumulation. Nature geoscience, 7(5), 345-349.

Monteith, J. L. (1965), Evaporation and environment. In: B. D. Fogg, (Ed.), The state and movement of water in living organism. Proceedings of 19.º Symposium of the Society of Experimental Biology (pp. 205-234), New York: Cambridge University Press.

Moss RH, Edmonds JA et al (2010) The next generation of scenarios for climate change research and assessment. Nature 463(7282):747–756

Nikulin, G., Jones, C., Giorgi, F., Asrar, G., Büchner, M., Cerezo-Mota, R., ... & van Meijgaard, E. (2012). Precipitation climatology in an ensemble of CORDEX-Africa regional climate simulations. Journal of Climate, 25(18), 6057-6078.

Palmer, W. C. (1965). Meteorological drought (Vol. 30). Washington, DC: US Department of Commerce, Weather Bureau.

Panitz, H. J., Dosio, A., Büchner, M., Lüthi, D., & Keuler, K. (2014). COSMO-CLM (CCLM) climate simulations over CORDEX-Africa domain: analysis of the ERA-Interim driven simulations at 0.44 and 0.22 resolution. Climate Dynamics, 42(11-12), 3015-3038.

Peel, M. C., Finlayson, B. L., & McMahon, T. A. (2007). Updated world map of the Köppen-Geiger climate classification. Hydrology and Earth System Sciences Discussions, 4(2), 439-473.

Perkins SE, Alexander LV, Nairn JR (2012) Increasing frequency, intensity and duration of observed global heatwaves and warm spells. Geophys Res Lett 39:1–5. doi:10.1029/2012GL053361

Priestley, C. H. B. and Taylor, R. J. (1972). On the assessment of surface heat flux and evaporation using large-scale parameters. Monthly Weather Review, 100(2), 81–92.

Ramos, A. M., Trigo, R. M., & Santo, F. E. (2011). Evolution of extreme temperatures over Portugal: recent changes and future scenarios. Climate Research, 48(2/3), 177-192.

Robinson, P. J. (2001). On the definition of a heat wave. Journal of applied Meteorology, 40(4), 762-775.

Rhee, J., & Cho, J. (2016). Future changes in drought characteristics: regional analysis for South Korea under CMIP5 projections. Journal of Hydrometeorology, 17(1), 437-451.

Russo, S., Dosio, A., Graversen, R. G., Sillmann, J., Carrao, H., Dunbar, M. B., ... & Vogt, J. V. (2014). Magnitude of extreme heat waves in present climate and their projection in a warming world. Journal of Geophysical Research: Atmospheres, 119(22), 12500-12512.

Russo, S., Sillmann, J., & Fischer, E. M. (2015). Top ten European heatwaves since 1950 and their occurrence in the coming decades. Environmental Research Letters, 10(12), 124003.

Russo, S., Marchese, A. F., Sillmann, J., & Immé, G. (2016). When will unusual heat waves become normal in a warming Africa?. Environmental Research Letters, 11(5), 054016.

Sanderson, M. G., Hemming, D. L., & Betts, R. A. (2011). Regional temperature and precipitation changes under high-end (≥ 4 C) global warming. Philosophical Transactions of the Royal Society of London A: Mathematical, Physical and Engineering Sciences, 369(1934), 85-98.

Schär, C., Vidale, P. L., Luthi, D., Frei, C., Häberlin, C., Liniger, M. A., & Appenzeller, C. (2004). The role of increasing temperature variability in European summer heatwaves. Nature, 427(6972), 332-336.

Schreck, C. J., & Semazzi, F. H. (2004). Variability of the recent climate of eastern Africa. International Journal of Climatology, 24(6), 681-701.
Serdeczny, O., Adams, S., Baarsch, F., Coumou, D., Robinson, A., Hare, W., ... & Reinhardt, J. (2017). Climate change impacts in Sub-Saharan Africa: from physical changes to their social repercussions. Regional Environmental Change, 17(6), 1585-1600.
Seneviratne, S. I., Lüthi, D., Litschi, M., & Schär, C. (2006). Land-atmosphere coupling and climate change in Europe. Nature, 443(7108), 205-209.
Seneviratne, S. I., Corti, T., Davin, E. L., Hirschi, M., Jaeger, E. B., Lehner, I., ... & Teuling, A. J. (2010). Investigating soil moisture–climate interactions in a changing climate: A review. Earth-Science Reviews, 99(3), 125-161.
Shongwe, M. E., van Oldenborgh, G. J., van den Hurk, B. J. J. M., de Boer, B., Coelho, C. A. S., & van Aalst, M. K. (2009). Projected changes in mean and extreme precipitation in Africa under global warming. Part I: Southern Africa. Journal of Climate, 22(13), 3819-3837.
Shongwe, M. E., van Oldenborgh, G. J., van den Hurk, B., & van Aalst, M. (2011). Projected changes in mean and extreme precipitation in Africa under global warming. Part II: East Africa. Journal of Climate, 24(14), 3718-3733.Soulé, P. T. (1992). Spatial patterns of drought frequency and duration in the contiguous USA based on multiple drought event definitions. International Journal of Climatology, 12(1), 11-24.
Schulzweida, U., Kornblueh, L., & Quast, R. (2006). CDO user's guide. Climate Data Operators, Version, 1(6).
Stedinger, J. R. (1993). Frequency analysis of extreme events. Handbook of hydrology, 18.
Stull, R. B. (1988). An Introduction to Boundary Layer Meteorology. Dordrecht, Boston, London: Kluwer Academic Publishers.
Taylor, K. E. (2001). Summarizing multiple aspects of model performance in a single diagram. Journal of Geophysical Research: Atmospheres, 106 (D7), 7183- 7192.
Teuling, A. J., Seneviratne, S. I., Stöckli, R., Reichstein, M., Moors, E., Ciais, P., ... & Dellwik, E. (2010). Contrasting response of European forest and grassland energy exchange to heatwaves. Nature Geoscience, 3(10), 722.
Thornthwaite, C. W. (1948). An approach toward a rational classification of climate. Geographical Review, 38(1), 55-94.
Trenberth, K. E., Dai, A., Van der Schrier, G., Jones, P. D., Barichivich, J., Briffa, K. R., & Sheffield, J. (2014). Global warming and changes in drought. Nature Climate Change, 4(1), 17-22.
Vautard, R., Gobiet, A., Jacob, D., Belda, M., Colette, A., Déqué, M., ... & Halenka, T. (2013). The simulation of European heat waves from an ensemble of regional climate models within the EURO-CORDEX project. Climate Dynamics, 41(9-10), 2555-2575.
Vautard, R., P. Yiou, F. D'Andrea, N. de Noblet, N. Viovy, C. Cassou, J. Polcher, P. Ciais, M. Kageyama, and Y. Fan (2007), Summertime European heat and drought waves induced by wintertime Mediterranean rainfall deficit, Geophys. Res. Lett., 34, L07711, doi:10.1029/2006GL028001
Vicente-Serrano, S. M. (2006). Differences in spatial patterns of drought on different time scales: an analysis of the Iberian Peninsula. Water Resources Management, 20(1), 37-60.
Vicente-Serrano, S. M., Beguería, S., & López-Moreno, J. I. (2010). A multiscalar drought index sensitive to global warming: the standardized precipitation evapotranspiration index. Journal of Climate, 23(7), 1696-1718.
Vicente-Serrano, S. M., Gouveia, C., Camarero, J. J., Beguería, S., Trigo, R., López-Moreno, J. I., ... & Morán-Tejeda, E. (2013). Response of vegetation to drought time-scales across global land biomes. Proceedings of the National Academy of Sciences, 110(1), 52-57.
Wang, H., Rogers, J. C., & Munroe, D. K. (2015). Commonly used drought indices as indicators of soil moisture in China. Journal of Hydrometeorology, 16(3), 1397-1408.
Wagner, W., Dorigo, W., de Jeu, R., Fernandez, D., Benveniste, J., Haas, E., & Ertl, M. (2012). Fusion of active and passive microwave observations to create an essential climate variable data record on soil moisture. ISPRS Annals of the Photogrammetry, Remote Sensing and Spatial Information Sciences (ISPRS Annals), 7, 315-321.
Weber, L., & Kkemdirim, L. (1998). Palmer's drought indices revisited. Geografiska Annaler: Series A, Physical Geography, 80(2), 153-172.
Wells, N., Goddard, S., & Hayes, M. J. (2004). A self-calibrating Palmer drought severity index. Journal of Climate, 17(12), 2335-2351.
Wilhite, D. A. (2000). Drought as a natural hazard: concepts and definitions. In: A. Donald and A. Wilhite, Eds., Drought: *A Global Assessment*, Routledge: New York, pp. 3-18.
Xoplaki, E., Gonzalez-Rouco, J. F., Luterbacher, J., & Wanner, H. (2003). Mediterranean summer air temperature variability and its connection to the large-scale atmospheric circulation and SSTs. Climate Dynamics, 20(7-8), 723-739.

# Annex

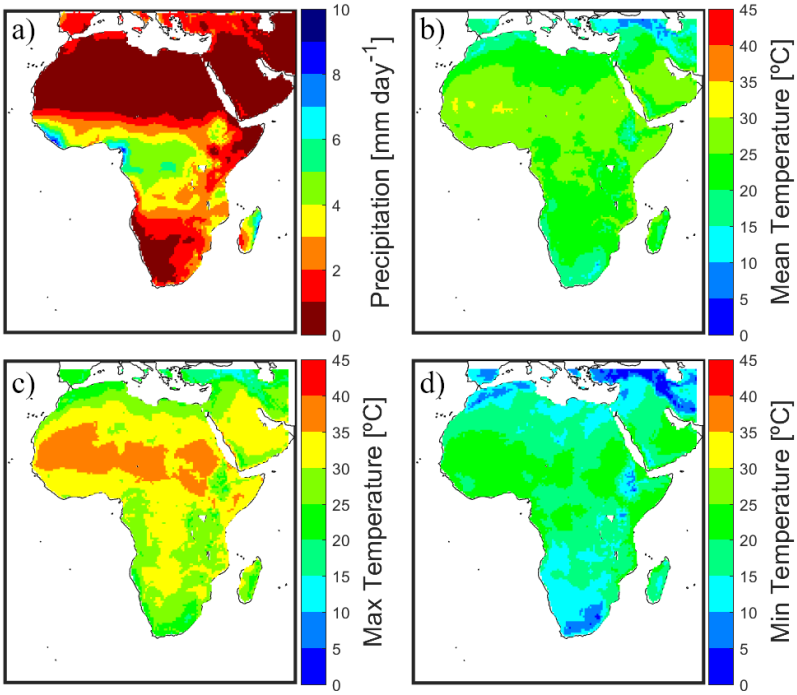


*Fig A.1.* (a) Climatological mean Precipitation in mm $day^{-1}$, (b) Mean Daily temperature in ºC, (b) Maximum Daily Temperature in ºC and (c) Minimum Daily Temperature in ºC, derived from the Climate Research Unit (CRU) gridded monthly data for the Hindcast period (1990 to 2008).

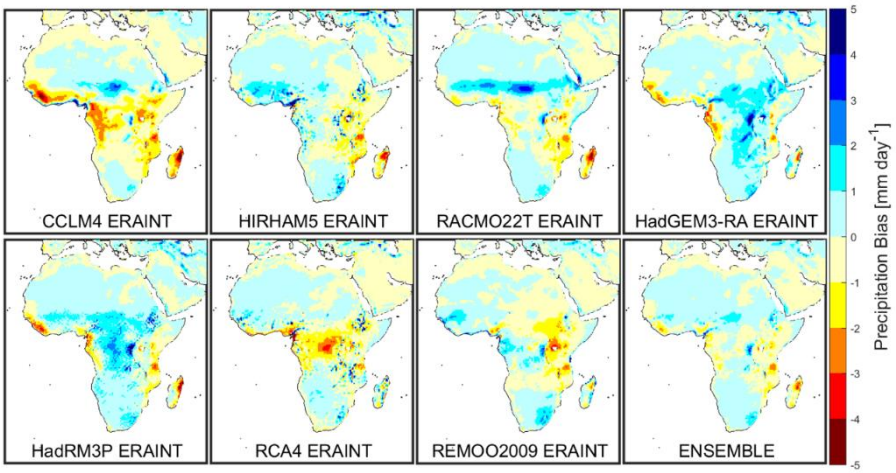


*Fig A.2.* Precipitation bias in mm $day^{-1}$ relative to CRU database (Figure 3.1a) for the climatological mean for Hindcast (1990-2008).

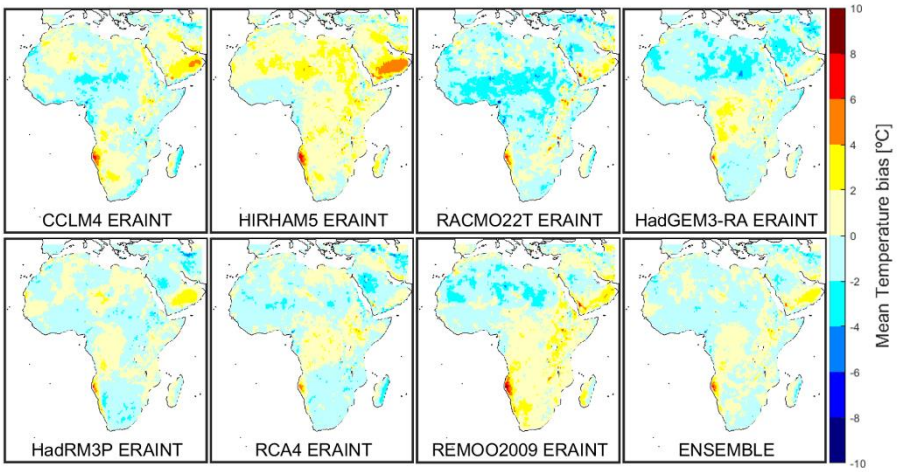


*Fig A.3.* Mean temperature bias in ºC relative to CRU database (Figure 3.1b) for the climatological mean for Hindcast (1990-2008).

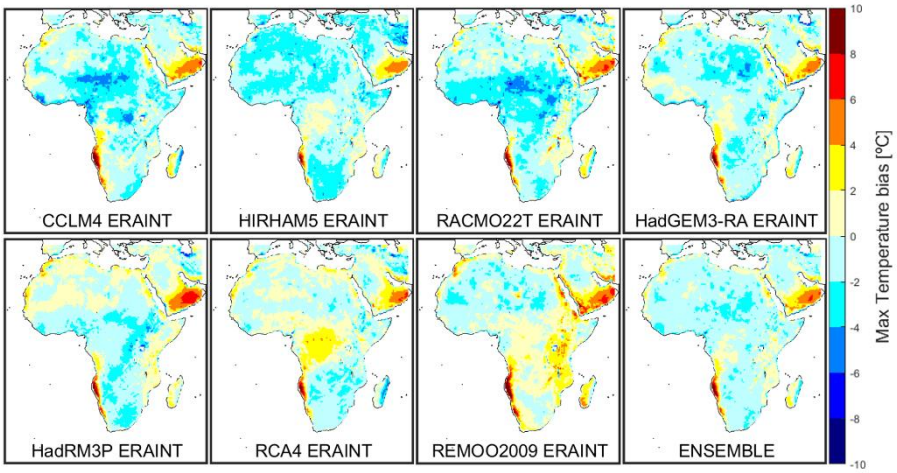


*Fig A.4.* Maximum temperature bias in ºC relative to CRU database (Figure 3.1c) for the climatological mean for Hindcast (1990-2008).

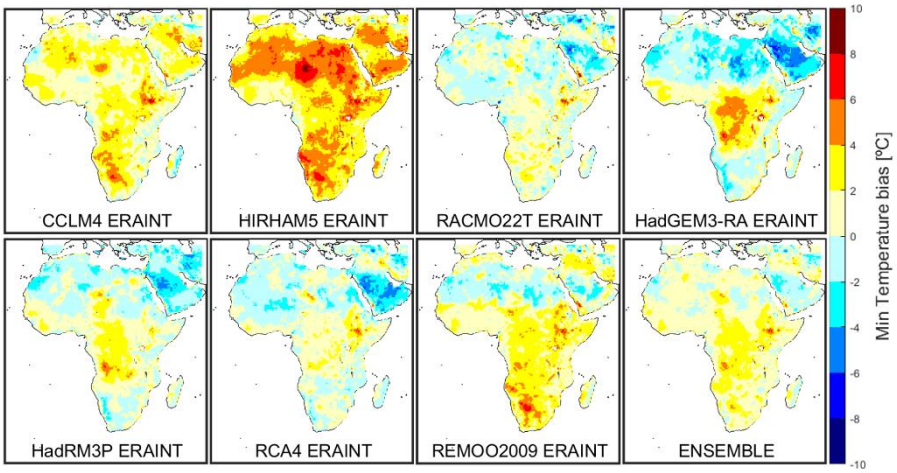


*Fig A.5.* Minimum temperature (TASMIN) bias in ºC relative to CRU database (Figure 3.1d) for the climatological mean for Hindcast (1990-2008).

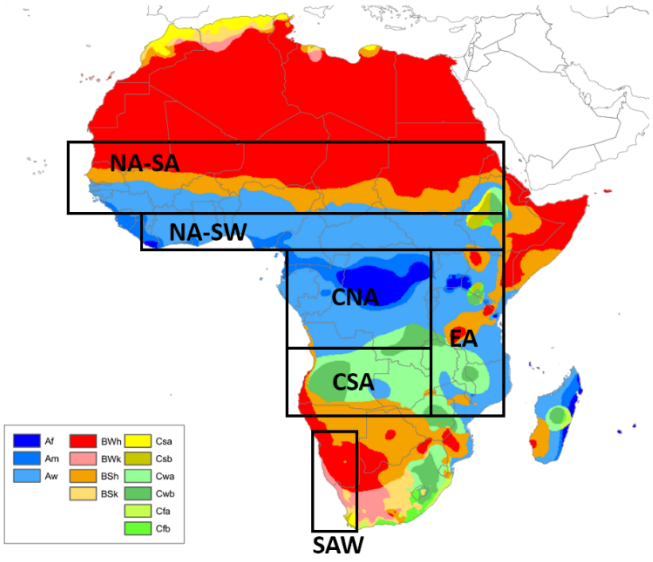


| 1st | 2nd | 3rd | Description | Criteria* |
|---|---|---|---|---|
| A | | | Tropical | $T_{cold} \geq 18$ |
| | f | | - Rainforest | $P_{dry} \geq 60$ |
| | m | | - Monsoon | Not (Af) & $P_{dry} \geq 100 - MAP/25$ |
| | w | | - Savannah | Not (Af) & $P_{dry} < 100 - MAP/25$ |
| B | | | Arid | $MAP < 10 \times P_{threshold}$ |
| | W | | - Desert | $MAP < 5 \times P_{threshold}$ |
| | S | | - Steppe | $MAP \geq 5 \times P_{threshold}$ |
| | | h | - Hot | $MAT \geq 18$ |
| | | k | - Cold | $MAT < 18$ |
| C | | | Temperate | $T_{hot} > 10$ & $0 < T_{cold} < 18$ |
| | s | | - Dry Summer | $P_{sdry} < 40$ & $P_{sdry} < P_{wwet}/3$ |
| | w | | - Dry Winter | $P_{wdry} < P_{swet}/10$ |
| | f | | - Without dry season | Not (Cs) or (Cw) |
| | | a | - Hot Summer | $T_{hot} \geq 22$ |
| | | b | - Warm Summer | Not (a) & $T_{mon10} \geq 4$ |
| | | c | - Cold Summer | Not (a or b) & $1 \leq T_{mon10} < 4$ |
| D | | | Cold | $T_{hot} > 10$ & $T_{cold} \leq 0$ |
| | s | | - Dry Summer | $P_{sdry} < 40$ & $P_{sdry} < P_{wwet}/3$ |
| | w | | - Dry Winter | $P_{wdry} < P_{swet}/10$ |
| | f | | - Without dry season | Not (Ds) or (Dw) |
| | | a | - Hot Summer | $T_{hot} \geq 22$ |
| | | b | - Warm Summer | Not (a) & $T_{mon10} \geq 4$ |
| | | c | - Cold Summer | Not (a, b or d) |
| | | d | - Very Cold Winter | Not (a or b) & $T_{cold} < -38$ |
| E | | | Polar | $T_{hot} < 10$ |
| | T | | - Tundra | $T_{hot} > 0$ |
| | F | | - Frost | $T_{hot} \leq 0$ |

*Fig A.6.* Regions localizations and climate types over Africa mainland and Madagascar island following the Köppen-Geiger climate classification. These regions were chosen based on land-atmosphere coupling results from Koster et al. (2006); Seneviratne et al (2010); Miralles et al. (2012) and Lorenz et al. (2015); and from the domains used by Hernández-Díaz et al. (2013) overlapped on Figure 4 from Peel et al. (2007).

*Table A.1.* Pearson correlations between Hindcast (1990-2008) total soil moisture and root-zone soil moisture taken from GLEAM database for the Africa-CORDEX focus domain and regions defined on Table 3.1 and Figure A.6.

| RCM | AFRICA | NA-SA | NA-SW | EA | CNA | CSA | SA-W |
|---|---|---|---|---|---|---|---|
| CCLM4 ERAINT | 0.5134 | 0.6703 | 0.3167 | 0.3841 | 0.6551 | 0.5290 | 0.4498 |
| HIRHAM5 ERAINT | 0.6560 | 0.7849 | -0.0151 | 0.3635 | -0.1122 | 0.1896 | 0.6070 |
| RACMO22T ERAINT | 0.6918 | 0.7033 | 0.4714 | 0.4219 | 0.5889 | 0.5539 | 0.1562 |
| HaDGEM3-RA ERAINT | 0.7608 | 0.7612 | 0.5021 | 0.5248 | 0.4260 | 0.7677 | 0.3422 |
| HadRM3P ERAINT | 0.8237 | 0.8336 | 0.3771 | 0.5724 | 0.5364 | 0.7920 | 0.4508 |
| RCA4 ERAINT | 0.6920 | 0.8759 | 0.5918 | 0.5911 | 0.6711 | 0.7801 | 0.7195 |
| REMOO2009 ERAINT | 0.7282 | 0.8264 | 0.0527 | 0.3176 | -0.1659 | 0.4305 | 0.5493 |
| ENSEMBLE HINDCAST | 0.8897 | 0.9117 | 0.5066 | 0.6981 | 0.8608 | 0.7652 | 0.7003 |

a)

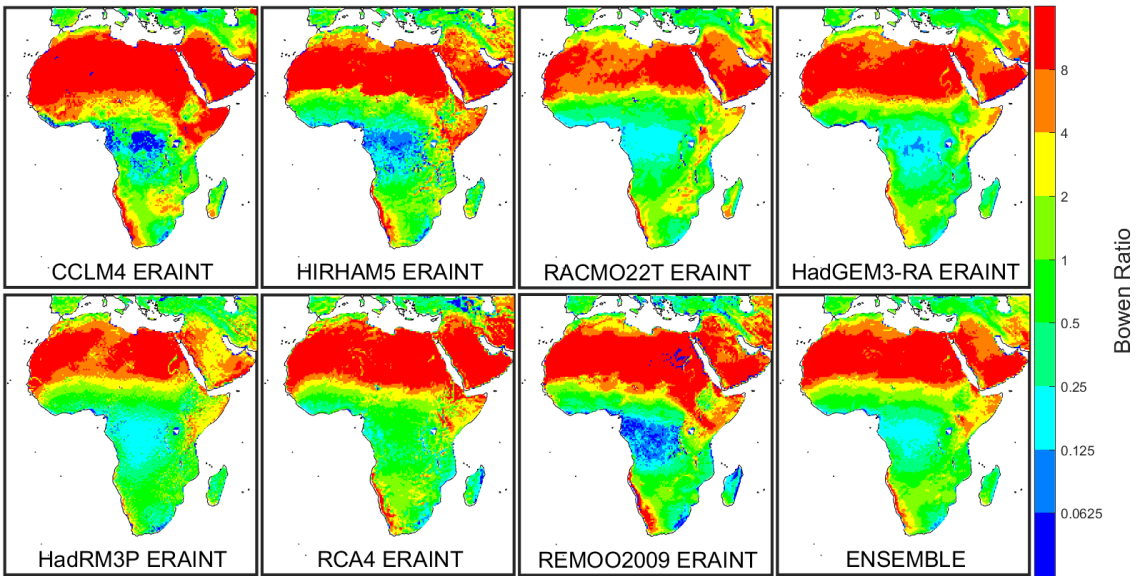


b)

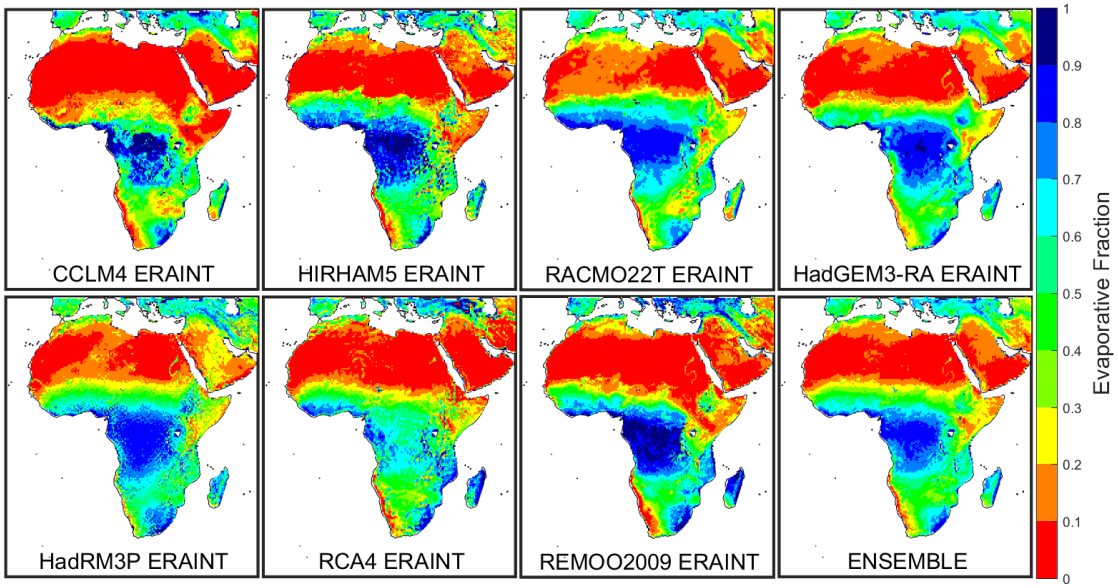


*Fig A.7.* MAM (a) Bowen ratio and (b) Evaporative Fraction for Hindcast (1990-2008).

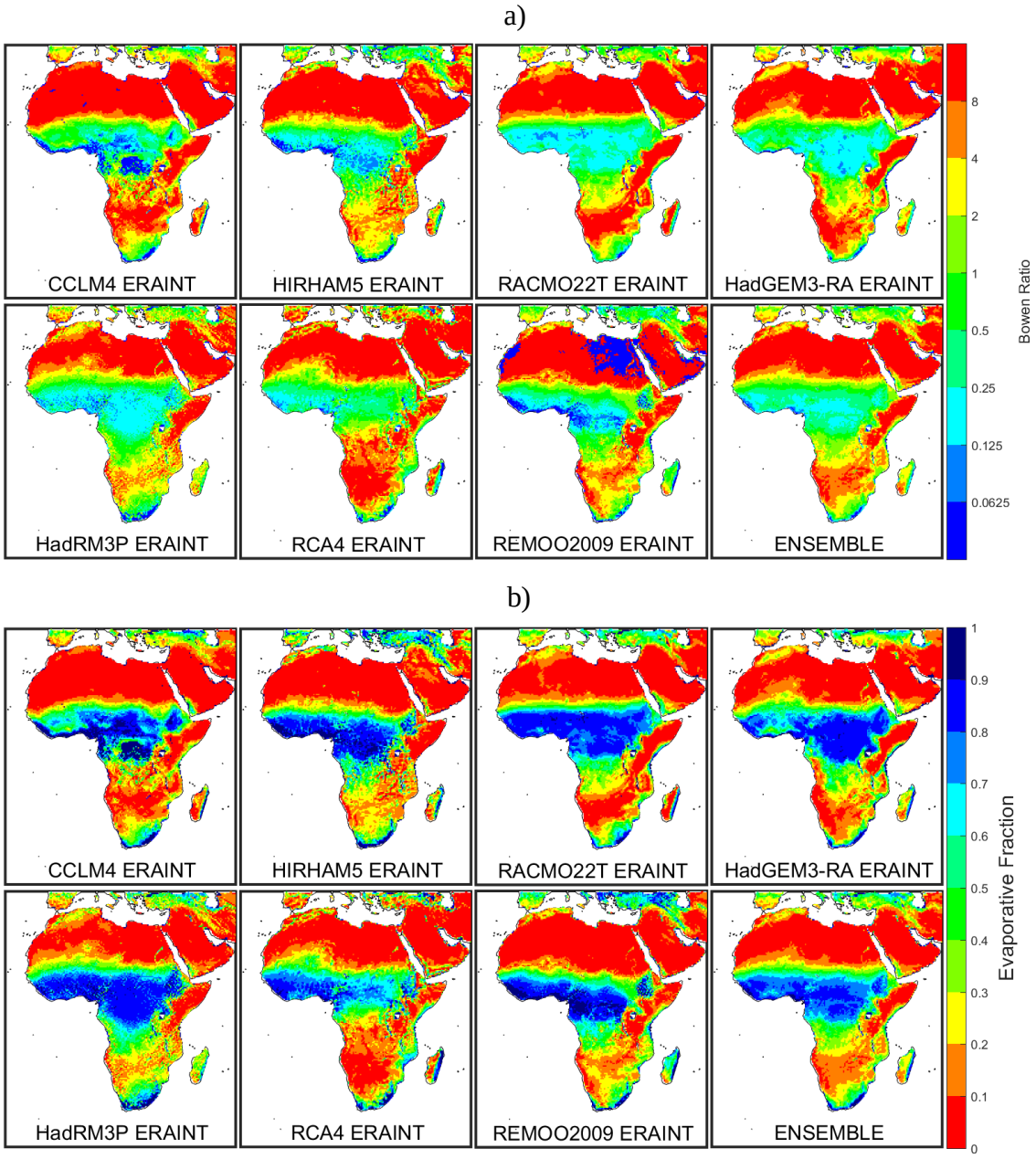


*Fig A.8* JJA (a) Bowen ratio and (b) Evaporative Fraction for Hindcast (1990-2008).

a)

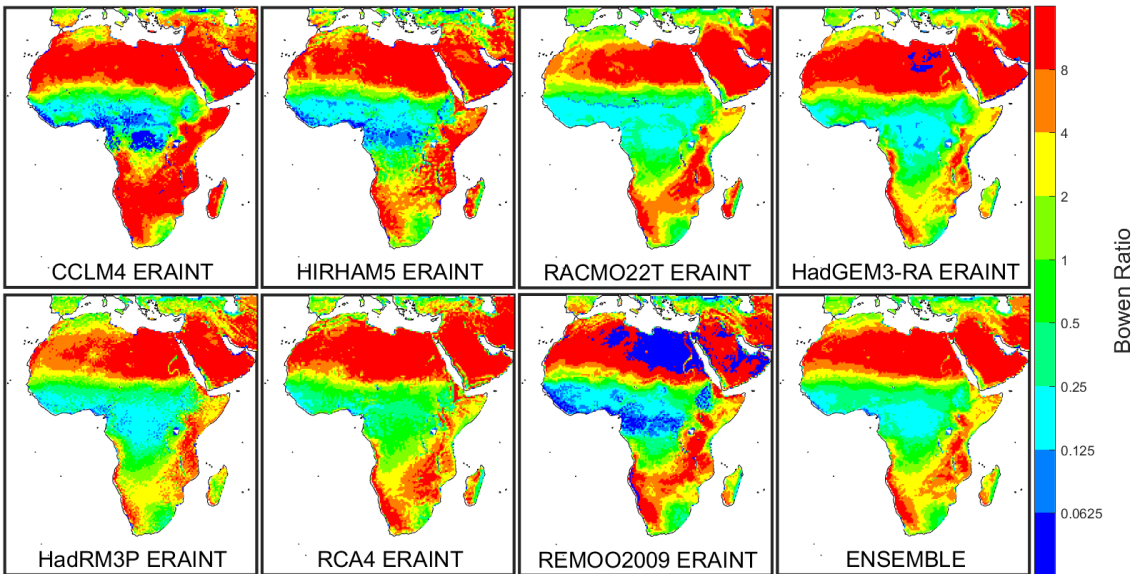


b)

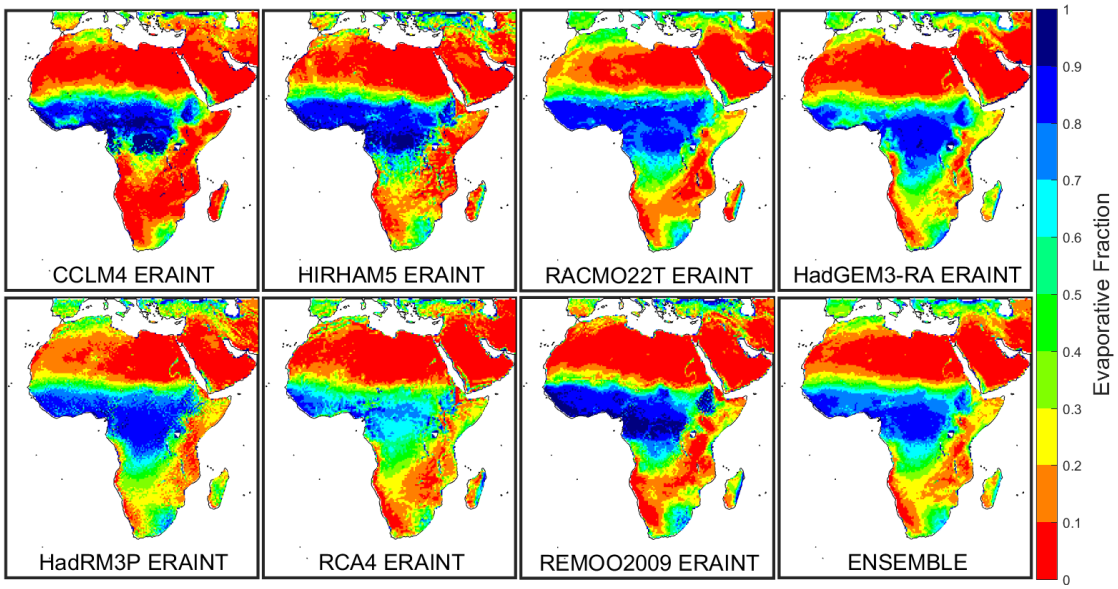


*Fig A.9.* SON (a) Bowen ratio and (b) Evaporative Fraction for Hindcast (1990-2008).

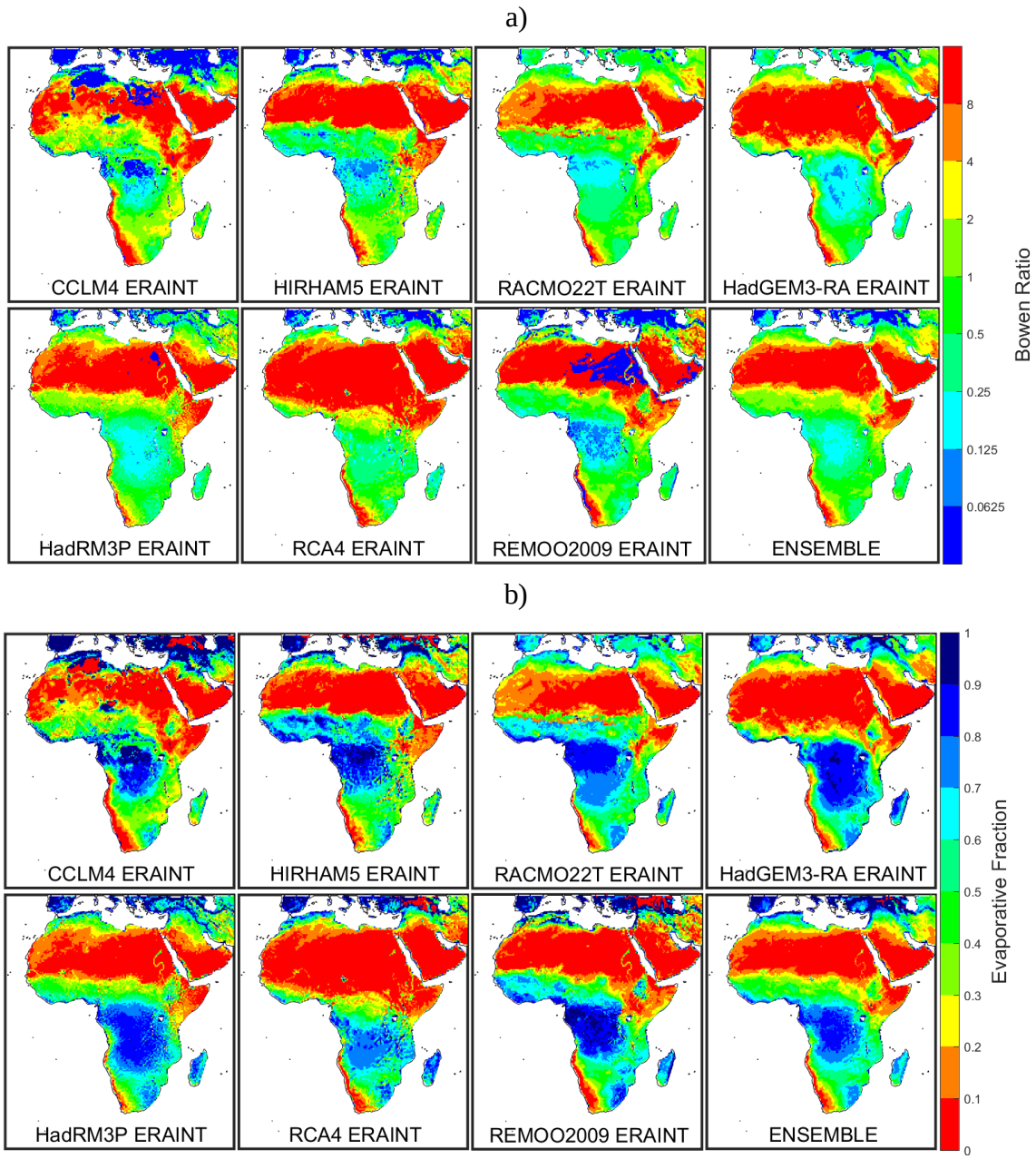


*Fig A.10.* DJF (a) Bowen ratio and (b) Evaporative Fraction for Hindcast (1990-2008).

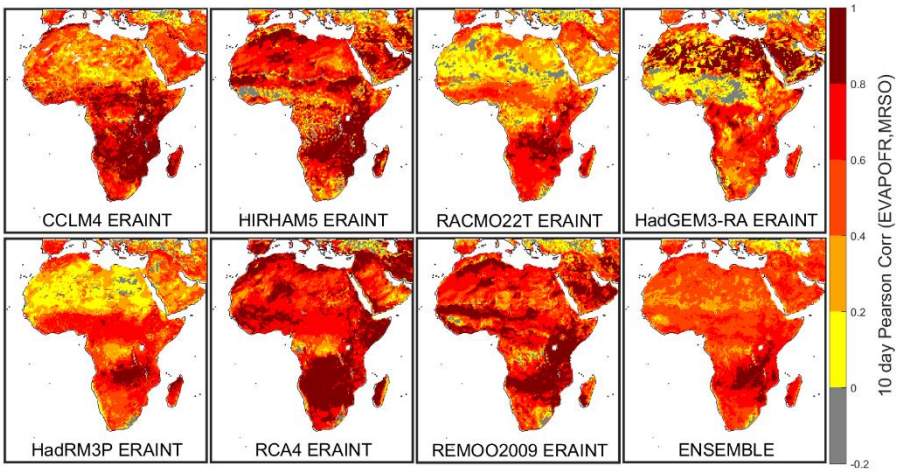


*Fig A.11.* MAM 10 days of nonoverlapping means correlation between MRSO and Evaporative Fraction (EVAPFR) for Hindcast (1990-2008). Values lower than 0 are depicted as gray.

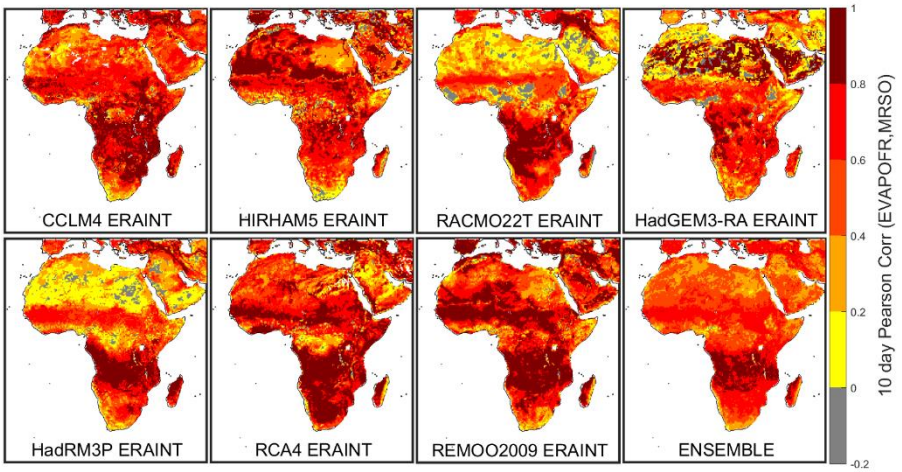


*Fig A.12.* JJA 10 days of nonoverlapping means correlation between MRSO and Evaporative Fraction (EVAPFR) for Hindcast (1990-2008). Values lower than 0 are depicted as gray.

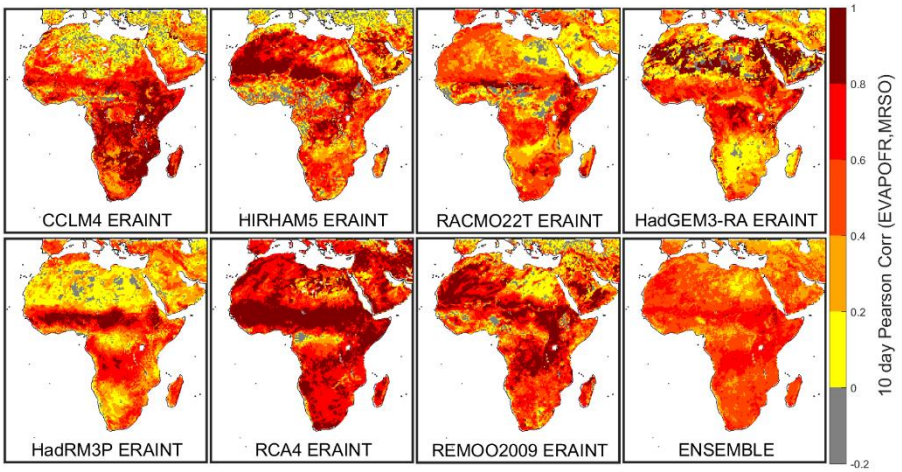


*Fig A.13.* SON 10 days of nonoverlapping means correlation between MRSO and Evaporative Fraction (EVAPFR) for Hindcast (1990-2008). Values lower than 0 are depicted as gray.

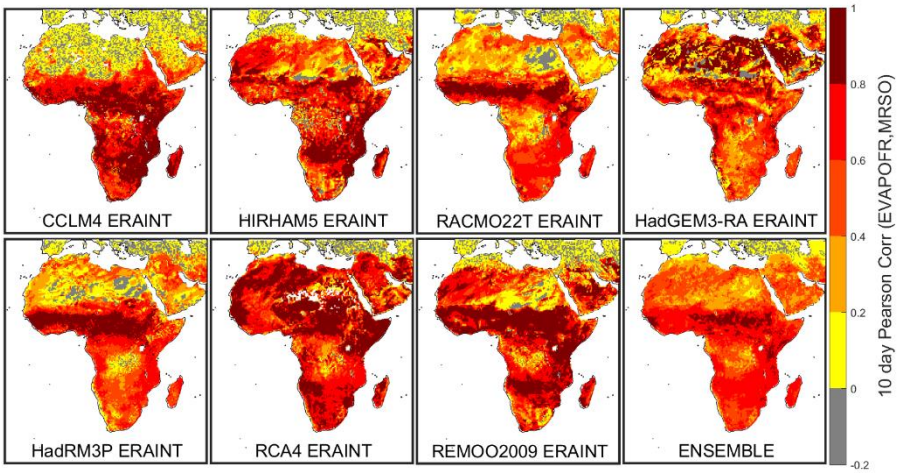


*Fig A.14.* DJF 10 days of nonoverlapping means correlation between MRSO and Evaporative Fraction (EVAPFR) for Hindcast (1990-2008). Values lower than 0 are depicted as gray.

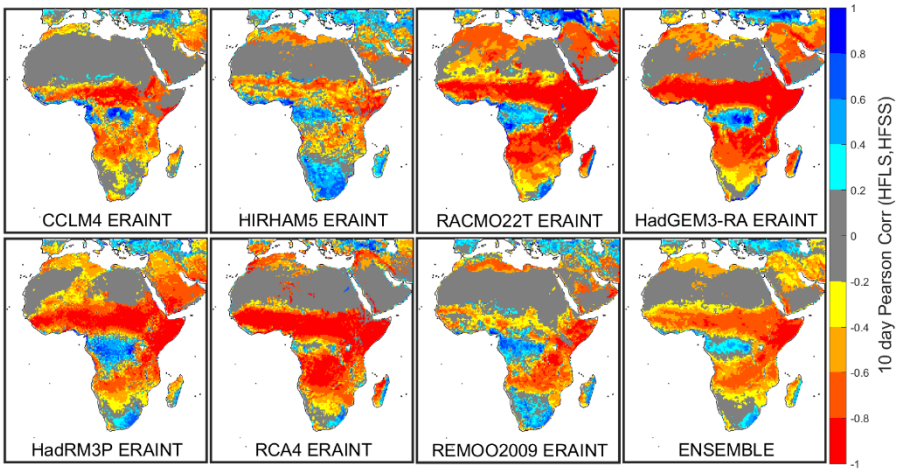


*Fig A.15.* MAM 10 days of nonoverlapping means correlation between HFLS and HFSS for Hindcast (1990-2008). Correlations below the 20% significance level and areas of low Evaporative Fraction (less than 0.1) are depicted as gray.

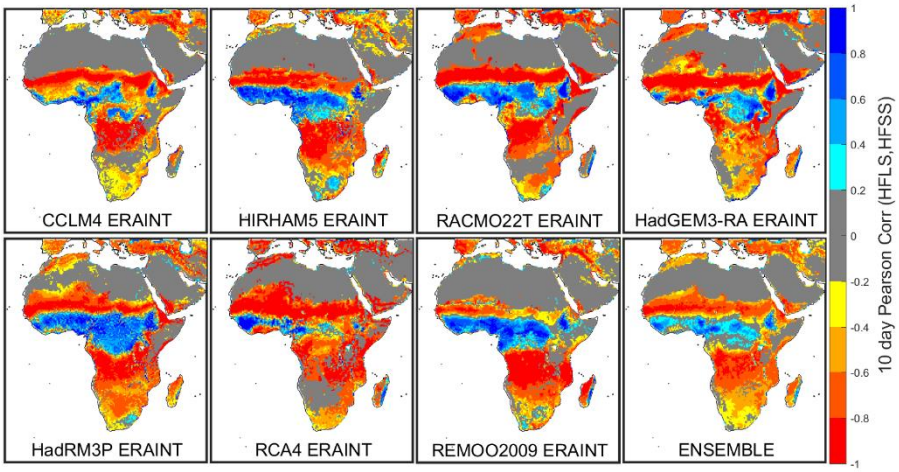


*Fig A.16.* JJA 10 days of nonoverlapping means correlation between HFLS and HFSS for Hindcast (1990-2008). Correlations below the 20% significance level and areas of low Evaporative Fraction (less than 0.1) are depicted as gray.

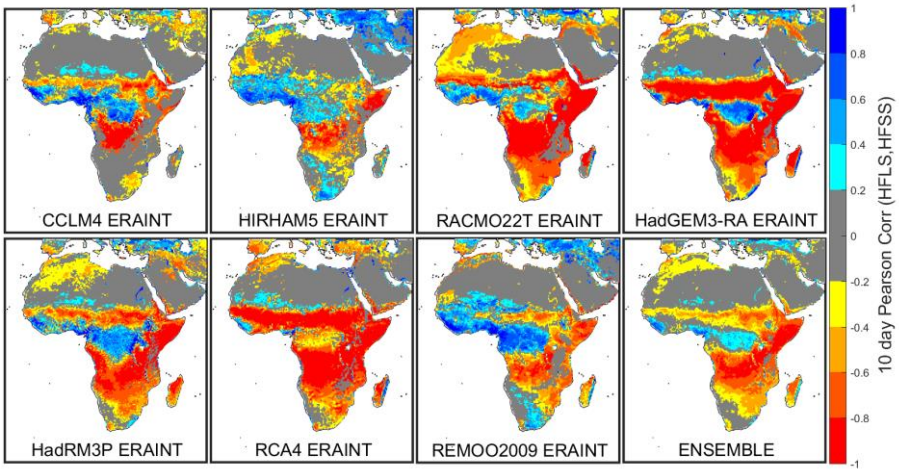


*Fig A.17.* SON 10 days of nonoverlapping means correlation between HFLS and HFSS for Hindcast (1990-2008). Correlations below the 20% significance level and areas of low Evaporative Fraction (less than 0.1) are depicted as gray.

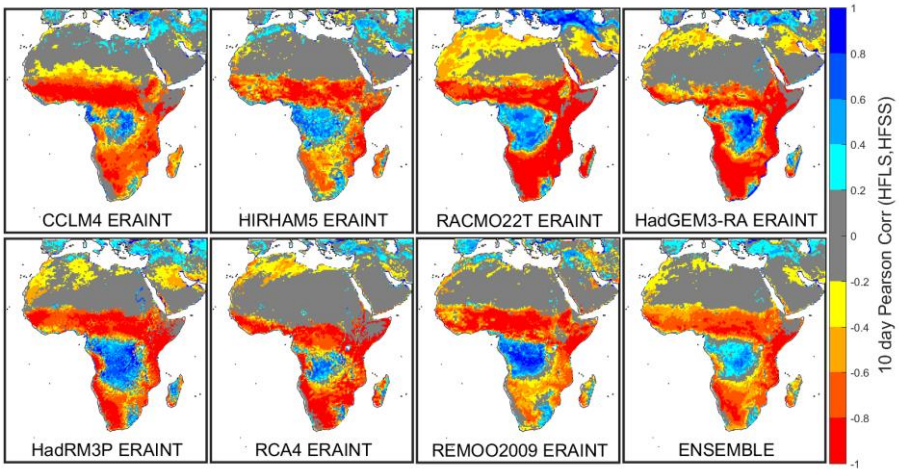


*Fig A.18.* DJF 10 days of nonoverlapping means correlation between HFLS and HFSS for Hindcast (1990-2008). Correlations below the 20% significance level and areas of low Evaporative Fraction (less than 0.1) are depicted as gray.

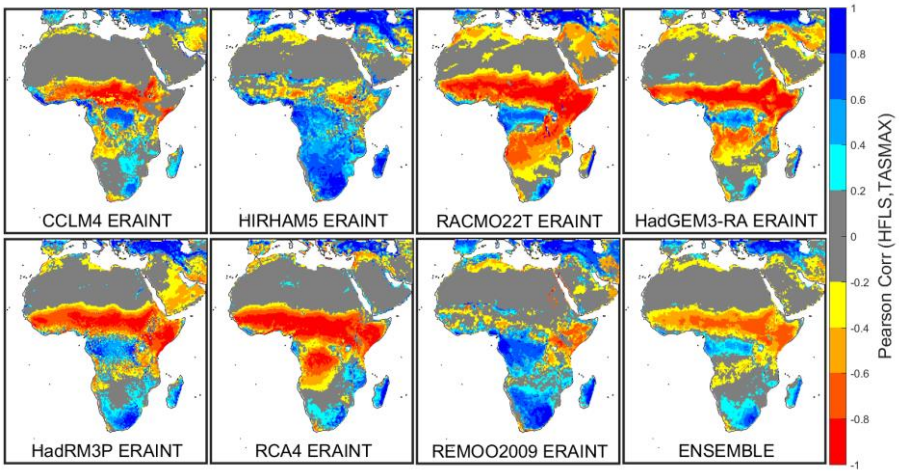


*Fig A.19.* MAM 10 days of nonoverlapping means correlation between HFLS and TASMAX for Hindcast (1990-2008). Correlations below the 20% significance level and areas of low Evaporative Fraction (less than 0.1) are depicted as gray.

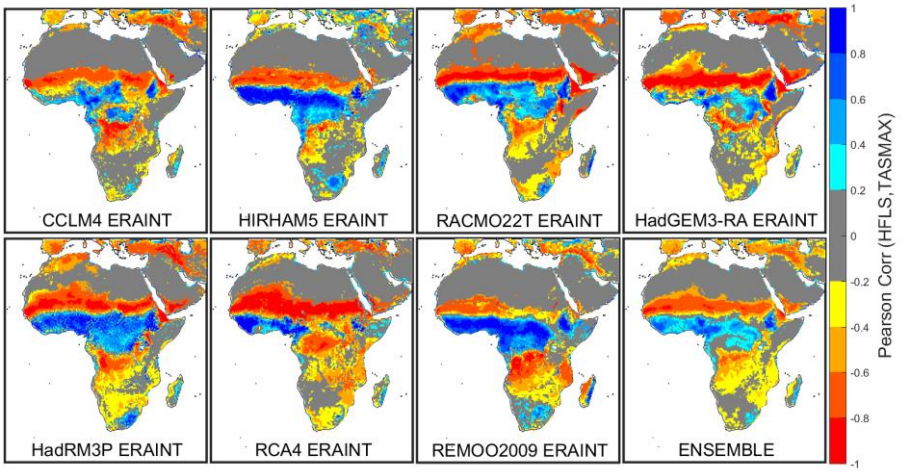


*Fig A.20.* JJA 10 days of nonoverlapping means correlation between HFLS and TASMAX for Hindcast (1990-2008). Correlations below the 20% significance level and areas of low Evaporative Fraction (less than 0.1) are depicted as gray.

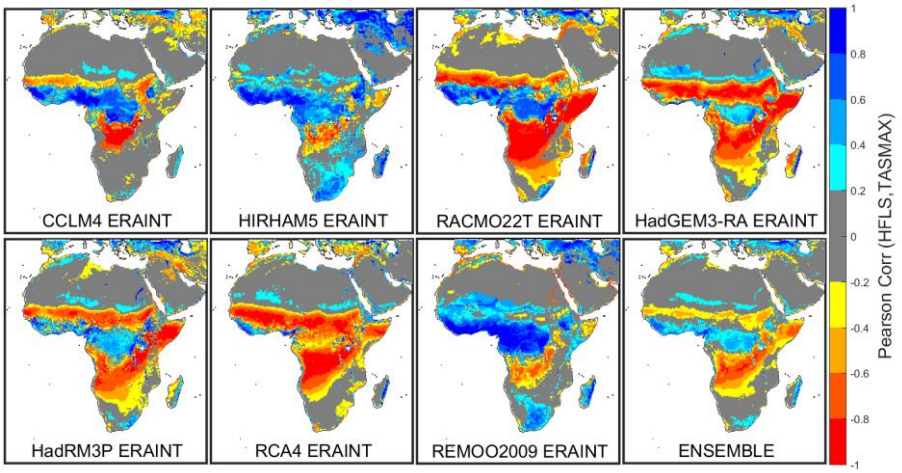


*Fig A.21.* SON 10 days of nonoverlapping means correlation between HFLS and TASMAX for Hindcast (1990-2008). Correlations below the 20% significance level and areas of low Evaporative Fraction (less than 0.1) are depicted as gray.

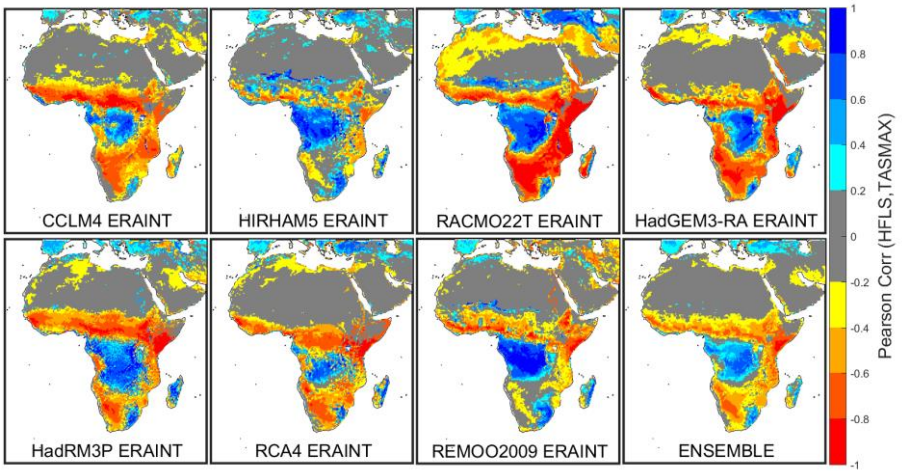


*Fig A.22.* DJF 10 days of nonoverlapping means correlation between HFLS and TASMAX for Hindcast (1990-2008). Correlations below the 20% significance level and areas of low Evaporative Fraction (less than 0.1) are depicted as gray.

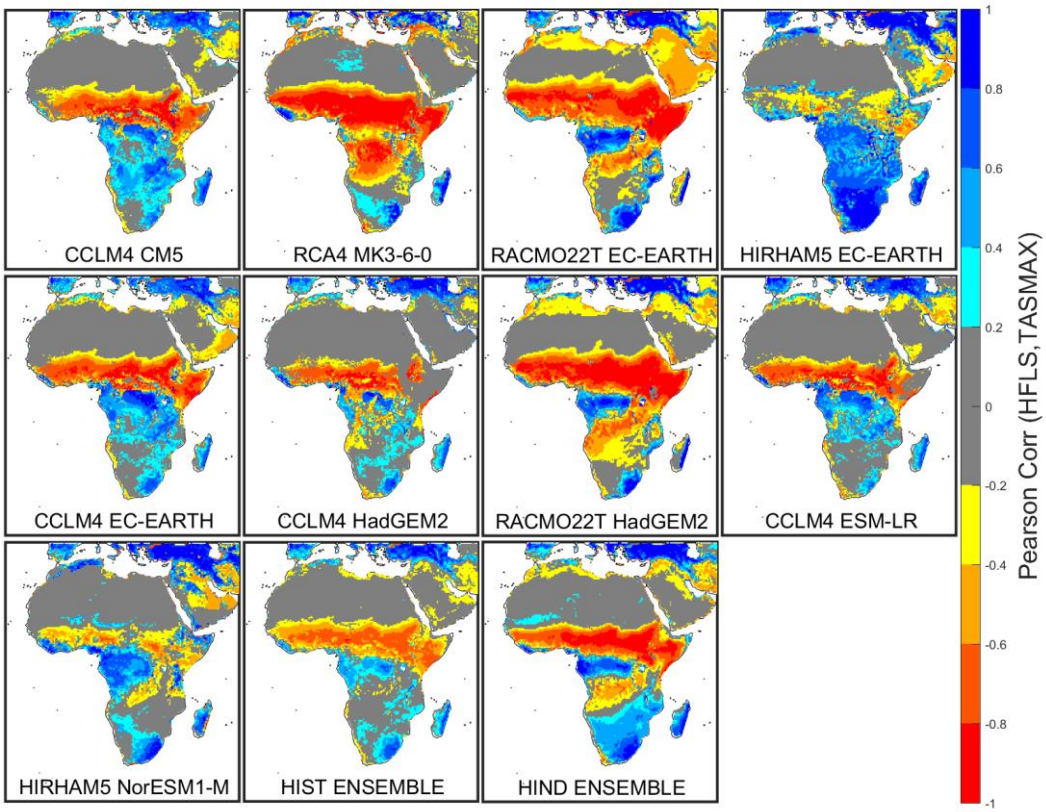


*Fig A.23.* MAM 10 days of nonoverlapping means correlation between HFLS and Daily Maximum Near Surface Air Temperature (TASMAX) for Historic (1971-2000). Hindcast (1990-2000) ensemble is also shown. Correlations below the 20% significance level and areas of low Evaporative Fraction (less than 0.1) are depicted as gray.

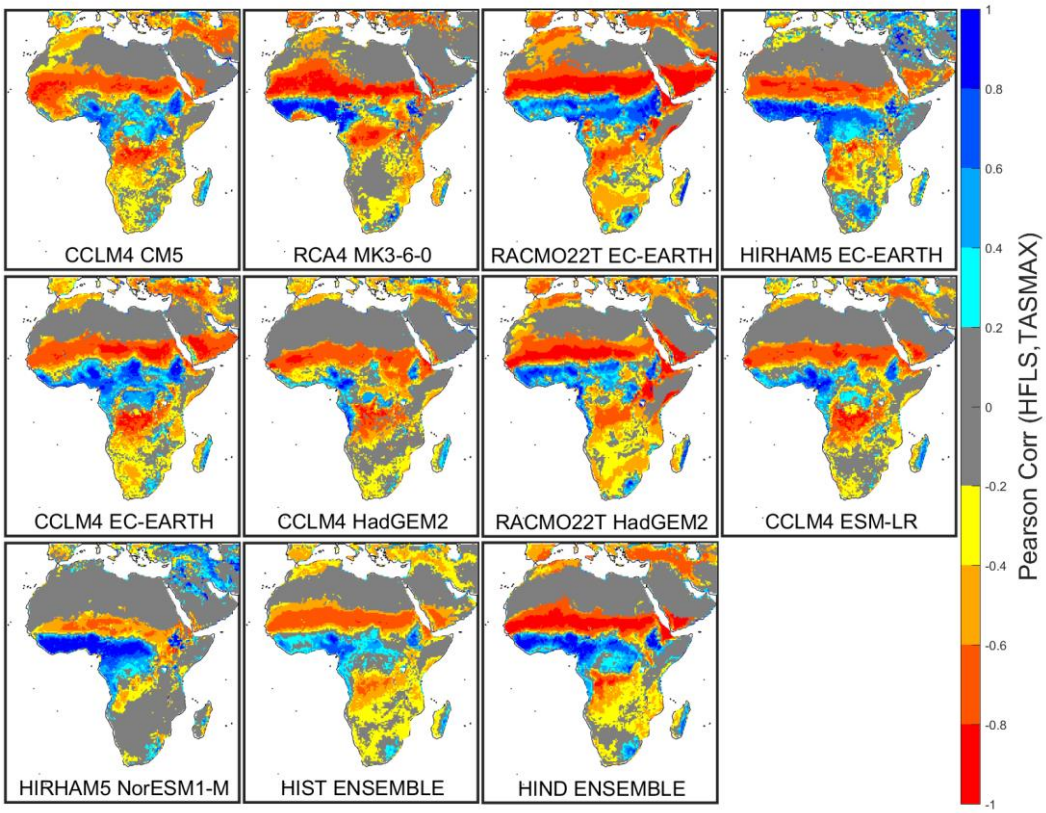


*Fig A.24.* JJA 10 days of nonoverlapping means correlation between HFLS and Daily Maximum Near Surface Air Temperature (TASMAX) for Historic (1971-2000). Hindcast (1990-2000) ensemble is also shown. Correlations below the 20% significance level and areas of low Evaporative Fraction (less than 0.1) are depicted as gray.

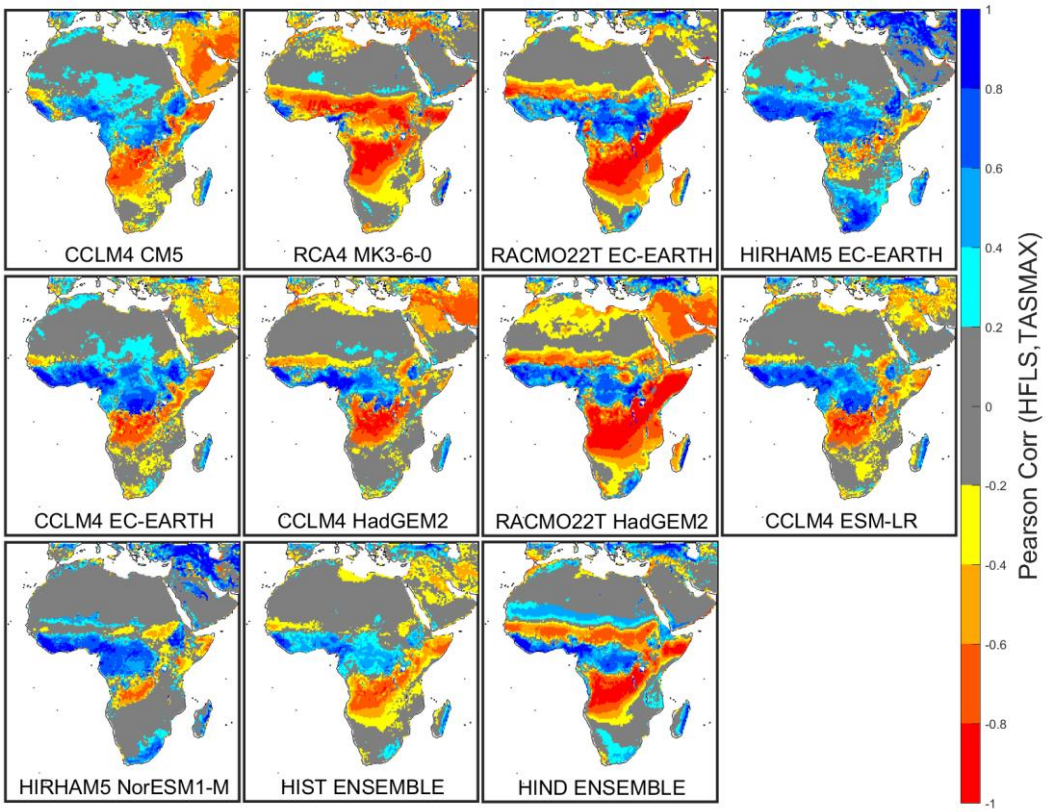


*Fig A.25.* SON 10 days of nonoverlapping means correlation between HFLS and Daily Maximum Near Surface Air Temperature (TASMAX) for Historic (1971-2000). Hindcast (1990-2000) ensemble is also shown. Correlations below the 20% significance level and areas of low Evaporative Fraction (less than 0.1) are depicted as gray.

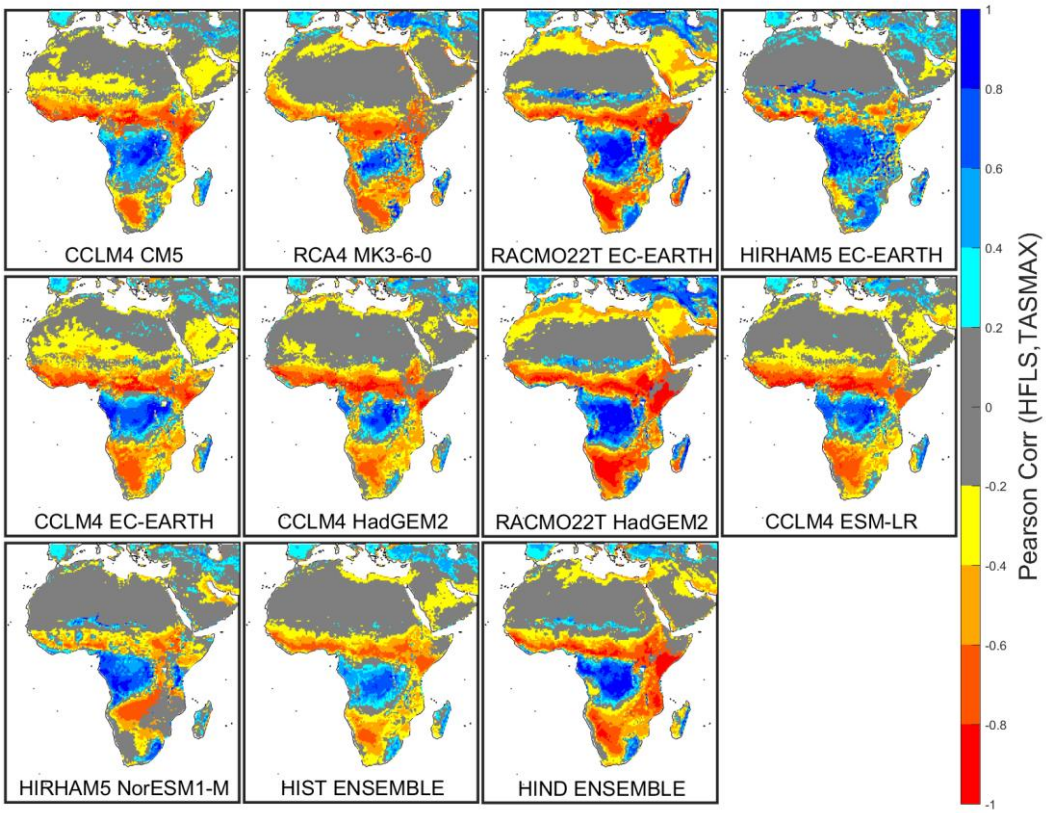


*Fig A.26.* DJF 10 days of nonoverlapping means correlation between HFLS and Daily Maximum Near Surface Air Temperature (TASMAX) for Historic (1971-2000). Hindcast (1990-2000) ensemble is also shown. Correlations below the 20% significance level and areas of low Evaporative Fraction (less than 0.1) are depicted as gray.

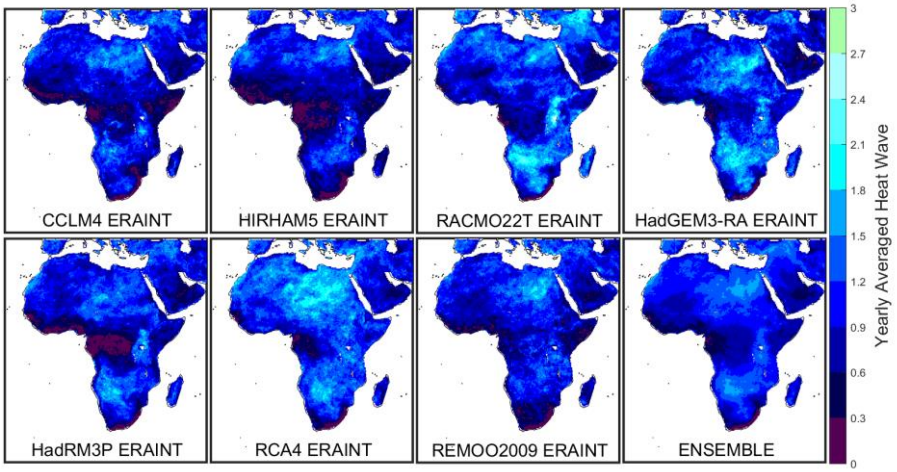


*Fig A.27.* Yearly average number of heat waves for the Hindcast (1990-2008).

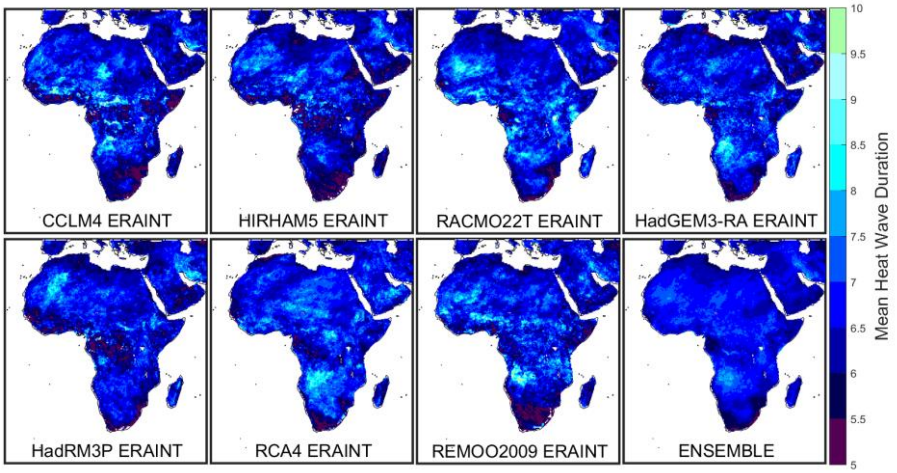


*Fig A.28.* Mean heat wave duration for Hindcast (1990-2008).

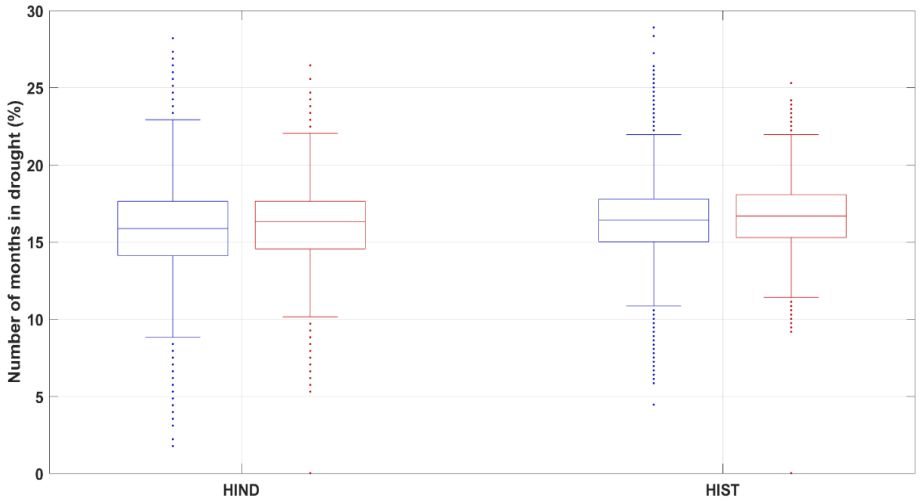


*Fig A.29.* Boxplots of number of months in drought (percentage of moths with SPEI below -1) for all land points for the (left) Hindcast ensemble (1990-2008) and (right) Historic ensemble (1971-2000), against SPEI computed with CRU database for the same periods respectively. Blue boxplots are relative to modeled SPEI and red boxplots are relative to CRU SPEI

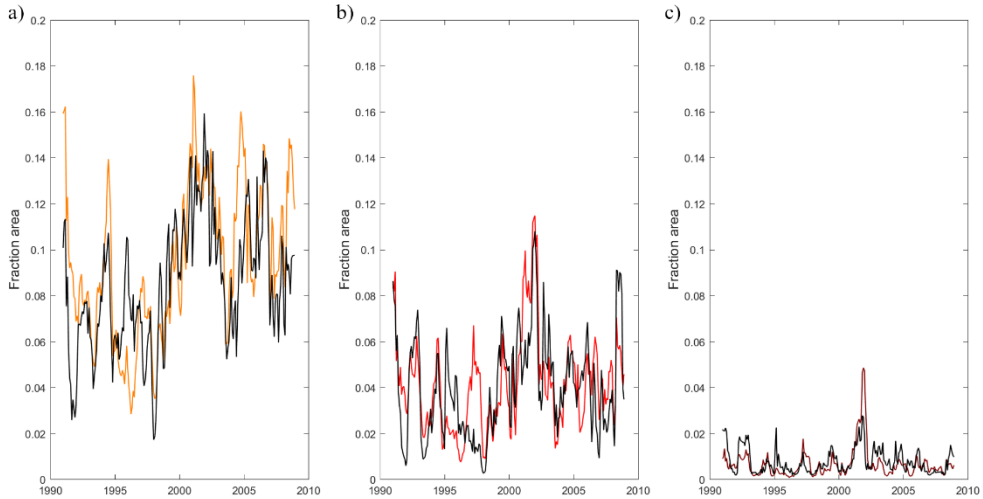


*Fig A.30.* Fraction Area in (a) moderate drought (SPEI between -1 and -1.5), (b) severe drought (SPEI between -1.5 and -2) and (c) extreme drought (SPEI bellow -2) for all land points for the Hindcast ensemble (1990-2008) against SPEI computed with CRU database for the same period (black line).

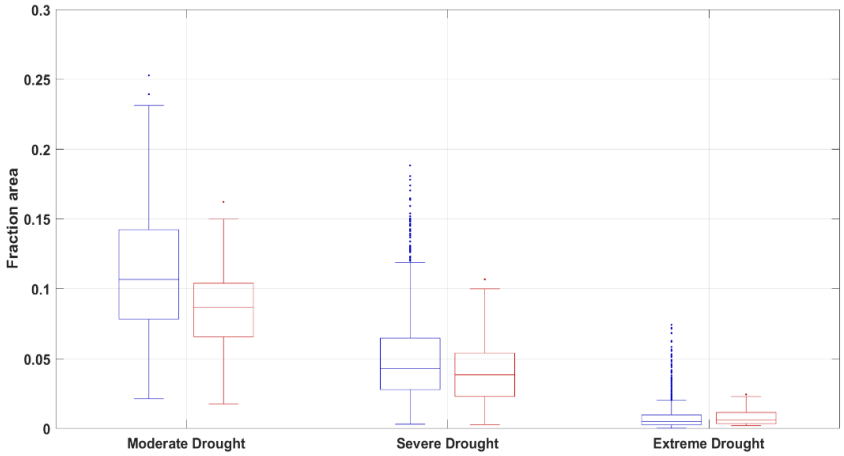


*Fig A.31.* Boxplots of fraction area in (left) moderate drought (SPEI between -1 and -1.5), (center) severe drought (SPEI between -1.5 and -2) and (right) extreme drought (SPEI bellow -2) for Hindcast (1990-2008) against SPEI computed with CRU database. Blue boxplots are relative to modeled SPEI and red boxplots are relative to CRU SPEI.

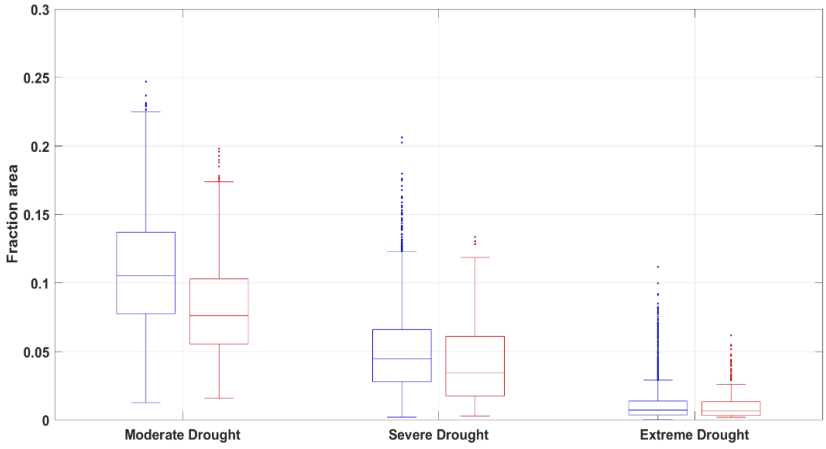


*Fig A.32.* Boxplots of fraction area in (left) moderate drought (SPEI between -1 and -1.5), (center) severe drought (SPEI between -1.5 and -2) and (right) extreme drought (SPEI bellow -2) for Historic (1971-2000) against SPEI computed with CRU database. Blue boxplots are relative to modeled SPEI and red boxplots are relative to CRU SPEI.

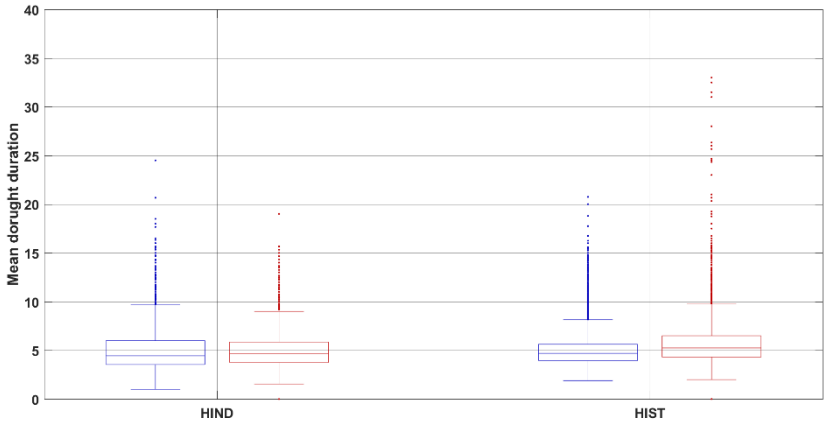


*Fig A.33.* Boxplots of mean drought duration for all land points for (left) Hindcast (1990-2008) and (right) Historic (1971-2000) against SPEI computed using CRU database. Blue boxplots are relative to modeled SPEI values and red boxplots are relative to CRU SPEI.

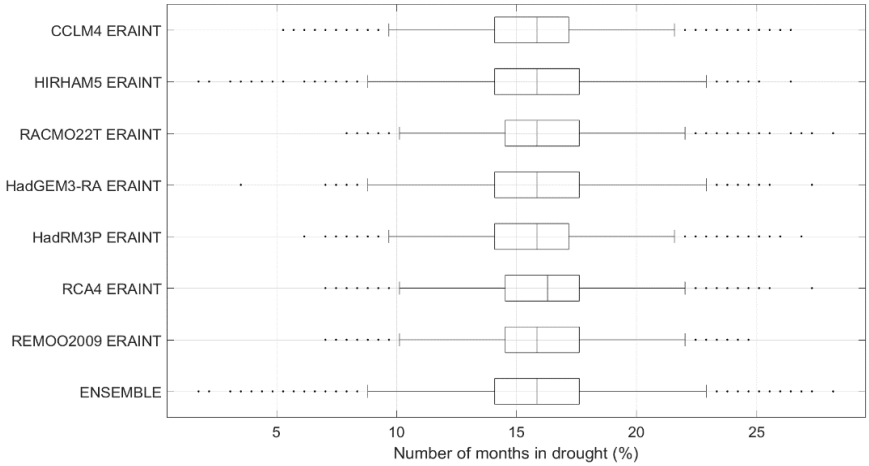


*Fig A.34.* Boxplots of the percentage of number of months in drought, for all land points of the Hindcast (1990-2008). The ensemble is the data of all models.

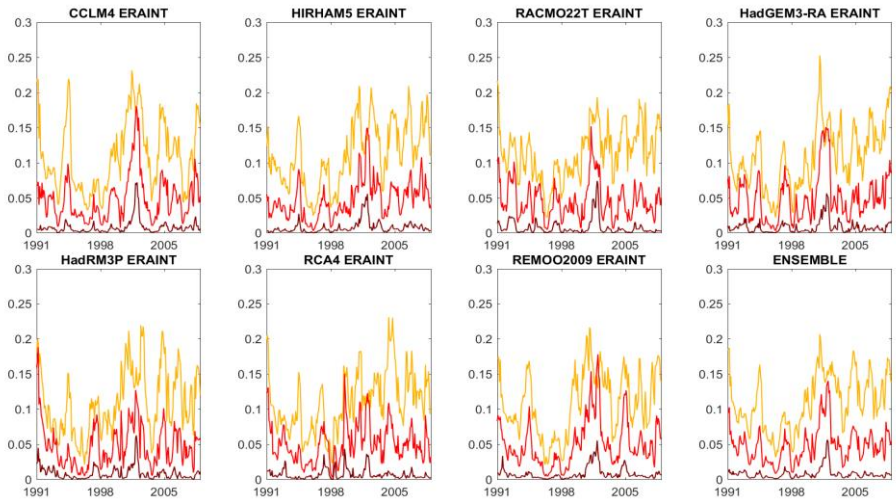


*Fig A.35.* Fraction area in drought, with different intensities (yellow: fraction area in moderate drought; red: fraction area in severe drought; dark red: fraction area in extreme drought), over time for all land points for the Hindcast (1990-2008).

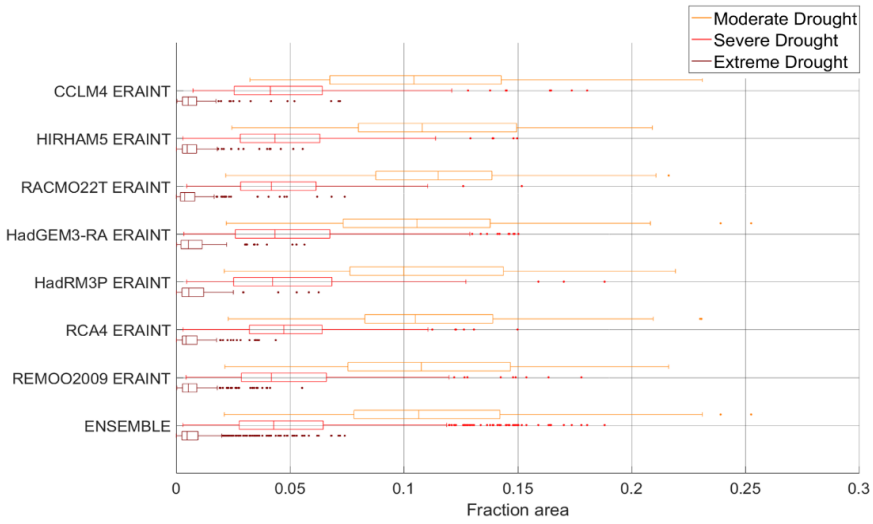


*Fig A.36.* Boxplots of the fraction area in drought with different intensities (yellow: fraction area in moderate drought; red: fraction area in severe drought; dark red: fraction area in extreme drought), over time for all land points for the Hindcast (1990-2008). The ensemble is the data of all models.

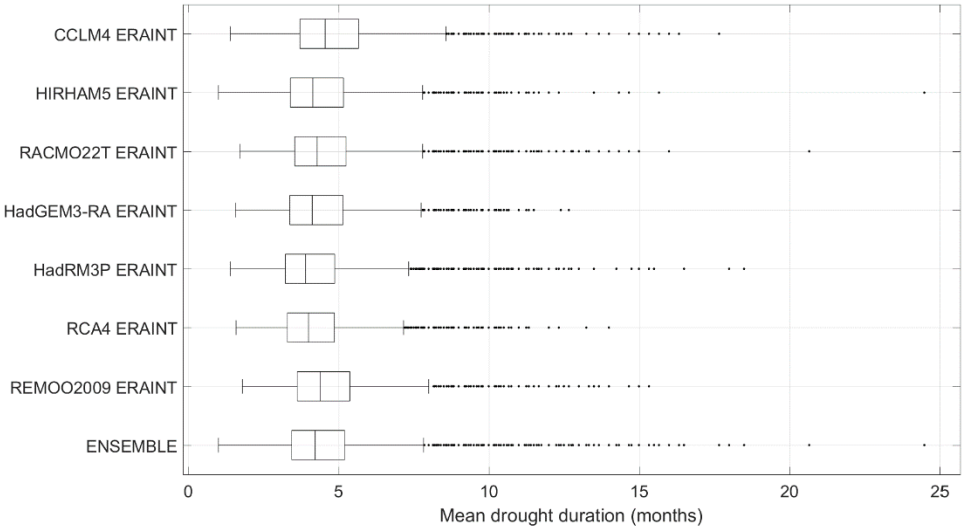


*Fig A.37.* Boxplot of mean drought duration for all land points of Hindcast (1990-2008) divided by the number of years. The ensemble is the data of all models.

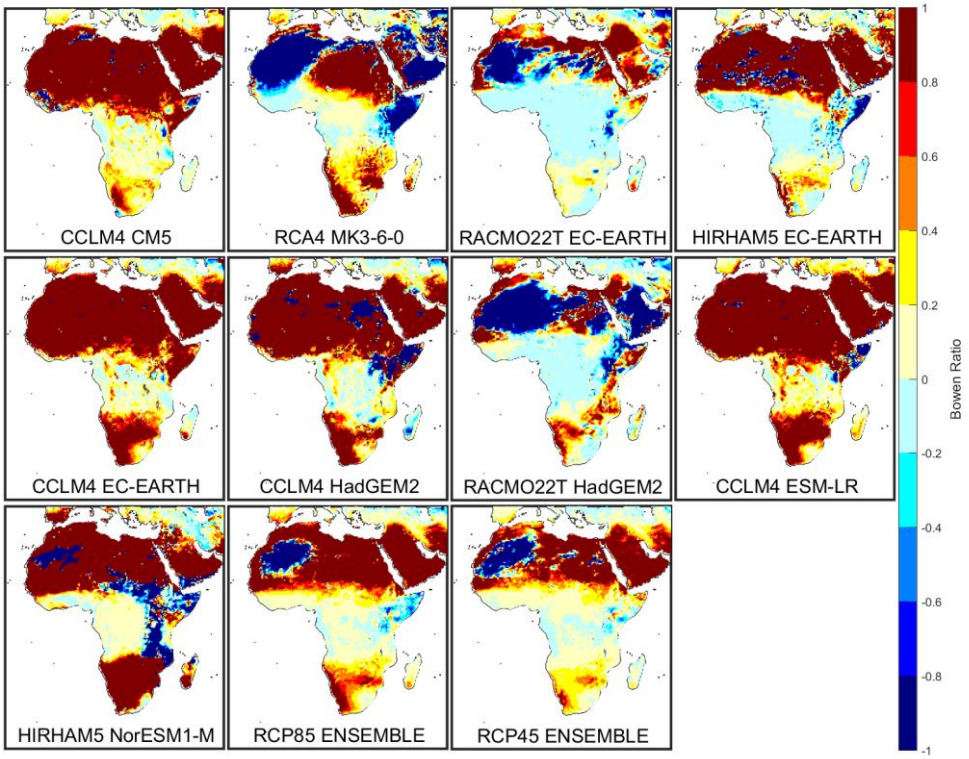


*Fig A.38.* MAM Bowen ratio anomalies between RCP8.5 (2071-2100) and Historic (1971-2000). The RCP4.5 (2071-2100) ensemble is also shown.

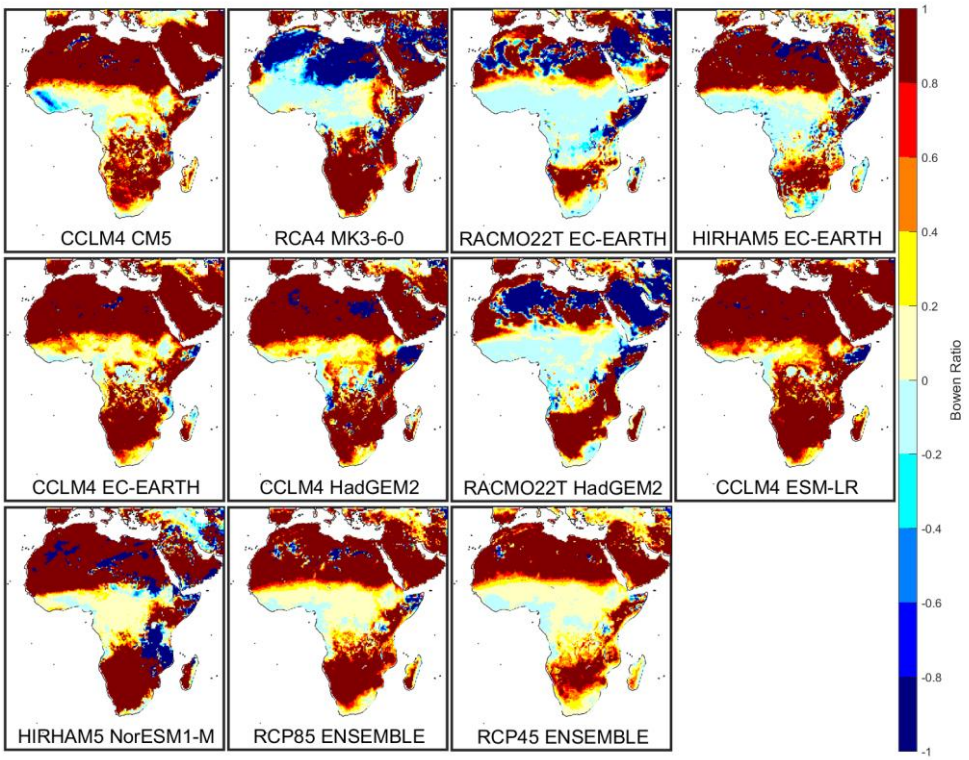


*Fig A.39.* JJA Bowen ratio anomalies between RCP8.5 (2071-2100) and Historic (1971-2000). The RCP4.5 (2071-2100) ensemble is also shown.

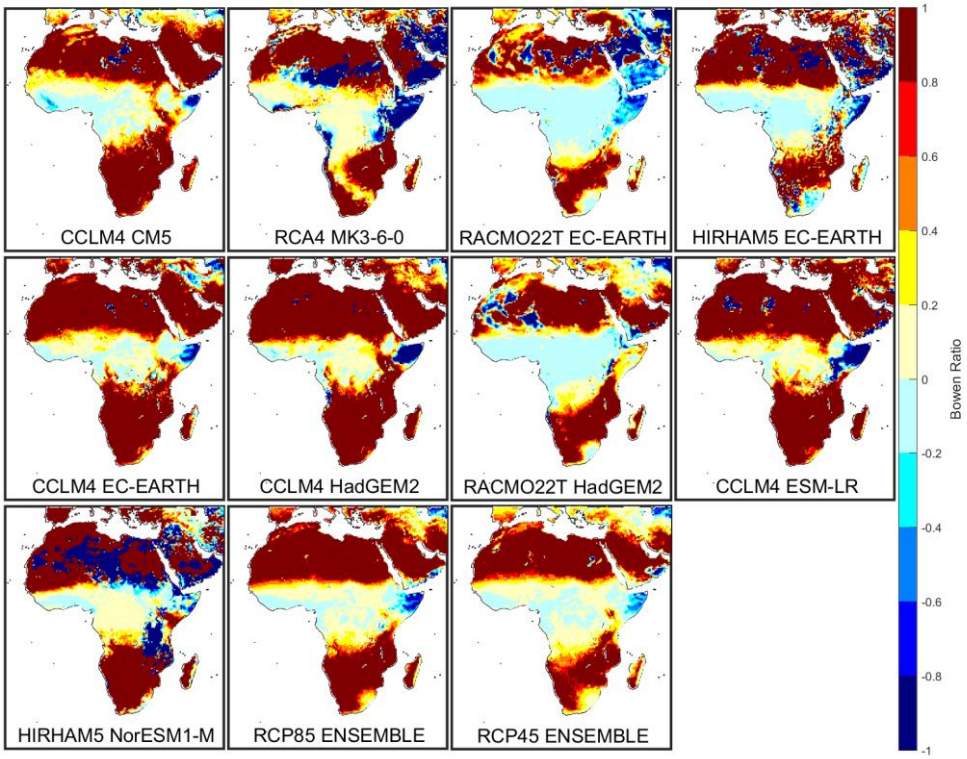


*Fig A.40.* SON Bowen ratio anomalies between RCP8.5 (2071-2100) and Historic (1971-2000). The RCP4.5 (2071-2100) ensemble is also shown.

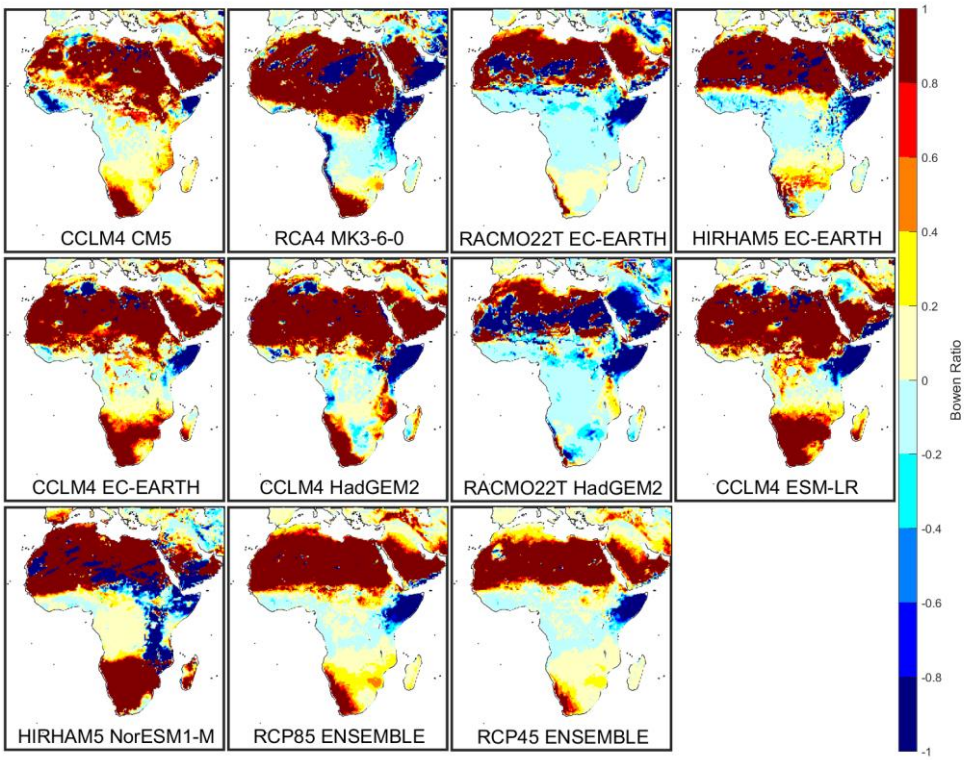


*Fig A.41.* DJF Bowen ratio anomalies between RCP8.5 (2071-2100) and Historic (1971-2000). The RCP4.5 (2071-2100) ensemble is also shown.

a)

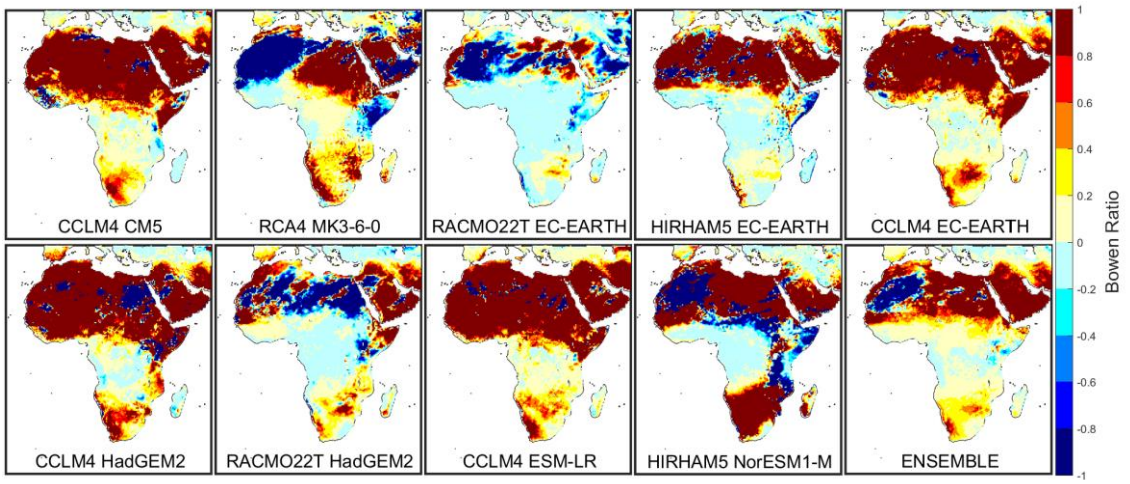


b)

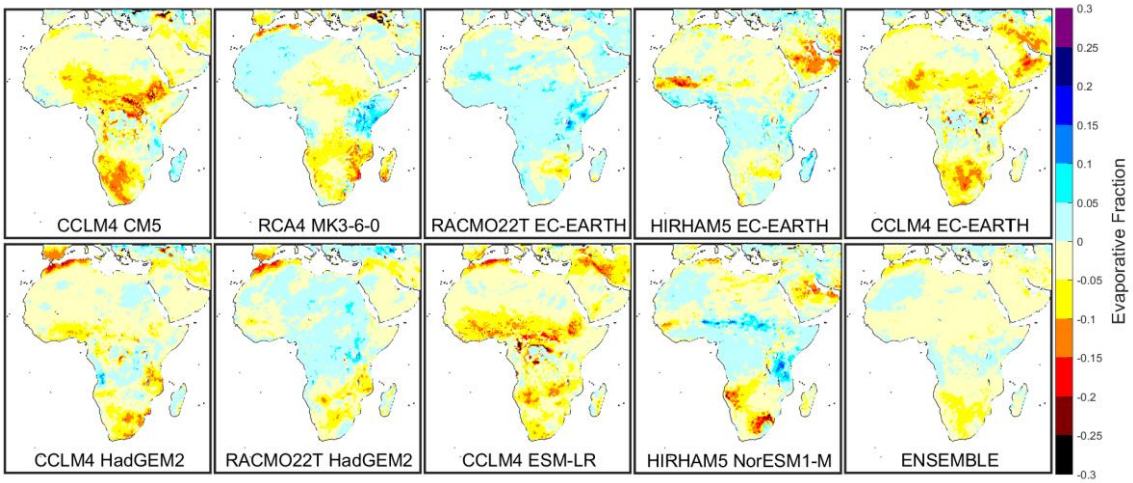


*Fig A.42.* MAM (a) Bowen ratio and (b) Evaporative Fraction anomalies between RCP4.5 (2071-2100) and Historic (1971-2000).

a)

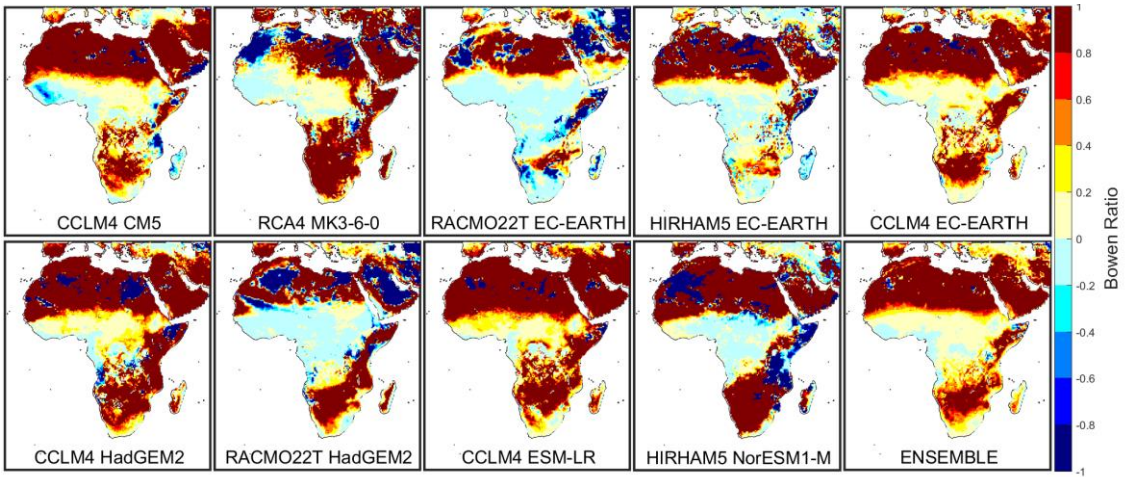


b)

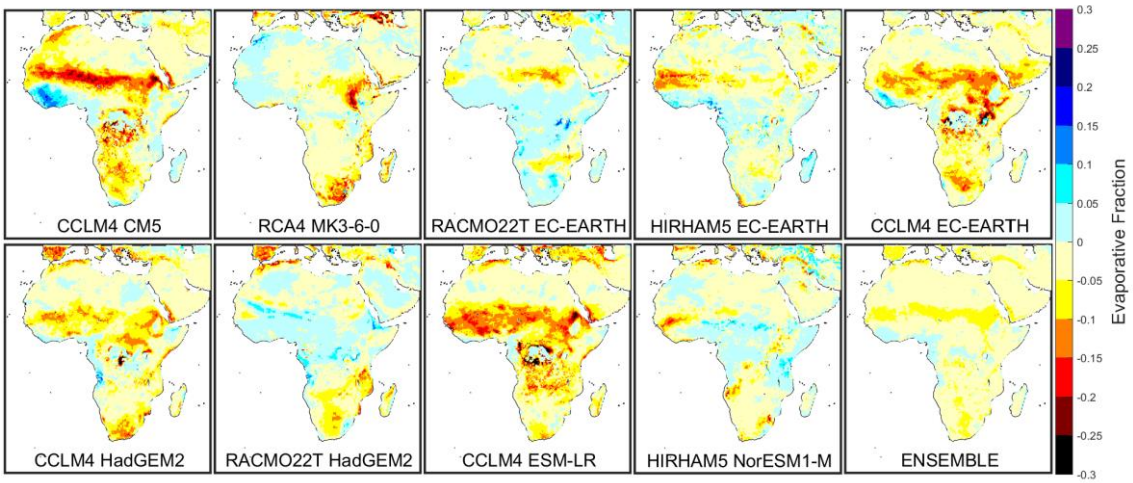


*Fig A.43.* JJA (a) Bowen ratio and (b) Evaporative Fraction anomalies between RCP4.5 (2071-2100) and Historic (1971-2000).

a)

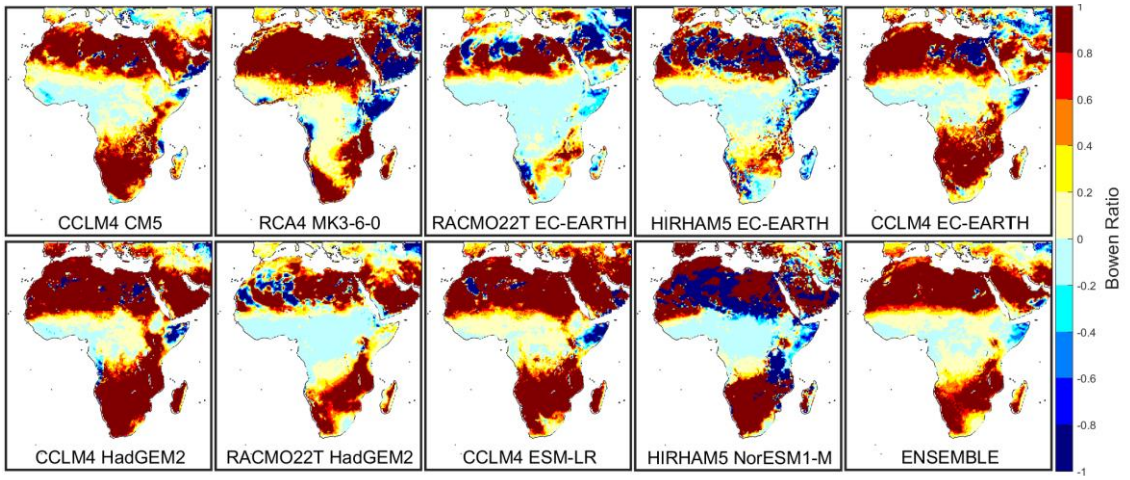


b)

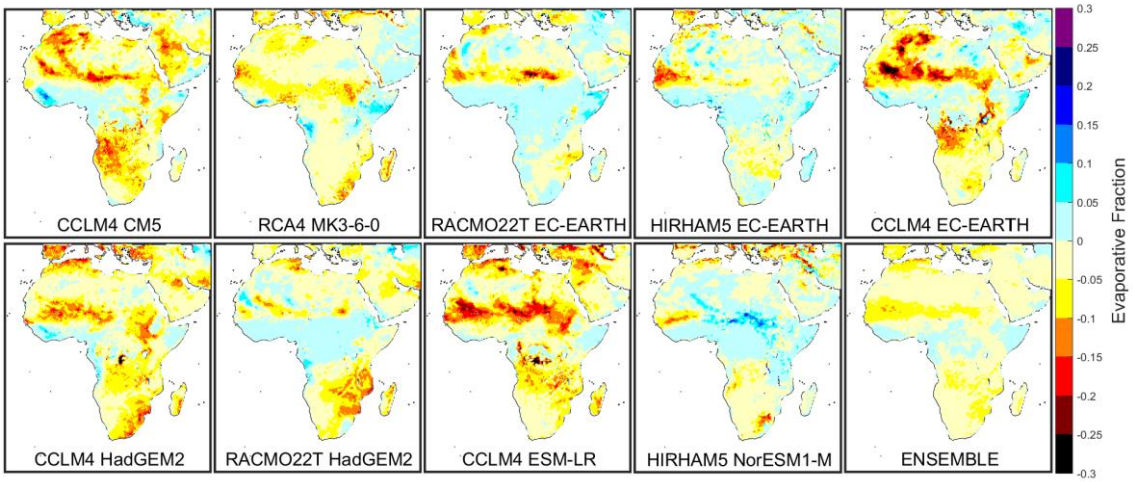


*Fig A.44.* SON (a) Bowen ratio and (b) Evaporative Fraction anomalies between RCP4.5 (2071-2100) and Historic (1971-2000).

a)

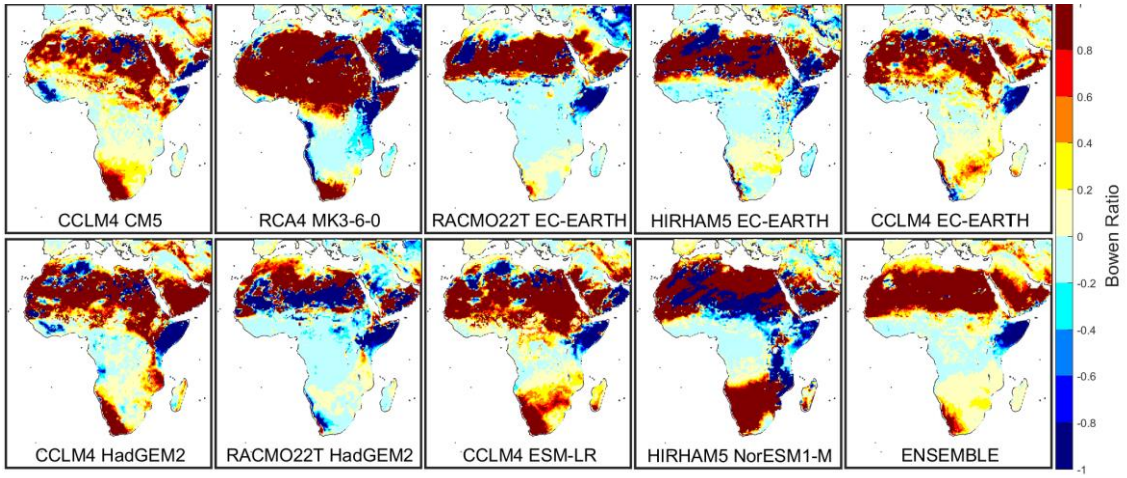


b)

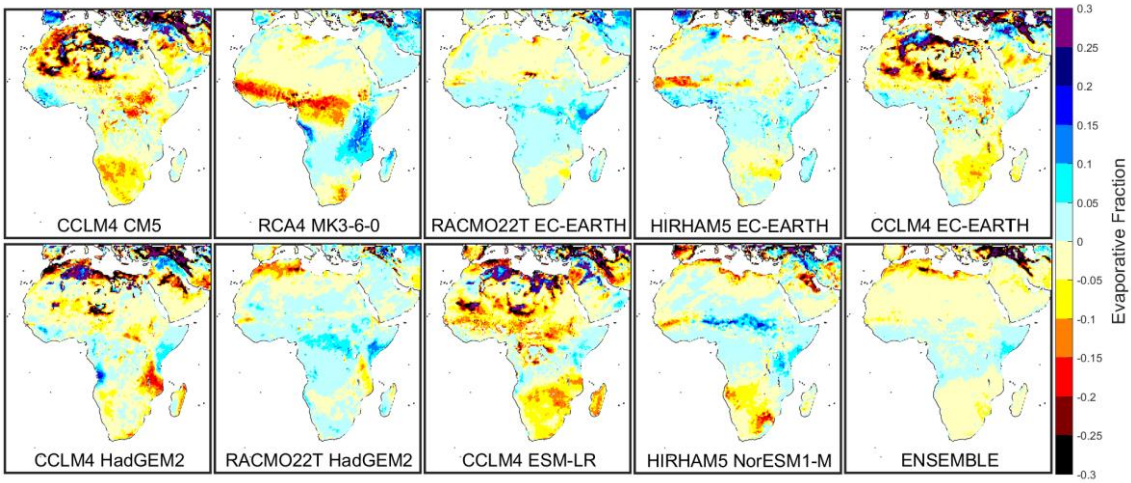


*Fig A.45. DJF* (a) Bowen ratio and (b) Evaporative Fraction anomalies between RCP4.5 (2071-2100) and Historic (1971-2000).

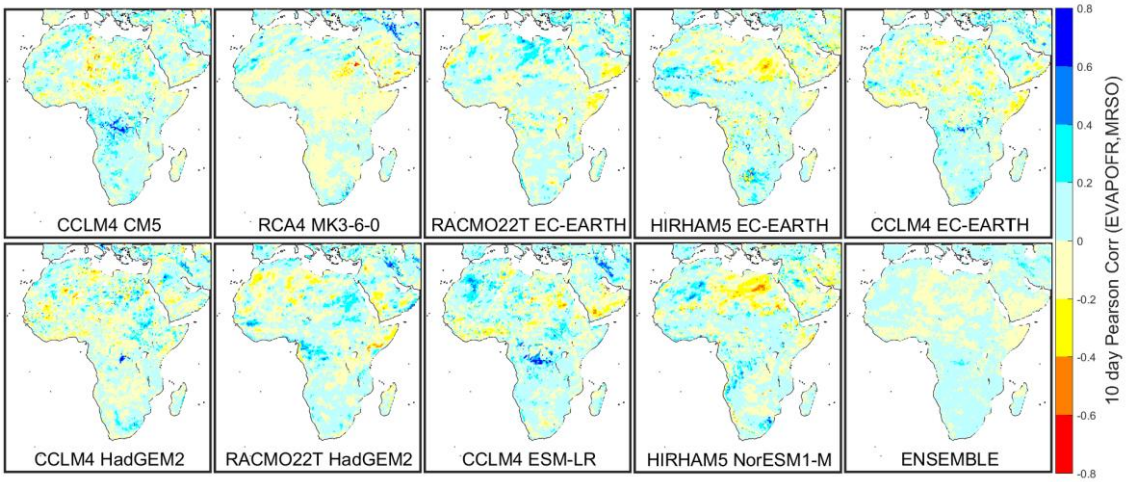


*Fig A.46.* MAM 10 days of nonoverlapping means correlation between MRSO and Evaporative Fraction (EVAPOFR) anomalies between RCP4.5 (2071-2100) and Historic (1971-2000).

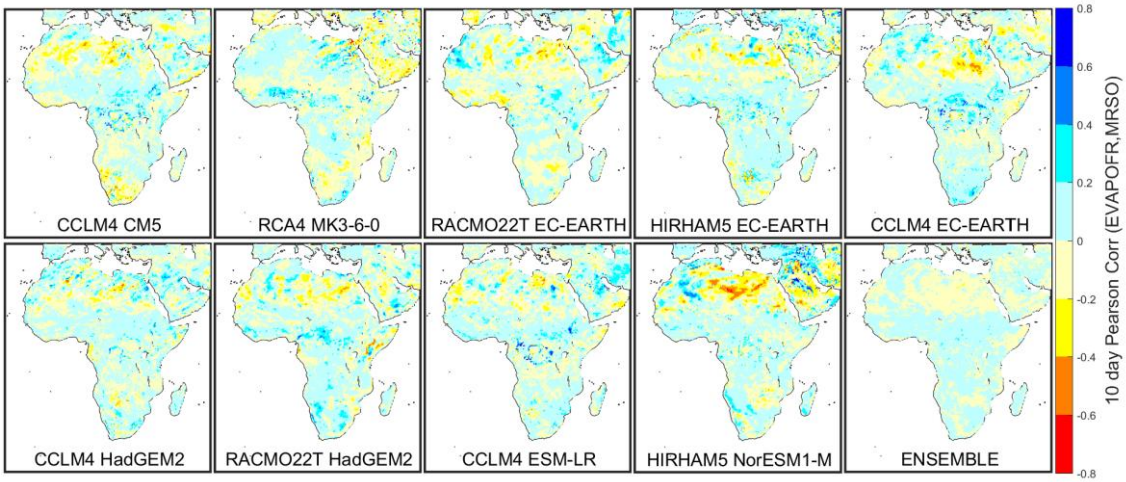


*Fig A.47.* JJA 10 days of nonoverlapping means correlation between MRSO and Evaporative Fraction (EVAPOFR) anomalies between RCP4.5 (2071-2100) and Historic (1971-2000).

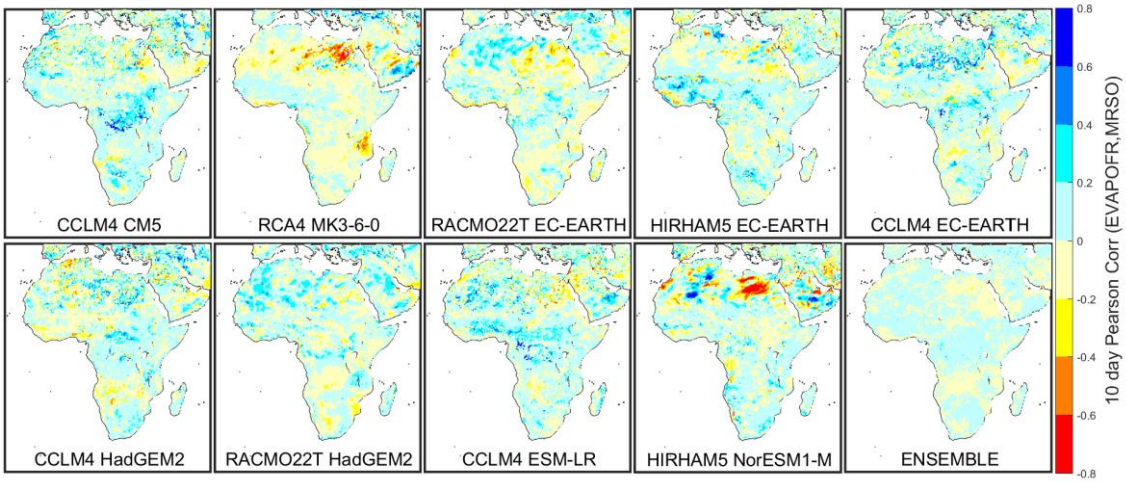


*Fig A.48.* SON 10 days of nonoverlapping means correlation between MRSO and Evaporative Fraction (EVAPOFR) anomalies between RCP4.5 (2071-2100) and Historic (1971-2000).

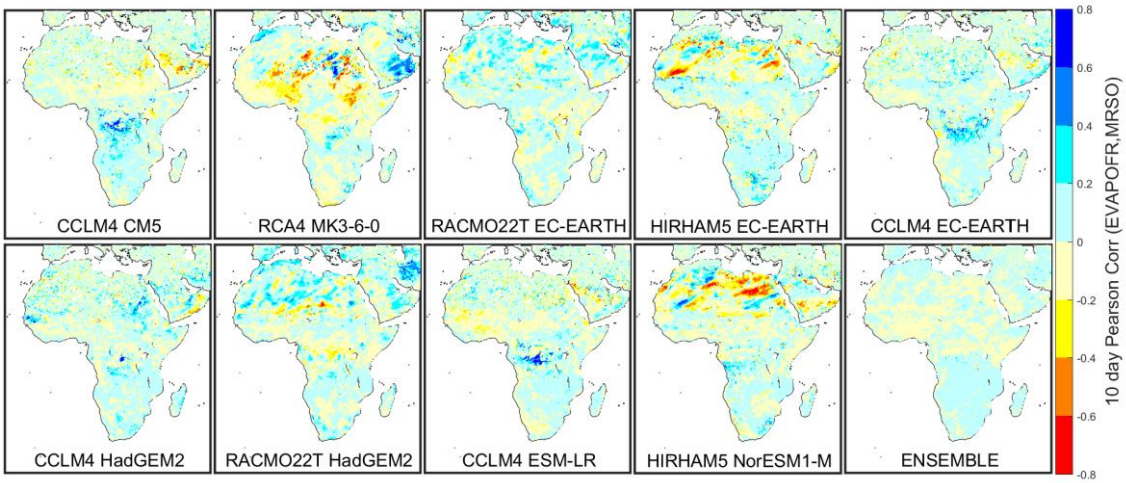


*Fig A.49.* DJF 10 days of nonoverlapping means correlation between MRSO and Evaporative Fraction (EVAPOFR) anomalies between RCP4.5 (2071-2100) and Historic (1971-2000).

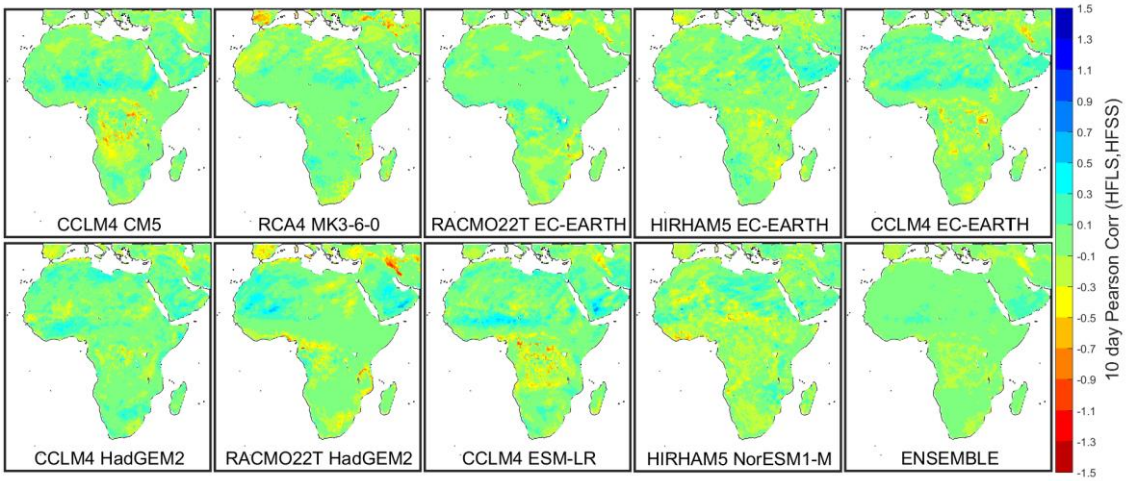


*Fig A.50.* MAM 10 days of nonoverlapping means correlation between HFLS and HFSS anomalies between RCP4.5 (2071-2100) and Historic (1971-2000) for all models and ensemble.

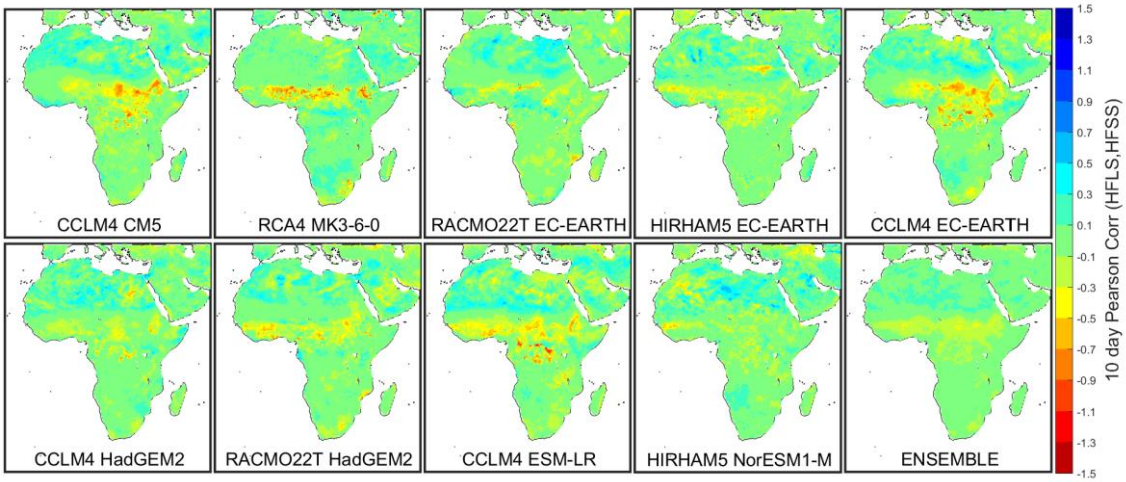


*Fig A.51.* JJA 10 days of nonoverlapping means correlation between HFLS and HFSS anomalies between RCP4.5 (2071-2100) and Historic (1971-2000) for all models and ensemble.

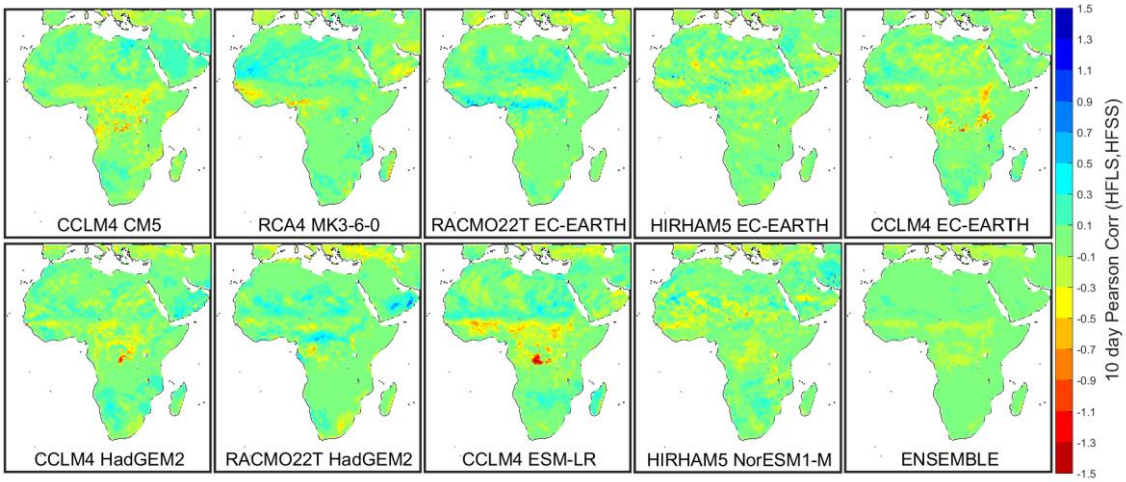


*Fig A.52.* SON 10 days of nonoverlapping means correlation between HFLS and HFSS anomalies between RCP4.5 (2071-2100) and Historic (1971-2000) for all models and ensemble.

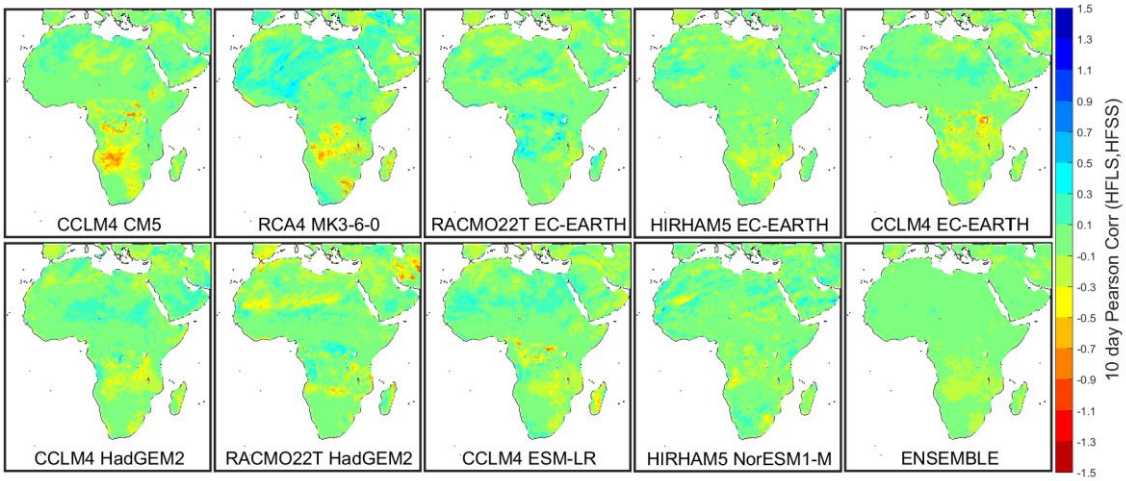


*Fig A.53.* DJF 10 days of nonoverlapping means correlation between HFLS and HFSS anomalies between RCP4.5 (2071-2100) and Historic (1971-2000) for all models and ensemble.

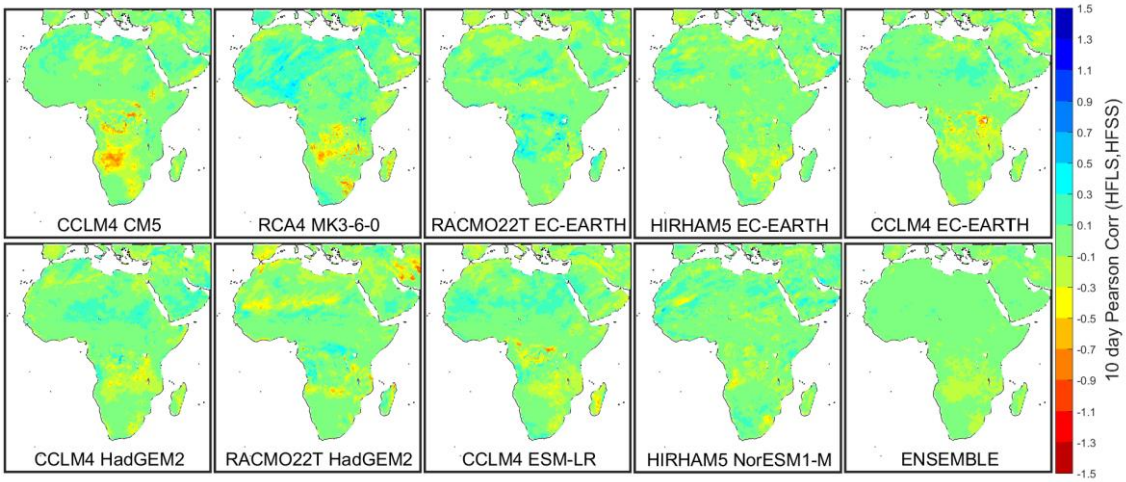


*Fig A.54.* MAM 10 days of nonoverlapping means correlation between HFLS and TASMAX anomalies between RCP4.5 (2071-2100) and Historic (1971-2000) for all models and ensemble.

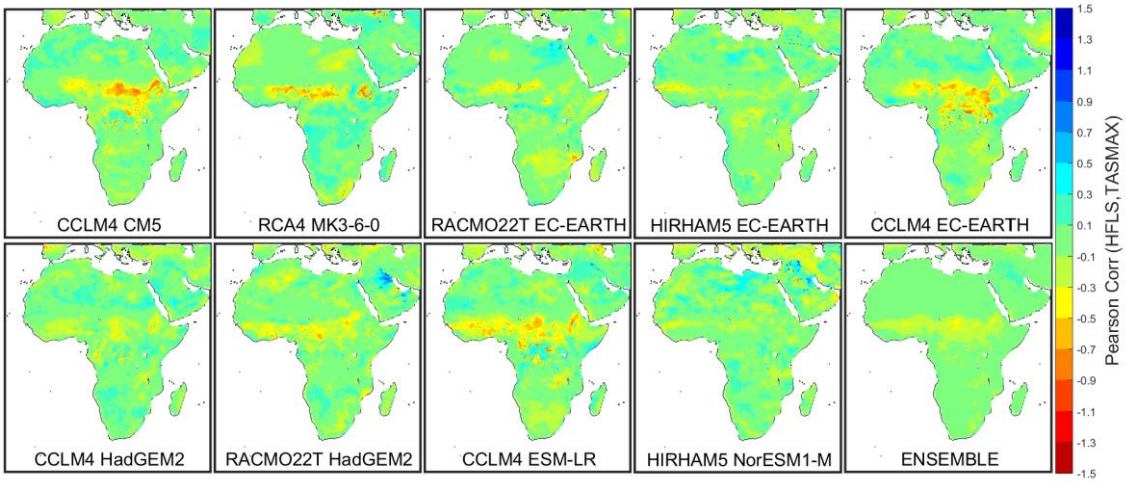


*Fig A.55.* JJA 10 days of nonoverlapping means correlation between HFLS and TASMAX anomalies between RCP4.5 (2071-2100) and Historic (1971-2000) for all models and ensemble.

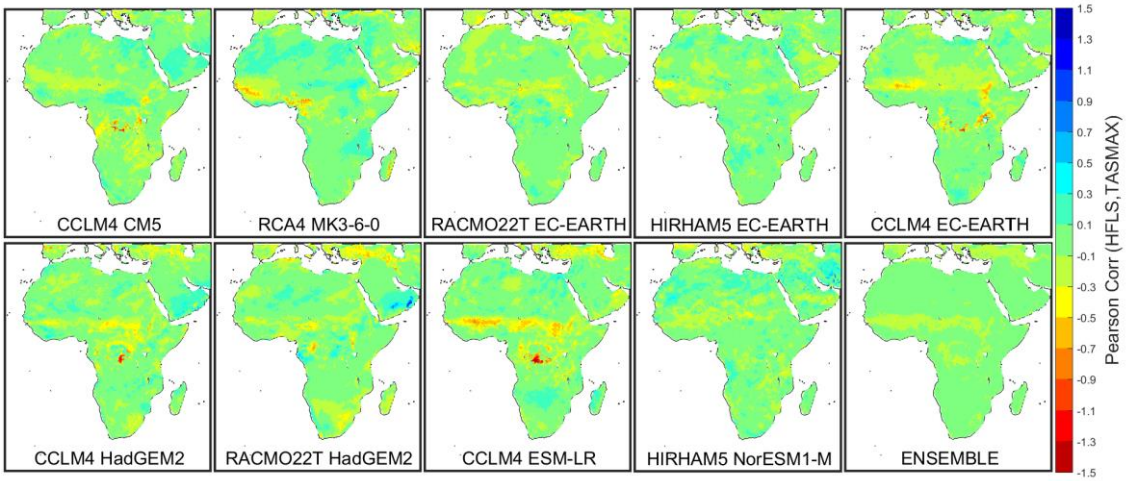


*Fig A.56.* SON 10 days of nonoverlapping means correlation between HFLS and TASMAX anomalies between RCP4.5 (2071-2100) and Historic (1971-2000) for all models and ensemble.

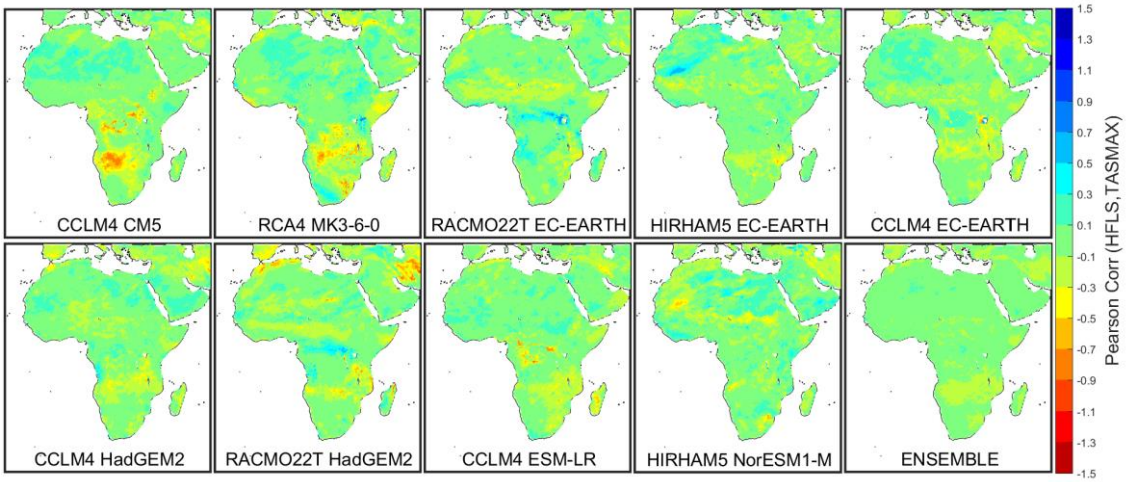


*Fig A.57.* DJF 10 days of nonoverlapping means correlation between HFLS and TASMAX anomalies between RCP4.5 (2071-2100) and Historic (1971-2000) for all models and ensemble.

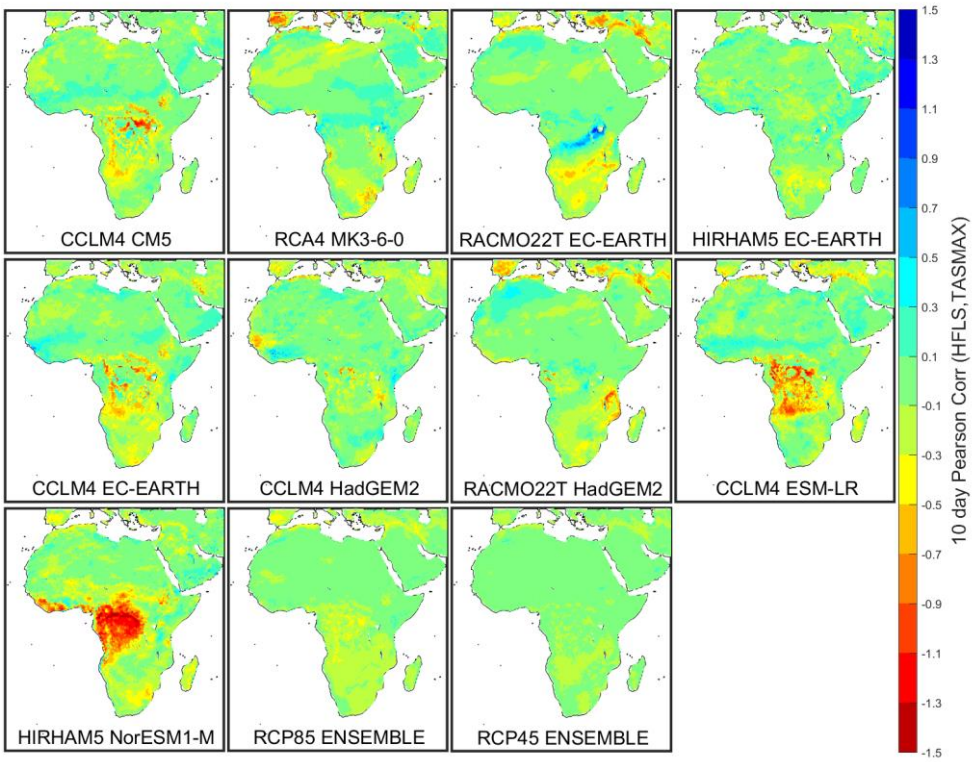


*Fig A.58.* MAM 10 days of nonoverlapping means correlation between latent heat flux (HFLS) and TASMAX anomalies between RCP8.5 (2071-2100) and Historic (1971-2000). The RCP4.5 (2071-2100) ensemble is also shown.

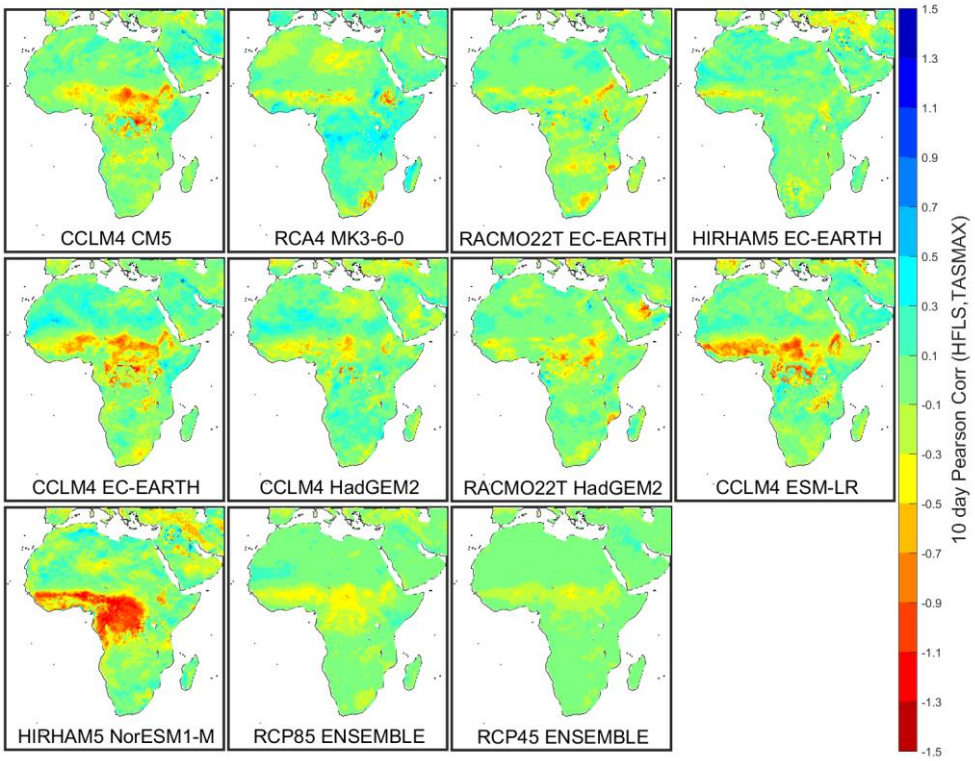


*Fig A.59.* JJA 10 days of nonoverlapping means correlation between latent heat flux (HFLS) and TASMAX anomalies between RCP8.5 (2071-2100) and Historic (1971-2000). The RCP4.5 (2071-2100) ensemble is also shown.

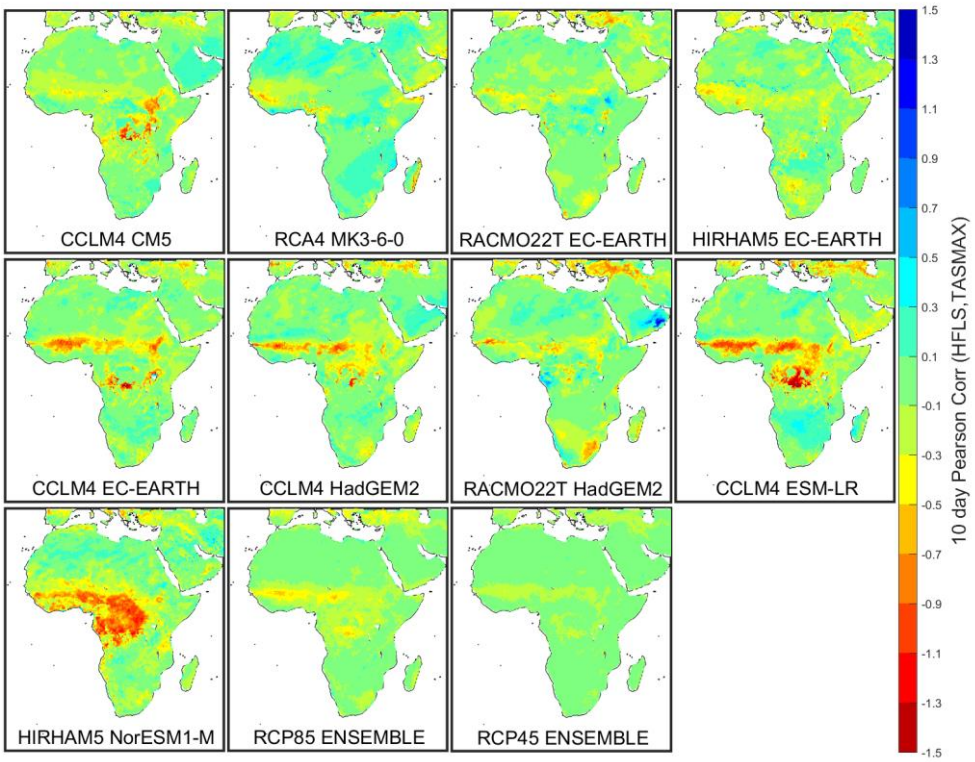


*Fig A.60.* SON 10 days of nonoverlapping means correlation between latent heat flux (HFLS) and TASMAX anomalies between RCP8.5 (2071-2100) and Historic (1971-2000). The RCP4.5 (2071-2100) ensemble is also shown.

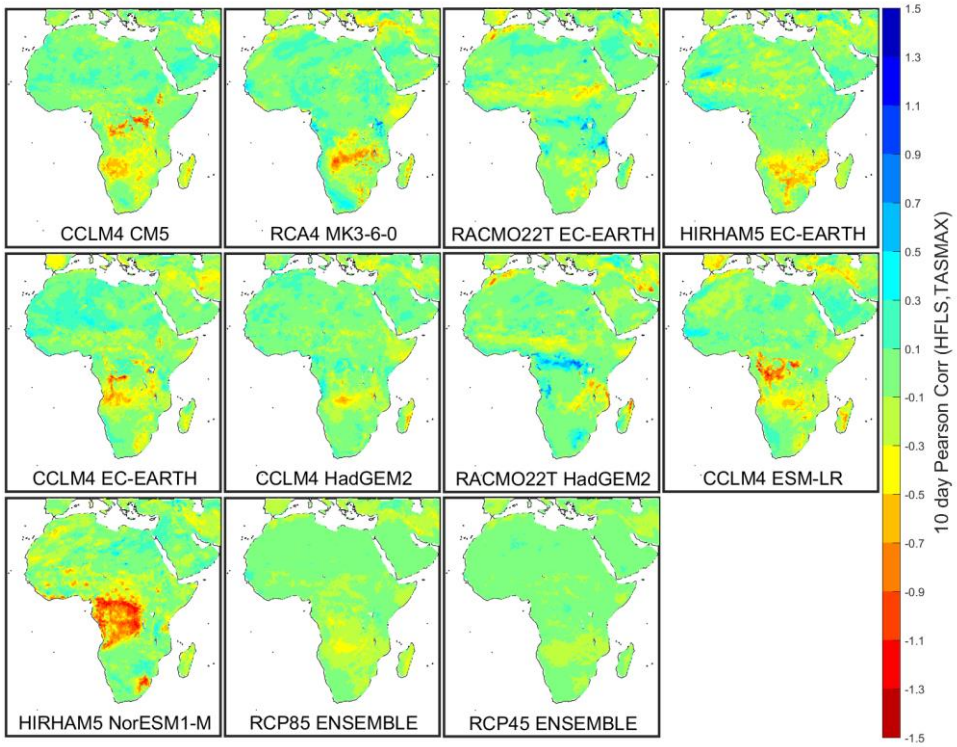


*Fig A.61.* DJF 10 days of nonoverlapping means correlation between latent heat flux (HFLS) and TASMAX anomalies between RCP8.5 (2071-2100) and Historic (1971-2000). The RCP4.5 (2071-2100) ensemble is also shown.

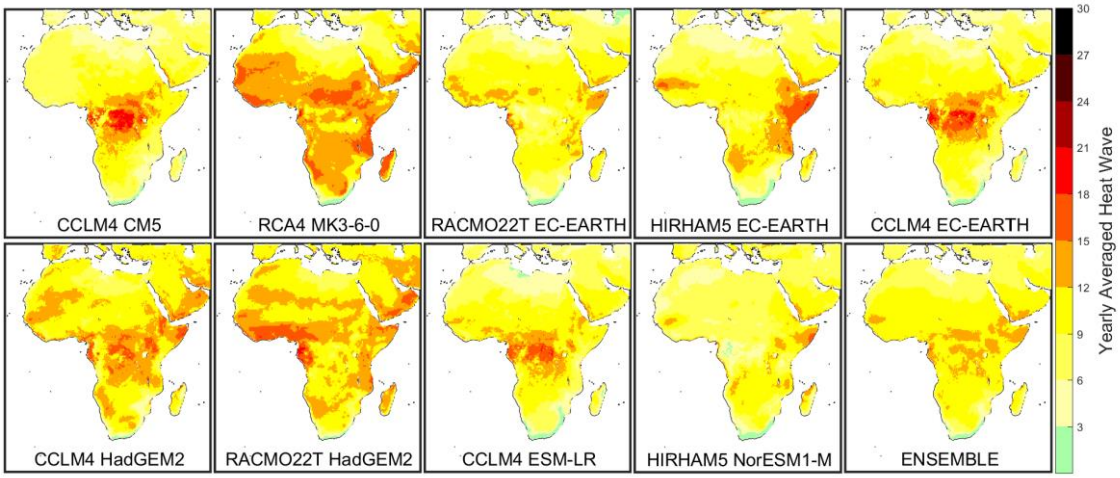


*Fig A.62.* Yearly average number of heat waves for RCP4.5 (2071-2100).

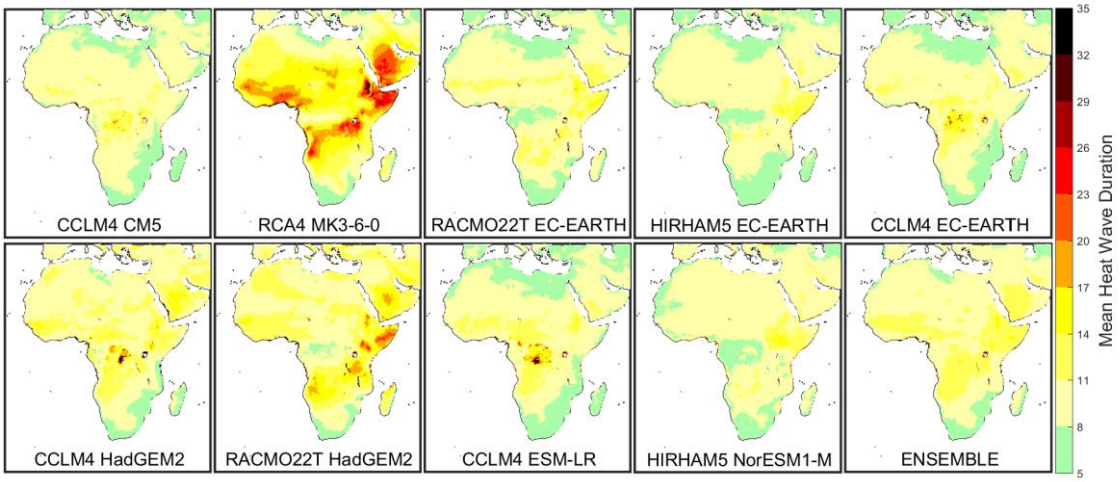


*Fig A.63.* Mean heat wave duration for RCP4.5 (2071-2100).

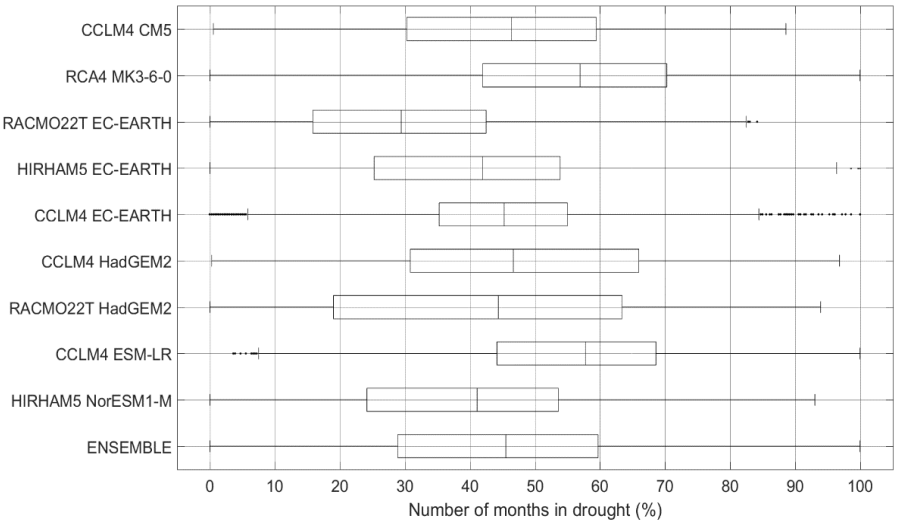


*Fig 64.* Boxplot of months in drought (percentage of months with SPEI bellow -1) for all land points of the RCP4.5 (2071-2100). The ensemble is the data of

all models.

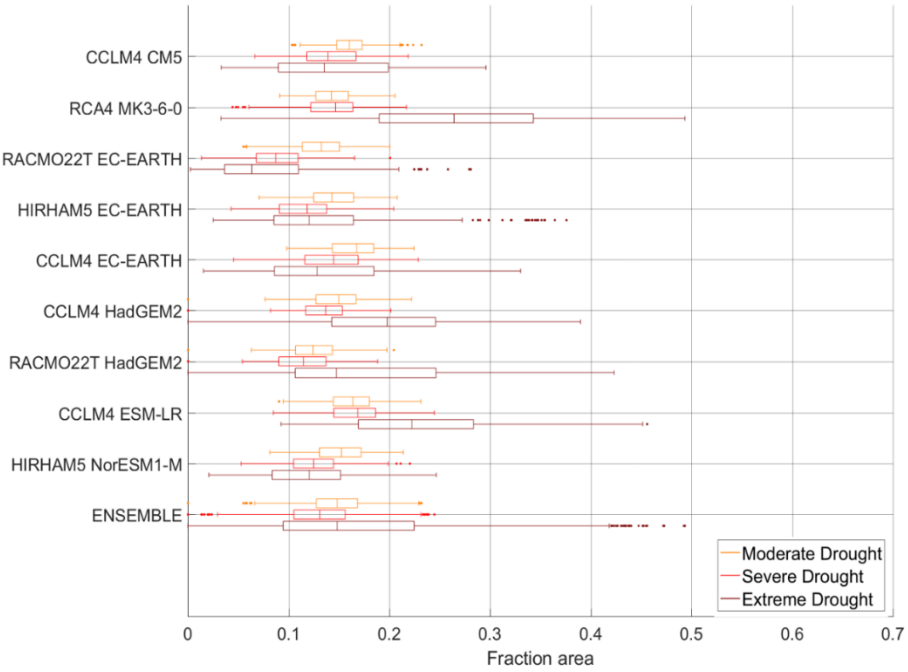


*Fig A.65*. Boxplot of the fraction area with different drought intensities (orange – Moderate drought, red – Severe drought and dark red – Extreme drought) for all land points for RCP4.5 (2071-2100). The ensemble is the data of all models.

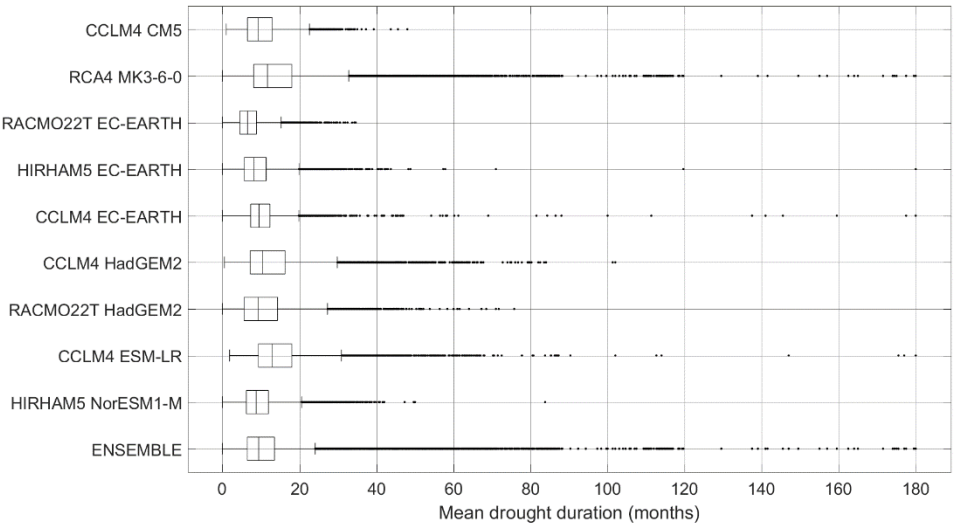


*Fig A.66.* Boxplots of mean drought duration for all land points for RCP4.5 (2071-2100) models, divided by the number of years. The ensemble is the data of all models.